

Regionalization of surface flux densities and moisture indicators in composite terrain

Promotor : dr. ir. R.A. Feddes
hoogleraar in de bodemnatuurkunde,
agrohydrologie en grondwaterbeheer

Co-promotor : dr. ir. M. Menenti
hoofd van de afdeling waterhuishouding aride gebieden
van DLO-Staring Centrum (SC-DLO) te Wageningen

NN08201, 2012

W.G.M. Bastiaanssen

Regionalization of surface flux densities and moisture indicators in composite terrain

A remote sensing approach under clear skies in Mediterranean climates

Proefschrift

ter verkrijging van de graad van doctor
in de landbouw- en milieuwetenschappen
op gezag van de rector magnificus,
dr. C.M. Karssen,
in het openbaar te verdedigen
op vrijdag 17 november 1995
des namiddags te vier uur in de Aula
van de Landbouwuniversiteit te Wageningen.

usnq18192

The research presented in this thesis was performed at the DLO Winand Staring Centre for Integrated Land, Soil and Water Research (SC-DLO)

Marijkeweg 11/22
P.O. Box 125
6700 AC Wageningen
The Netherlands

This thesis was financially supported by the Netherlands Remote Sensing Board (BCRS, Delft), the International Committee on Atmosphere-Soil-Vegetation Relations (ICASVR/IAHS) and the European Community (ECHIVAL)

**BIBLIOTHEEK
LANDBOUWUNIVERSITEIT
WAGENINGEN**

CIP DATA KONINKLIJKE BIBLIOTHEEK, DEN HAAG

Bastiaanssen, W.G.M.

Regionalization of surface flux densities and moisture indicators in composite terrain: a remote sensing approach under clear skies in Mediterranean climates / W.G.M. Bastiaanssen. - [S.l. : s.n.]

Thesis Landbouwwuniversiteit Wageningen, - With ref. - With summary in Dutch.

ISBN 90-5485-465-0

Subject headings: surface energy balance / moisture indicators

Stellingen

- 1) De dagelijkse verdeling tussen voelbare en latente warmtestroom van homogene en heterogene landoppervlaktes is eenvoudiger te beschrijven met de verdampingsfractie van de energiebalans (latente warmtestroom/netto beschikbare energie) dan met de Bowen-ratio, de Priestley & Taylor alfa of de verdampingsweerstand.
 - *Dit proefschrift*

- 2) De door Hall et al. (1992) getrokken conclusie dat de voelbare warmtestroom nauwelijks uit remote-sensingmetingen is af te leiden, zegt meer over de manier waarop de ruwheidslengte voor warmtetransport door hen is geparameteriseerd, dan over de toekomstige potenties van warmtebeelden.
 - *Hall F.G., K.F. Huemmrich, S.J. Goetz, P.J. Sellers and J.E. Nickeson, 1992. Satellite remote sensing of surface energy balance: succes, failures and unresolved issues in FIFE, J. of Geophysical Research, special issue FIFE, vol. 97, no. D17: 19061-19089*
 - *Dit proefschrift*

- 3) De conclusie van Brutsaert et al. (1993) over de vereiste nauwkeurigheid van 0,5 K voor temperatuurbeelden van het landoppervlak is alleen essentieel indien oppervlakte-temperatuur en luchttemperatuur als onafhankelijke parameters worden beschouwd.
 - *Brutsaert, W., A.Y Hsu and T.J Schumge, 1993. Parameterization of surface heat fluxes above forest with satellite thermal sensing and boundary layer soundings, J. of Applied Met., vol 32 (5): 909-917*
 - *Dit proefschrift*

- 4) De voelbare warmtestroom is verwaarloosbaar klein voor landeenheden met een oppervlakte-albedo kleiner dan 0,10 en die een oppervlakte-temperatuur hebben die het laagst is uit de regio. De latente warmtestroom is verwaarloosbaar klein voor landeenheden met een oppervlakte-albedo groter dan 0,30 en die de hoogste oppervlakte-temperatuur uit de regio hebben.
 - *Dit proefschrift*

- 5) Verdampingsweerstand voor kale bodems hebben een fysische betekenis; het gebruik van empirische relaties tussen bodemweerstand en bodemvocht zoals voorgesteld door Mafhouf & Noilhan (1991) en van de Griend & Owe (1994) zijn daarom overbodig.
 - *Mafhouf, J.F. & J. Noilhan, 1991. Comparative study of various formulations of evaporation from bare soil using in-situ data, J. of applied Met., vol 30: 1354-1365*
 - *Griend, van de, A.A. & M. Owe, 1994. Bare soil surface resistance to evaporation by vapor diffusion under semiarid conditions, Water Resources Research, vol. 30, no. 2: 181-188*
 - *Dit proefschrift*

- 6) Het directe gebruik van thermisch-infrarood metingen in een combinatievergelijking voor verdamping heeft tot gevolg dat het dampspanningstekort en de helling van de verzadigde dampspanning op regionale schaal als lastige additionele parameters moeten worden opgelost.
 - *Moran, M.S., et al., 1994. Estimating crop water deficit using the relation between surface-air temperature and spectral vegetation index, Rem. Sens. of Env. 49: 246-263*
 - *Dit proefschrift*

- 7) De procedure voor het schatten van bodemvocht op basis van de verdeling tussen voelbare en latente warmtestroom verdient evenveel aandacht als de procedure gebaseerd op backscattercoëfficiënt en emissiviteit.
- 8) De functies van Clapp & Hornberger voor de beschrijving van de onverzadigde hydraulische doorlatendheid geven meestal een verkeerde waarde. Het feit dat nagenoeg in alle hydrologische klimaatstudies deze functies worden gebruikt en dan ook nog op een schaal waarvoor ze niet zijn bedoeld, zegt iets over het klakkeloos volgen van gepubliceerde resultaten.
– Clapp, R.B. and G.M. Hornberger, 1978. *Empirical equations for some soil hydraulic properties*, *Water Resources Research* 14(4): 601-604
- 9) De noodzaak van het aanleggen van drainage in verzoute irrigatiegebieden laat zich het beste vergelijken met die van het aanleggen van het stedelijk riool.
- 10) Vanwege het latente karakter wordt verdamping ten onrechte minder interessant voor de bodemvochtcondities beschouwd, dan neerslag.
- 11) Getabuleerde gewasfactoren om potentiële verdamping van (nog) niet-gesloten gewassen via een referentieverdamping te berekenen, zijn onbruikbaar.
- 12) Het berekenen van potentiële verdamping met behulp van standaard meteorologische metingen gedaan op de gebruikelijke waarnemingshoogte die niet aan de eis van kort en goed van water voorzien groen gras voldoen, is meer regel dan uitzondering.
- 13) De hydrologische en agro-meteorologische kennisoverdracht tussen Wageningen en bewoners van het landelijke gebied stagneert omdat onderzoekers en plattelandbewoners een lage dunk van elkaar hebben.
- 14) Het gedrag van het straatverkeer is een goede indicator voor het organisatorisch en maatschappelijk functioneren van een land.
- 15) Na enige jaren werkervaring zou de prestatie maatgevend moeten zijn voor de financiële regeling van onderzoekers. De genoten opleiding is wel voor het startsalaris van belang, maar behoort geen altijddurend prijskaartje te zijn.
- 16) De persoonlijke status in de maatschappij dient niet aan drukte te worden afgeleid.
- 17) Het persoonlijk feliciteren op afscheidsrecepties, jubilea en promoties duurt te lang.

Stellingen behorende bij het proefschrift van W.G.M. Bastiaanssen

Regionalization of surface flux densities and moisture indicators in composite terrain
Wageningen, 17 November, 1995

Uitdamping

'Daar de uitdamping voornamelijk van de meerdere of mindere vochtigheid der lucht, de temperatuur en den wind afhangt, en deze weder verschillen naar gelang de ligging, zal zij onderscheiden zijn en naar de jaargetijden gewijzigd worden. Wij bezitten slechts weinig waarnemingen aangaande de uitdamping van den bodem en van met verschillende begroeide gronden. Het is welligt deels aan de omstandigheid van het ontzigtbaar zijn der dampen bij hunne opstijging, deels aan de moeite die de bepaling van de verdamping oplevert, toe te schrijven, dat wij zoo weinig waarnemingen dienaangaande bezitten'

(H. Krecke, 1869. Natuurlijke historie van Nederland, deel I, Het Klimaat)

Cover: Three-dimensional representation of actual evaporation at Las Tiesas in an irrigated agricultural area near Barrax, Castilla la Mancha, Spain.

Abstract

W.G.M. Bastiaanssen, Regionalization of surface flux densities and moisture indicators in composite terrain. Doctoral thesis, Wageningen Agricultural University, Wageningen The Netherlands. 273 pp.

The growing concern about environment has increased the number of land surface processes studies. Computer simulation models of land surface processes have been developed for a range of scales and with different levels of physical complexity. Because the interactions between soil, vegetation and atmosphere vary both spatially and temporally, regional evaporation in heterogeneous natural landscapes is difficult to predict by means of computer simulation models. Remote sensing measurements of land surface radiative properties offer however a means to indirectly measure land surface state conditions at a range of scales. A straightforward estimation of evaporation from radiative properties of the land surface is hampered by the fact that only a very few parameters of the classical flux-profile relationships can be estimated directly from remote sensing measurements. Moreover, the accuracy of surface temperature measurements necessary to solve flux-profile relationships is still poor. Inclusion of ground measurements is a possible solution, but the absence of such data on large scales and for heterogeneous land surfaces where these parameters are not measured, forms an immediate obstacle for the implementation of remote sensing algorithms.

A Surface Energy Balance Algorithm for Land (SEBAL) has been developed in a way that the need for collateral measurements is partly eliminated, a very accurate surface temperature map is no longer required (although it should be as good as possible) and a land use classification to relate surface temperature to evaporation is not needed. Each pixel is characterized by a surface hemispherical reflectance, surface temperature and a vegetation index. The methodology composes of multiple flux-profile relationships for small sub-areas. Although the concept has a physical basis, the parameters are estimated by empirical relationships, for instance a relationship between near-surface vertical air temperature difference and surface temperature forms an essential component in the estimation of the sensible heat flux density.

The absolute surface energy balance terms are estimated on an instantaneous time basis. Temporal integration of instantaneous surface flux densities is feasible using the evaporative fraction (latent heat flux density/net available energy): The evaporative fraction remains fairly constant during daytime hours for both homogeneous and heterogeneous areas. A physical explanation for this is given. A bulk surface resistance of a heterogeneous landscape has been related analytically to canopy and bare soil evaporation resistances. Measurements in central Spain have shown that the evaporative fraction and bulk surface resistance are suitable indicators to describe areal patterns

of near-surface soil water content. Although the bulk surface resistance has a distinct diurnal variation, it is much less affected by changes in net available energy and therefore preferred to describe the energy partitioning for longer time series (weeks, months).

SEBAL has been validated with data available from regional evaporation projects in Egypt and Spain. The error of high resolution evaporative fraction estimations decreases from 20% to 10% at a scale of 1 km to 5 km respectively. The error of low resolution evaporative fraction images at a scale of 100 km is approximately 1 to 5 %. Hence, the error averages out if a larger set of pixels is considered. It is concluded that the uncertainty of evaporation in regional water balances and model studies can be substantially reduced by estimating evaporation with remote sensing measurements using the proposed SEBAL technique.

Key words: evaporation, surface energy balance, land surface flux densities, remote sensing, surface temperature, surface hemispherical reflectance, vegetation index, land surface parameterization schemes, surface resistance, evaporative fraction, heterogeneity, diffusivity, validation

This thesis is also published as Report 109, DLO Winand Staring Centre (SC-DLO), Wageningen, The Netherlands

Woord vooraf

De wetenschappelijke omscholing die ik als een op de praktijk gerichte irrigatie-ingenieur nodig had om aan de beschrijving van de regionale verdamping in aride gebieden te kunnen bijdragen, kwam geheel van de zijde van mijn co-promotor Dr. Massimo Menenti. Zonder diens inhoudelijke ondersteuning en visie op het interpreteren en beschrijven van onderzoeksresultaten had mijn werk nooit de vorm van een proefschrift kunnen krijgen. Promotor Prof. dr. Reinder Feddes ben ik zeer erkentelijk voor zijn zorgvuldige begeleiding en het wetenschappelijke vertrouwen dat hij mij heeft gegeven. De gezamenlijke discussies met Reinder en Massimo gaven altijd genoeg stof en houvast om mijn manuscripten te verbeteren. De directeur van DLO-Staring Centrum, Ir. Gerard Oosterbaan, wil ik bedanken voor de ruimte die ik heb gekregen het in dit proefschrift beschreven onderzoek uit te voeren en via internationale symposia met vakgenoten te bespreken.

Voor het kraken van de bits en bytes waren naast hardware ook aandachtige operators nodig. De beeldanalyses werden verricht door Ir. Kees de Zeeuw, Ir. Henk Pelgrum, Ir. Tamme van der Wal en Ir. Rob Roebeling. Hopelijk vind ik nog eens tijd om zelf de bewerkingen uit te voeren.

Met plezier blik ik terug op de inhoudelijke discussies gevoerd met (ex-) Staringgenoten Ir. Klaas Metselaar, Ir. Gerard Nieuwenhuis, Dr. Han Dolman, Dr. Jan Hoeks, Ir. Koen Roest, Dr. Pavel Kabat, en Ir. Herman Thunnissen. Slechts bij een nauwkeurige ondersteuning kan een proefschrift tot in detail worden afgerond: Bram ten Cate, Erik van Ravenstein, Oskar Albers, Martin Jansen en Sylvia Kuster hebben de opmaak verzorgd. Leo van Zwam ben ik dank verschuldigd voor de hoge efficiëntie waarmee hij mij een sub-bibliotheek met kopieën over verdamping heeft verschaft.

I thank Ir. Han Stricker and the members of the Department of Water Resources of Wageningen Agricultural University for provision of the soil moisture data collected during EFEDA as well as the acquisition of Figure (4.10). A word appreciation goes also to the co-operative attitude of the other EFEDA participants and to Dr. Henk de Bruin in particular who made the surface flux densities available to me. I am indebted to Eng. Mohammed Hussein Abd El Karim from the Groundwater Research Institute in Cairo for the necessary preparations of the field expeditions towards the Qattara Depression in Egypt. I wish to acknowledge the cooperation with the team members of the Reuse of Drainage Water Project and for provision of the SIWARE output data. The assistance of Prof. Jiemin Wang from the Lanzhou Institute for Plateau Atmospheric Physics in Lanzhou, China, for delivering land surface radiative data is highly appreciated.

Waardering gaat tevens uit naar Prof. dr. Bert Holtslag van het Koninklijk Nederlands Meteorologisch Instituut (KNMI) en het Instituut voor Marien en Atmosferisch onderzoek Utrecht (IMAU) die me heeft aangespoord zoveel mogelijk algemeen geaccepteerde standaard micro-meteorologische grondslagen in SEBAL te verwerken.

De in dit proefschrift beschreven methodiek voor het karteren van energiebalansen op regionale schaal kon slechts worden uitgevoerd door meerjarige financiële middelen van de BeleidsCommissie Remote Sensing (BCRS) te Delft. De BCRS en Dr. Nico Bunnik en Drs. Gerard van der Kolff van het programmabureau in het bijzonder, ben ik erkentelijk voor de ondersteuning van het onderzoek.

Na het afronden van deze studie, hoop ik samen met Corrie, Loes en Gijs, de dagelijkse gebeurtenissen op een meer onbelemmerde manier te beleven.

Due to unforeseen technical limitations, greek symbols appear in this thesis as roman characters whereas they should have been printed as italics

Contents

	page
Abstract	vii
Woord vooraf	ix
1 Introduction	1
1.1 Natural variability of land surface flux densities	1
1.2 Land surface parameterization schemes	5
1.3 Remote Sensing and land surface flux densities	7
1.4 Objectives	10
1.5 Outline of the thesis	10
2 Theory of land surface evaporation	13
2.1 Coupling of energy and mass balances	13
2.2 Moisture and heat transport processes in the soil	20
2.2.1 Soil water transport processes	20
2.2.2 Soil heat transport processes	31
2.3 Moisture and heat transport processes in the atmosphere	33
2.3.1 Planetary Boundary Layer	33
2.3.2 Flux-profile relationships for homogeneous land surfaces	35
2.4 Concluding remarks	42
3 Parameterization of land surface flux densities in the soil-vegetation-atmosphere continuum	45
3.1 Layered resistance schemes	45
3.2 Resistance schemes for homogeneous individual land surface elements	47
3.2.1 Sensible heat flux density	47
3.2.2 Soil heat flux density	48
3.2.3 Latent heat flux density	49
3.3 Resistance schemes for heterogeneous land surfaces	54
3.3.1 Sensible heat flux density	55
3.3.2 Latent heat flux density	58
3.4 Surface temperature and evaporation	61
3.5 Length scale of land surface flux densities	62
3.6 Concluding remarks	65

4 The Mediterranean study areas	67
4.1 Selection of test sites	67
4.2 Qattara Depression, Egypt	68
4.3 Eastern Nile Delta, Egypt	72
4.4 Castilla la Mancha, Spain	75
5 Experimental evaluation of the diurnal variation of moisture indicators	81
5.1 Space and time variation of surface flux densities	81
5.2 Minimum and maximum evaporation	82
5.3 Measurement techniques used in the Qattara Depression	85
5.4 Temporal behaviour of surface flux densities and moisture indicators	86
5.5 Understanding bare soil surface resistance using simulations with EVADES	91
5.6 Evaporative fraction and relative evaporation	95
5.7 Concluding remarks	99
6 Derivation of empirical relationships between hydro-meteorological parameters and radiative properties of the land surface	101
6.1 Land surface radiative properties and exchange processes	101
6.2 Surface vs. planetary reflectance: $r_0(r_p)$ relationship	104
6.3 Surface vs. satellite temperature: $T_0(T_{sat})$ relationship	107
6.4 Soil heat / net radiation flux density ratio: $G_0(Q)$ relationship	110
6.5 Surface temperature vs. hemispherical surface reflectance: $T_0(r_0)$ relationship	116
6.5.1 Soil physical explanation	116
6.5.2 Experimental evidence of regional $T_0(r_0)$ relationships	122
6.6 Near-surface vertical air temperature differences vs. surface temperature: $\delta T_{a-sur}(T_0)$ relationship	125
6.7 Concluding remarks	132
7 SEBAL parameterization for distributed land surface flux densities	135
7.1 General schematization	135
7.2 Determination of surface radiative properties	138
7.3 Net radiation flux density	145
7.4 Soil heat flux density	146
7.5 Momentum flux density	146
7.6 Sensible heat flux density	158
7.7 Latent heat flux density	161
7.8 Concluding remarks	162
8 Surface flux densities and moisture indicators estimated with SEBAL: Validation, spatial variability and length scales	167
8.1 Validation of surface flux densities and moisture indicators	167

8.1.1 Validation strategy of surface flux densities	167
8.1.2 Validation of surface flux densities with NS001 data	169
8.1.3 Validation of moisture indicators with NS001 data	173
8.1.4 Validation of surface flux densities with Thematic Mapper data	175
8.1.5 Validation of moisture indicators with Thematic Mapper data	178
8.1.6 Low resolution observations in Egypt	178
8.2 Spatial variability	185
8.2.1 Spatial variability of surface hemispherical reflectance, vegetation index and surface temperature	185
8.2.2 Length scale of land surface flux densities	192
8.2.3 Multi-resolution land surface flux densities	193
8.3 Space and time integration of surface flux densities and moisture indicators	197
8.3.1 Spatial integration in Castilla la Mancha	197
8.3.2 Lower Egypt	208
8.4 Concluding remarks	210
9 Parameter variability and impact on surface flux densities and moisture indicators	213
9.1 Approach	213
9.2 Physical characteristics of the selected land surfaces	215
9.3 Sensitivity analysis of surface flux densities and moisture indicators	219
9.4 Uncertainty analysis of surface flux densities and moisture indicators	223
9.5 Concluding remarks	227
10 Conclusions	229
References	233
Annexes	
Annex 1 Solar radiation and near-surface vertical air temperature difference observations in the Qattara Depression	251
Annex 2 Calibration of EVADES simulations	253
Annex 3 EFEDA heat flux densities, June 29, 1991	255
Annex 4 EFEDA heat flux densities, June 12, 1991	257
Annex 5 Radiative land surface properties of the main land use categories in the Eastern Nile Delta and Eastern Desert	259

Colour Plates

1 Hemispherical surface reflectance, Qattara Depression, 7 August, 1986	179
2 Surface temperature, Qattara Depression, 7 August, 1986	179
3 Latent heat flux density, Tomelloso, 29 June, 1991	182
4 Latent heat flux density, Barrax, 29 June, 1991	183
5 Evaporative fraction, Barrax, 29 June, 1991	186
6 Daily integrated evaporation, Nile Delta, 5 August 1986	187
7 Surface resistance to evaporation, Castilla la Mancha, 12 June, 1991	190
8 Surface resistance to evaporation, Iberian peninsula, 29 June, 1991	191
9 Surface energy balance, Eastern Nile Delta, 27 July, 1987	194
List of frequently used symbols	261
List of acronyms	267
Samenvatting	269
Curriculum Vitae	273

1 Introduction

1.1 Natural variability of land surface flux densities

Surface energy balance

The exchange processes occurring at the land surface are of paramount importance for the re-distribution of moisture and heat in soil and atmosphere. The land surface connects the moisture and heat balances of the soil and atmosphere. The thermodynamic equilibrium between dominantly turbulent transport processes in the atmosphere and dominantly laminar processes in the soil manifests itself in the energy balance which for land surfaces reads as:

$$Q^* = G_0 + H + \lambda E \quad (\text{W m}^{-2}) \quad (1.1)$$

where

- Q^* = net radiation flux density
- G_0 = soil heat flux density at the land surface
- H = sensible heat flux density
- λE = latent heat flux density

In Eq. (1.1), the energy required for photosynthesis and the heat storage of the vegetation are ignored. The sign convention of Eq. (1.1) is that Q^* is considered positive when radiation is directed towards the land surface, while G_0 , H and λE are considered positive when directed away from the land surface. In this study, the energy balance terms of Eq. (1.1) are denoted as land surface flux densities. The partitioning between G_0 , H and λE is controlled by the exhalation of water vapour through stomata, bare soil and open water bodies. The soil wetness conditions are to a large extent established by hydrological processes such as evaporation, infiltration, capillary rise, percolation and drainage. The land surface hydrology affects the near-surface moisture conditions and thus controls the partitioning between G_0 , H and λE .

Spatial scales

As a result of the spatial heterogeneity of water availability, soil physical properties, vegetation cover and hydrological processes, the soil moisture status and land surface flux densities vary spatially. The scale of variability of land surface flux densities may be as low as a fraction of a metre, and time variations over a period of minutes may be significant. There is no general consensus how to aggregate soil moisture, θ , and land surface flux densities, G_0 , H , and λE from patch to regional scale and beyond. Knowledge of the area average land surface flux density is however an essential component in many hydrological and meteorological studies on the regional scale.

From a statistical point of view, a semivariogram may provide a concise description of the extent of spatial variability. A semivariogram is a plot that expresses the spatial dependence of a parameter value on the parameter value at a neighbouring location. Classically, semivariograms are used to express the heterogeneity of static parameters in *inter alia* hydrogeology (e.g. de Marsily, 1986) and subsurface hydrology (e.g. Gelhar, 1993). A semivariogram of land surface processes such as H and λE , holds for short periods only. Expressions related to energy partitioning such as the Bowen ratio ($\beta = H/\lambda E$, Bowen, 1926) or evaporative fraction ($\Lambda = \lambda E/(\lambda E + H)$) are simplified tools for describing the relationship between H and λE . The semi-variance of Bowen ratio observations collected at a distance z , $\gamma_\beta(z)$, can be expressed as half the mean-squared difference between many β -ratio samples separated by a distance which is commonly referred to as the lag z :

$$\gamma_\beta(z) = \frac{1}{2n} \sum_{i=1}^n [\beta(x_i) - \beta(x_i + z)]^2 \quad (-) \quad (1.2)$$

where n represents the number of sample pairs and x_i is the position of sample i . The sill in Figure 1.1 represents the level of constant semi-variance $\gamma(z)$. The nugget represents the smallest scale semi-variance. The range or correlation length is a statistical measure used, to establish the degree of similarity between sample values and their distance. Beyond the correlation length, the parameter value is uncorrelated with distance and a statistically stationary situation is obtained.

The degree of spatial variability in land surface processes changes with scale. An area is statistically homogeneous if the observation scale exceeds the correlation length (Gelhar, 1993). The semi-variance expresses the intra-variability of the considered parameter. Hence, the variability in land surface flux densities can be significant at micro-scale but will not be noticed if samples are taken at a much larger horizontal scale. At space intervals smaller than the correlation length, $d\gamma/dz \neq 0$, and spatial heterogeneity is a function of $d_z\gamma(z)$ with the largest variability arising at the steepest slopes. In most hydrological and meteorological studies, the correlation length is only a fraction of the horizontal scale on which the process needs to be quantified. Field observations of the H and λE flux densities and soil moisture are usually available for areas that are smaller than the correlation length and thus an area-integration procedure is needed to obtain the area-representative value.

A specific form of application for correlation lengths in soil science is the Representative Elementary Volume (REV). REV can be used to conceptualize the natural spatial variability of soil volumes. Bear (1972) described the REV as the scale at which soil parameters are independent of their sample size, which coincides with our definition of correlation length for land surface processes. In the framework of landscape heterogeneity, Wood et al. (1988) used the two-dimensional Elementary Representative Area (ERA)

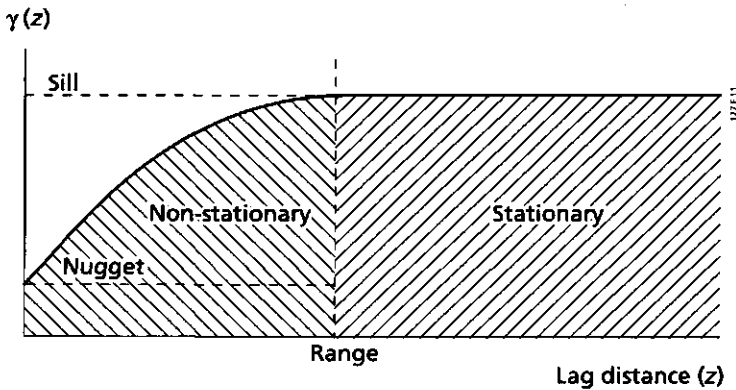


Fig. 1.1 Semivariogram of spatially variable parameters, emphasizing the scale at which land surface processes are spatially independent and the scale where heterogeneity expressed as $d_2\gamma(z)$ is fully developed

for distinguishing the threshold scales at which the statistical characterization of area-average hydrological processes in catchments are similar.

Temporal scales

A further difficulty in regionalizing land surface flux densities is the wide range of temporal scales. Due to the large daily amplitude of Q^* , the turbulent H and λE flux densities behave very dynamically and, in meteorological studies, are usually described in time frames of seconds to minutes. The Planetary Boundary Layer (PBL) is the region of the lower atmosphere which responds continuously to the 'fast' H and λE flux densities. Since the PBL conditions above land unit i can be governed by land unit ii upstream of unit i , the interpretation of atmosphere-vegetation interactions under advective conditions needs ample attention when extrapolating land surface flux densities to a larger length scale (Klaassen, 1992).

Compared to the atmospheric medium, the porous soil matrix creates much more resistance to mass and heat flow with less mixing. Consequently, length scales are smaller and the temporal scales larger. Evaporation in hydrological studies is therefore usually considered as a time integral for a 24 hours period of λE .

Spatial aggregation of non-linear processes

A proper quantification of the area-average surface flux density $\langle F_0 \rangle$ in composite terrain, either from a single point observation or from a limited number of distributed data, is one of the most challenging questions in regional environmental studies:

$$\langle F_0 \rangle = \frac{1}{A} \int_A F_{0,i}(a_i) da_i \quad (1.3)$$

where a_i is the fractional area belonging to class i and A is the size of the total study area. The spatial aggregation of flux densities $F_{0,i}$ arising in a land mosaic over larger scales (Figure 1.2), is usually achieved by a weighted integration of distributed flux densities (Koster and Suarez, 1992).

The vertical H and λE flux densities in homogeneous terrain can be more generally expressed as special versions of Ohm's law:

$$F_0 = \frac{c_2 - c_1}{r_{1,2}} \quad (1.4)$$

where the numerator represents the vertical difference of the entity c (i.e. potential difference) and r is the resistance to flow of entity c . Moisture and heat flux densities depend in a strictly non-linear way on their state variables and physical properties of the Soil-Vegetation-Atmosphere-Transfer scheme (SVAT). The non-linearity between flux densities and state variables, flux densities and system properties and state variables and system properties implies that simple linearly averaging does not yield the correct area-effective land surface flux density \bar{F}_0 . The occurrence of non-linear processes implies that in general $\langle \delta c \rangle / \langle r \rangle \neq \langle F_0 \rangle$ and that a solution with $\delta \bar{c} \bar{r} = \bar{F}_0$ (where

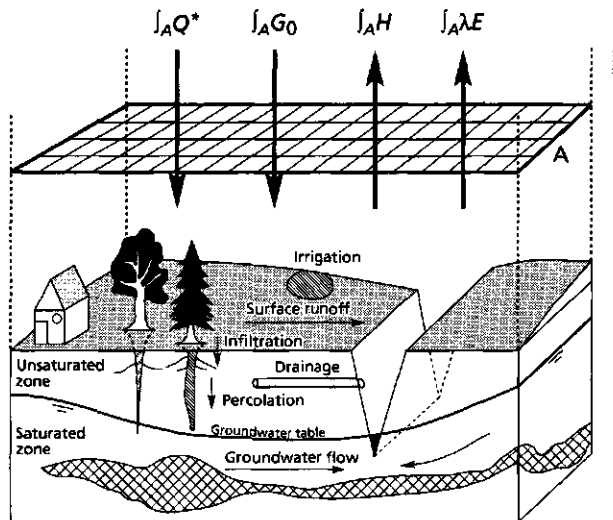


Fig. 1.2 Schematic representation for obtaining area-average surface flux densities from spatially variable hydrological processes

$\tilde{F}_0 = \langle F_0 \rangle$) has to be found. The basic issues addressed in upscaling studies of land surface flux densities can therefore be reduced to:

- How to derive \tilde{F}_0 from an extremely limited set of point observations or complete absence of distributed *in-situ* $F_{0,i}$ flux densities ?
- Are effective parameters sufficiently accurate to predict \tilde{F}_0 ?
- How to obtain effective parameter values for \tilde{c} and \tilde{r} from a very limited set of distributed c_i and r_i -values?

1.2 Land surface parameterization schemes

One-dimensional land surface parameterization schemes

A land surface parameterization scheme dynamically simulates the water (and heat) flow processes below and at the land surface by recognizing the following components:

- Vertical distribution of water content (and temperature) within a schematized soil profile;
- Vertical moisture (and heat) flow between the layers of a schematized soil profile;
- Radiation balance at the land surface;
- Surface energy balance from the available energy and sub-surface moisture and heat flow rates.

Two well known one-dimensional advanced land surface parameterization schemes are BATS (Dickinson et al. 1986) and SiB (Sellers et al. 1986). An example of a model which is traditionally more oriented towards the description of unsaturated zone hydrology and daytime values of evaporation, is SWATRE (Feddes et al., 1978). The simplest tool for predicting land surface evaporation processes is the so-called *bucket model* (e.g. Manabe, 1969). Land surface parameterization schemes can be coupled with atmospheric models to describe the effect of atmospheric horizontal interferences on the vertical exchange rates at the land surface. Kroon and de Bruin (1993) provided multiple examples of coupling a two-dimensional PBL model with one-dimensional land surface parameterization schemes of different complexity.

The area-average flux densities for each gridsquare in large scale studies are usually predicted by lumped models that consider the processes within a gridsquare to be strictly uniform. Lumped models describe the heterogeneous land surface flux densities with effective parameters such as \tilde{r} which implicitly assumes that laws designed for patch scale (Eq. 1.4) provides the correct gridsquared-average flux density. The aforementioned BATS and SiB models are examples of lumped models.

Over against that, semi-distributed models account for spatial variability by using probability density functions, pdf's, on one or more of their model parameters, i.e. the stochastic-dynamic approach. Entekhabi and Eagleson (1989) improved the predictions of spatial patterns of infiltration by considering a gamma type pdf for the degree of soil moisture saturation. Famiglietti and Wood (1991) used a so-called 'topography-soils' index for similar reasons. Avissar (1991) and Dolman (1992) accounted for spatial heterogeneity in stomatal conductance by considering a log-normal and gamma type of pdf, respectively.

Avissar and Pielke (1989) and also Koster and Suarez (1992) identified multiple independent sources of heat and water vapour in land surface parameterization schemes, which provide a much more accurate representation of composite vegetation stands. In that case, a total area will be divided in a number of smaller and energetically independent sub-areas or tiles. The total area-average behaviour is obtained by weighing the individual sub-area flux densities.

Two and three dimensional land surface parameterization schemes

One-dimensional schemes may fail when lateral transport of surface water through open networks (channels, rivers), overland flow in sloping terrain and groundwater movement in aquifers are important hydrological phenomena. In all those cases, non-local hydrological processes may be of overriding importance for local energy partitioning. The incorporation of long distance lateral transfer seems to be crucial for predicting the energy and water balance at the irrigated pediments of mountainous regions (e.g. Himalaya, Andes, Alps etc) and deltas, e.g. the Nile Delta. Two and three-dimensional distributed parameter hydrological models with physical attributes of the land surface predict both vertical and lateral water movement (e.g. SHE→Abbott, 1986). Although the latter category of models accounts for both vertical and horizontal flow components and allows for interactions between surface and groundwater, they rarely recognize turbulent H and λE flux densities and are less data friendly for the prediction of land surface hydrology on a large scale. The combination of two and three dimensional land surface parameterization schemes with PBL models that apply to similar length scales is still a gap in the era of modelling. Although ideal from a descriptive point of view, such coupling implies a computational burden and a high demand on terrain description. Hence, a trade-off between data availability and complexity of the land surface parameterization schemes has to be made.

In the era of model development, the number of land surface parameterization schemes is still growing, while research on techniques for verifying the model outputs at heterogeneous land surfaces remains an issue that need future attention (McGuffie and Henderson-Sellers, 1987). Figure 1.1 has shown that model predictions at a horizontal scale exceeding the correlation length may not be compared with field observation executed at a scale $d, \gamma(z) \neq 0$. Hence, there is a serious question in large-scale hydrology and meteorology studies: *How do we test the performance of the land surface*

parameterization schemes? Testing against real data is necessary, but it is immediately obvious that such attempts involve a gradation of scales to establish the link with field observations. In this respect, the benefit of remote sensing measurements is worth investigating, since information related to the land surface characteristics can be measured by satellite platforms at a range of length scales and with varying spatial and temporal resolutions.

1.3 Remote Sensing and land surface flux densities

Conventional measurements of land surface flux densities

With conventional measurements of land surface flux densities, one must address the question of what is actually being measured: a point, a weighted spatial average, a temporal point average, etc. (Cushman, 1986). If the area influencing the field measurement of F_0 is larger than the correlation length of that particular flux density, the semi-variance will be at sill level and the exact position of the measurements is of less relevance. If the area of influence lies within the correlation length, the site selection for conducting measurements becomes a very crucial issue. If the goal is to measure natural variability, measurement should be conducted simultaneously at various points with small horizontal scales (e.g. Andre et al., 1986) so that $d_2\gamma(z)$ is large.

Remote sensing estimations of land surface flux densities

Remote sensing data provided by satellites are a means of obtaining consistent and frequent observations of spectral reflectance and emittance of radiation at elements in a patchy landscape and on a global scale (Sellers et al., 1990). Since only the parameters mentioned in Table 1.1 are measurable, regional latent and sensible heat flux densities with current satellite systems need to be estimated indirectly (Pinker, 1990).

An ensemble of satellite pixels with the resolution being a small fraction of the correlation length, provides a sound basis for measuring the spatial variation of the land surface process being examined. Consequently, the histograms for a series of high-resolution pixels in composite terrain exhibit natural scatter (see Figure 1.3). If on the contrary the resolution is equal to or exceeds the correlation length, all pixels will get approximately similar values and the histograms will be flat (see Figure 1.3). Curran (1988) stated perfectly that 'a ground resolution element larger than the statistical range will probably average the spatial variability within a field and will, therefore, be a suitable ambassador for that particular field'.

Table 1.1 Radiometric characteristics of the land surface and their interpretation into attributes being linked to sensible and latent heat flux densities

Remote sensing version	Land surface attribute	Source
Surface radiation temperature	Surface temperature, T_0	Wan and Dozier, 1989; Becker and Li, 1990
Spectral radiation temperature	Surface thermal emissivity, ϵ_0	Kahle and Alley, 1992; Schmugge et al., 1995
Surface directional reflectance	Surface hemispherical reflectance, r_0	Pinty et al., 1985; Menenti et al., 1989a
Degree of cloudiness	Solar radiation, K^d	Dedieu et al., 1987; Raschke et al., 1991
Spectral reflected radiances	Vegetation indices, <i>NDVI</i>	Justice et al., 1985; Tucker, 1986
Laser beam profiles	Aerodynamic roughness length, z_{0m}	Menenti and Ritchie, 1994
Laser beam profiles	Leaf area index, <i>LAI</i>	Menenti and Ritchie, 1994
Spectral reflected radiances	Leaf area index, <i>LAI</i>	Asrar et al., 1992; Pierce et al. 1992
Backscatter coefficient	Soil moisture, θ	Fung et al., 1992; Oh et al., 1992
Microwave emissivity	Soil moisture, θ	Schmugge et al., 1992; Owe et al., 1993

Remotely sensed surface albedo, vegetation index and surface temperature affecting land surface flux densities are nowadays available at a wide range of spatial (1m - 5km) and temporal (30 minutes -16 days) scales. Although promising results were reported for determining land surface flux densities by remote sensing at patch scale and for relative homogeneous land surfaces, the ability to use remote sensing measurements for deriving land surface flux densities in heterogeneous land surfaces and on large scale has not been fully developed yet.

An algorithm using surface albedo, vegetation index and surface temperature synergetically, has been developed by the author of this study to calculate the land surface flux densities on the basis of existing physical laws and is presented in Chapter 7. This new Surface Energy Balance Algorithm for Land (SEBAL) algorithm creates the possibility to analyse natural variation of Q^* , G_0 , H and λE if the pixel resolution is smaller than the correlation length. Spatial aggregation at any scale coarser than the pixel resolution can be achieved by aggregating the land surface flux densities for a certain ensemble of pixels which creates the opportunity to make a comparison of $\langle F_0 \rangle$ with the large scale \bar{F}_0 values predicted by land surface parameterization schemes.

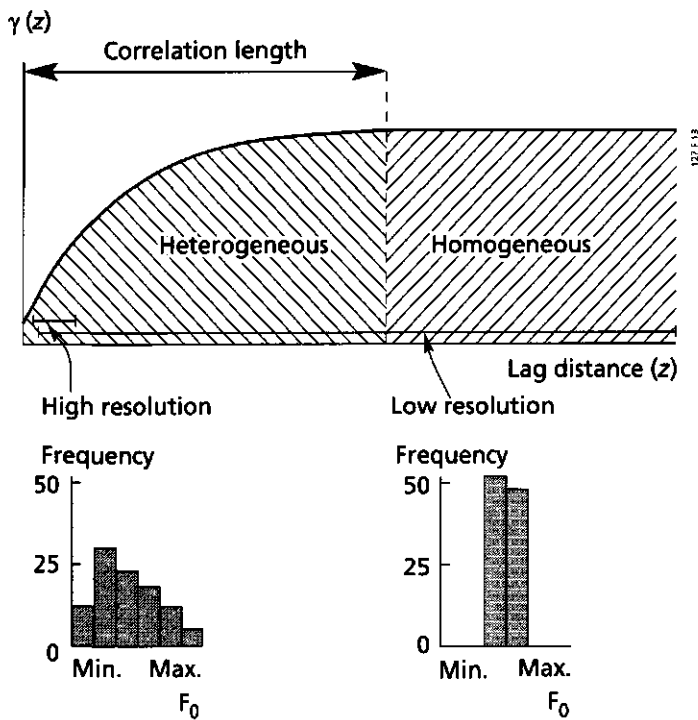


Fig. 1.3 Distribution functions in relation with correlation length and horizontal sampling resolution

It is widely known that λE relates to soil moisture, θ , and vice versa. Microwave radiometry and Synthetic Aperture Radar measurements of the backscatter coefficient are both microwave technologies that are able to detect the soil dielectric properties remotely (see Table 1.1). Since the soil dielectric properties are highly sensitive to the presence of water, soil water content can be indirectly obtained. Results with field experiments confirm that spatial moisture patterns in semi-arid environments can be interpreted from microwave measurements with reasonable accuracy (Botswana: Owe et al., 1993; Pennsylvania: Wood et al., 1993). In the absence of microwave measurements or microwave measurements on the wrong scale, resolution, wavelength or moment, soil moisture may alternatively be indicated by means of the energy partitioning between H and λE (Table 1.2). Hence, estimations of pixel-scale energy partitioning can be employed to retrieve classes of land wetness.

Table 1.2 Conceptually different approaches for determining soil water content by remote sensing

Spectral range	Moisture indicator
Microwave spectral range	Soil dielectric constant
Visible/infrared spectral range	Energy partitioning

1.4 Objectives

The necessity to determine area-representative flux densities and related soil moisture for large-scale heterogeneous land surfaces which cannot be measured conventionally, has motivated the development of a remote sensing flux-algorithm on the basis of visible, near-infrared and thermal-infrared data. A general conceptual framework is described in this thesis for achieving the following ultimate objective:

Providing a basis for estimating the surface energy balance and moisture indicators for a wide spectrum of land types ranging from patch to regional scale in which the necessity for ground measurements is reduced as much as possible.

This study will address:

- The derivation of empirical relationships between hydro-meteorological and remotely observable parameters;
- The identification of the semi-variances and pdf's of relevant parameters controlling the surface energy balance;
- The estimation of the natural variability of the land surface flux densities ;
- The aggregation of distributed surface flux densities into area-average land surface flux densities ;
- The identification of a suitable moisture indicator which normalizes energy partitioning;
- The aggregation of area-average moisture indicators and validation of these indicators with in- situ and airborne data;
- The interpretation of moisture indicators into soil water content;
- The evolution of area-average surface energy partitioning and soil water content.

1.5 Outline of the thesis

The present investigation firstly summarizes the basic environmental physics needed to understand and parameterize the surface energy balance (Chap. 2). Emphasis will be given to evaporation, being the bridge between the surface energy balance and the soil water balance. Since the study areas in Egypt and Spain have an arid climate often with partially covered soils and sparse canopies, much attention is given to the description of bare soil evaporation. A list of essential hydro-meteorological parameters affecting land surface flux densities will be provided.

A one-layer parameterization scheme will be proposed in Chapter 3 to reduce the total amount of hydro-meteorological parameters required for the calculation of surface flux densities. The concept of effective parameters will be introduced for heterogeneous land

surfaces and a trade-off between what is physically desirable and practically attainable will be outlined.

Chapter 4 addresses the location of the study areas in the Mediterranean region, including the Qattara Depression in the Western Desert (Egypt), Nile Delta (Egypt) and Castilla la Mancha (Spain). Field observations carried out in the Qattara Depression form the baseline for investigating the temporal behaviour of a number of common moisture indicators (Chap. 5). The diurnal variation of fractional flux densities will be addressed.

The use of simplified relationships between environmental and remotely observable parameters will be experimentally justified in Chapter 6. Chapter 7 deals with a full explanation of the new physically based remote sensing algorithm SEBAL using the simplifications derived in Chapter 6. The required equations will be discussed stepwise.

Two heavily instrumented sites in Castilla la Mancha have been used to explore the degree of accuracy achieved by mapping land surface flux densities and moisture indicators with SEBAL (Chap. 8). The remote sensing estimations were compared with field and aircraft observations. To better explore the algorithm performance on large-scale, a comparative study with a Nile Delta water balance was carried out. Chapter 9 addresses the sensitivity and uncertainty of the SEBAL-based flux densities and moisture indicators.

2 Theory of land surface evaporation

2.1 Coupling of energy and mass balances

Radiation balance

The principal energy source that drives the land surface flux densities G_0 , H and λE , is delivered by net radiation flux density Q^* . For a flat horizontal and homogeneous surface, the all wavelength electromagnetic balance in terms of the up (\uparrow) and downwelling (\downarrow) radiative propagation is related to Q^* as follows:

$$Q^* = K^\downarrow - K^\uparrow + L^\downarrow - L^\uparrow \quad (\text{W m}^{-2}) \quad (2.1)$$

where K represents the shortwave (0.3-3 μm) and L the longwave (3 to 100 μm) radiation components. When electromagnetic radiation strikes an object, different interactions such as transmission, absorption, reflection, scattering and emission between radiation and objects arise. Planck's law for emission describes the distribution of the emitted spectral radiance electromagnetic radiation as a function of temperature:

$$L_\lambda(T)^{bb} = \frac{3.74 \cdot 10^8}{\lambda^5} \left[e^{\left(\frac{1.44 \cdot 10^4}{\lambda T}\right)} - 1 \right]^{-1} \quad (\text{W m}^{-2} \mu\text{m}^{-1}) \quad (2.2)$$

where λ (μm) is the wavelength, L_λ^{bb} ($\text{W m}^{-2} \mu\text{m}^{-1}$) is the spectral black body radiance and T (K) the temperature. The constants of Eq. (2.2) comprise the Plancks constant, the speed of light and Boltzmann constant. Eq. (2.2) gives the radiation for a perfect black body with an emissivity of one ($\epsilon = 1.0$). On the other hand, grey body radiators reflect a small fraction of longwave radiation ($\epsilon \neq 1.0$). Natural materials are usually grey bodies and consequently the emissivity is required to convert $L_\lambda(T)^{bb}$ into temperature:

$$L_\lambda(T) = \epsilon_\lambda L_\lambda(T)^{bb} \quad (\text{W m}^{-2} \mu\text{m}^{-1}) \quad (2.3)$$

Salisbury and D'Aria (1992) provided tables on ϵ_λ for terrestrial materials. Between 11.3 and 11.6 μm , the emissivity is fairly similar and close to one (0.97 - 0.99) for rocks, soils, water and vegetation. Spectral integration of Eqs. (2.2) and (2.3), yields the Stefan Boltzmann equation which for land surfaces reads as:

$$L = \int_0^\infty \epsilon_\lambda L_\lambda(T)^{bb} d\lambda = \sigma \epsilon_0 T_0^4 = \sigma (T_0^R)^4 \quad (\text{W m}^{-2}) \quad (2.4)$$

where σ ($5.67 \cdot 10^{-8} \text{ W m}^{-2} \text{ K}^{-4}$) is the Stefan Boltzmann constant, T_0 (K) is the land surface temperature and T_0^R (K) is the land surface radiation temperature. The atmosphere

consists of several layers with different concentrations of water vapour and dust. Each layer has its own heat content. The thermal stratification between near-surface level ($T \sim 300$ K) and higher altitude clouds ($T \sim 210$ K), makes a direct application of Eq. (2.4) for radiation emitted by the atmosphere impossible. Therefore, a practical approach, either with an effective black body sky radiation temperature or an effective emissivity, has to be chosen. Brunt (1932) chose the second path and introduced an overall ϵ'_a -value applying to a near surface reference where the air temperature T_a is used to estimate the downward longwave radiation reaching the land surface:

$$L^\downarrow = \epsilon'_a \sigma T_a^4 \quad (\text{W m}^{-2}) \quad (2.5)$$

Based on Planck's law, Wien's displacement law basically states that the wavelength of maximum emission is inversely proportional to temperature:

$$\lambda_{\max} = \frac{2897.8}{T} \quad (\mu\text{m}) \quad (2.6)$$

where 2897.8 is a constant $\mu\text{m} \cdot \text{K}$. Eq. (2.6) implies that at the mean Earth surface temperature of 300 K, emission is largest at $\lambda_{\max} = 9.66 \mu\text{m}$, i.e. longwave radiation. At the temperature of the sun, i.e. 6000 K, emission is largest at $0.48 \mu\text{m}$, i.e. shortwave radiation. The amount of shortwave solar radiation reaching the land surface, K^\downarrow , depends on atmospheric absorption and scattering of shortwave radiation. Atmospheric interaction of shortwave solar radiation consists of three main categories: (i) Rayleigh scattering at molecules which are small in comparison to wavelength, (ii) Mie scattering at aerosols which have roughly the size of the scattered wavelength and (iii) gaseous absorption by ozone, water vapour and mixed gases. Effects caused by Rayleigh scattering are well understood. Values for absorptivity range usually between 0.05 for a clear sky and 0.15 for cloudy and dusty atmospheres (Raschke et al., 1991). More troublesome is the quantification of aerosol Mie scattering. An explicit description of aerosol scattering can be avoided by recognizing a macroscopic atmospheric perturbation on radiation transfer by means of an effective transmission coefficient, τ_{sw} in the shortwave range:

$$\tau_{sw} = \frac{K^\downarrow}{K_{TOA}^\downarrow} \quad (-) \quad (2.7)$$

where K_{TOA}^\downarrow is the radiation entering the Top Of the Atmosphere at a horizontal plane between 0.3 and $3.0 \mu\text{m}$ (Figure 2.1). A portion of the direct solar beam K_{TOA}^\downarrow is due to Rayleigh scattering converted into the path radiance in the upper part of the atmosphere, K_a^\uparrow . For a cloud-free atmosphere and an infinite Lambertian land surface,

the radiation leaving Top Of Atmosphere, K_{TOA}^{\uparrow} can be expressed as (Fraser and Kaufman, 1985):

$$K_{TOA}^{\uparrow} = K_a^{\uparrow} + \frac{r_0 \tau_{sw}'' K_{TOA}^{\downarrow}}{1 - r_d r_0} \quad (-) \quad (2.8)$$

where

- K_{TOA}^{\downarrow} = radiation entering the Top Of Atmosphere ($W\ m^{-2}$)
- K_{TOA}^{\uparrow} = radiation leaving the Top Of Atmosphere ($W\ m^{-2}$)
- K_a^{\uparrow} = path radiation ($W\ m^{-2}$)
- r_d = atmospheric reflectance of diffuse radiation (-)
- r_0 = hemispherical reflectance of the land surface (-)
- τ_{sw}'' = two-way transmittance (-)

The atmospheric reflectance r_d can be described as the fraction of surface radiance reflected by the atmosphere. In several application studies, the hemispherical surface reflectance r_0 is commonly referred to as 'surface albedo', 'technical' or 'meteorological' albedo, being the fraction of incoming shortwave radiation at the land surface which at

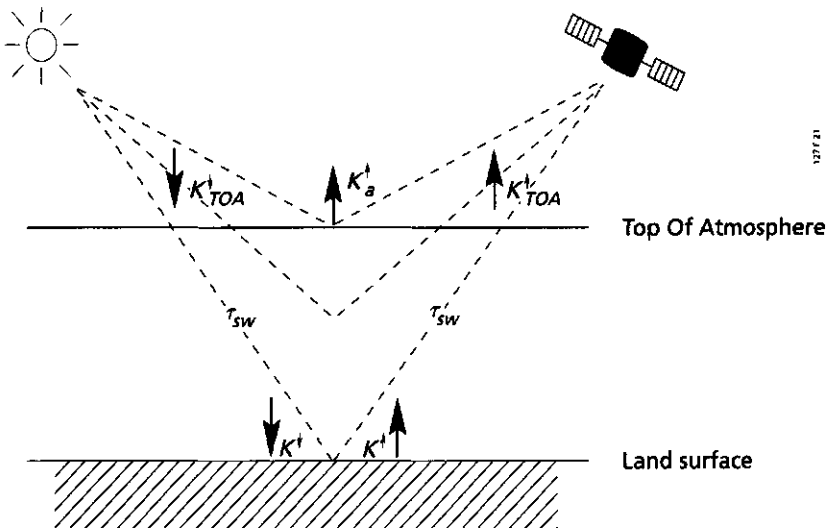


Fig. 2.1 Simplified shortwave radiation interactions between the atmosphere and the land surface

one particular moment $r_0(t)$ is reflected from land surface elements integrated across all solar wavelengths (λ) and all directions of observation (ϕ'_{su}, ψ'_{su}):

$$r_0(\phi_{su}, \psi_{su}) = \int_{0.3}^3 \int_0^\pi \int_0^{2\pi} r_0(\lambda, \phi_{su}, \psi_{su}, \phi'_{su}, \psi'_{su}) d\lambda d\phi'_{su} d\psi'_{su} \quad (-) \quad (2.9)$$

where

$r_0(\lambda, \phi_{su}, \psi_{su}, \phi'_{su}, \psi'_{su})$	= bi-directional spectral reflectance (-)
$r_0(\phi_{su}, \psi_{su})$	= hemispherical surface reflectance (-)
λ	= wavelength (μm)
ϕ'_{su}	= off nadir view angle (rad)
ϕ_{su}	= incident solar zenith angle (rad)
ψ'_{su}	= azimuth view angle (rad)
ψ_{su}	= incident solar azimuth angle (rad)

Most satellites measure a directional spectral reflectance $r_0(\lambda, \phi_{su}, \psi_{su}, \phi'_{su}, \psi'_{su})$ which by means of a bidirectional function can be converted into $r_0(\lambda, \phi_{su}, \psi_{su})$. K^\uparrow of Eq. (2.1) can be calculated after involving Eq. (2.9) and $r_0 = r_0(\phi_{su}, \psi_{su})$:

$$K^\uparrow = r_0 K^\downarrow \quad (-) \quad (2.10)$$

If $(1-\epsilon_0)$ furthermore describes reflectance in the longwave spectral range, the radiation balance of Eq. (2.1) reads:

$$Q^* = (1-r_0)K^\downarrow + \epsilon'_a \sigma T_a^4 - (1-\epsilon_0)\epsilon'_a \sigma T_a^4 - \epsilon_0 \sigma T_0^4 \quad (\text{W m}^{-2}) \quad (2.11)$$

which after introducing $\epsilon' = \epsilon_0 \epsilon'_a$ reduces to:

$$Q^* = (1-r_0)K^\downarrow + \epsilon' \sigma T_a^4 - \epsilon_0 \sigma T_0^4 \quad (\text{W m}^{-2}) \quad (2.12)$$

where

ϵ_0	= thermal infrared emissivity of the land surface (-)
ϵ'_a	= effective thermal infrared emissivity of the atmosphere (-)
ϵ'	= apparent thermal infrared emissivity of the atmosphere (-)

Evaporation from individual land surface elements

The surface energy balance introduced in Chapter 1 relates net radiation flux density Q^* , to the latent heat flux density, λE . Since water is present in vegetation stands, in herbaceous layers, in open water bodies, in soils and on foliage, a stratum of evaporation surfaces or evaporation fronts exists. Hence, multi-source land evaporation into the atmosphere occurs from several evaporating sites. Vapour arises inside the stomatal cavities of vegetated land surfaces as canopy evaporation (E_c). Substrate evaporation

(E_{sub}) refers to the vapour removed from herbaceous layers. The evaporation from open water is usually described by E_0 . Bare soil evaporation, E_{soil} and evaporation of water intercepted at foliages (E_i) are other forms of moisture exchange between land and atmosphere. These isolated vapour flux densities E_i , E_i relate to individual micro scale elements of the land surface and can be termed microscopic. Heterogeneous land surfaces with multiple evaporation fronts exhibit a three-dimensional domain for evaporation (Figure 2.2). The contributions of these individual vapour sources to a schematical flat field average latent heat flux density λE^{field} can be determined according to Eq. (2.13):

$$\lambda E^{field} = \frac{1}{Az} \int_A \int_{-z_1}^{z_2} \lambda E(a_i, z) da_i dz \quad (\text{W m}^{-2}) \quad (2.13)$$

where $z = -z_1$ represents the lowest sub-surface level where vaporization takes place and $z = z_2$ the position of the highest level. For water balance studies, only the total amount of water evaporated from a field (λE^{field}) or (sub-) catchment (λE^{catch}) is worth solving. Then, evaporation has to be aggregated further from micro-scale to macro-scale. The set of three-dimensional distributed microscopic evaporation rates λE_i , $\lambda E(x, y, z)$ can be related to λE^{catch} , using weighing coefficients ω to account for the fractional area a_i/A of each micro-scale element (see Figure 2.2):

$$\lambda E^{catch} = \lambda(\omega_1 E_i + \omega_2 E_{sub} + \omega_3 E_0 + \omega_4 E_{soil} + \omega_5 E_i) \quad (\text{W m}^{-2}) \quad (2.14)$$

The area-average latent heat flux density for a (sub-) catchment λE can also be obtained from a number of n fields:

$$\langle \lambda E \rangle = \sum_{i=1}^n \omega_i \lambda E_i^{field} \quad (\text{W m}^{-2}) \quad (2.15)$$

where

ω = fractional area of each individual vapour-producing site ($\text{m}^2 \text{m}^{-2}$)

λ = latent heat of vaporization (J kg^{-1})

E = microscopic evaporation ($\text{kg m}^{-2} \text{s}^{-1}$)

$\langle \lambda E \rangle$ = area-average latent heat flux (W m^{-2})

i = 1, n number of fields

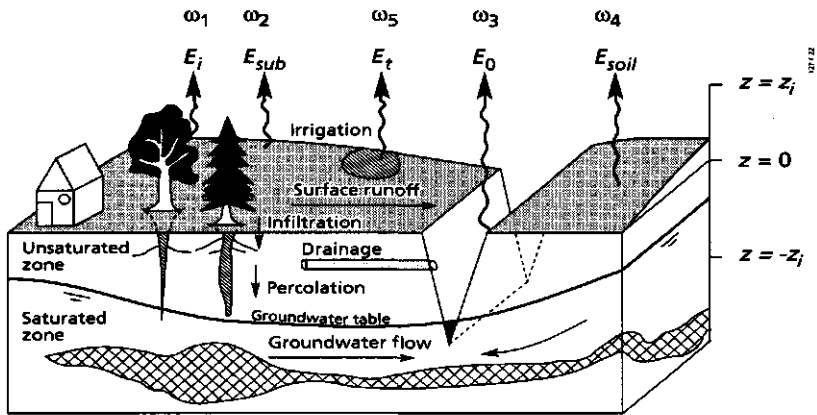


Fig. 2.2 Schematic three-dimensional representation of multiple evaporation sites in complex landscapes. The hypothetical flat land surface at $z = 0$ acts as the reference level for the computation of patch scale and regional scale evaporation rates

The horizontal homogeneous flat interface between land and atmosphere to which Eq. (1.1) applies is therefore a conceptual framework designed to assist computations. It is not intended for describing multiple pore scale and leaf scale processes.

Soil water balance

Besides net radiation flux density Q^* , λE is controlled by the availability of soil moisture. The volumetric soil water content, θ ($\text{cm}^3 \text{cm}^{-3}$), describes the volume of soil occupied by water in the liquid phase. Taking $z = 0$ at the land surface and soil depth $|z| = |-z_3|$, then water storage W is the total amount of soil water per unit area being defined as:

$$W = \int_{-z_3}^0 \theta(z) dz \quad (\text{m}) \quad (2.16)$$

Since the land surface hydrological processes related to infiltration and evaporation are in a flat area primarily vertical moisture movements, the soil water balance may be written in a one-dimensional form. The soil water balance for a single field or sub-catchment connects the bulk evaporation of soil moisture E' with the change in water storage dW , from $z = -z_3$ to $z = 0$ during a time interval dt according to:

$$\frac{dW}{dt} = P_{net} + I_r + Q - E' - R \quad (\text{m s}^{-1}) \quad (2.17)$$

where

P_{net} = net precipitation rate

I_r = irrigation water supply rate

Q = bottom flux density at $z = -z_3$, being positively upwards

- E' = evaporation rate without interception E ,
 R = runoff rate at $z = 0$
 t = time

The magnitude of the water balance terms depends on the hydrological situation and on the evaporative demand of the atmosphere. The difference between potential and actual evaporation rate, i.e. the evaporation deficit, is mainly controlled by soil water storage, W . If the soil is sufficiently moist to maintain evaporation at the maximum rate, i.e. potential evaporation, the latent heat flux density will be determined by the atmospheric demand, i.e. the radiation balance controls the evaporation process. Under drier conditions when there is a persistent soil moisture deficit, the soil water balance controls the evaporation process.

Soil heat balance

The soil heat flux density which is part of Eq. (1.1) adds heat to the soil during daytime and extracts heat from the soil during nighttime. The near-surface heat storage is the total amount of soil heat content $\rho_s c_s T_s(z)$ in a soil volume between $z = -z_4$ and $z = 0$. Per unit area it can be expressed as:

$$J_s = \int_{z=-z_4}^0 \rho_s c_s T_s(z) dz \quad (\text{J m}^{-2}) \quad (2.18)$$

Since the integration limits for water and heat balances are due to the different physical processes not necessarily identical, z_3 and z_4 have to be distinguished. The one-dimensional soil heat balance for a certain slab between $z = -z_4$ and $z = 0$ is also governed by the latent heat exchanges within this slab (see Figure 2.3):

$$\frac{d(\rho_s c_s T_s)}{dt} \delta z = G_0 + G_{bot} - \lambda E_v \quad (\text{W m}^{-2}) \quad (2.19)$$

where

- ρ_s = soil bulk density (kg m^{-3})
 c_s = soil specific heat ($\text{J kg}^{-1} \text{K}^{-1}$)
 T_s = soil temperature (K)
 G_0 = soil heat flux density at the land surface, which is positive downward (W m^{-2})
 G_{bot} = soil heat flux density at depth $z = -z_4$, which is positive upwards (W m^{-2})
 λE_v = mean latent heat flux density across depth interval δz which is positive for evaporation (W m^{-2})

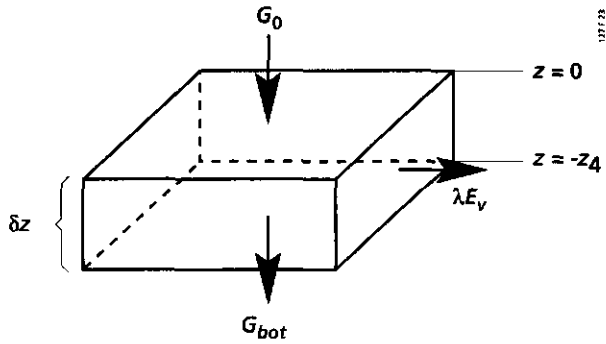


Fig. 2.3 Schematic soil heat balance in a slab with depth increment δz for a daytime situation with downward oriented flux densities.

Hence, the surface energy balance affects the soil heat content and vice versa because Eq. (2.19) demonstrates that G_0 depends on $\rho_s c_s T_s$ dynamics as well. Furthermore, Eq. (2.19) shows that the soil heat and soil water balance are directly coupled by means of λE_v , which is coupled to E' by means of E_{soil}

2.2 Moisture and heat transport processes in the soil

Due to dry and warm near-surface soil conditions, an explicit recognition of liquid, vapour and heat flow processes in soils located in (semi-) arid climates is essential to determine the surface energy, soil water and soil heat balance properly. This section does not purport to give a detailed picture on the role of combined water and heat flow mechanisms. It merely aims to provide an overview of the factors controlling the spatial and temporal variability of evaporation and how this is manifested in radiative properties of the land-surface. Furthermore, it is the purpose of this section to provide a sound basis for understanding the surface energy balance of bare soils.

2.2.1 Soil water transport processes

Soil water potential

Soil water potential is the measure of the capacity of soil water in a soil matrix at equilibrium for doing work as compared to the capacity of pure free water at the same temperature and pressure. Since soil particles are hydrophilic, water in unsaturated soil has a lower capacity for doing work, yielding a lower potential compared to free water. The soil water potential is therefore considered negative. In hydrological studies, the soil water potential is usually expressed according to an energy on weight basis, yielding

an equivalent pressure head with the dimension of a length (unit metre). A series of pressure heads may be distinguished in soil (e.g. Feddes et al., 1988):

$$h = h_m + h_{osm} + h_{pneu} + h_g \quad (m) \quad (2.20)$$

where

- h = total pressure head
- h_m = pressure head due to matric forces
- h_{osm} = pressure head due to osmotic forces
- h_{pneu} = pressure head due to gaseous forces
- h_g = pressure head due to gravitational forces

The matric pressure head, h_m , describes the effect of various soil-water interactions reflecting the attraction of water molecules by the soil matrix as well as to each other. The gravitational pressure head, h_g , describes the influence of gravity. In a non-saline environment with exclusion of h_{osm} and for conditions where gaseous pressure heads h_{pneu} make a minor contribution, h may be approximated as:

$$h = h_m + h_g \quad (m) \quad (2.21)$$

Liquid-soil interactions

Adhesion in soil becomes apparent when water in the liquid phase adheres to the soil matrix. The mutual attraction of molecules in liquid is known as cohesion. Cohesion between liquid molecules at the air-water interface is not equal from all directions yielding a net attraction inwards the bulk of the liquid resulting in a surface tension between liquid and air. The shape of the meniscus in a soil pore reveals the combined effect of the surface tension at the water interface and attraction of forces between the soil matrix and liquid. The angle of contact between the meniscus and pore wall is therefore a measure of this combined effect:

$$F_{ad} = \sigma_{wa} 2\pi r_m \cos\Psi_a \quad (N) \quad (2.22)$$

where

- F_{ad} = adhesive force (N)
- σ_{wa} = surface tension of water against air (N m⁻¹)
- Ψ_a = angle of contact (°)
- r_m = pore radius (m)

The surface tension pulls liquid up to a height where the adhesive force F_{ad} equilibrates the force which tends to pull the liquid down (the weight of the water column). When the contact angle is 0°, the relationship between matric pressure head and pore radius can be approximated as:

$$h_m = -\frac{1}{\rho_w g} \frac{2\sigma_{wa}}{r_m} \quad (\text{m}) \quad (2.23)$$

where g (m s^{-2}) is the acceleration due to gravity and ρ_w (kg m^{-3}) the water density. Eq. (2.23) underlines that for macroscopically described soil matrices h_m is inversely proportional to the radius r_m of water filled pores. The latter characteristic causes soils with different pore size distributions to have different moisture retentive properties. The relationship between matric pressure head h_m and soil water content θ depends besides this $h_m(r_m)$ effect also on the type and shape of the mineral elements and is therefore difficult to predict on a theoretical basis. The maximum soil water content is equal to the soil porosity, θ_{sat} i.e. the volume occupied when all pores are filled with water. The degree of moisture saturation, S_e , is a way to normalize the soil water content between 0 and 1:

$$S_e = \frac{\theta - \theta_r}{\theta_{sat} - \theta_r} \quad (-) \quad (2.24)$$

The term residual soil water content, θ_r , is introduced to account for the fact that some soil types bind θ strongly at low moisture contents so that θ_r is not available for water transport and related evaporation processes. In fully saturated soils, $S_e = 1$ and $h_m = 0$.

Liquid-vapour interactions

Water vapour obeys the ideal gas law which relates vapour density in soil to vapour pressure according to:

$$e = \rho_v \frac{R_u}{M_w} T_s \quad (\text{N m}^{-2}) \quad (2.25)$$

where

- e = water vapour pressure (N m^{-2})
- R_u = universal gas constant ($8.134 \text{ J mol}^{-1} \text{ K}^{-1}$)
- M_w = molecular mass of water ($0.018 \text{ kg mol}^{-1}$)
- ρ_v = vapour density (kg m^{-3})

The vapour concentration at the liquid-vapour interface, i.e. an evaporating front, is given by the Maxwell-Boltzmann distribution. The concentration of vapour molecules can be derived from the total potential energy. The potential energy and vapour pressure changes with height according to the hydrostatic equation which in the differential form reads as:

$$de = -g\rho_v(z) dz \quad (\text{N m}^{-2}) \quad (2.26)$$

Combination of the hydrostatic and ideal gas law under iso-thermal conditions leads to:

$$\frac{de}{e} = -\frac{gM_w}{R_u T_s} dz \quad (\text{N m}^{-3}) \quad (2.27)$$

After height integration of Eq. (2.27) between the evaporating front at soil depth $z = 0$ ($e = e_{sat}$) and the air layer with $z = h$ (being the total pressure head with dimension length), the vapour pressure in the area surrounding the liquid wedge becomes (Edlefsen and Anderson, 1943):

$$h = \frac{R_u T_s}{gM_w} \ln \frac{e}{e_{sat}} \quad (\text{m}) \quad (2.28)$$

According to Eq. (2.28), the relative humidity of soil air e/e_{sat} varies with pressure head. The upper limit of the vapour pressure e_{sat} is the temperature-dependent concentration of water vapour that can exist in equilibrium with a plane surface of pure water. The saturated water vapour pressure e_{sat} in a closed system can be approximated by the Clausius-Clapeyron equation, which accounts for the fact that changes in the heat content of the air due to a change in its temperature must be equal to the latent heat consumed by water evaporated into the air:

$$\frac{de_{sat}}{dT_s} = e_{sat}(T_s) \frac{\lambda M}{R_u T_s^2} \quad (\text{N m}^{-2} \text{K}^{-1}) \quad (2.29)$$

The theoretical derivations of the $h(h_m)$, $h_m(r_m)$, $h(T_s)$, $h_m(\theta)$ and $h(e/e_{sat})$ relationships posed, enable to link r_m , T_s , θ and e/e_{sat} through the common prognostic variable h for various soil types, which is essential for the description of the liquid, vapour and heat flow as well as their interactions.

Liquid transport processes in a soil matrix

The latent heat flux density at a bare land surface, λE_{soil} , can be conceived as being composed of a fraction which evaporates at the surface, q_0^{tot} , and a fraction of latent heat exchange occurring in the sub-surface and transported into the atmosphere, q_v^{tot} .

$$\lambda E_{soil} = \lambda \rho_w q_e^{tot} + \lambda q_v^{tot} \quad (\text{W m}^{-2}) \quad (2.30)$$

where q_0^{tot} (m s^{-1}) is the total liquid flow in small pores with the meniscus maintained at the land surface and q_v^{tot} ($\text{kg m}^{-2} \text{s}^{-1}$) is the total vapour flow arising from sub-surface evaporation. Figure 2.4 shows that a macroscopic h_m -value in a soil matrix having small and large pores accomodates liquid and gaseous phases simultaneously. The soil water

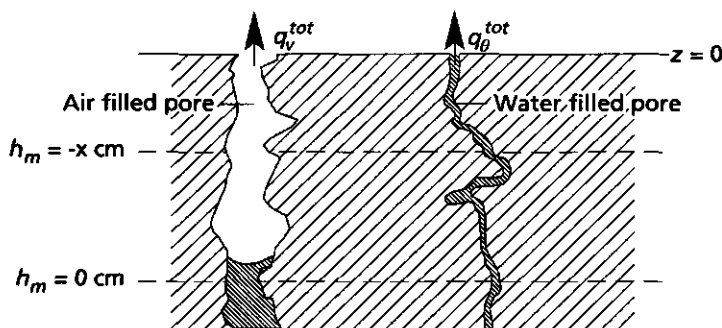


Fig. 2.4 Effect of different sized pores on water transport and macroscopic matrix pressure head.

transport processes of water in liquid phase, q_θ^{tot} , will be discussed first, while the second part of this section deals with vapour flow mechanisms, q_v^{tot} .

Soil water in the liquid phase moves in the direction of decreasing energy status, i.e. towards locations with lower total pressure heads. The soil hydraulic conductivity $k(h_m)$ describes the response of the soil water flux density to a gradient in total pressure head $\nabla_z h$. If the soil matrix is conceived to be sufficiently large that the internal microscopic geometry of the soils becomes irrelevant, a macroscopic treatment at REV scale may be applied. The Darcy equation for liquid flow in the unsaturated zone is applicable to a continuum representation of mass balances that average unsaturated hydraulic conductivity $k(h_m)$ over a large number of flow pathways (Gelhar, 1993):

$$q_\theta = -k(h_m)\nabla_z(h_m+h_g) \quad (\text{m s}^{-1}) \quad (2.31)$$

where q_θ is the one-dimensional vertical iso-thermal liquid flow being positive upward and $h_g = z$. The Darcy equation can alternatively be expressed with θ as the prognostic variable:

$$q_\theta = -D_\theta\nabla_z(\theta+h_g\frac{d\theta}{dh_m}) \quad (\text{m s}^{-1}) \quad (2.32)$$

with the iso-thermal liquid diffusivity being specified as

$$D_\theta = k(h_m)\frac{dh_m}{d\theta} \quad (\text{m}^2 \text{s}^{-1}) \quad (2.33)$$

It is widely recognized that the $k(h_m)$ relationship (sometimes expressed as $k(\theta)$) is extremely non-linear and that it depends on soil texture and structure. Both $h_m(\theta)$ and $k(\theta)$ characteristics have to be experimentally determined for samples that are sufficiently large to give a meaningful statistical average which does not change if the volume of consideration changes (i.e. the principle of Representative Elementary Volume, see

Chapter 1). Although the elementary hydro and thermodynamics are most appropriate at the individual particles of the solid phase and of individual pores, the REV scale offers the best perspective for relating flow equations to measurable properties and quantities. Miller and Miller (1956) used a set of scale factors α_r to relate distributed micro scale values to macroscopic soil physical characteristics, describing correctly an ensemble of microscopic processes:

$$h_m^{REV} = \frac{h_{m-i}^{micro}}{\alpha_{r-i}} \quad (m) \quad (2.34)$$

and

$$k_\theta^{REV} = k(\theta)_i^{micro} \alpha_{r-i}^2 \quad (m \text{ s}^{-1}) \quad (2.35)$$

The theoretical concept of the scaling factors $\alpha_{r,i}$ which relates the soil property at a location i of an individual pore to the soil property of the REV, is based upon the concept of similar media. Measurements of the h_m^{REV} and k_θ^{REV} relationships can be described by analytical functions (e.g. Clapp and Hornberger, 1978; van Genuchten, 1980)

The gravitational contribution to moisture flow in the topsoil under evaporative conditions with $|\nabla_z h_m| \gg |\nabla_z h_g|$ is of minor importance, so that $h_g d\theta/dh_m$ in Eq. (2.32) in the near-surface layer is often ignored. Then, the average D_θ -value representative of a thin slab between $h_m(1)$ at the top and $h_m(2)$ at the bottom can be estimated as:

$$D_\theta^{eff} = \frac{1}{\theta_{h_m(2)} - \theta_{h_m(1)}} \int_{h_m(2)}^{h_m(1)} k(h_m) dh_m \quad (m^2 \text{ s}^{-1}) \quad (2.36)$$

which, after analytical or numerical integrating $k(h_m) dh_m$ yields a function of the matrix flux density potential $M(h_m)$ (Gardner, 1958):

$$D_\theta^{eff} = \frac{1}{\theta_{h_m(2)} - \theta_{h_m(1)}} M(h_m) \quad (m^2 \text{ s}^{-1}) \quad (2.37)$$

If non-isothermal conditions prevail, a formal extension of the Darcy flux density q_θ introduced in Eq. (2.32) is required (Philip and de Vries, 1957):

$$q_\theta^{tot} = q_\theta + q_{\theta T} = -D_\theta \nabla_z \theta - k(\theta, T_s) - D_{\theta T} \nabla_z T_s \quad (m \text{ s}^{-1}) \quad (2.38)$$

with

$$D_{\theta T} = k(\theta, T_s) \frac{dh_m}{dT_s} \quad (\text{m}^2 \text{ s}^{-1} \text{ K}^{-1}) \quad (2.39)$$

where $q_{\theta T}$ is the thermal liquid flow (m s^{-1}) and the $D_{\theta T}$ thermal liquid diffusivity ($\text{m}^2 \text{ s}^{-1} \text{ K}^{-1}$). Note that $D_{\theta T}$ represent the so-called cross conductivity coefficients for the thermal response of moisture gradients (Feddes et al., 1988). The thermal liquid diffusivity describes the variations in the bulk properties of water induced by differences in soil temperature. If q_{θ} and $q_{\theta T}$ do not have the same direction, a countergradient type of transport will arise (Goudriaan, 1989).

The continuity equation for the conservation of liquid water in unsaturated soil can be written as:

$$\frac{\partial \theta}{\partial t} = -\nabla_z q_{\theta}^{tot} - S_{\theta} \quad (\text{s}^{-1}) \quad (2.40)$$

where S_{θ} (s^{-1}) is the sink of soil water which comprises among other elements water extraction by roots and sub-surface latent heat exchanges to maintain thermodynamic equilibrium. The involvement of the differential soil water capacity, $C(h_m)$, makes it feasible to express the mass continuity equation as a function of pressure head:

$$\frac{\partial h_m}{\partial t} = \frac{1}{C(h_m)} (-\nabla_z q_{\theta}^{tot} - S_{\theta}) \quad (\text{m s}^{-1}) \quad (2.41)$$

where the differential soil water capacity is defined as:

$$C(h_m) = \frac{d\theta}{dh_m} \quad (\text{m}^{-1}) \quad (2.42)$$

The advantage of applying Eq. (2.41) in comparison to Eq. (2.40) is that the pressure head remains continuous in layered soils as well as under multi-phase flow conditions (Feddes and Bastiaanssen, 1992) which is a sound basis for moisture transfer calculations in heterogeneous soils in arid regions (both e/e_{sat} and θ are a function of h).

Vapour transport processes in pores of different size

In air-filled pores, water remains in the vapour phase. Traditionally, density driven air flow i.e. thermal convection, is not accounted for when predicting water vapour movement in dry soils. Convection of water vapour by air movement however enhances the diffusion processes and depends on pore size. These pore size-dependent flow mechanisms make the formulation of a macroscopic permeability to vapour molecules more cumbersome compared to the derivation of a macroscopic $k(\theta)$ relationship. The flow processes need to be discussed for classes of equal pore size (Table 2.1).

Table 2.1 Fundamental vapour transport mechanisms in relation to pore size)

Flow process	Symbol	Pore size (m)	Symbol	Source
Gas molecular Fickian flow	q_v^F	5×10^{-4} to 5×10^{-2}	r_m^F	Heinonen, 1985
Free molecular Knudsen flow	q_v^K	1×10^{-7} to 5×10^{-9}	r_m^K	Knudsen 1909
Viscous Darcian air flow,	q_v^D	1×10^{-6} to 3×10^{-3}	r_m^D	Carman, 1956
Turbulent air flow	q_v^{TUR}	3×10^{-3} to 3×10^{-1}	r_m^{TUR}	Menenti, 1984

According to Table 2.1, turbulent air flow q_v^{TUR} and classical Fickian vapour diffusion, q_v^F , arise in large pores. Intermediate sized pores allow for viscous flow q_v^D , while free molecular Knudsen flow, q_v^K arises in small pores. Hence, each transport phenomenon has a specific role depending on soil geometries. The dominant process controlling the vapour transfer from the inner soil towards the land surface depends on the connectivity between pores, the ambient temperature and total air pressure, besides pore size. Mason and Malinauskas (1983) developed a framework which integrates these various flux density mechanisms and properties for multi-component gas transport in the soil, i.e. the dusty gas model. An electric analogue is given in Figure 2.5. A comprehensive vapour flux density, q_v^{tot} , can be quantified after identifying the probability $p(r_m^{\hat{}})$ that a particular pore radius $p(r_m^{\hat{}})$ exists and is filled with air (see Table 2.1). The sum of the subsequent probabilities $p(r_m^K)$ to $p(r_m^{TUR})$ must be one:

$$q_v^{tot} = \left(\frac{1}{q_v^K p(r_m^K) + q_v^F p(r_m^F)} + \frac{1}{q_v^D p(r_m^D)} + \frac{1}{q_v^{TUR} p(r_m^{TUR})} \right)^{-1} \text{ (kg m}^{-2} \text{ s}^{-1}) \quad (2.43)$$

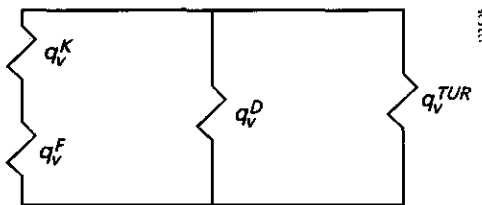


Fig. 2.5 An electric analogue circuit to indicate the role of ordinary Fickian and Knudsen diffusion in series and in parallel respectively with viscous and turbulent air flow (adapted after Mason and Malinauskas, 1983)

A. Gas molecular Fickian flow, q_v^F

Water vapour molecules in large quantities that flounder in dry air will have a net flow in the direction of the decreasing concentration. Fick's 1st law of molecular vapour diffusion is similar in shape to Fourier's law of heat conduction:

$$q_v^F = -D_v^F \nabla_z \rho_v \quad (\text{kg m}^{-2} \text{ s}^{-1}) \quad (2.44)$$

where D_v^F ($\text{m}^2 \text{ s}^{-1}$) is the vapour diffusion coefficient in a soil matrix. Since interaction with the soil matrix should be minimized, the bulk molecular gas diffusion takes place mainly in pores that have a sufficient large aggregate diameter. Many collisions are needed to average random walks of the molecules. Therefore, Fick's law for the diffusion of gases only remains valid in pores with a radius (r_m), a few orders of magnitude larger than the mean free path of a water vapour molecule, ℓ_m (Menenti, 1984).

B. Free molecular Knudsen flow, q_v^K

The Knudsen diffusion, Knudsen flow or free molecular diffusion, is restricted to conditions where gas molecules do not collide (Knudsen, 1909). The Knudsen flow arises when the transport is determined by collisions of the molecule with the pore wall. Although the theorem of Knudsen flow in porous media has existed for years, its introduction into soil physics has only just begun (Menenti, 1984; Clifford and Hillel, 1986; Thorstenson and Pollock, 1989). The speed of vapour movement associated with Knudsen flow is equal to the molecular speed given by:

$$v_m = \left(\frac{8 T_s R_u}{\pi M} \right)^{0.5} \quad (\text{m s}^{-1}) \quad (2.45)$$

The vapour speed, v_m , in small air-filled pores where Knudsen flow applies, is many orders of magnitude higher (600 m s^{-1}) than the mean vapour flow hindered by the gas-gas collisions in large air-filled pores. The intensity of vapour flow can be calculated as the vapour load (mol or kg) passing a unit area (m^2) at a certain rate (s). As such, the permeability for Knudsen flow can be schematized as a diffusion parameter, D_v^K . Knudsen (1909) showed that for a schematized soil with straight parallel cylindrical pores of constant radii, D_v^K can be approached as:

$$D_v^K = \frac{4}{3} v_m r_m \quad (\text{m}^2 \text{ s}^{-1}) \quad (2.46)$$

Note that D_v^K with an average pore radius of $5 \cdot 10^{-8} \text{ m}$ and molecular speed of 600 m s^{-1} yields a diffusivity of $4 \cdot 10^{-5} \text{ m}^2 \text{ s}^{-1}$ which is significantly higher than that for D_v^F which lies usually between $1 \cdot 10^{-6}$ to $1 \cdot 10^{-8} \text{ m}^2 \text{ s}^{-1}$. The collisions between a molecule and the pore wall takes place in any capillary and at any time but are negligible as a flow controlling processes when r_m/ℓ_m is large. Yet, a small range of critical diameters exists, at which gaseous transport is not hindered by gas-gas collisions. The pore size distribution of a particular soil in combination with the degree of moisture saturation, S_e , determines whether or not q_v^K is an important process. According to Clifford and Hillel (1986), the r_m range, where Eq. (2.47) remains valid is $0.1 < r_m/\ell_m < 10$:

$$q_v^K = -D_v^K \nabla_z \rho_v \quad (\text{kg m}^{-2} \text{ s}^{-1}) \quad (2.47)$$

C. Viscous Darcian air flow, q_v^D

Air is a mixture of partial gas pressures such as N_2 , O_2 , CO_2 and H_2O . Dalton has stated that the total air pressure is the sum of the partial pressures of the gasses in mixtures because each constituent occupies the same volume. The average molecular mass for dry air without water vapour is $M_a = 0.029 \text{ kg mol}^{-1}$. Then, the total air pressure, p , can be computed from the dry air pressure and the water vapour pressure (Eq. (2.25):

$$p = \rho_d \frac{R_u}{M_a} T_s + \rho_v \frac{R_u}{M_w} T_s \quad (\text{N m}^{-2}) \quad (2.48)$$

where ρ_d is the dry air density and the moist air density becomes:

$$\rho_a = \rho_d + \rho_v \quad (\text{kg m}^{-3}) \quad (2.49)$$

The ρ_v/ρ_a ratio is also known as the specific humidity q_a . Expressing the total air pressure p on a weight basis yields the pneumatic pressure head h_{pneu} (Eq. 2.20). With the existence of small gradients of total air pressure head in soil, $\nabla_z h_{pneu}$, water vapour can be advected by moist air movement. If $\nabla_z h_{pneu}$ is caused by $\nabla_z T_s$, it will account for thermal convection (not being necessarily turbulent flow, q_v^{TUR}). Very small pressure gradients can produce viscous flux densities, that are greater than q_v^f . Such viscous Darcian flow is a function of the specific or intrinsic permeability, K . Accordingly, the total moist air movement can be expressed using a Darcy type of equation for gas flow driven by differences in total air pressure p corrected for gravity flow:

$$q_v^D = \rho_a v_a = -\rho_a \frac{K}{\eta_a} \nabla_z (p - \rho_a g z) \quad (\text{kg m}^{-2} \text{ s}^{-1}) \quad (2.50)$$

where

- v_a = air flow velocity (m s^{-1})
- η_a = dynamic viscosity of air (N s m^{-2})
- K = specific permeability (m^2)

D. Turbulent air flow, q_v^{TUR}

Wind action will arise from pressure gradients in soil capillaries where the build-up of total air pressure gradients, $\nabla_z h_{pneu}$, cannot be compensated by viscous flow alone. If the air moves rapidly, a point is reached where laminar flow changes into irregular motions, i.e. turbulent flow. Thermal convection implies turbulent transfer of momentum

in the fluid. Menenti (1984) provided criteria for the transition from laminar to turbulent flow in air-filled soil pores on the basis of the Reynolds number. He showed that for $k > 10^{-8} \text{ m}^2$, soil air flow should be estimated by turbulent transfer equations (Ergun, 1952):

$$\nabla_x \rho = \frac{1-x_a}{2r_m} \left[\frac{150(1-x_a)}{Re} + 1.75 \right] \rho_a (v'_a) \quad (\text{N m}^{-3}) \quad (2.51)$$

where R_e is the Reynolds number and x_a the volumetric soil air content and consequently

$$q_v^{TUR} = \rho_a v'_a \quad (\text{kg m}^{-2} \text{ s}^{-1}) \quad (2.52)$$

Note that the first term on the right hand side of Eq. (2.51) describes viscous flow, q_v^D . When the total vapour flux density q_v^{tot} needs to be specified at pedon scale rather than at the pore scale where gas kinetics apply, Fick's 1st law with an effective vapour diffusivity, D_v^{eff} is traditionally considered to account for the many separated flow mechanisms (Philip and de Vries, 1957):

$$q_v^{tot} = -D_v^{eff} \nabla_z \rho_v \quad (\text{kg m}^{-2} \text{ s}^{-1}) \quad (2.53)$$

Inversion of Eq. (2.53) in combination with Eq. (2.43) allows to derive D_v^{eff} . Transient $\rho_v(z,t)$ -patterns can be obtained from in- and out flow of q_v^{tot} in a pedon with thickness δz in association to its sinks (condensation) S_v :

$$\frac{\partial \rho_v}{\partial t} = -\nabla_z q_v^{tot} - S_v \quad (\text{kg m}^{-3} \text{ s}^{-1}) \quad (2.54)$$

with

$$S_v = -\frac{E_v}{\delta z} \quad (\text{kg m}^{-3} \text{ s}^{-1}) \quad (2.55)$$

where the minus sign in Eq. (2.55) is added to indicate that condensation is the counterpart of evaporation. A multi-scale description of these fluid processes is necessary to understand large scale land surface processes (Figure 2.6). A microscopic description is only useful at pedon scale. Macroscopic or effective permeabilities have to be introduced on the scale at which many soil types and land use are present. The effective permeability for fluid transfer at meso scale can neither be described as a macroscopic permeability nor be measured. Of considerable interest is the identification of using inverse methods to determine these effective parameters. Feddes et al. (1993) suggested to derive effective soil physical properties by inverse modelling of area-average evaporation and near-surface soil water content.

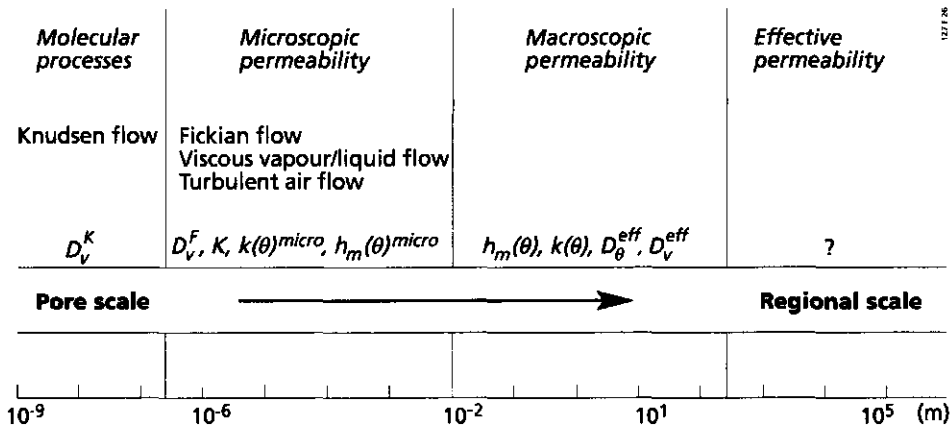


Fig. 2.6 Soil water transport processes and system permeabilities on various spatial scales

2.2.2 Soil heat transport processes

Thermal energy in porous media may be transferred by conduction, q_{hc} , and convection, q_{ha} ; Fluid movement in liquid and vapour phase contributes to the convection component. Classical soil heat transport theory considers conductive heat flux densities through the various soil constituents (e.g. De Vries, 1958) (Figure 2.7):

- soil moisture, q_{hc}^{water}
- soil air, q_{hc}^{air}
- soil minerals, q_{hc}^{min}
- soil organic material, q_{hc}^{org}

Effective heat conduction through porous soil media, q_{hc} , comprises the separated q_{hc}^{water} , q_{hc}^{air} , q_{hc}^{min} and q_{hc}^{org} flux densities and can be mathematically expressed as:

$$q_{hc} = -\lambda_s^* \nabla_z T_s \quad (\text{W m}^{-2}) \quad (2.56)$$

where λ_s^* ($\text{W m}^{-1} \text{K}^{-1}$) is the effective soil thermal conductivity which has a hypothetical character since it strictly speaking applies to soils without fluid movement. The effective thermal conductivity λ_s^* of moist soil is an average of the thermal conductivities of the individual soil constituents λ_i weighted with the ratio of the average temperature gradient

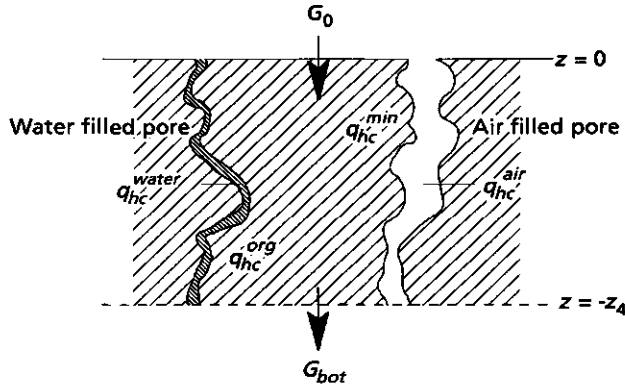


Fig. 2.7 Schematic soil structure and soil heat flow components; Daytime situation with downward oriented flux densities

k_i in the i^{th} constituent to the average temperature gradient of the bulk medium and the relative volume occupied by the i^{th} constituent, v_i :

$$\lambda_s^* = \frac{\sum(k_i v_i \lambda_i)}{\sum(k_i v_i)} \quad (\text{W m}^{-1} \text{K}^{-1}) \quad (2.57)$$

The particle shape, and especially the surface of contact between the particle edges affects the ratio of the temperature gradients k_i (de Vries, 1958). Due to the fact that $\lambda_s^{\text{water}} \gg \lambda_s^{\text{air}}$ and that k_i is modulated by v_{water} and v_{air} , the $\lambda_s^*(\theta)$ relationship is non-linear.

Liquid flow, q_{θ}^{tot} , and air movement by means of q_v^D and q_v^{TUR} carry soil heat content. The heat convection process is driven by different forces: A gradient $\nabla_z h_m$ causing liquid flow and a gradient $\nabla_z h_{pneu}$ causing air flow. The partial convective processes (q_{θ} , $q_{\theta T}$, q_v^D , q_v^{TUR}) can be lumped together in a mixed convective heat flow, q_{ha} , comprising q_v^{tot} and q_{θ}^{tot} (de Vries, 1958):

$$q_{ha} = -c_p q_v^{\text{tot}} \delta_z T_s - \rho_w c_w q_{\theta}^{\text{tot}} \delta T_s \quad (\text{W m}^{-2}) \quad (2.58)$$

where c_w ($\text{J kg}^{-1} \text{K}^{-1}$) is the specific heat of water. The first and second term covers the transfer of thermal energy by vapour and liquid transport respectively. By introducing an apparent thermal conductivity term, λ_s' , $q_{hc} + q_{ha}$ can be formally expressed as effective soil heat flow:

$$q_h^{\text{tot}} = q_{hc} + q_{ha} = -\lambda_s' \nabla_z T_s \quad (\text{W m}^{-2}) \quad (2.59)$$

The merit of λ_s' values is that they directly relate gradients of soil temperature to flux densities q_h^{tot} . The Nusselt number λ_s'/λ_s is a measure to indicate the relative importance of convective enhancement of conductive heat transport.

Transient $T_s(z,t)$ patterns can be obtained when the heat transport equation (Eq. 2.59) is re-arranged into Fourier's 2nd law, being a more generalized form of Eq. (2.19):

$$\rho_s c_s \frac{\partial T_s}{\partial t} = -\nabla_z q_h^{tot} - S_h \quad (\text{W m}^{-3}) \quad (2.60)$$

with the sink of heat content being defined as:

$$S_h = \frac{\lambda E_v}{\delta z} \quad (\text{W m}^{-3}) \quad (2.61)$$

E_v in Eq. (2.61) is equal to E_v in Eq. (2.55) because liquid to vapour transition adds vapour and removes heat. It should be noted that the heat of wetting affects λ in Eq. (2.61) because absorbed soil water has an enthalpic content which changes soil air humidity.

The movement of liquid, vapour and heat in the sub-surface has now been briefly described and it is shown that they are coupled by sinks and sources (S_θ , S_h , S_v). The dry topsoil undergoes strong thermal forcing and many of the transport phenomena mentioned in this section occur within a 24 hour cycle. A more exact prediction of time scales on which certain process such as q_{hs} , q_{hc} and q_v^D , q_v^{TUR} and q_θ^T are relevant and how they affect λE and G_0 can be achieved on the basis of field measurements and/or model simulations. The numerical EVaporation DESerts (EVADES) simulation model (Bastiaanssen et al., 1989; 1990) has been built to compute the transient patterns of θ , ρ_v , T and h , and will be used to explain observed field phenomena being described in Chapters 5 and 6.

2.3 Moisture and heat transport processes in the atmosphere

2.3.1 Planetary Boundary Layer

The lower part of the atmosphere, where the influence of land surface flux densities on atmospheric motion is evident, is called the Planetary Boundary Layer, PBL. In this zone, the effects of the Earth's rotation (Coriolis forces) may be disregarded in

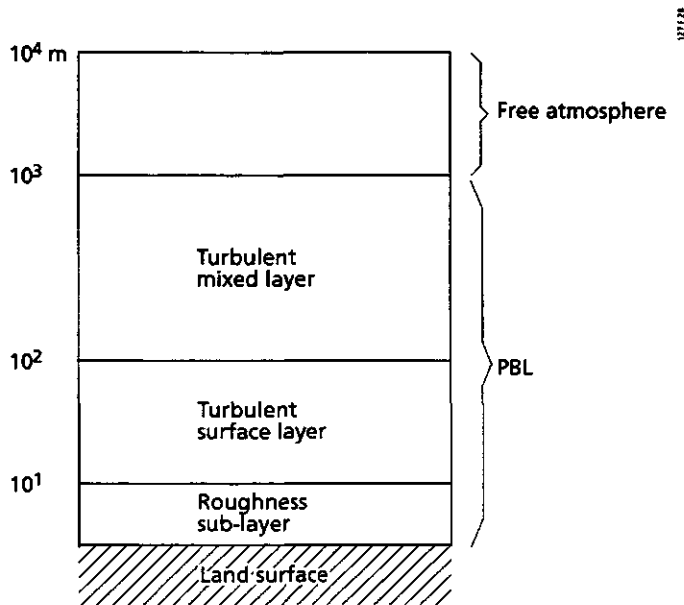


Fig. 2.8 Schematic representation of the hybrid Planetary Boundary Layer (PBL) into sub-layers with typical heights. The vertical profiles of horizontal wind speed and potential temperature during an unstable daytime condition are indicated

comparison with the effects from land surface processes. Generally, the flow in the PBL has a turbulent character generated by wind shear and thermal convection. The hybrid PBL for a dry, well-mixed ideal case consists of different sub-layers as depicted in Figure 2.8.

The turbulent surface-layer is the lower part of the PBL and might be typically 10% of the PBL height (Holtslag and Nieuwstadt, 1986). Monin and Obukhov (1954) proposed a similarity hypothesis for this turbulent surface layer. Holtslag (1984) showed for a pasture area at Cabauw, the Netherlands, that the Monin-Obukhov hypothesis is valid up to an altitude of 100 m. A roughness sub-layer with variable surface roughnesses like canopy layers or bluff surface shapes, lies just above the land surface (see Figure 2.8). Throughout the mixed layer, potential temperature and humidity are quasi-constant with height. The top of the PBL is limited by the free atmosphere. The entrainment layer is the zone where the laminar process of the free atmosphere are hit by the turbulent eddies leaving the PBL. Entrainment is the mixing process of these air parcels.

The greatest horizontal variations in H and λE over composite terrain are found close to their source at the land surface, i.e. the turbulent surface layer. Vertical transport of momentum, heat and vapour flux densities above heterogeneous terrain exhibits non-uniformity in space, which causes horizontal advection. The height in the PBL at which momentum flux density becomes approximately independent of surface modifications, is called the 'blending height' (Wieringa, 1986). Below the blending height, it is assumed that the wind profiles primarily respond to local roughness elements. The concept of blending height is a practical tool from which area-average momentum flux densities can be deduced (Wieringa, 1986; Mason, 1988; Claussen, 1990). The height at which the momentum flux density becomes areally constant varies with the geometry of the surface roughness elements and the convective conditions. Multiple blending heights at different levels and horizontal scales may therefore arise. For the purpose of the present study it is convenient to consider a simple expression for z_B being based on general internal boundary layer theory (Mason, 1988):

$$z_B = \left(\frac{u^*}{u}\right)^2 x \quad (\text{m}) \quad (2.62)$$

where x (m) is the characteristic length scale for horizontal distances between obstacles. The height of the PBL as a whole follows a daily cycle. The final PBL height from surface forcings increases with the square root function of the time integrated values of H and λE (Driedonks, 1981) and will typically be in the order of about 500 m up to 2.5 km. Dry surfaces exposed to Q^* contribute to rapid warming of the air (significant H flux), causing to increase swiftly the PBL height.

2.3.2 Flux-profile relationships for homogeneous land surfaces

The similarity hypothesis (Monin and Obukov, 1954) of wind, temperature and humidity profiles in the surface layer above extensive horizontal homogeneous terrain implies that:

- flux densities of momentum, moisture and heat vary by less than 10% with height;
- flux densities are linearly related to gradients of wind, temperature and humidity;
- the effect of buoyancy on flux densities can be accounted for by a dimensionless variable.

Since the land surface is not smooth, shear stress arises. Shear stress is a sink for kinetic energy at the land-atmosphere interface, which has to be compensated by a vertical flux density of momentum. A measure of shear stress is provided by a typical velocity, u_* , of the resulting eddies:

$$\tau = \rho_a u_*^2 \quad (\text{N m}^{-2}) \quad (2.63)$$

where u_* (m s^{-1}) is the friction velocity. Since the actual mechanisms for turbulent transport are difficult to quantify, a mathematical approach similar to diffusion is usually considered, whereby shear stress is linearly related to the vertical gradients of horizontal windspeed:

$$\tau = K_m \nabla_z (\rho_a u) \quad (\text{N m}^{-2}) \quad (2.64)$$

where K_m ($\text{m}^2 \text{s}^{-1}$) is the eddy diffusion coefficient and u (m s^{-1}) is the mean horizontal wind speed. The vertical gradients of horizontal wind speed over flat and homogeneous surfaces in a neutral atmosphere ($H = 0$) depend on friction velocity u_* and height z as (Monin and Yaglom, 1971):

$$\frac{du}{dz} = \frac{u_*}{kz} \quad (\text{s}^{-1}) \quad (2.65)$$

where k is the Von Karman constant (0.41). Eq. (2.65) indicates that the shape of the $u(z)$ profile is determined by u_* . Thermal or free convection may arise in the surface layer because of gradients in moist air density. If thermal convection is indeed present, a combination of thermal and forced convection arises: mixed convection. Buoyancy is upward momentum transport, so it tends to offset the downward (mechanical) transport due to shear stress. The non-dimensional Monin-Obukhov stability correction factor for momentum transfer, $\phi_m(\xi)$, corrects the vertical gradient of $u(z)$ for the effect of buoyancy:

$$\frac{du}{dz} = \frac{u_*}{kz} \phi_m(\xi) \quad (\text{s}^{-1}) \quad (2.66)$$

where ξ (-) is the ratio of z and L , being a suitable determinant to assess the height dependency of buoyancy transfer:

$$\xi = \frac{z}{L} \quad (-) \quad (2.67)$$

The Monin-Obukhov length L is a length scale for mixed convection (Obukhov, 1946) and was defined as the ratio of mechanical production of kinetic energy divided by the thermal convective production of turbulent kinetic energy:

$$L = -\frac{\rho_a c_p u_*^3 T_p}{kgH} \quad (\text{m}) \quad (2.68)$$

where T_p (K) is the mean air potential temperature of the flow region under consideration, which implies that L changes slightly with height z in the constant flux density layer. Note that L is negative under unstable conditions. Overall accepted standard empirical expressions on $\phi_m(\xi)$ are among others provided by Dyer and Hicks (1970). The most frequently used ϕ_m -functions in unstable cases ($T_0 > T_p$, $\xi < 0$) are:

$$\phi_m = (1 - 16 \frac{z}{L})^{-0.25} \quad (-) \quad (2.69)$$

and stable cases ($T_0 < T_p$, $\xi > 0$):

$$\phi_m = 1 + 5 \frac{z}{L} \quad (-) \quad (2.70)$$

Under neutral conditions with $\xi = 0$, ϕ_m will become 1 and $u(z)$ is fully determined by shear stress. Eq. (2.69) remains valid as long as $-7 < \xi < 0$ while for Eq. (2.70) $0 < \xi < 1$ applies (Holtslag, 1984). For neutral stratification where H theoretically tends to zero, L approaches infinity. Combining Eq. (2.63), (2.64) and (2.66) yields an explicit expression of the eddy diffusion coefficient:

$$K_m = \frac{kzu_*}{\phi_m} \quad (\text{m}^2 \text{ s}^{-1}) \quad (2.71)$$

The equation for potential temperature profiles being equivalent to Eq. (2.66) is:

$$\frac{dT_p}{dz} = \frac{T_*}{kz} \phi_h(\xi) \quad (\text{K m}^{-1}) \quad (2.72)$$

where T_* (K) is the temperature scaling parameter in analogy to u_* for wind profiles. In stable conditions, ϕ_h and ϕ_m are often treated to be similar while for unstable conditions $\phi_h = \phi_m^2$ applies (Dyer and Hicks, 1972). The eddy diffusion coefficient for atmospheric heat transport then becomes:

$$K_h = \frac{kzu_*}{\phi_h} \quad (\text{m}^2 \text{ s}^{-1}) \quad (2.73)$$

Potential temperature, T_p , is the air temperature corrected for the adiabatic gradient (-0.0065 K m^{-1}) which makes a comparison between temperatures at different atmospheric pressures feasible (e.g. Stull, 1988):

$$T_p = T_a \left(\frac{p_0}{p} \right)^{0.286} \quad (\text{K}) \quad (2.74)$$

where p_0 represents the reference air pressure. A formal extension of Monin Obukhov's similarity hypothesis for the flux-profile relationship of water vapour becomes:

$$\frac{dq_a}{dz} = \frac{q_*}{kz} \phi_v(\xi) \quad (\text{m}^{-1}) \quad (2.75)$$

where q_* (-) is the humidity scaling coefficient. The factors ϕ_h and ϕ_v may be considered to be similar (Monin and Yaglom, 1971). If ϕ_h and ϕ_v do not differ, Eq. (2.73) describes K_v as well. The scaling parameters for momentum, heat and vapour are related to their surface flux densities respectively as:

$$u_* = \left(\frac{\tau}{\rho_a} \right)^{0.5} \quad (\text{m s}^{-1}) \quad (2.76)$$

$$T_* = \frac{-H}{\rho_a c_p u_*} \quad (\text{K}) \quad (2.77)$$

$$q_* = \frac{-\lambda E}{\rho_a u_* \lambda} \quad (-) \quad (2.78)$$

The impact of τ on H and λE is evident from Eqs. (2.76) to (2.78). The integrated form of Eqs. (2.65, 2.72 and 2.75) in the surface layer between the land surface and a reference height yields the well known logarithmic profiles of state variables. The vertical profile of mean horizontal windspeed $u(z)$ under conditions of mixed convection then becomes:

$$\frac{u}{u_*} = \frac{1}{k} \left[\ln \left(\frac{z_{sur} - d}{z_{0m}} \right) - \psi_m(z_{sur} - d, L) + \psi_m(z_{0m}, L) \right] \quad (-) \quad (2.79)$$

where z_{sur} represents the near-surface reference height to which the τ -flux densities apply and d is the displacement height. The combination of the $\tau(u_*)$, $H(T_*)$ and $\lambda E(q_*)$ scale-flux density functions with the scale-profile functions yields the flux-profile relationships. The ψ_m -function in Eq. (2.79) is the integral of $\phi_m(z_{sur} - d, L)$. Examples of ψ -functions can be found in literature (e.g. Paulson, 1970). For unstable conditions ($\xi < 0$) one can take:

$$\psi_m = 2\ln\left(\frac{1+x}{2}\right) + \ln\left(\frac{1+x^2}{2}\right) - 2\arctan(x) + 0.5\pi \quad (-) \quad (2.80)$$

where $x = \phi_m^{-1}$ so that

$$x = \left(1 - 16 \frac{z_{sur}-d}{L}\right)^{-0.25} \quad (-) \quad (2.81)$$

while for stable conditions, the integral atmospheric stability correction becomes (Webb, 1970):

$$\psi_m = -5 \frac{z_{sur}-d}{L} \quad (-) \quad (2.82)$$

Since the $\psi_m(z_{sur}-d, L)$ term in Eq. (2.79) depends implicitly on u . through the Monin-Obukhov length L (see Eq. 2.68), an iterative procedure is needed to let solve Eq. (2.79) for u/u_* . The value of $\psi_m(z_{om}, L)$ is a small fraction of $\psi_m(z_{sur}-d, L)$ and is usually ignored.

The height at which the windspeed mathematically vanishes is the roughness length for momentum transfer, z_{om} . According to Eq. (2.79), the roughness length is mathematically defined as a constant appearing in the integration of Eq. (2.66). The presence of open areas, wind breaks, forests and built up areas in the upwind direction may be of overriding importance for the local roughness conditions. The roughness length representative for a larger area depends on the surface geometry, viz. height and distance of vegetation stands and other landscape elements such as windbreaks and buildings. The Davenport classification table has been designed to support the z_{om} estimation for homogeneous landscapes (Wieringa, 1986).

In micro-meteorological studies, local z_{om} -values for local surface conditions are usually derived from $u(z)$, L and flux densities of τ and H . In the absence of wind profiles to estimate z_{om} from $u(z)$, the height of vegetation stands, h_v , can be used to assess z_{om} . It is an established fact that z_{om}/h_v changes with geometry of the land surface (Wooding et al., 1973). For vegetated surfaces, it was shown that the peak of z_{om}/h_v arises at intermediate LAI values (Seginer, 1974). Figure 2.9 demonstrates that z_{om}/h_v increases with LAI until the onset is passed above which 'over-sheltering' of the canopies occur. Then, additional leaves will create an environment where leaves merely shelter their neighbouring leaves and the surface behaves more aerodynamically smooth. For complete canopies, Brutsaert (1982) proposed $z_{om} = 0.13h_v$. For a range of partial vegetation cover, Raupach (1994) proposed to use:

$$\frac{z_{0m}}{h_v} = \left(1 - \frac{d}{h_v}\right) \exp\left(-k \frac{u}{u_*} - \psi_n\right) \quad (2.83)$$

and

$$\left(1 - \frac{d}{h_v}\right) = \frac{1 - \exp[-(7.5LAI)^{0.5}]}{(7.5LAI)^{0.5}} \quad (-) \quad (2.84)$$

and

$$\frac{u_*}{u} = (0.003 + 0.3 \frac{LAI}{2})^{0.5} \quad (-) \quad \text{if } LAI \leq LAI^{shel} \quad (2.85)$$

and

$$\frac{u_*}{u} = 0.3 \quad (-) \quad \text{if } LAI > LAI^{shel} \quad (2.86)$$

where LAI^{shel} is the onset where further terrain roughness elements does not affect the bulk drag. Eq. (2.83) can be applied to find z_{0m} if vegetation is characterized by h_v and LAI . Hence, the use of a z_{0m}/h_v ratio is definitely not an overall solution, but has to be seen as a practical tool if no other data sources are available.

In taller crops with closed canopies, the wind profile of Eq. (2.79) is displaced upward when compared to the surface level. The latter shift in height of the reference level is often indicated by the displacement height, d . If the principle of displacement height holds, the wind profile is lifted by a height d and consequently the windspeed will vanish at $d+z_{0m}$. Wieringa (1992) showed that d/h_v changes with the degree of wind profile curvature because of obstacle density. Only for rather closed canopies and in skimming flow conditions where the obstacle height is about five times the typical distance between the obstacles, the d/h_v fraction such as indicated in Eq. (2.84) seems to be a workable approach. There is a general consensus that $d \sim 0$ in sparse canopies with semi-smooth flow conditions (distance between obstacles being more than 15 times the obstacle height). Discussions as to how d can be obtained regionally from scarce information represent an issue that will continue to be debated. If $z_{sur} \gg d$, the need to describe d explicitly can be eliminated anyhow.

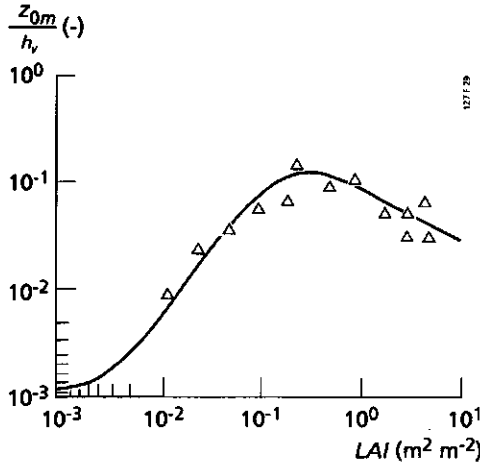


Fig. 2.9 Measurements of normalized roughness length, z_{0m}/h_v , as a function of the leaf area index, LAI (adapted after Raupach, 1994)

The vertical profile for potential temperature in the surface layer is obtained after integrating Eq. (2.72):

$$\frac{T_{z_{0h}} - T_p}{T_*} = \frac{1}{k} \left[\ln \left(\frac{z_{sur} - d}{z_{0h}} \right) - \psi_h(z_{sur} - d, L) + \psi_h(z_{0h}, L) \right] \quad (-) \quad (2.87)$$

The roughness lengths for momentum (z_{0m}) and heat (z_{0h}) are not identical per se, because the transfer processes in close proximity of obstacles are not similar (Thom, 1972). If z_{0m} and z_{0h} are identical, $T_{z_{0h}}$ in Eq. (2.87) is called the aerodynamic surface temperature $T_{z_{0m}}$ but this is rather hypothetical and a standard expression to account for z_{0m} and z_{0h} differences is the introduction of the kB^{-1} factor (Chamberlain, 1966) which is defined as:

$$kB^{-1} = \ln \frac{z_{0m}}{z_{0h}} \quad (-) \quad (2.88)$$

Garrat (1978) demonstrated that z_{0h} can be oneseventh of z_{0m} ($kB^{-1} = 2$). Brutsaert (1982) indicated that z_{0h} is one or more orders of magnitude smaller than z_{0m} ($kB^{-1} \geq 2.3$). Hence, one should take care that different definitions of land surface temperature and roughness lengths exists such that $T_{z_{0m}} \neq T_{z_{0h}} \neq T_0 \neq T_0^R$, where there is a slight indication that for 'permeable rough' surfaces such as canopies, kB^{-1} is approximately two to three (Prevot et al., 1994). However heterogenous surfaces consisting of distinct components, for example bare soil and vegetation, respond with different momentum and heat flux

densities and kB^1 can hardly be solved in a straightforward manner (Blyth and Dolman, 1995).

For atmospheric vapour transfer, the $q_a(z)$ profile can be computed from:

$$\frac{q_{z_{0v}} - q_a}{q_*} = \frac{1}{k} \left[\ln \left(\frac{z_{sur} - d}{z_{0v}} \right) - \psi_v(z_{sur} - d, L) + \psi(z_{0v}, L) \right] \quad (-) \quad (2.89)$$

The ψ_h and ψ_v functions necessary to solve Eqs. (2.87) and (2.89), respectively for unstable conditions ($\xi < 0$) are:

$$\psi_v = \psi_h = 2 \ln \left(\frac{1 + x^2}{2} \right) \quad (-) \quad (2.90)$$

while for stable conditions $\psi_m \sim \psi_h \sim \psi_v$ applies.

2.4 Concluding remarks

The description of evaporation as a function of soil moisture dynamics in the unsaturated zone involves the radiation, energy, liquid, vapour and soil heat balance. Physical interpretation and mathematical formulation of such complex events cannot be done without a certain degree of simplification i.e. macroscopic system treatment with effective diffusivities such as D_o^{eff} , D_v^{eff} , λ_s' . The same remark applies to the diffusivities in the atmospheric surface layer: K_m , K_h and K_v . The continuous interactions between liquid and vapour phases in a non-isothermal surrounding, a moving fluid and strong diurnal variation in radiation makes the process description intricate at field scale and beyond. Mechanistic simulation such as EVADES may help to understand bare soil evaporation under arid conditions.

Eqs. (2.4), (2.87) and (2.88) have demonstrated that the aerodynamic surface temperature $T_{z_{0m}}$, the surface radiation temperature T_o^R , the surface temperature T_o and the surface temperature where the heat source emerges $T_{z_{0h}}$ have different definitions. Ample attention should be paid to kB^1 when interpreting remotely observed T_o values. The relevant soil and atmosphere properties, and variables which control the land-atmosphere interactions in terms of effective parameters, can be summarized as follows:

Variables:

- Atmospheric state variables (u, T_p, q_a) ;
- Land surface state variables (θ_o, T_o) ;
- Soil state variables (θ, T_{st}, ρ_v) ;
- Radiative flux densities $(K^{\downarrow}, K^{\uparrow}, L^{\downarrow}, L^{\uparrow})$;

— Atmospheric scaling variables (u, T, q)

Properties:

- Soil effective liquid diffusivity (D_s^{eff}) ;
- Soil effective vapour diffusivity (D_v^{eff}) ;
- Soil apparent thermal conductivity (λ'_s) ;
- Land surface properties $(r_0, \epsilon_0, z_{0m}, z_{0h}, z_{0v}, h_v, d, LAI)$;

The relative magnitude of heat flux densities at land surfaces depends on the above-mentioned variables and properties:

$$Q_s(r_0, L^\downarrow, \epsilon_0, T_0, K^\downarrow) = G_0(\lambda'_s T_s, T_0) + H(z_{0m}, kB^{-1}, u, L, T_p, T_{z0h}) + \lambda E(z_{0m}, kB^{-1}, u, L, q_{z0v}, q_a) \quad (2.91)$$

Because of the direct dependance of q_{z0v} on soil water content, the latent heat flux density λE is the most difficult term to solve and it is therefore preferred to consider it as the budget residue in surface energy balance studies:

$$\lambda E = Q^* - G_0 - H \quad (2.92)$$

3 Parameterization of land surface flux densities in the soil-vegetation-atmosphere continuum

3.1 Layered resistance schemes

Land surface flux densities may be parameterized as Ohm's type of transport equations comprising a resistance term to account for the flow obstruction:

$$F_0 = \frac{c_2 - c_1}{r_{1,2}} \quad (1.4)$$

Resistance schemes are built such that the value of the entity c is related to the two reference locations 1,2 which define the domain of the resistance. Resistance schemes may form the basis of flux density calculations in simulation models, i.e. land surface parameterization schemes (e.g. Dolman, 1993) and remote sensing algorithms (e.g. Camillo, 1991). Resistance schemes with different levels of sophistication are developed (Figure 3.1) and they will be discussed in this section by decreasing complexity. The two-layer version for partial canopies has separated land surface flux densities for the bare soil surface and the vegetation canopy, and allows for interactions between them (Figure 3.1, part A). Subsequently, the balance equations for vegetation (subscript v) and soil (subscript $soil$) for a two layer scheme read as:

$$Q_v^* = G_{0-v} + H_v + \lambda E_v \quad (\text{W m}^{-2}) \quad (3.1)$$

$$Q_{soil}^* = G_{0-soil} + H_{soil} + \lambda E_{soil} \quad (\text{W m}^{-2}) \quad (3.2)$$

The flux densities above the vegetation and soil may be combined using weighing coefficients which are *inter alia* based on fractional soil coverage, s_c , or LAI (see Eq. 2.14). Note that the individual E_v , E_{sub} , E_0 , E_{soil} and E_i contributions to evaporation are not recognized in a two-layer resistance scheme. Theoretically speaking, multi-level schemes may be developed to include more types of land surface elements and more layers of vegetation. For instance, a four-layer version was developed and applied by Choudhury and Monteith (1988). A major advantage of two and multi-level resistance schemes is the explicit recognition of canopy and soil evaporation from which the crop water use can be found. Resistance schemes for homogeneous individual land surface elements are the simplest ones (one-layer schemes) and assume either complete soil or complete canopy coverage (Figure 3.1, part B).

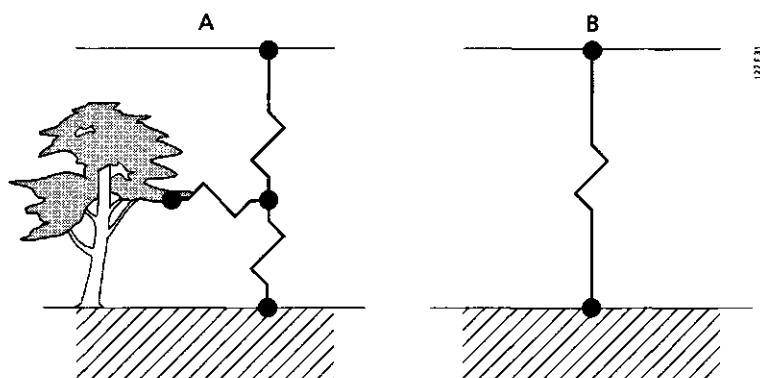


Fig. 3.1 Conceptual resistance scheme for two (Part A) and one layer (Part B) heat transfer systems to be used in land surface parameterization schemes and remote sensing algorithms

Table 3.1 clarifies the number of prognostic variables (including forcing variables if the scheme is not connected to a PBL model) minimally needed to execute one and two-layer resistance schemes. Besides more prognostic variables, the two-layer version requires (depending on the scheme chosen) information about the geometry of the vegetation. For the Simple Biosphere Model (SiB) (Sellers et al., 1986), fractional area covered by the canopy, leaf angle distributions, canopy leaf and stem area density, ground cover leaf and stem area index, green leaf fractions of total leaf and stem area indices, roughness lengths z_0 , and the shelter factor of a canopy leaf are needed in addition to the variables required by a one-layer scheme. Different canopy and soil surface reflectances have to be considered as well. Hence, significantly more model parameters are required when multi-level schemes are applied, which hampers the application of these schemes to a regional scale with distinct spatial variation in all these parameters. Section 3.2 deals with the description of resistances for homogeneous land surface elements whereas Section 3.3 covers the formulation of resistance schemes in composite terrain.

Table 3.1 List of state variables used by one and two-layer schemes. The subscripts *t* and *soil* refer to the canopy and bare soil components, respectively

One-layer model	Two-layer model
T_0	T_{0-t}, T_{0-soil}
T_a	$T_{a-t}, T_{a-inside}$
e_{sat}	$e_{sat-t}, e_{sat-soil}$
e	$e, e_{t-inside}$
u	$u, u_{t-top}, u_{t-inside}$
W	W

3.2 Resistance schemes for homogeneous individual land surface elements

3.2.1 Sensible heat flux density

The resistance r_{ah} to heat transfer between z_{0h} and reference height z_{sur} can be related to the eddy diffusion coefficient for heat K_h in the constant flux density layer according to:

$$r_{ah} = \int_{z_{0h}}^{z_{sur}} \frac{1}{K_h} dz = \int_{z_{0h}}^{z_{sur}} \frac{\phi_h(z, L)}{ku_* z} dz \quad (\text{s m}^{-1}) \quad (3.3)$$

After integration and neglecting the zero-plane displacement d , the resistance can be written as:

$$r_{ah} = \frac{1}{ku_*} \left[\ln\left(\frac{z_{sur}}{z_{0h}}\right) - \psi_h(z_{sur}, L) \right] \quad (\text{s m}^{-1}) \quad (3.4)$$

When Eq. (2.79) is substituted for u_* in Eq. (3.4), r_{ah} is explicitly related to windspeed u :

$$r_{ah} = \frac{1}{k^2 u} \left[\ln\left(\frac{z_{sur}}{z_{0m}}\right) - \psi_m(z_{sur}, L) \right] \left[\ln\left(\frac{z_{sur}}{z_{0h}}\right) - \psi_h(z_{sur}, L) \right] \quad (\text{s m}^{-1}) \quad (3.5)$$

The resistance version of the transport equation for sensible heat flux density then becomes:

$$H = \rho_a c_p \frac{T_{z_{0h}} - T_p}{r_{ah}} \quad (\text{W m}^{-2}) \quad (3.6)$$

As specified along with Eq. (1.1), the turbulent flux densities are positive when directed away from the land surface. The values for $T_{z_{0h}}$ and T_p apply to $z = z_{0h}$ and $z = z_{sur}$ respectively (see Eq. 3.3). If the upper limit of the region of integration z is kept small in such a way that $p \approx p_0$, T_a becomes approximately equal to T_p (see Eq. 2.74). Then Eq. (3.6) can also be re-expressed as a function of the near-surface vertical air temperature difference δT_{a-sur} being positive when $T_{z_{0h}} > T_a$:

$$H = \rho_a c_p \frac{\delta T_{a-sur}}{r_{ah}} \quad (\text{W m}^{-2}) \quad (3.7)$$

3.2.2 Soil heat flux density

The soil heat flux density, G_0 , represents the at-surface component of the total soil heat flux density, q_h^{tot} , addressed earlier at Eq. (2.59):

$$G_0 = -q_h^{tot} \quad \text{for } z=0 \quad (\text{W m}^{-2}) \quad (3.8)$$

The minus sign in Eq. (3.8) is due to the different sign conventions applied to flow along vertical gradients and the surface energy balance. For infinitely small space domains, G_0 may be approximated as the mean flux density across $\nabla_z T_s$:

$$G_0 \approx \lambda'_s \nabla_z T_s \quad (\text{W m}^{-2}) \quad (3.9)$$

Fourier's 2nd law presented earlier at Eq. (2.60) for a thin slab without sinks and sources alternatively reads:

$$\frac{\partial T_s}{\partial t} = a'_s \frac{\partial^2 T_s}{\partial z^2} \quad (\text{K s}^{-1}) \quad (3.10)$$

where the apparent soil thermal diffusivity, a'_s is defined as:

$$a'_s = \frac{\lambda'_s}{\rho_s c_s} \quad (\text{m}^2 \text{ s}^{-1}) \quad (3.11)$$

Hence, G_0 can be expressed as a diffusivity term:

$$G_0 \approx a'_s \rho_s c_s \nabla_z T_s \quad (\text{W m}^{-2}) \quad (3.12)$$

In analogy with the diffusivity - resistance approach applied for H, the form of Eq. (3.12) gives the opportunity to estimate a resistance to sensible heat transport in soil, r_{sh} (Menenti, 1984). In a thin quasi-constant flux density layer, the diffusivity term can be integrated to get a resistance:

$$r_{sh} = \int_{-z_4}^0 \frac{1}{a'_s} dz \quad (\text{s m}^{-1}) \quad (3.13)$$

The lower integration limit $z = -z_4$ is free to select but usually much smaller than $z = -z_3$ because Eq. (3.12) applies to a thin layer to eliminate heat storage effects. Then, G_0 can be written in terms of a potential difference and a resistance as presented by Choudhury and Monteith (1988):

$$G_D = \rho_s c_s \frac{T_0 - T_s}{r_{sh}} \quad (\text{W m}^{-2}) \quad (3.14)$$

3.2.3 Latent heat flux density

Figure 3.2 illustrates the path followed by a water vapour molecule travelling from a homogeneous evaporation front, located at depth $z = -z_e$, to the turbulent surface layer of the lower atmosphere at height $z = z_{0v}$. The domain of vapour flow in the transition region between vapour source and atmosphere is upper bounded by z_{0v} . An internal resistance, r_i describes the blockade the vapour molecule will meet between z_e and z_{0v} . The temperatures at the evaporation front $z = z_e$, at the land-atmosphere interface $z = 0$ and at the roughness length for vapour transport $z = z_{0v}$ should be different: T_{ze} , T_0 and T_{z0v} respectively (Figure 3.2).

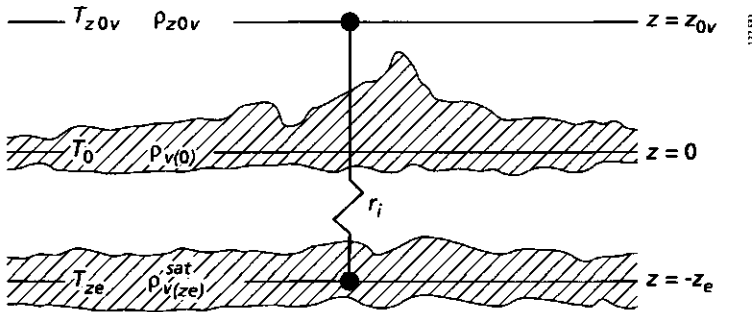


Fig. 3.2 Representation of the internal vapour transport resistances of a homogeneous land surface in a thermally stratified environment

Canopy evaporation model, λE_i

If the homogeneous latent heat flux density of Figure 3.2 is fully related to the evaporation from a single leaf, the internal resistance r_i is built up in the stomatal cavity with a stomatal resistance, i.e. $r_i = r_{st}$. The air humidity in a stomatal cavity is saturated, i.e. $\rho_v(z_e) \approx \rho_v^{sat}(z_e)$. The transfer of vapour from the evaporation front with a temperature T_{ze} to the lower boundary of the atmospheric surface layer with actual vapour density ρ_{z0v} that is not saturated and has an ambient temperature T_{z0v} can be written as:

$$E_t = \frac{\rho_v^{sat}(T_{ze}) - \rho_{z0v}}{r_{st}} \quad (\text{kg m}^{-2} \text{ s}^{-1}) \quad (3.15)$$

The evaporation from a leaf having various stomata can be described by a set of r_{st} values. The canopy resistance, r_c , may be considered to relate to the vapour removal from a canopy. The physical description of r_{st} is of less practical use to describe canopy evaporation. Since T_{ze} and T_{z0v} for a canopy system with many T_{ze}, T_{z0v} -pairs reflecting stomata temperature is difficult to quantify, almost impossible to measure and the $T_{ze}-T_{z0v}$ difference is small enough to be ignored in canopies ($T_{ze} \approx T_{z0v} \approx T_0$), Eq. (3.15) for a large number of stomata is often put forward in the form of Eq. (3.16):

$$E_t = \frac{\rho_v^{sat}(T_0) - \rho_{z0v}}{r_c} \quad (\text{kg m}^{-2} \text{ s}^{-1}) \quad (3.16)$$

This is generally known as the 'Big Leaf' concept (Monteith, 1965; Rijtema, 1965). If the maximum rate of water uptake by roots is less than the atmospheric demand, reduction of crop evaporation is accounted for in Eq. (3.16) as an increment of r_c . The latter suggests that Eq. (3.16) is suitable to describe both the actual and potential evaporation rates of biophysical systems. Even at full exposure and optimal moisture conditions, r_c is not negligible and reaches a minimum value which depends on LAI , i.e. r_c^{min} . The actual value for r_c is besides r_c^{min} being controlled by soil moisture θ , vapour pressure deficit Δe , solar radiation K^{\downarrow} , temperature T_a and carbon dioxide CO_2 . The impact of these factors on canopy conductance r_c^{-1} , the reciprocal of canopy resistance r_c , may be expressed as a product of the maximum conductance and a number of empirical reduction factors which range between 0 and 1 (Jarvis, 1976) or (Baldochi et al., 1991):

$$r_c^{-1} = r_c^{min^{-1}} (LAI) g_1(\theta) g_2(\Delta e) g_3(K^{\downarrow}) g_4(T_a) g_5(CO_2) \quad (\text{m s}^{-1}) \quad (3.17)$$

where $g_1..g_5$ are response functions. The conceptual shape of response function g_1 to g_4 vs. its prognostic variable is illustrated in Figure 3.3.

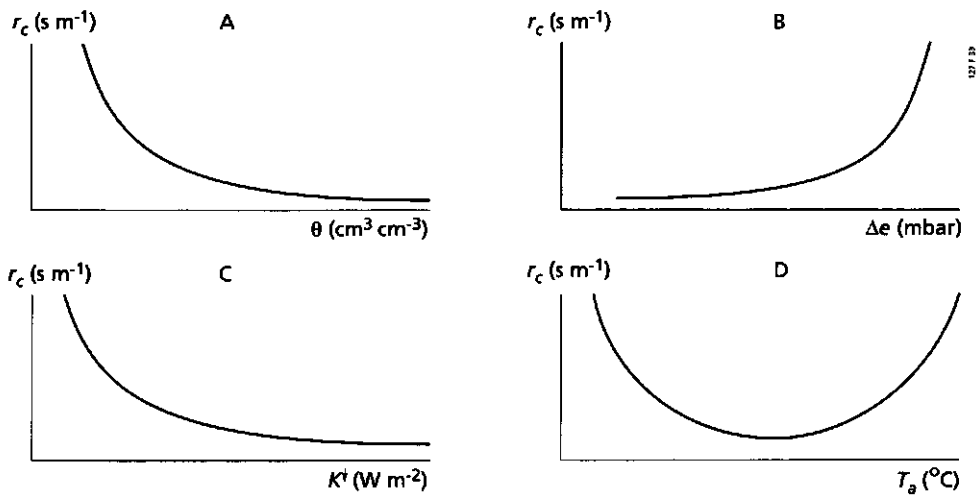


Fig. 3.3 Impact of environmental conditions on the biophysical behaviour of canopy resistance. (Part A) soil water content θ ; (Part B) vapour pressure deficit Δe ; (Part C) incoming shortwave radiation K^s and (Part D) air temperature T_a .

At-surface bare soil evaporation model, λE ,

Bare soils which remain at field capacity evaporate more or less according to the atmospheric demand (O'Kane, 1991). When the soil dries out, moisture is retained in micropores while macropores become air filled (see Figure 2.4). Vaporization of the liquid present in micro pores occurs at the pore end, i.e. at the land surface. Soil water transport in the liquid phase towards the bare land surface between a certain depth $z = -z_l$ and $z = 0$, q_{θ}^{tot} , can also be described by means of a soil physical transport resistance (Bastiaanssen and Metselaar, 1990):

$$E_l = \rho_w q_{\theta}^{tot} = \rho_w \frac{\theta_{z_l} - \theta_0}{r_{sl}} \quad (\text{kg m}^{-2} \text{ s}^{-1}) \quad (3.18)$$

where

$$r_{sl} = \frac{z_l}{D_{\theta}^{eff}} \quad (\text{s m}^{-1}) \quad (3.19)$$

where r_{sl} (s m^{-1}) is the soil resistance to liquid transport and z_l (m) is the sub-surface depth to which θ_{z_l} applies. Since D_{θ}^{eff} changes usually significantly with depth, it is suggested to keep z_l small. Note that the combination of Eqs. (3.18) and (3.19) yields a finite difference form of Eq. (2.32) without gravity driven flow.

Sub-surface soil evaporation model, λE_v

Dry soils exhalate water vapour through air filled pores towards the bare land surface at a rate of:

$$E_v = \frac{\rho_v^{sat}(T_{ze}) - \rho_{z0v}}{r_{sv}} \quad (\text{kg m}^{-2} \text{ s}^{-1}) \quad (3.20)$$

Due to thermal storage in the topsoil, the soil temperature at the evaporation front T_{ze} , will be different from the surface temperature T_0 and T_{ze} may not be equated to T_0 as was done for the 'Big Leaf' concept. Eq. (3.20) differs fundamentally in this respect from Eq. (3.16) because $T_{ze} \neq T_0$. The macroscopic soil resistance to vapour flow, r_{sv} , is the integral of the effective D_v^{eff} -value along a small distance z_e :

$$r_{sv} = \int_{-z_e}^0 \frac{1}{D_v^{eff}} dz \quad (\text{s m}^{-1}) \quad (3.21)$$

Because micropore gas kinetics needs to be involved to quantify D_v^{eff} (see Chapter 2), the quantification of r_{sv} is more complex than its definition. Again, it should be recalled that the transformation of a diffusion parameter D_v^{eff} into a resistance r_{sv} valid for a vertical distance z_e holds as long as the flux density divergence of q_v^{tot} is relatively small.

E_i and E_v may occur simultaneously under natural conditions from the soil matrix yielding a total bare soil evaporation rate E_{soil} (Eq. 2.30). The total resistance r_{soil} for bare soil evaporation E_{soil} should therefore comprise r_{si} and r_{sv} . Because in many conditions, $E_i \gg E_v$ and the evaporation front of a one-layer scheme reflects mainly E_i , the overall bare soil evaporation may be schematized to occur from a 'Big Pore' at the land surface with temperature T_0 :

$$E_{soil} = E_i + E_v = \frac{\rho_v^{sat}(T_0) - \rho_{z0v}}{r_{soil}} \quad (\text{kg m}^{-2} \text{ s}^{-1}) \quad (3.22)$$

Eq. (3.22) implies that the air is always saturated at T_0 , which is rather unlikely to occur under dry conditions and it is physically preferred to compute the soil air relative humidity from Eq. (2.28) to check the saturation conditions from total pressure head, h . The reason of substituting $\rho_v^{sat}(T_e)$ by $\rho_v^{sat}(T_0)$ was given before. The fact that ρ_v inside the soil is very often at near-saturation and that $\rho_v^{sat}(T_0)$ can be obtained for large areas using T_0 -measurements from remote sensing data in a relatively easy manner, gives Eq. (3.22) a macroscopic character. After substituting Eqs. (3.18) and (3.20) into Eq. (3.22) it becomes:

$$\frac{\rho_v^{sat}(T_0) - \rho_{z0v}}{r_{soil}} = \frac{\rho_w(\theta_{zi} - \theta_0)}{r_{si}} + \frac{\rho_v^{sat}(T_e) - \rho_{z0v}}{r_{sv}} \quad (\text{kg m}^{-2} \text{ s}^{-1}) \quad (3.23)$$

Eq. (3.23) is a suitable basis for relating the total bare soil resistance r_{soil} to r_{si} and r_{sv} and thus coupling r_{soil} to D_θ^{eff} and D_v^{eff} in a physically correct manner. The role of r_{sv} is significant in evaporation from arid rangelands and deserts (Menenti, 1984; Wang and Mitsuta, 1992). For more moderate climate conditions, r_{soil} is essentially determined by r_{si} . Despite the important role of r_{soil} in regional energy partitioning (r_{soil} is often larger than r_{ci} , e.g. Shuttleworth and Wallace, 1985), literature to clarify r_{soil} on a physical sound basis is rare. A concise overview of r_{soil} -formulations currently used in hydro-meteorological studies is presented in Table 3.2.

Menenti (1984) and Choudhury and Monteith (1988) attributed r_{soil} fully to vapour flow processes. Under conditions of $E_p \gg E_v$ when the degree of saturation S_θ is large, r_{sv} in Eq. (3.23) automatically becomes small and the role of D_v^{eff} and E_v is subsequently eliminated. Chanzy (1991) as well as Wallace (1995) demonstrated for a standard series of soil water content that r_{soil} with the formulations given in Table 3.2, differs considerably from soil to soil. An obvious reason for the non-univocality between r_{soil} and θ lies in the different response of soil characteristics to the presence of soil moisture. The standard soil hydraulic $h_m(\theta)$, $k(h_m)$, $M(h_m)$ and D_θ properties basically explain that $r_{soil}(\theta)$ must change with soil type. The call for further elaborations of empirical $r_{soil}(\theta)$ relationships by Mahfouf and Noilhan (1991) is therefore to a certain extent superfluous since r_{si} can be directly related to θ using Eq. (3.19) and r_{soil} is physically connected to r_{si} by means of Eq. (3.23).

Table 3.2 Expressions of the bare soil resistance (r_{soil}) to evaporation (E_{soil}) as a function of soil water content (θ), soil vapour density (ρ_v), soil vapour diffusivity (D_v), air molecular diffusivity (D_a), soil liquid diffusivity (D_0^{eff}), diffusion enhancement factor (ξ), potential evaporation (E_{sp}) and wind speed (u).

Source	Type of expression	Formulation
<i>based on liquid flow</i>		
Shu Fen Sun, 1982	empirically based	$r_{soil} = 33.5 + 3.5(\theta_{sat}/\theta)^{2.3}$
Camillo and Gurney, 1986	empirically based	$r_{soil} = -805 + 4140(\theta_{sat} - \theta)$
Passerat de Silan, 1986	empirically based	$r_{soil} = 3.811 \cdot 10^4 \exp(-13.5\theta/\theta_{FC})$
Wallace et al., 1986	empirically based	$r_{soil} = 2.4 \theta^{-1.9}$
Bastiaanssen and Metselaar, 1990	physically based	$r_{soil} = \{[\rho_v^{sat}(T_0) - \rho_{z0}]/[\rho_w \theta_{z1} - \rho_w \theta_0] (z/D_0^{eff})\}$
Kondo et al., 1990	semi-empirically based	$r_{soil} = 216 [(\theta_{sat} - \theta)]^{10}/D_a$
Dolman, 1993	empirically based	$r_{soil} = 3.5 \theta^{-2.3}$
Chanzy and Bruckler, 1993	semi-empirically based	$r_{soil} = \{(\theta_{0.5}, E_{sp}, u)$
van de Griend and Owe, 1994	empirically based	$r_{soil} = 10 \exp [35.6 (0.15 - \theta)]$
<i>based on vapour flow</i>		
Monteith, 1981	semi-empirically based	$r_{soil} = m \int E_v dt$
Menenti, 1984	physically based	$r_{soil} = z_d/D_v^{eff}$
Choudhury and Monteith, 1988	physically based	$r_{soil} = \xi z_d/(D_a \theta_{sat})$

3.3 Resistance schemes for heterogeneous land surfaces

The spatial resolution of current operational thermal radiometers ranges between 120 m for Thematic Mapper and 5 km at the equator for geostationary satellites. On this scale, a landscape is often composited. The parameterization for sensible heat flux density over composite land surfaces based upon remotely sensed thermal infrared measurement can then be solved in a twofold manner:

- a one-layer scheme with effective system parameters;
- a multi-layer scheme with separate parameters for canopies, substrate, open water, bare soil and foliage.

The two-layer scheme is the simplest multi-layer scheme. A two-layer scheme contains several semi-empirical transfer equations which substantially increase the number of model parameters (see Table 3.1). Besides, implementation to regions where the model parameters are not even marginally known, is not feasible. When a two-layer scheme is fed by remote sensing data, the area occupied by canopies and bare soil should be larger than an individual pixel, which is not likely, especially in arid regions. The feasibility

of using a one-layer resistance scheme for composite land surfaces will therefore be examined.

3.3.1 Sensible heat flux density

Surface temperature from remote sensing measurements either delivers a 'pure' or a 'mixed' pixel value. The chance of getting 'mixed' pixels increase with pixel size and with the degree of variability of land surface processes. For 'mixed' pixels, \tilde{T}_0 is only useful to drive a one-layer sensible heat flux density model if the remaining parameters of Eq. (3.6) refer to the same horizontal scale at which they need to be measured or estimated and thus have an effective status too. Then, Eq. (3.6) needs some re-writing using \tilde{r}_{ah} and \tilde{T}_0 which for the air layer adjacent to the land surface $T_a \sim T_p$ becomes:

$$\tilde{H} = \rho_a c_p \frac{\tilde{T}_{z0h} - \tilde{T}_a}{\tilde{r}_{ah}} \quad (\text{W m}^{-2}) \quad (3.24)$$

The intriguing question of whether a one-layer parameterization scheme suffices to provide a correct description of \tilde{H} above composite terrain is a research issue that has been examined by several authors (see Choudhury, 1989, for a review). Basically two questions need reply:

- 1 What is the relationship between \tilde{T}_{z0h} required by Eq. (3.24) and \tilde{T}_0 that can be derived from space measurements after atmospheric and emissivity corrections ?
- 2 Does linear averaging of H_i from individual land surface elements into $\langle H \rangle$ yield \tilde{H} obtained from \tilde{T}_{z0h} and other effective parameters such as \tilde{T}_a and \tilde{r}_{ah} using Eq. (3.24)?

In mathematical terms, the statement to be verified is:

$$(\tilde{T}_0 - \tilde{T}_a) \frac{\rho_a c_p}{\tilde{r}_{ah}} = \frac{1}{n} \sum_{i=1}^n [(T_{z0h} - T_a) \left(\frac{\rho_a c_p}{r_{ah}} \right)]_i \quad (\text{W m}^{-2}) \quad (3.25)$$

where n denotes the number of elementary land units ($i = 1, \dots, n$) located within the area encompassed by a single \tilde{T}_0 measurement. The answer to question 1 will be dealt with first.

The relationship between surface temperature T_0 and 'heat source' surface temperature T_{z0h} was studied by Kalma and Jupp (1990), who analysed diurnal variations of $T_0 - T_{z0h}$ above Australian pastures using $kB^{-1} = 2.3$ as proposed by Garrat (1978) (which implies that T_{z0h} is the temperature at one-tenth of z_{0m} and $T_{z0h} \neq T_{z0m}$). Negative values of $T_0 - T_{z0h}$

appeared in the early morning and late afternoon under stable atmospheric conditions. Kalma and Jupp (1990) concluded that the errors in H are less than 30 W m^{-2} on average if $T_0 = T_{z_{0h}}$ and $kB^{-1} = 2.3$. Choudhury et al., (1986) showed for $kB^{-1} = 2.3$ and unstable conditions above a wheat crop, that deviations in the order of $T_0 - T_{z_{0h}} = 1\text{-}3 \text{ }^\circ\text{C}$ may arise. Taking an arbitrary value of $r_{ah} = 50 \text{ s m}^{-1}$, such derivation yields to H discrepancies of $25\text{-}70 \text{ W m}^{-2}$.

Kustas (1990) tested the hypothesis of Eq. (3.24) in partial canopies (assuming $\tilde{T}_0 = \tilde{T}_{z_{0h}}$) and $kB^{-1} = 2.0$ for a cotton field composed of furrows and a dry soil surface between the rows (Figure 3.4). The cotton crop covered only 20 percent of the soil surface. He showed that the one-layer H formulation performs even better than the two-layer version. For typical bluff-body conditions when the size of the furrows relative to the height of the vegetation are significant, some adjustments in the aerodynamic resistance had to be made.

Kustas et al. (1989) optimized kB^{-1} by assuming $\tilde{T}_{z_{0h}} = \tilde{T}_0$ as a starting point thus making z_{0h} merely an integration limit intimately linked to T_0 . Sugita and Brutsaert (1990) did the same and called z_{0h} therefore the 'radiometric scalar roughness'. The authors found an average value of $kB^{-1} = 5.6 \pm 3.2$ for natural vegetative surfaces in California. Beljaars and Holtslag (1991) advocated that z_{0m} should be 3 to 4 orders of magnitude larger than z_{0h} ($kB^{-1} = 8.8$) for complex terrain and for $\tilde{T}_{z_{0h}} = \tilde{T}_0$. Brutsaert et al. (1993) also calibrated kB^{-1} inversely assuming that $\tilde{T}_0 = \tilde{T}_{z_{0h}}$, and found that $kB^{-1} = 1$ to 2.3 for forests on a regional scale in HAPEX MOBILHY. Stewart et al. (1994) summarized kB^{-1} investigations in several large-scale field experiments and found values between $kB^{-1} = 4$ (grass) to $kB^{-1} = 12.4$ (shrubs).

Hence, more than one ($z_{0h}, T_{z_{0h}}$) pair at a constant sensible heat flux density (constant T_s) may reproduce the same $T_p(z)$ profile (e.g. Qualls et al., 1993) so that z_{0h} may be defined more straightforwardly as the height at which T_0 and $T_{z_{0h}}$ are equal.

The retrieval of \tilde{H} from \tilde{T}_0 was also executed for EFEDA (see Chap. 4) using the Tomelloso field experiments (Gallinaro, 1993). Gallinaro first established the H -flux densities of a representative vineyard using the Bowen-ratio surface energy balance approach. The value of \tilde{T}_0 was retrieved from a thermal infrared radiometer installed at sufficient height to record a temperature which effectively represents vine shrub and soil temperature. The maximum canopy temperature on 28 June, 1991 was around 30°C while the bare soil at the same moment indicated 55°C . Calibration of a mean daily value of $kB^{-1} = 6.5$ was necessary to obtain \tilde{H} -values in agreement with the flux densities observed with the Bowen ratio surface energy balance (Figure 3.5). The standard error of the one-layer model of H was 21.3 W m^{-2} .

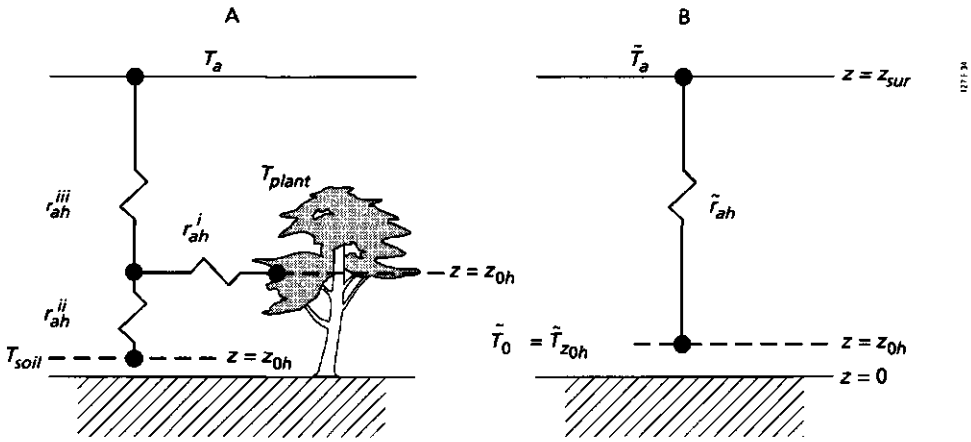


Fig. 3.4 (Part A) Common representation of sensible heat flow in dual source schemes and (Part B) a bulk resistance formulation for sensible heat transfer taking into account an idealized surface plane having a surface temperature \bar{T}_0 equal to the 'heat source' temperature $T_{z_{0h}}$

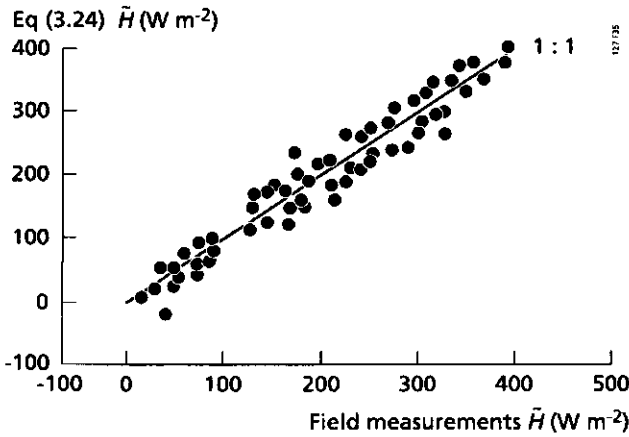


Fig. 3.5 Sensible heat flux densities of heterogeneous land surfaces measured with the Bowen-ratio surface energy balance method and estimated with a one-layer resistance formulation for a Tomelloso vineyard using patch scale effective surface temperature and an optimized $kB^{-1} = 6.5$ (after Gallinaro, 1993).

Lhomme et al. (1994) forced $kB^{-1} = 2$ to calculate H over sparse millet in Niger and came to the conclusion that the root mean square error in H was 384 W m^{-2} , which shows that kB^{-1} cannot be chosen arbitrarily. Although Kalma and Jupp (1990) and Lhomme et al. (1994) preferred two-layer formulations, the view of the present author is that such

application on a regional scale is inconceivable because of the uncertainties of many additional parameters. However, the possibility exists to optimize one-layer model parameters by adjusting kB^{-1} . Since one-layer schemes have been proved to perform well under semi-arid conditions, the SEBAL scheme will rely on a one-layer resistance scheme.

Although the preceding examples indicate that it is possible to estimate \tilde{r}_{ah} to obtain realistic \tilde{H} flux densities, another possibility is to optimize $\delta\tilde{T}_{a-sur}$ at pre-defined kB^{-1} values because multiple $(z_{0h}, T_{z0h} - T_a)$ pairs yield the same flux density. The latter option is worth trying it, the more so since kB^{-1} changes with land surface type and spatial scale and is not mature for implementation studies.

3.3.2 Latent heat flux density

A microscopic description of λE requires the recognition of many different evaporation fronts, surface roughnesses and resistances associated with it. Therefore, the following question in the framework of resistance schemes in heterogeneous landscapes needs to be addressed:

Is the performance of multi-layer latent heat resistance schemes at meso-scale better than one-layer schemes using an effective roughness length \tilde{z}_{0v} , an effective surface temperature \tilde{T}_0 and an effective bulk surface resistance to evaporation, r_s ?

Bougeault et al. (1991) used a one-layer resistance scheme with only five prognostic variables for a study area in Southwest France (Noilhan and Planton, 1989), and came to the conclusion that the prediction of H and λE for isolated sites equipped with flux density stations was adequate. Coupling schemes representing water, desert, vineyards, forests and arable land to a three-dimensional atmospheric model using this type of scheme, yielded a fair agreement between radio soundings, satellite-based surface temperatures and aircraft flux densities.

Beljaars and Holtslag (1991) revised an older version of the European Centre for Medium range Weather Forecasts one-layer scheme and tested an updated version with data collected at Cabauw in the Netherlands and LaCrau in France. The authors stated that simple parameterizations of the surface energy balance such as the Priestley and Taylor equation using a constant α -value for bulk evaporation are sufficiently accurate to predict large-scale evaporation flux densities. Hence, it seems convenient to consider evaporation from heterogeneous land surface systems with a one-layer scheme which at the same time requires considerably less input data.

There is a general consensus in the literature that $z_{0v} = z_{0h}$, which implies that T_{z0h} can be equated to T_{z0v} as well (hence $\tilde{T}_0 = \tilde{T}_{z0h} = \tilde{T}_{z0v}$) if the correct kB^{-1} value is chosen.

The water vapour density at $z = z_{0v}$ is not saturated; ρ_v is over against that always saturated at the evaporation front, $\rho_v^{sat}(T_{soil})$ and depth $z = -z_e$ may be considered as a 'Big Cavity'. Since $\tilde{T}_{z_{0v}} = \tilde{T}_0$ and \tilde{T}_0 can be obtained from remote sensing measurements, from a practical point of view it is preferred to further assume $\tilde{\rho}_v^{sat}(T_e) = \tilde{\rho}_v^{sat}(T_0)$. An equation for water vapour transport similar to Eq. (3.24) is finally obtained:

$$\bar{E} = \frac{\tilde{\rho}_v^{sat}(T_0) - \tilde{\rho}_{z_{0v}}}{r_s} \quad (\text{kg m}^{-2} \text{ s}^{-1}) \quad (3.26)$$

The canopy and soil resistances r_c and r_{soil} are by now replaced by a bulk surface resistance to evaporation, r_s . The value for r_s reflects several plant and soil physical properties (see Section 3.2.3) such as r_c^{min} , g_1, g_5 response functions, D_v^{eff} , D_θ^{eff} , $\theta(z)$ and $\rho_v(z)$. Jordan and Ritchie (1972) proposed a simple expression to split r_s into r_t and r_{soil} :

$$\frac{1}{r_s} = \frac{s_c}{r_t} + \frac{1-s_c}{r_{soil}} \quad (\text{m s}^{-1}) \quad (3.27)$$

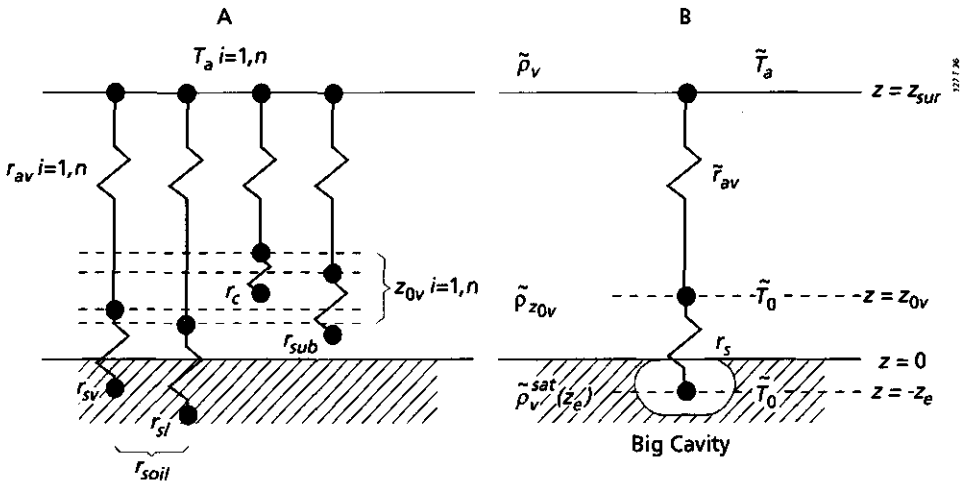


Fig. 3.6 Resistance scheme for the latent heat flux densities of heterogeneous land surface processes (the same evaporation processes as those introduced in Chap. 2). (Part A) micro-scale evaporative sites are included and (Part B) a Big Cavity with a single macroscopic bulk surface resistance to evaporation

where s_c is the fractional soil coverage. Figure (3.6) provides a graphical presentation of the various sources of water vapour and how an effective source can be described. The resistance for near-surface atmospheric vapour transport can be parameterized as:

$$r_{av} = \int_{z_v}^{z_{sur}} \frac{1}{K_v} dz = \int_{z_v}^{z_{sur}} \frac{\phi_v(z, L)}{k u_{*z}} dz \quad (\text{s m}^{-1}) \quad (3.28)$$

which yields after integration:

$$r_{av} = \frac{1}{k u_*} \left\{ \ln\left(\frac{z_{sur}}{z_{0v}}\right) - \psi_v(z_{sur}, L) \right\} \quad (\text{s m}^{-1}) \quad (3.29)$$

which, in terms of a vertical effective atmospheric vapour flux density above composite land surfaces, can be written as:

$$\tilde{E} = \frac{\tilde{\rho}_{z_{0v}} - \tilde{\rho}_v}{\tilde{r}_{av}} \quad (\text{kg m}^{-2} \text{ s}^{-1}) \quad (3.30)$$

where $\tilde{\rho}_v$ and \tilde{r}_{av} apply to the reference height z_{sur} . Eqs. (3.26) and (3.30) suggest that the vapour density at the roughness length, $\tilde{\rho}_{z_{0v}}$ is known, which is seldom the case. Assuming vapour sinks offsets vapour sources at $z = z_{0v}$ continuity of vapour flux densities holds and Eqs. (3.26) and (3.30) may be combined:

$$\tilde{E} = \frac{\tilde{\rho}_v^{sat}(T_0) - \tilde{\rho}_v}{\tilde{r}_{av} + r_s} \quad (\text{kg m}^{-2} \text{ s}^{-1}) \quad (3.31)$$

It is customary to re-express ρ_v into vapour pressure e using Eqs. (2.25) , (2.48) and the expression for latent heat of vaporization, λ :

$$\lambda = \frac{R_a c_p p}{R_v \gamma} \quad (\text{J kg}^{-1}) \quad (3.32)$$

where R_a ($287 \text{ J kg}^{-1} \text{ K}^{-1}$) is the specific gas constant for dry air, R_v ($461 \text{ J kg}^{-1} \text{ K}^{-1}$) is the specific gas constant for water vapour, γ (mbar K^{-1}) is the psychrometric constant and p (mbar) the total air pressure. Eq. (3.31) might alternatively be expressed as:

$$\lambda \tilde{E} = \rho_a c_p \frac{\tilde{e}^{sat}(T_0) - \tilde{e}}{\gamma(\tilde{r}_{av} + r_s)} \quad (\text{W m}^{-2}) \quad (3.33)$$

The minimum bulk resistance for saturated soils and open water bodies is $r_s = 0$, while for vegetation a value between $r_c^{min} = 30\text{-}150 \text{ s m}^{-1}$ usually applies (Sud et al., 1990). Wet land surfaces which contain a fraction bare soil will therefore get a lower minimum r_s value in comparison to wet complete canopies. The controlling factor for energy

partitioning in heterogeneous land surfaces, r_a , is regulated by soil water storage W through $g_r(\theta)$ in Eq. (3.17) and $r_{s_r}(\theta)$ in Eq. (3.19) while s_c of Eq. (3.27) weights these contributive effects. The usefulness of a 'Big Cavity', with a bulk resistance and surface temperature is very well suited to describe the regulation of pixel-scale evaporation rates for large areas (Bastiaanssen et al., 1994a). Chapter 8 describes the areal r_s behaviour for a range of scales using Eq. (3.33).

Monteith (1965) used a canopy version of Eq. (3.33) in conjunction with the surface energy balance and a Taylor expansion of $e_{sat}(T_0) = e_{sat}(T_a) + s_a(T_0 - T_a)$ to derive his one-step combination equation for canopy evaporation. Since Penman did the same earlier for open water surfaces, this energy balance combination equations is commonly referred to as the Penman-Monteith equation, λE^{PM} :

$$\lambda E^{PM} = \frac{s_a(Q^* - G_0) + \rho_a c_p \Delta e / r_a}{s_a + \gamma(1 + r_d / r_a)} \quad (\text{W m}^{-2}) \quad (3.34)$$

where s_a (mbar K^{-1}) is the slope of the saturated vapour pressure curve and Δe (mbar) is the vapour pressure deficit at height $z = z_{sur}$

A simplification of the Penman-Monteith equation was proposed by Priestley and Taylor (1972) who found that the atmospheric drying power in Eq. (3.34), $\rho_a c_p \Delta e / r_a$, is a constant multiple of $s_a(Q^* - G_0)$ over wet surfaces. Substitution of $\rho_a c_p \Delta e / r_a$ by a parameter α and assuming $r_c = 0$ for wet surfaces, reduces λE^{PM} to λE^{PT} :

$$\lambda E^{PT} = \alpha(Q^* - G_0) \frac{s_a}{s_a + \gamma} \quad (\text{W m}^{-2}) \quad (3.35)$$

For wet surfaces, the α -value ranges between 1.0 and 1.35 (Choudhury et al., 1994). The advantage of λE^{PT} is that r_a and r_c do not need to be specified for composite land surfaces. Because of its simple formulation and the ability to use α as an evaporation control parameter ($\alpha = 0$ means zero evaporation), Eq. (3.35) became popular in hydrological studies of complex terrain (Barton, 1979). As a matter of fact, α is a simplified substitute of r_s with a less profound physical meaning which may be sufficiently precise to predict the regional exchange processes between land and atmosphere on a coarser scale (de Bruin and Holtslag, 1982b; Beljaars and Holtslag, 1991).

3.4 Surface temperature and evaporation

Remote sensing parameterizations of the land surface energy balance in general aim to relate H and λE to remotely measurable parameters: In the current Chapter, it has been shown that T_0 is related with G_0 , H and λE . If T_0 is equal to T_{20h} (by adjusting kB^{-1}),

the transfer equations for sensible heat (Eq. 3.24), soil heat (Eq. 3.14) in combination with the net radiation balance (Eq. (2.1) and the surface energy balance (Eq. 1.1) for a location at a certain moment can be combined to obtain:

$$(1-r_0)K^\downarrow + \varepsilon_0 L^\downarrow - \lambda E = (+\varepsilon_0 \sigma T_0^4 + \frac{\rho_a c_p}{r_{ah}} T_0 + \frac{\rho_s c_s}{r_{sh}} T_0) - (\frac{\rho_a c_p}{r_{ah}} T_a + \frac{\rho_s c_s}{r_{sh}} T_s) \quad (\text{W m}^{-2}) \quad (3.36)$$

which, after applying a first order Taylor's expansion to $\varepsilon_0 \sigma T_0^4$ and re-expressing Eq. (3.36) into T_0 , reduces to:

$$T_0 = \frac{c_1 + (1-r_0)K^\downarrow + \varepsilon_0 L^\downarrow - \lambda E}{c_2} \quad (\text{K}) \quad (3.37)$$

where

$$c_1 = \frac{\rho_a c_p}{r_{ah}} T_a + \frac{\rho_s c_s}{r_{sh}} T_s + 3\varepsilon_0 \sigma T_0^4 \quad (\text{W m}^{-2}) \quad (3.38)$$

and

$$c_2 = \frac{\rho_a c_p}{r_{ah}} + 4\varepsilon_0 \sigma T_0^3 + \frac{\rho_s c_s}{r_{sh}} \quad (\text{W m}^{-2} \text{ K}^{-1}) \quad (3.39)$$

Eq. (3.37) can be further reduced to:

$$T_0 = c_3 - c_4 \lambda E \quad (\text{K}) \quad (3.40)$$

where c_3 is $\{c_1 + (1-r_0)K^\downarrow + \varepsilon_0 L^\downarrow\}/c_2$ and c_4 is similar to c_2^{-1} . The application of Eqs. (3.36) to (3.40) is restricted to a place and time specific environment. If r_0 , K^\downarrow , ε_0 , r_{ah} , T_a , r_{sh} , T_s , c_3 and c_4 vary pixelwise within a composite landscape, an overall $\lambda E(T_0)$ relationship such as suggested by Seguin and Itier (1983) may not be used. The art of remote sensing techniques is therefore to identify the x,y -patterns of c_3 and c_4 during one particular satellite overpass. Thereafter, λE can be obtained according to Eq. (3.40).

3.5 Length scale of land surface flux densities

Surface energy balance studies fed by remote sensing data are traditionally based on a one-dimensional representation of the exchange rates between land and atmosphere. On heterogeneous land surfaces, horizontal advection arises and the vertical flux densities may be perturbed by lateral inflow of momentum, heat and moisture.

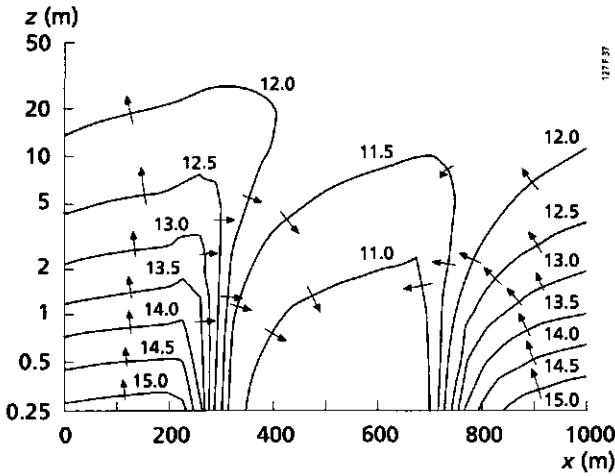


Fig. 3.7 Sketch of two-dimensional heat flow between two adjacent patches with different surface temperatures ($^{\circ}\text{C}$) (adapted after Blyth et al., 1993).

Landscape heterogeneity involves step-changes in surface conditions between neighbouring patches (e.g. surface roughness and surface temperature).

Surface elements with differences in temperature generate a horizontal sensible heat flux density (Figure 3.7). Advection of sensible heat is most strongly developed at the edges of land elements where the spatial difference in $T_a(x,y)$ at a fixed height z are most evident. The horizontal gradients are most evident at surface level ($z = 0$) (see Figure 3.7) because T_0 is dominantly controlled by slow hydrological processes such as infiltration, water uptake by roots and bare soil evaporation (Eq. 3.40).

Land surface flux densities can be reliably estimated from vertical profiles using the Monin-Obukhov similarity hypothesis. The vertical profiles at leading edges are however distorted and the flux densities should be calculated at some distance from this edge. The height integration of the eddy diffusivity coefficients needs to be consistent with the at-surface scale of temperature. The horizontal scale of a homogeneous land surface with a certain condition over which the surface flux density tends to equilibrate, depends primarily on the height above the terrain, i.e. the height of the internal adapted layer (de Bruin et al., 1991). For momentum transfer, horizontal x , and vertical length scales z , are related according to Townsend (1965):

$$\frac{z}{x} \approx \frac{u_*}{u} \quad (-) \quad (3.41)$$

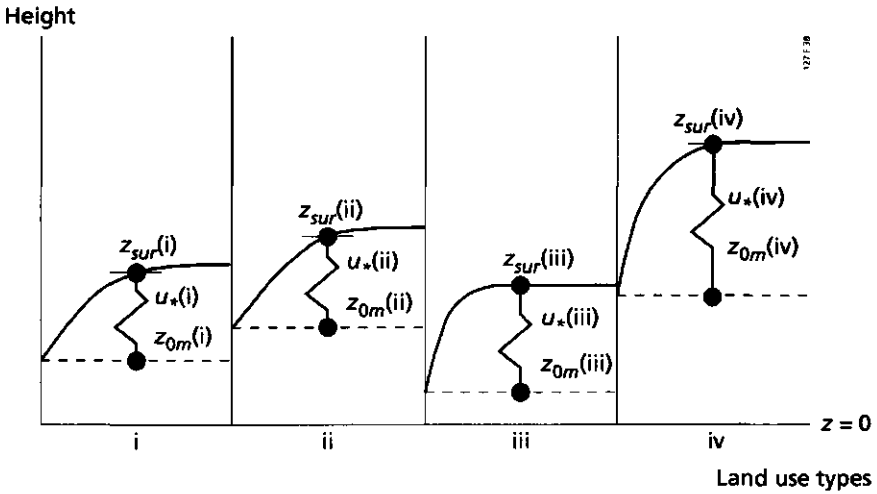


Fig. 3.8 Schematic representation of the pixelwise heights of the adapted air layer with the pixel edges being represented as the leading edges

Using typical values suggests that $z/x \approx 0.01$ to 0.1 applies and that the vertical profiles and flux densities are adapted at a height of one-tenth of the fetch length, i.e. the distance to the downwind edge. The schematic representation displayed in Figure 3.8 was established with Myake's model for the height of the internal layer, z , and the fetch length, x , necessary for the development of an adapted surface layer (Myake, 1965):

$$x = 2z_{0m} \left\{ \frac{10z}{z_{0m}} \left(\ln \frac{10z}{z_{0m}} - 1 \right) + 1 \right\} \quad (\text{m}) \quad (3.42)$$

Remote sensing measurements of an effective surface temperature \tilde{T}_0 , implies that spatial variation in T_0 cannot be detected at horizontal scales smaller than the size of a pixel. Hence, homogeneity is assumed for each pixel and step-changes in surface conditions are schematized to occur at the pixel edges (if the image comprises a composite terrain). If the \tilde{T}_0 -measurements are used for flux density analysis, the integration height z_{sur} in Eq. (3.3) should be selected according to Eq. (3.42). In remote sensing nomenclature, x should be equal to half the pixel size and $z = z_{sur}$. Between the land surface at $z = z_{0h}$ or $z = z_{0m}$ and $z = z_{sur}$, the physical processes are schematized to be strictly one-dimensional and horizontal advection of heat at the leading pixel edges is disregarded (Figure 3.8).

3.6 Concluding remarks

Resistance schemes for H and λE coupled to remote sensing measurements of composite terrain with pixel sizes comprising a mixture of individual terrain elements implies that effective hydro-meteorological parameters need to be specified. Former studies have indicated that the description of H and λE by one-layer resistance schemes for bulk H and λE sources appears to be adequate. Moreover, the number of required input parameter decreases substantially in one-layer compared to multi-layer schemes. Resolved and unresolved issues arising from one-layer schemes have been briefly discussed and it was concluded that some of the parameters of one-layer schemes require optimization to represent the areal effective properties and flux densities correctly. Notably, a modification of the roughness for momentum / heat ratio, kB^{-1} , is needed to assume $\tilde{T}_0 = \tilde{T}_{z_{0h}}$. Since z_{0h} and z_{0m} are definitely not equal, \tilde{T}_0 can never be equated to $T_{z_{0m}}$. Blyth and Dolman (1995) showed that z_{0h} for sparse canopies is affected by available energy, humidity deficit and vegetation cover and that *general rules for kB^{-1} on heterogenous land surfaces cannot be given a priori*. Dolman and Blyth (1995) used the concept of blending height to predict effective values for the momentum and heat resistance from which the corresponding roughness could be inverted. They showed that the partial vegetation cover and the contrast of r_s and z_{0m} between neighbouring patches have all significant effects on kB^{-1} . Their recommendation is to apply two-layer resistance schemes which explicitly deal with different τ , H and λE flux densities for soil and vegetation. Another concern related to the application of Eq. (3.25) is a correct quantification of $\tilde{T}_0 - \tilde{T}_a$ which is ultimately linked to kB^{-1} (see also Kustas et al., 1989) This will be dealt with in Chapter 6.

The representation of the bulk source of sensible and latent heat at z_{0h} assuming $z_{0h} = z_{0v}$, establishes the principal basis for using \tilde{T}_0 measurements for the determination of all land surface flux densities Q , G_0 , H and λE . Since $\tilde{T}_0 = \tilde{T}_{ze}$ will be assumed to hold independent of surface type, the vapour density in a 'Big Cavity' with a single effective evaporation front can be assessed from \tilde{T}_0 -measurements assuming saturated humidity conditions. The bulk resistance to evaporation r_s is favoured as a suitable trade-off between degree of physics and measurable radiative properties to specify λE at heterogeneous land surfaces. Bio and soil physical parameters such as r_c^{min} , g_1 to g_5 , D_v^{eff} , D_0^{eff} and s_c are analytically related to r_s . It can be concluded that it is easier to find λE as the rest term of the energy budget rather than estimating it from r_s , which implies that the skill of evaporation mapping depends on the possibility of mapping sensible heat transfer.

The relationship between T_0 and λE has been derived and the role of other temperatures and resistances on the $T_0(\lambda E)$ relationship has been analytically demonstrated. Since the $T_0(\lambda E)$ relationship is not constant in composite terrain, it is strictly necessary to estimate the intercept and slope of the $T_0(\lambda E)$ relationship in a distributed manner. Step-

changes in T_0 and the remaining parameters of Eq. (3.36) may induce horizontal heat advection between neighbouring pixels. The height of the internal adaption layer changes with the distance to the leading edge i.e. the pixel boundary. A vertical flow schematization with effective resistances can be maintained if the height of the vertical profiles for wind, heat and moisture, i.e. the integration limits for eddy diffusivity, are kept low and chosen according the pixel size and local roughness conditions (see also Klaassen and van den Berg, 1985).

4 The Mediterranean study areas

4.1 Selection of test sites

Testing a new remote sensing parameterization of land surface flux densities requires the availability of three different categories of ground data:

- Observations of radiative surface properties to design or evaluate simplified procedures for atmospheric corrections;
- Observations of specific hydro-meteorological parameters in relation to specific remote sensing parameters;
- Observations of in-situ surface flux densities to validate the land surface flux densities predicted by means of remote sensing.

Field data collected in the Qattara Depression in the Western Desert of Egypt will be mainly used for the first two items. The reason for investigating the Qattara Depression stems from the availability of multi-year field data by a previous investigation on the groundwater discharge of the Nubian Sandstone aquifer in the Western Desert of Egypt (Menenti et al., 1991). Within the latter project, the aim was to assess the groundwater flow to the Qattara Depression in Egypt and its subsequent evaporation. Knowledge of these evaporation losses facilitates the estimation of the groundwater balance in the Northern part of the Western Desert of Egypt. Conventional groundwater flow models of this area did not incorporate the groundwater evaporation losses from the Qattara Depression (e.g. Ezzat, 1983). Landsat Thematic Mapper data (TM) were used to survey the variability of the land surface radiative properties. The distributed evaporation values derived from TM data were applied to calibrate regional groundwater flow models (Bastiaanssen and Menenti, 1990).

Estimates of the regional evaporation of the Eastern Nile Delta were made by others (Abdel Gawad et al., 1991) and considered for a comparison study with remote sensing data. The data from a calibrated regional water and salt balance model were used as a suitable reference for areal evaporation. The available evaporation data were applied to validate the evaporation assessed by SEBAL at the level of an irrigation district and on a coarser scale (Bastiaanssen et al., 1992). In contrast to the field work in the Qattara Depression, no experimental fieldwork on radiation and surface energy budgets has been conducted in the Eastern Nile Delta.

Regional evaporation is extremely difficult to measure. Simultaneous measurements of heat flux densities were performed on the ground and with airborne eddy correlation sensors at various scales during the European Field Experiment in Desertification-

threatened Areas, EFEDA; These data were therefore of great value to test SEBAL. This large-scale collaborative experimental research project was executed during June 1991 in Castilla la Mancha, Spain. The EFEDA program (Bolle et al., 1993) is part of the Hydrological Atmospheric Pilot EXperiment HAPEX series. HAPEX promotes the general upgrading of the description of land surface processes from canopy to catchment and river basins by performing multi-disciplinary field studies.

4.2 Qattara Depression, Egypt

Location and climate

The Western Desert of Egypt stretches East-West between the Nile Valley and the border with Libya and North-South from the Mediterranean Sea to the Sudanese border. The largest and deepest depression in the Western Desert is the Qattara Depression between 29-31°N and 26-29° E. Its location is illustrated in Figure 4.1. Rainfall in this region is less than 10 mm yr⁻¹ and the aridity index according to the legend proposed by UNESCO is hyper-arid ($P/E_p < 0.05$). The desert climate inside the Qattara Depression is characterized by a strong diurnal variation of solar radiation, temperature and air humidity (Figure 4.2). One should note that the relative humidity can fluctuate between its physical limits within 24 hours.

Physiography and soils

The natural depressions are formed by tectonical movements in combination with powerful wind erosion. Differences in erosivity of the bedrock layers led to the formation of mesas, escarpments and plateaux. The Qattara Depression occupies an area of approximately 20,000 km². The elevation of the land surface varies between 20 to 130 m below mean sea level with the lowest point at 133 meter below mean sea level. At some locations, the depression floor remains permanently wet due to shallow groundwater tables. The combination of wet surface types located in a hyper-arid climate has induced a soil salinization process which has finally yielded highly structured saline sands. These are called playas in English and sebkhass in Arabic (e.g. Neal, 1965). The structure of the surface crust is determined by the evaporation rate and type of salt minerals. Agriculture is not feasible and occurs only in the oases of Qara and Siwa where faults recharge the oases with brackish and fresh groundwater.

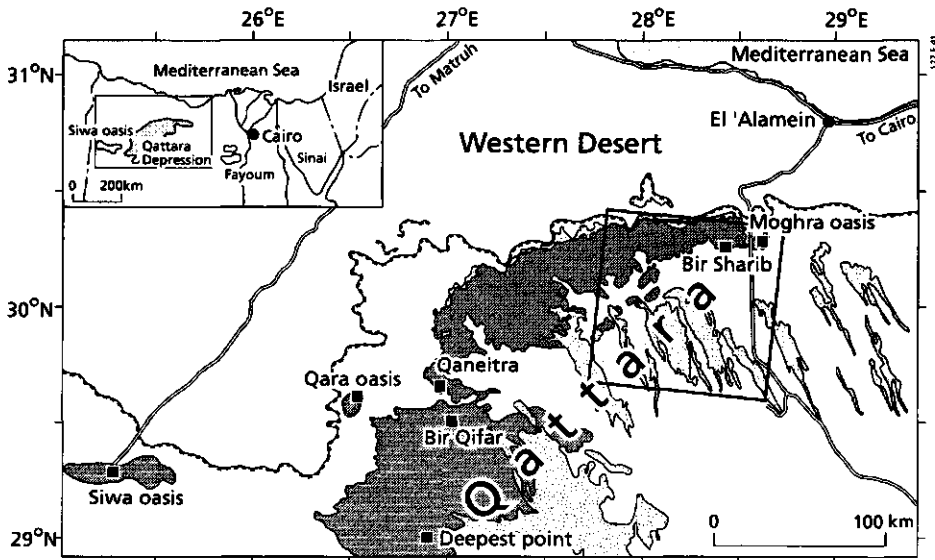


Fig. 4.1 Location of the **Qattara Depression** in the Western Desert of Egypt. The bold squares refer to the location of the field measurements described in Table 4.1. The shaded inset in the figure centre presents the position of Colour Plates 1 and 2

The field work focused on:

- Acquisition of ground truth data to convert satellite measurements via atmospheric correction procedures into land surface characteristics;
- Collection of auxiliary micro-meteorological data to investigate possible parameterizations in energy budget modelling;
- Measurements of the actual evaporation rate at different physiographical units such as sand, limestone, sebkha and salt marshes using the Bowen-ratio surface energy balance method;
- Collection of various soil physical data necessary to calibrate and validate EVADES.

Field investigation

Five expeditions have been carried out to the test sites specified in Table 4.1 between 1986 and 1989. By absence of roads, the collection of field data was restricted to the Eastern and Western ends of the Qattara Depression (Figure 4.1). A total number of 16 test sites were investigated, spread over 5 field expeditions. Most field work concentrated for practical reasons on an area of say 20 km around the artesian well Bir Qifar (Figure 4.3).

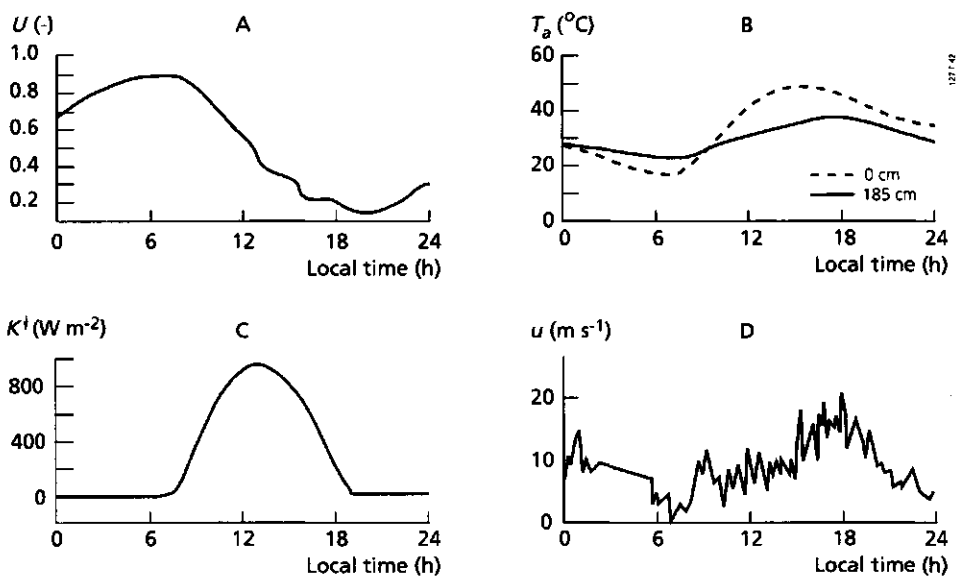


Fig. 4.2 Typical daily evolutions of (Part A) relative humidity U , (Part B) air temperature T_a , (Part C) incoming shortwave radiation K^i and (Part D) windspeed u measured at **Bir Qifar-6** on 12 September, 1989 at 200 cm height

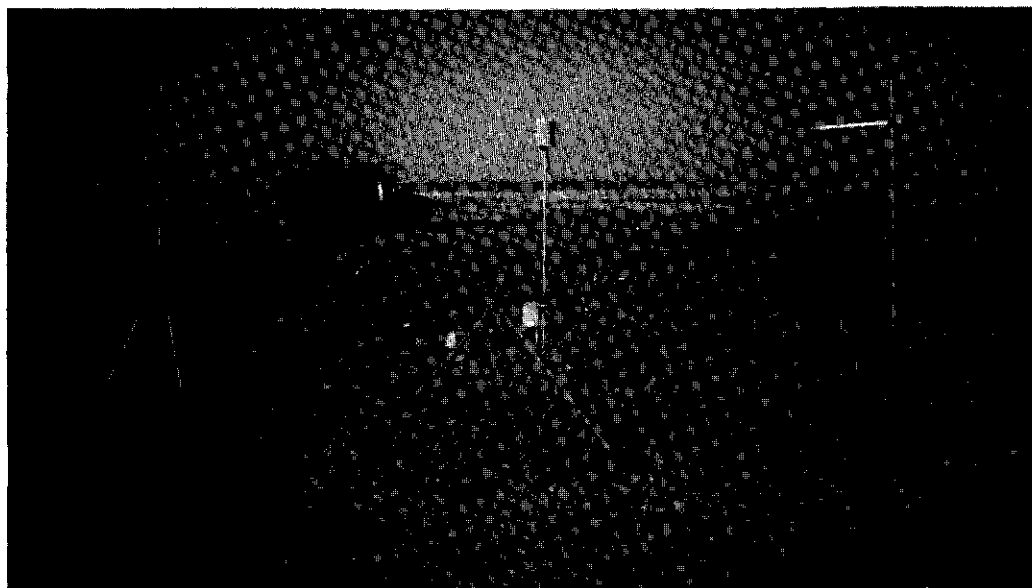


Fig. 4.3 Land surface conditions around Qara oasis inside the **Gattara Depression**, showing typical rough sebkha soil types. Measurements of the radiation and surface energy balance are depicted.

Table 4.1 Location and surface types investigated during the five field expeditions carried out in the **Qattara Depression, Western Desert of Egypt between 1986 and 1989**

Expedition	Date	Location	Longitude	Latitude	Surface type	Groundwater table depth below soil surface (cm)	Surface (0-1 cm) water content (cm ³ cm ⁻³)
1	1-3/8/86	Bir Sharib	28°23'	30°20'	Sand sheet	65	0.01
1	4-5/8/86	Moghra oasis	28°35'	30°22'	Rough sebkha	70	0.17
2	23/2/87	Kharga oasis	36°21'	28°05'	Dry flat sebkha	deep	0.02
2	25-27/2/87	Bir Tarfawi	28°52'	22°58'	Bare coarse sand	90	0.00
2	9-10/3/87	Siwa oasis Southeast	25°38'	29°09'	Salt marsh	30	0.06
2	11-13/3/87	Siwa oasis West	25°29'	29°13'	Dry flat sebkha, hard salt crust	32	0.07
2	15-16/3/87	Siwa oasis East	25°38'	29°16'	Rough sebkha	51	0.12
3	4-6/11/87	Qara oasis North	26°28'	29°37'	Brown rough sebkha	68	0.06
3	8-9/11/87	Deepest point	26°52'	29°04'	Dry flat sebkha hard salt crust	61	0.05
3	11-13/11/87	Qaneitra Muhasas	26°53'	29°44'	Grey brown flat sebkha	55	0.12
4	10-13/6/88	Bir Qifar-1	26°56'	29°32'	Wet flat sebkha	20	0.15
4	14-16/6/88	Bir Qifar-2	26°59'	29°34'	Sandy rough sebkha	59	0.05
4	17-19/6/88	Bir Qifar-3	27°07'	29°35'	Dry flat sebkha	43	0.04
4	20-22/6/88	Bir Qifar-4	26°58'	29°36'	Clayey flat sebkha	44	0.09
4	23-25/6/88	Bir Qifar-5	26°58'	29°31'	Rough sebkha	25	0.10
5	12-13/9/89	Bir Qifar-6	26°59'	29°32'	Sand on limestone	deep	0.02
5	14-18/9/89	Bir Qifar-7	26°59'	29°34'	Salt marsh, sebkha	105	0.03
5	19-21/9/89	Bir Qifar-8	26°56'	29°38'	Sandsheet, sebkha	38	0.05

The field investigation was most intensive during the 4th and 5th expedition to Bir Qifar, which *inter alia* focused on Bowen ratio measurements. The hydro-meteorological parameters measured are shown in Table 4.2. Most of the micro-meteorological measurements were collected automatically by scanning devices with a five minute integration time. A handheld thermal infrared camera was used every hour to manually register the surface radiation temperature at 5 to 15 pre-selected land surface units with a difference in colour, surface roughness and surface wetness. The vertical soil moisture profiles, $\theta(z)$, were determined by means of the gravimetric method. To prevent drying of the soil samples during transport from the desert to the laboratory at Cairo, the samples were weighted on site with an electronic balance. The volumetric water content was obtained afterwards by measuring the dry bulk density. Since the soil water in the toplayer was exposed to strong daily thermal forcing, the diurnal range of surface soil water content θ_0 was also investigated. Vertical gradients of matric pressure head $h_m(z)$ were measured with a mobile transducer system.

Table 4.2 Measured hydro-meteorological parameters relevant for energy and water balance studies, Qattara Depression, Western Desert of Egypt

Parameter	Symbol	Instrument	Elevation above surface level (cm)	Spatial variability (no. of units)
Micro-meteorological measurements				
Net radiation	Q^{\downarrow}	Net radiometer	50	1
Shortwave incoming radiation	K^{\downarrow}	Solarimeter	50	1
Shortwave reflected radiation	K^{\uparrow}	Solarimeter	50	6 to 7
Shortwave diffuse incoming radiation	K^{\downarrow}_{df}	Solarimeter	50	1
Surface radiation temperature	T_o^R	Thermal infrared radiometer	50	5 to 15
Soil temperature	T_s	Thermocouple	0.5, 1, 2.5, 5, 10, 25, 50	2
Air temperature	T_a	Thermocouple	50, 200, 300	1 to 3
Air relative humidity	U	Psychrometer	50, 200	1 to 3
Bowen-ratio	β	Psychrometer	50, 200	1 to 3
Wind speed	u	Anemometer	50, 200, 300	1
Soil heat flux density	q_{hc}	Flux density plates	0.5, 1.5 cm	2
Soil water measurements				
Soil water content	θ	Gravimetric	0,1,5,10,25,50,75,100	1 to 5
Matric pressure head	h_m	Tensiometer	0,1,5,10,25,50,75,100	1 to 5
Depth of groundwater table	z_{gw}	Piezometer	-	1 to 5

The soil physical relationships $h_m(\theta)$ and $k(h_m)$ were analyzed afterwards in the laboratory. The sampling scheme for undisturbed soil cores consisted of 30 cm depth increments. A total of 34 cores were collected across the 16 test sites to determine the $h_m(\theta)$ and $k(h_m)$ relationships using the evaporation method (Boels et al., 1978). The output of the evaporation method consisted of a $h_m(\theta)$ relationship ranging between $h_m = -50$ cm and -600 cm and a $k(h_m)$ relationship in a somewhat smaller range of h_m . The $h_m(\theta)$ and $k(h_m)$ data were fitted for each individual soil sample using the analytical fitting functions proposed by van Genuchten (1980).

4.3 Eastern Nile Delta, Egypt

Location and climate

The Eastern Nile Delta is geographically enclosed by the Eastern Desert and the Damietta branch of the river Nile. The study area lies between latitude 30-31°N and longitude 31-33°E (Figure 4.4). The desert fringe with the Eastern Desert is characterized by abrupt changes in land cover, land use and surface hydrology. An efficient utilization of Nile water is a vital necessity to cultivate crops in an agro-climatic zone that ranges from being arid at Cairo ($0.03 < P/E_p < 0.20$) to semi-arid at Alexandria ($0.20 < P/E_p < 0.5$). The humidity and air temperature vary accordingly with the highest humidities and lowest

temperatures occurring at the shore. The diurnal fluctuation of the major meteorological parameters is illustrated in Figure 4.5. Comparing the relative humidity of Figure 4.5 with Figure 4.2, it appears that the air layer overlying the irrigated land remains more humid and less warm throughout the whole day for this particular example.

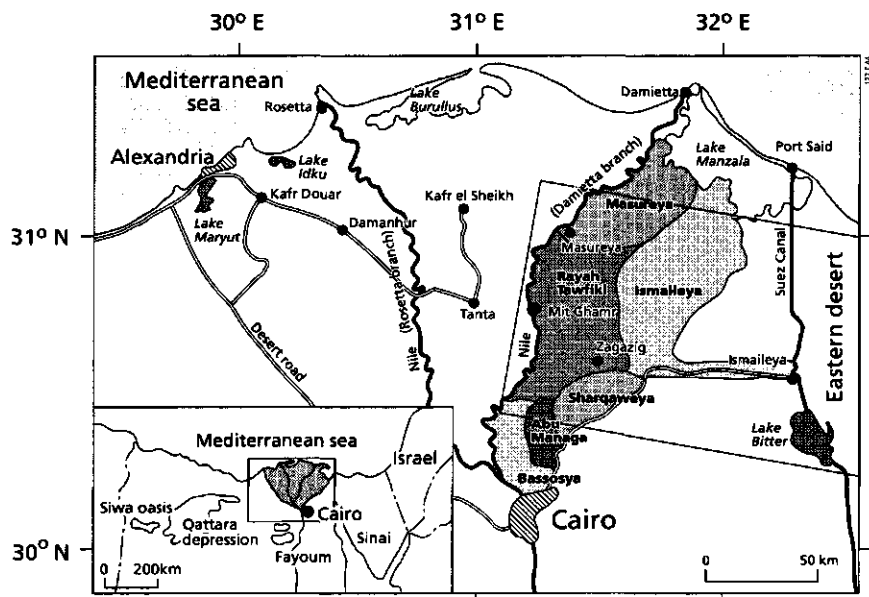


Fig. 4.4 Location of the **Eastern Nile Delta** in Egypt. The main irrigation command areas are indicated. The inset at the right hand side presents the position of Colour Plate 9.

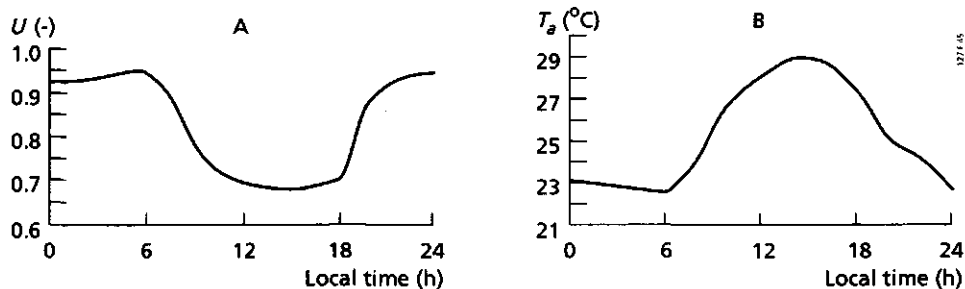


Fig. 4.5 Typical daily evolutions of (Part A) relative humidity U and (Part B) air temperature T_a measured near Kafr Douar in the **Nile Delta** on 6 August, 1991 at 200 cm height.



Fig. 4.6 Agricultural field conditions at small-scale irrigation borders in the Eastern Nile Delta

Land use

Because of family inheritance, the farm land is sub-divided into many small fields. Consequently the average size of fields is only 100 m × 100 m (Figure 4.6). The major summer crops cultivated in the Delta are wheat, rice, cotton, maize, berseem, deciduous trees and vegetables. Farmers get their irrigation water on the basis of a rotational schedule, traditionally by furrow or border irrigation. Due to the reuse of drainage water, not all irrigation water is of good quality. Reclamation activities are ongoing in the desert fringes where rotating pivot systems are often introduced. Many installations can be found on both sides of the Ismaileya canal between the edge of the Delta border and the town of Ismaileya on the Suez Canal (see Figure 8.7 and Colour Plate 9). The land irrigated with pivot systems is used to grow wheat and maize.

Physiography and soils

Clayey soils overlay a coarse textured aquifer of some considerable thickness. The clay cap is built up of deposits of sea transgressions and is absent in the desert fringe so that the aquifer crops out in seepage zones adjacent to the edge of the traditionally irrigated fields. Shanin (1985) divided the Nile Delta aquifer system into an unconfined, confined and leaky aquifer. The aquifers are fed by percolation due to excessive irrigation water supply. A rise of the groundwater table does however not develop, probably because of the balance between inflow and outflow. Besides discharge to the seepage

zones, outflow is realized by extraction of groundwater by individual farms for irrigation and by the natural drainage into the Mediterranean Sea which has created a number of coastal lakes: Lake Idku, Lake Burullus and Lake Manzala. These lakes receive the drainage effluent of the Delta and water quality is poor.

Field investigation

In the framework of the Reuse of Drainage Water Project (Abdel Gawad et al., 1991), data were collected on soil type, cropping patterns, meteorology, soil salinity, chemical composition, depth of the groundwater table and discharges through the open irrigation and drainage channels. To assess the actual flow rates in the channels, an extensive discharge measurement program was set-up (Anonymous, 1987). A database was established from which the total inflow and outflow of subregions can be obtained, as necessary for instance to calibrate regional hydrological models.

4.4 Castilla la Mancha, Spain

Location and climate

An area threatened with land degradation between 2°-3°30' W and 39°-40° N was selected for an in-depth analysis of heat and water exchanges between land and atmosphere. This EFEDA study area has a configuration consisting of three super-sites, with a mutual distance of 70 km: the dry farming area of Tomelloso, the irrigated area of Barrax and the hilly Rada de Haro area where agriculture is only marginally feasible (Figure 4.7). Many research institutes participated and the SC-DLO site was part of the Tomelloso super-site and located in an area locally known as Casa de Las Carascas. The site was cropped with grapes. A field programme was jointly organized with a large number of participants in order to conduct *simultaneous patch scale measurements* on land surface flux densities and associated hydro-meteorological parameters. The low and erratic rainfall (350 mm annually) in semi-arid Castilla la Mancha ($0.2 < P/E_p < 0.5$) with large water deficits arising in summer is the cause of the vulnerability of the agricultural areas. Figure 4.8 depicts the daily trends of the standard meteorological variables during the three weeks period that intensive field observations took place.

Land use

The combination of extensive solar exposure and calcareous soils creates a suitable environment for viticulture. Vineyards occupy 82 % of the cultivated area in the direct vicinity of Tomelloso. The grapes at the measurement site were planted 2.7 m apart, both along the row and between the rows (Figure 4.9). Unfortunately, all grapes were afflicted by frost in the first week of May 1991, which is exceptional at this time in spring.

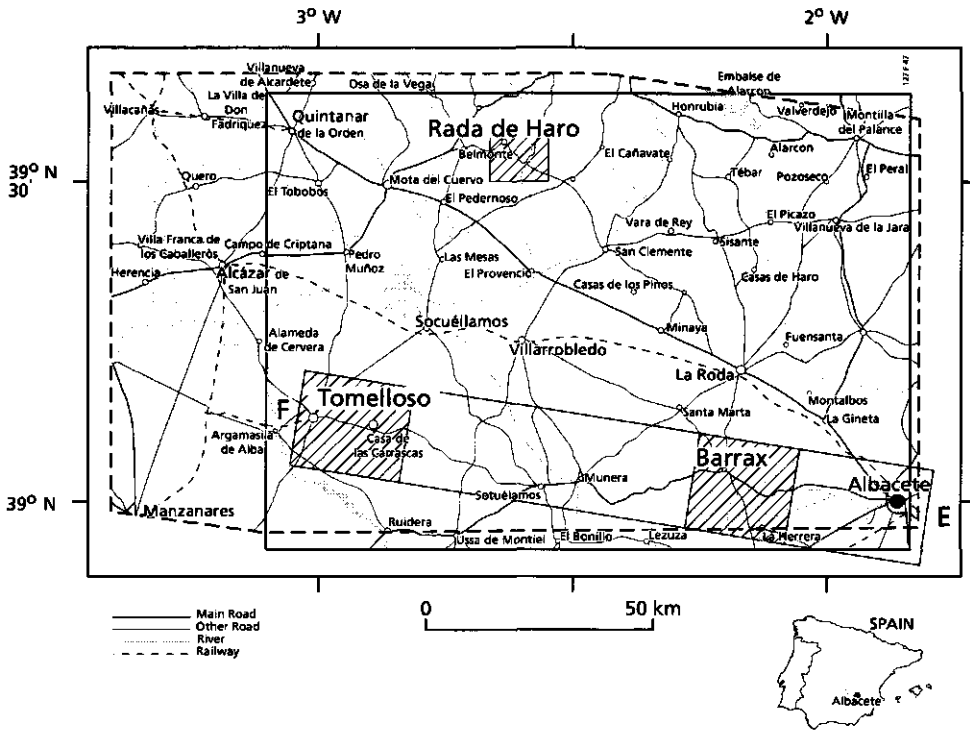


Fig. 4.7 Location of the EFEDA grid in Castilla la Mancha, Central Spain. The Barrax, Tomelloso and Rada de Haro super-sites are indicated. The masked insets of the E-F NASA ER-2 aircraft flightline between Tomelloso (left hand corner) and Barrax (right hand corner) present the positions of Colour Plates 3, 4 and 7. The dashed inserts represents the position of Colour Plate 5

Winter cereals and fallow land are dominant forms of land use outside the vineyards at Tomelloso.

The combination of water bearing formations, scarce rainfall and flat terrain, stimulated farmers to use irrigation devices wherever possible in the Province of Albacete. The crops irrigated by sprinkler systems at the Barrax super-site (Figure 4.10) are corn (62%), barley/sunflower (5%), alfalfa (2%) and vegetables (3%). The remaining dryland cultivated area consists of cereals (11%), olives (4%), others crops (3%) and fallow land (10%).

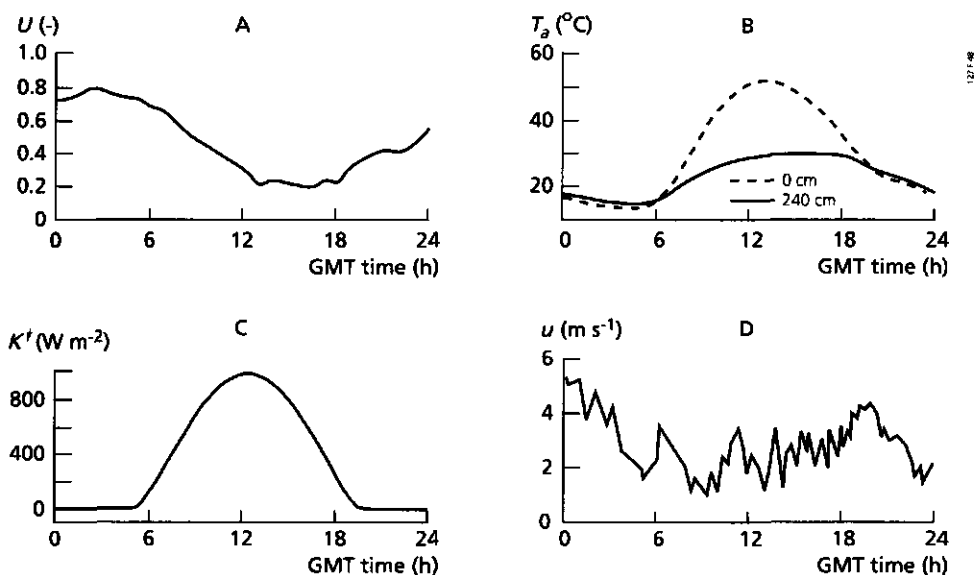


Fig. 4.8 Typical daily evolutions of (Part A) relative humidity U , (Part B) air temperature T_a , (Part C) incoming shortwave radiation K^i , (Part D) windspeed u , measured at Tomelloso on 29 June, 1991 at 240 cm height

Physiography and soils

The relative flat area of Castilla la Mancha was chosen from an orographical perspective as it was suitable for testing and validating atmospheric models. Typical altitudes are 700 to 800 m. Tomelloso is surrounded by slight undulating terrain. Artificial reservoirs for storage of irrigation water were created by the construction of high dams. The loamy soils in Tomelloso contain a calcic hard pan at a shallow depth (20-100 cm) with stones present everywhere. The cultivation of grapes was made possible by drilling holes in the calcic hard pan to make penetration by the grape roots possible. Grapes extract soil moisture from underneath this limestone layer. The groundwater table is at a depth of 30-60 meters.

The Barrax super-site is characterized by more poorly developed soils. The soils are very fine textured and contain a lower iron concentration than that observed in Tomelloso. After the introduction of modern irrigation, a dramatic decline of the water table due to groundwater extraction was reported which may have serious consequences for future water resources.

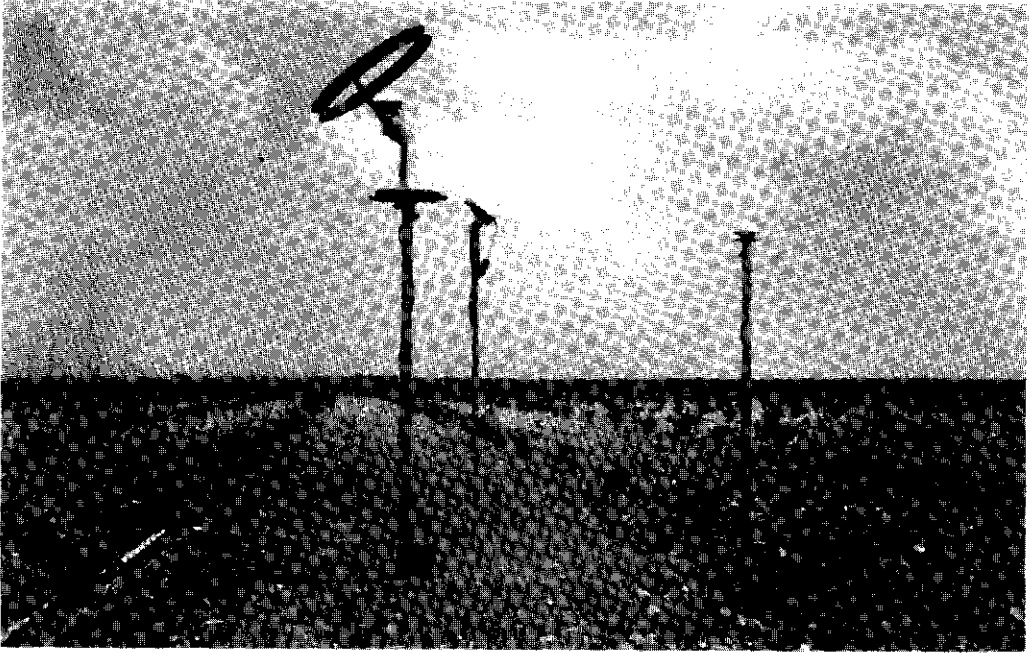


Fig. 4.9 Vineyard in the vicinity of Tomelloso. The delayed growth in June 1991 due to frost damage is visible

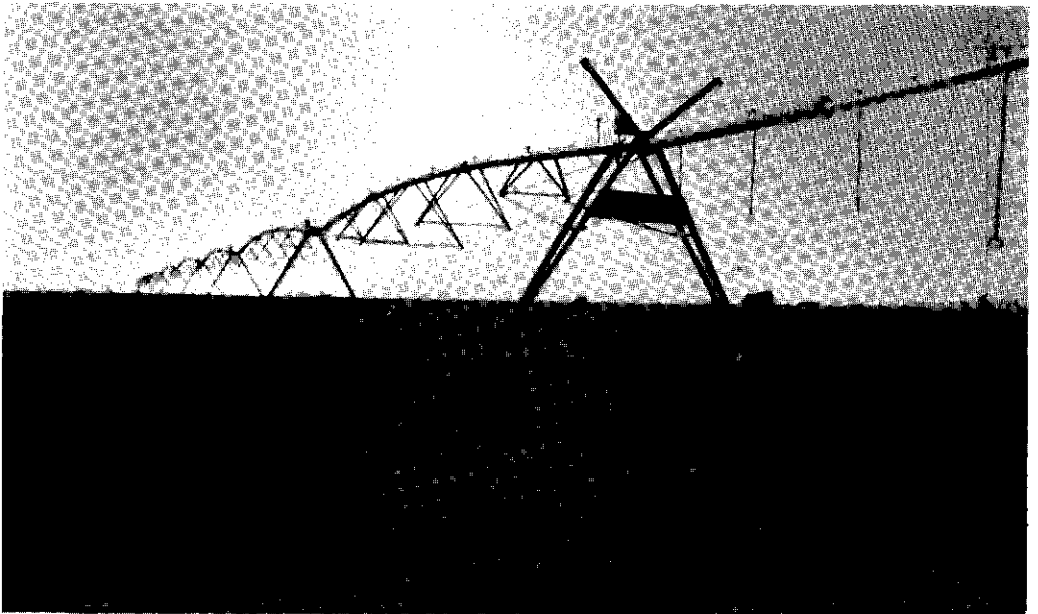


Fig. 4.10 Rotating pivot systems supply the crop with groundwater during the irrigation season, Barrax

Field investigation

EFEDA's fieldwork focused on multi-scale measurements of various hydro-meteorological variables which required the participation of several institutes. Surface flux densities were measured simultaneously at 21 stations, most of which were located at the Tomelloso super-site. These sites were equipped with eddy correlation, sigma-T, Bowen-ratio and/or aerodynamic profile methods to measure land surface flux densities. A lot of attention was devoted to measuring stomatal resistance r_c with porometers and stem flow E_s (= transpiration) with the heat balance method. Radio-soundings were launched regularly to monitor the atmospheric response to moisture and heat release from the land surface. The latter source of information is viable for estimating the regional heat and mass flux densities. At regular time intervals, aircraft measurements of turbulent H and λE flux densities were made. These aircraft also measured transects of atmospheric humidity and temperature (see Table 4.3).

Table 4.3 Hydro-meteorological parameters measured during the EFEDA experiment from micro up to the meso scale by the various participants

Parameter	Symbol	Platform
Micro scale		
Surface energy balance	$Q^{\downarrow}, G_0, H, \lambda E$	in-situ
Radiation balance	$K^{\downarrow}, K^{\uparrow}, L^{\downarrow}, L^{\uparrow}$	in-situ
Water balance	$P, E, I_m, dW/dt$	in-situ
Soil heat balance	$q_h^{soil}, dT_s/dt, T_0$	in-situ
Stomatal resistance	r_c	in-situ
Stem flow	E_s	in-situ
Leaf Area Index	LAI	in-situ
Spectral reflectance	$r_s(\lambda)$	in-situ
Soil moisture	θ	in-situ
Soil matric pressure head	h_m	in-situ
Meso-scale		
Atmospheric humidity	p_v	Falcon-20 and D0128 aircraft, radio-soundings
Potential temperature	T_p	Falcon-20 and D0128 aircraft, radio-soundings
Wind speed	u	Falcon-20 and D0128 aircraft, radio-soundings
Pressure	p	Falcon-20 and D0128 aircraft, radio-soundings
Turbulent flux densities	$H, \lambda E$	Falcon-20 and D0128 aircraft
Backscatter coefficient	σ_0	AIRSAR aboard a DC8
Spectral radiances	L_{λ}	TMS-NS001, AVIRIS

5 Experimental evaluation of the diurnal variation of moisture indicators

5.1 Space and time variation of surface flux densities

A polar orbiting satellite basically provides information on spectrally reflected and emitted radiances at one specific moment and on a pixel-by-pixel basis. Chapters 6 and 7 deal with the explanation of the SEBAL algorithm to convert these spectral radiances into surfaces flux densities. Consistently with the spectral radiances, the surface flux densities should be expressed on the same spatial scale, i.e. one pixel. Since spectral radiances changes rapidly, and especially the ones measured in the thermal infrared range, the surface flux density obtained from remote sensing is basically characterized by an instantaneous time scale. Regionalization of surface flux densities can be achieved by spatially integrating the pixelwise flux densities for a large number of pixels, for instance for the instantaneous latent heat flux density:

$$\langle \lambda E(t) \rangle = \frac{1}{A} \int_A \lambda E(x,y,t) da, \quad (\text{W m}^{-2}) \quad (5.1)$$

where $\lambda E(x,y)$ is the pixelwise latent heat flux density, $\langle \lambda E \rangle$ is the area-averaged latent heat flux density and A is the total area. A great similarity between Eqs. (5.1) and (1.3) may be noted. The daily surface flux density can be obtained by a time integration of the hourly surface flux densities:

$$\lambda E_{24}(x,y) = \int_0^{24} \lambda E(x,y,t) dt \quad (\text{J m}^{-2} \text{ d}^{-1}) \quad (5.2)$$

which in this particular example results into a 24 hour evaporation rate, λE_{24} . Feddes et al. (1993) gave an example of Eq. (5.2) using $\lambda E(t)$ obtained at each hour using geostationary METEOSAT measurements. For polar orbiting satellites, such an approach is not feasible and unless $\lambda E/Q^*$ can be assumed to be constant throughout the day, λE_{24} cannot be reliably estimated from one single λE value. Considering the complex flow mechanisms discussed in Chapter 2, and resistances affecting λE in Chapter 3, *a constant $\lambda E/Q^*$ behaviour seems to be too much of a simplification* and alternative descriptions of the time integration need to be investigated.

Seguin and Itier (1983) and also Nieuwenhuis et al. (1985) used one single T_0 -measurement around noon to assess λE_{24} and $\lambda E_{24} / \lambda E_{p-24}$ respectively. Both algorithms have in common that several hydro-meteorological parameters are treated to be areally

constant (e.g. net radiation, soil heat flux density, wind speed and air temperature) and that the fractional flux densities do not change with time. The effects of spatial and temporal variability are merged into one single expression which restricts the application of these algorithms to homogeneous conditions for which land use dependent calibration parameters to relate flux densities to T_0 are applied. A similar empirical approach was worked out by Lagouarde and McAney (1992) who gave also crop-dependent calibration coefficients. The application of these semi-empirical relationships to large-scale heterogeneous land surfaces with sparse canopies is not recommended: Kustas et al. (1990) remarked that 'errors of 2 mm d⁻¹ may be expected when one has a large range in soil, plant and meteorological conditions', following this approach.

The energy partitioning between H and λE is hydrologically controlled and the available soil moisture for evaporation changes slowly (Chap. 1). It may therefore be expected that moisture indicators reveal the surface energy partitioning for longer time spells. Instantaneous H and λE maps from SEBAL can then be fruitfully employed to derive 'self-preservative' terms, i.e. terms with a constant partitioning of surface flux densities among their components during daytime (Brutsaert and Sugita, 1992). The following moisture indicators are commonly used in large-scale hydro-meteorological studies:

- Bowen ratio, β (e.g. Avissar and Pielke, 1989)
- Evaporative fraction, Λ (e.g. Shuttleworth et al., 1989)
- Priestley & Taylor, α (e.g. de Bruin and Holtslag, 1982a)
- Bulk surface resistance to evaporation, r_s (e.g. Hunt et al, 1991)

5.2 Minimum and maximum evaporation

A moisture indicator expresses the magnitude of evaporation between zero and potential evaporation, λE_p . Methods to quantify λE_p need to be discussed first, with the emphasis on heterogeneous and large-scale land surfaces. A common definition for λE_p is 'the loss of water from a moist soil tract completely covered with vegetation and large enough for oasis effects to be negligible' (Thornwaite, 1944, as quoted by Monteith, 1994). There are a variety of evaporation formulae to compute the potential vapour transfer rates from land surfaces into the atmosphere in the literature. The λE_p -models can be classified into the main groups presented in Table 5.1.

The Penman-Monteith model combines radiative, conductive, mechanical and turbulent processes, and is theoretically preferred. If the spatial variations of the λE_p^{PM} -model parameters could be identified for heterogeneous land surfaces, notably Q^* , G_0 , T_a , Δe , r_a and r_c^{min} (or actually r_s^{min} when dealing with heterogeneous surfaces), pixel-dependent

λE_p values could be obtained. Besides Q' and G_0 , this is however neither practically feasible from remote sensing nor from micro-meteorological observations.

Table 5.1 Some models for the computation of potential evaporation (mainly after Doorenbos and Pruitt, 1977)

Energy balance combination models	Radiation models	Temperature models
Penman, 1948	Budyko, 1956	Thornwaite, 1944
Monteith, 1965	Makkink, 1957	Bianey and Criddle, 1950
Rijtema, 1965	Priestley and Taylor, 1972	Hargreaves, 1993

Two different approaches remain for tackling:

- *Simplification of the areal patterns of T_a , Δe , r_a and r_c^{min}* : These parameters are usually kept areally constant and extracted from one or a few synoptic observations. Although it is somewhat hypothetical, because it is not likely that the values at reference level are spatially constant (Hutjes, 1995), Moran et al., (1994) used this approach to express relative evaporation. Menenti and Choudhury (1993) also followed the same concept but took the T_a and Δe parameter values from the mixed layer which is much more reasonable.
- *Selection of a simplified λE_p -model*: Table 5.1 denotes the Priestley and Taylor equation as a possible way for getting λE_p . The present author feels that the radiation models are worth considering, especially since remote sensing measurements can be applied to obtain $Q'-G_0$ on a pixel-by-pixel basis (e.g. Choudhury, 1991a).

Furthermore, some imperfections of λE_p^{PM} must be mentioned, which reduces the potential for assessing λE_p by λE_p^{PM} in arid regions:

- 1 A source of ambiguity is introduced when meteorological variables measured under reduced wetness conditions are applied to predict λE_p . In (semi-) arid climates, the meteorological stations are usually not supplied with water, resulting in depleted soil moisture conditions in the direct vicinity of the instruments. Consequently, the synoptic records do not reflect an environment with optimum moisture conditions and T_a and Δe will be overestimated as compared to the micro-meteorological conditions over prescribed reference conditions (0.12 m clipped grass having a bulk surface resistance of 70 s m^{-1} , Allen et al., 1995). λE_p^{PM} with T_a and Δe measured over dry land surfaces in conjunction with $r_s = 70 \text{ s m}^{-1}$ will yield unrealistically high λE_p -values. To exclude this T_a and Δe effects, Kumar and Bastiaanssen (1993) pleaded for the use of the Priestley and Taylor formula in arid zones (Eq. 3.34).

- 2 Because of the non-linear character of s_a and its linearized solutions to assess $e_{sat}(T_0)$ from $e_{sat}(T_a)$, the application of the λE_p^{PM} model should be restricted to cases where thermal storage is limited (e.g. open shallow water or irrigated land). Paw U and Gao (1988) found that the restriction $T_0 - T_a < 5$ K is sufficiently precise to predict $e_{sat}(T_0)$ from T_a -data. In arid regions, 5K is easily exceeded (e.g. Figure 4.8B).
- 3 Although Penman (1948) evaded the need to measure T_0 explicitly by using $e_{sat}(T_a) + s_a(T_0 - T_a)$ instead of $e_{sat}(T_0)$, the aim of avoiding T_0 -observations is only partially realized because T_0 is still needed to quantify Q^* (Eq. 2.10) and G_0 (Eq. 3.14), especially if λE_p^{PM} is applied on instantaneous times scales and G_0 may not be ignored. If no observation of T_0 are available, the equilibrium surface temperature associated with the Q^* , G_0 and H flux densities can be obtained after having solved λE_p^{PM} and H from energy budget closure:

$$H^{PM} = Q^* - G_0 - \lambda E_p^{PM} \quad (\text{W m}^{-2}) \quad (5.3)$$

Where λE_p^{PM} is a function of $Q^* - G_0$ (see Eq. 3.34). The equilibrium temperature for heat transport calculated by Penman-Monteith T_0^{PM} can be approximated as:

$$T_0^{PM} = H^{PM} \frac{r_{ah}}{\rho_a c_p} + T_a \quad (^\circ\text{C}) \quad (5.4)$$

An inconsistency in the solution arises if T_0^{PM} at Eq. (5.4) is not related to T_0 used to compute Q^* and G_0 in Eq. (5.3) and λE_p^{PM} in Eq. (3.34). From experience it becomes apparent that a small number of iterations are necessary to let T_0^{PM} equilibrate with Q^* , G_0 , H^{PM} and λE_p^{PM} . Ideally kB^1 is optimized such that $T_0^{PM} = T_{z0h}$ and the radiometric scalar roughness z_{0h} corresponds to T_0^{PM}

Hence, potential evaporation can be defined by different methods and ample attention has to be spent on the quality of the meteorological data. Application of the λE_p^{PM} model on an instantaneous time basis requires iterations if T_0 is not available. If T_0 is measured by radiometers, Q^* and G_0 can directly be assessed and an iterative procedure is not needed.

The numerical range of each moisture indicator between *dry* and *wet* depends on λE_p and H :

$$\begin{aligned}
\beta_{dry} = \infty & \quad \beta_{wet} = \frac{H}{\lambda E_p} \\
\Lambda_{dry} = 0 & \quad \Lambda_{wet} = \frac{\lambda E_p}{Q^* - G_0} \\
\alpha_{dry} = 0 & \quad \alpha_{wet} = \frac{\lambda E_p}{Q^* - G_0} \frac{s_a + \gamma}{s_a} \\
r_s^{dry} = \infty & \quad r_s^{wet} = \frac{\rho_a c_p}{\lambda E_p \gamma} \{ e_{sat}(T_0) - e \} - r_{av}
\end{aligned}$$

Moisture indicators are useful since their diurnal variation is smaller than surface flux densities and an instantaneous value can be used to estimate the flux densities for a long period of time. The five year data from the Qattara Depression will be used to experimentally evaluate this hypothesis.

5.3 Measurement techniques used in the Qattara Depression

The Bowen-ratio values measured in the Qattara Depression reflect the sensible and latent heat transfer from several bare soil surfaces upwind of the installed Bowen-ratio tower. The surface flux densities were computed from β ratio measurements as:

$$H = \frac{Q^* - G_0}{1 + 1/\beta} \quad (\text{W m}^{-2}) \quad (5.5)$$

and

$$\lambda E = \frac{Q^* - G_0}{1 + \beta} \quad (\text{W m}^{-2}) \quad (5.6)$$

while Q^* is measured by a net radiometer and G_0 by soil heat flux plates. The Λ -values can be directly derived from β using:

$$\Lambda = \frac{1}{1 + \beta} \quad (-) \quad (5.7)$$

Furthermore, α and Λ can be simply interrelated as:

$$\frac{\alpha}{\Lambda} = \frac{s_a + \gamma}{s_a} \quad (-) \quad (5.8)$$

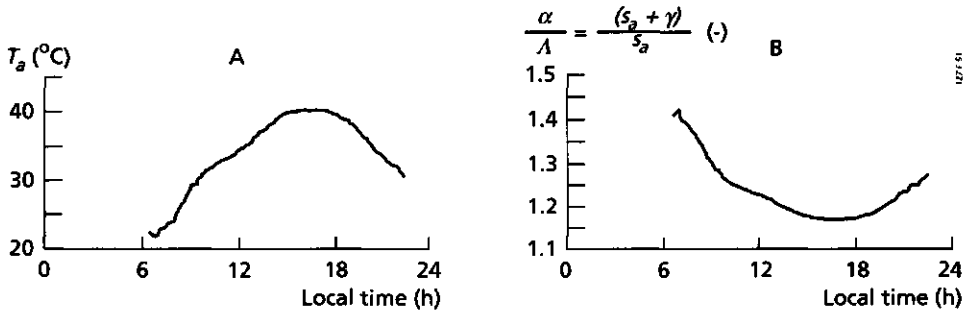


Fig. 5.1 (Part A) Impact of the daytime air temperature T_a behaviour on (Part B) the ratio between the Priestly & Taylor α parameter and evaporative fraction Λ

The $(s_a + \gamma)/s_a$ term of Eq. (5.8) can be calculated from T_a . If $\Lambda(t)$ shows approximately constant behaviour in time, then it follows directly from Eq. (5.8) that $\alpha(t)$ must by definition be more variable than $\Lambda(t)$. Figure 5.1 has been added to pinpoint the diurnal variation of $s_a(t)$; $s_a(t)$ has been calculated from time series of T_a -measurements at 200 cm height. Figure 5.1B shows that the $(s_a + \gamma) / s_a$ fraction is largest at lower solar altitudes, i.e. when T_a is relatively low. At midday, when $T_a \approx 40^\circ\text{C}$, α/Λ is approximately 1.15 to 1.2.

The bulk surface resistance to evaporation is related to the Bowen-ratio after combining Eqs. (3.33) and (5.6):

$$r_s = \frac{\rho_a c_p}{\gamma(Q^* - G_0)} [e_{sat}(T_0) - e] \{1 + \beta\} - r_{av} \quad (\text{s m}^{-1}) \quad (5.9)$$

The near surface vertical vapour pressure difference $e_{sat}(T_0) - e$ necessary to calculate r_s was obtained from at-surface thermal infrared measurements of T_0 . Actual vapour pressure e was obtained via observations of U and T_a at 200 cm elevation (the same level to which β and r_{av} applies). The aerodynamic resistance r_{av} is calculated according to Eq. (3.29) In the case of fully bare soil conditions ($s_c = 0$), $r_s = r_{soil}$ applies

5.4 Temporal behaviour of surface flux densities and moisture indicators

Field data observed at Bir Qifar-2 on 15 June 1988, have been selected to discuss the diurnal variation of the heat flux densities and moisture indicators. The soil was a typical sandy rough sebkha and did not have any vegetation, i.e. $\lambda E = \lambda E_{soil}$ and $r_s = r_{soil}$. The groundwater table was at a depth of 59 cm. The hyper-arid climate of the Qattara

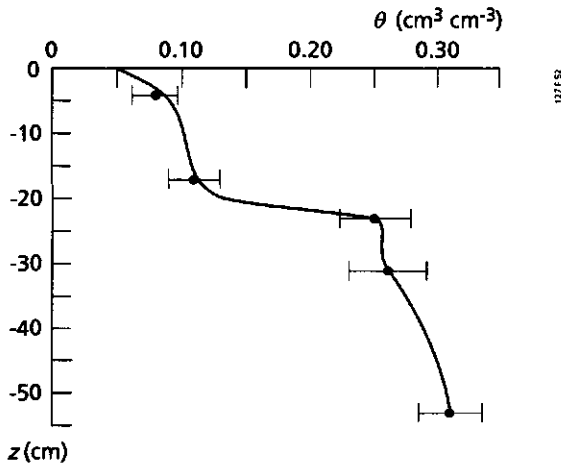


Fig. 5.2 Measured and interpreted soil water content profile at Bir Qifar-2, 15 June, 1988, Qattara Depression. The horizontal bars reveal a possible 15% error in the field measurements

Depression creates a visually dry land surface ($\theta_0 = 0.05 \text{ cm}^3 \text{ cm}^{-3}$) laying on top of a wet sub-soil (Figure 5.2).

Figure 5.3A shows that on June 15, λE_{soil} is dominant over H and G_0 . Figure 5.3B displays a smooth pattern of $\delta T_{a-sur}(t)$ following virtually the $K^l(t)$ radiation pattern ($\delta T_{a-sur} = T_{20h} - T_a$). The time lag between the peak in $K^l(t)$ and the peak in $\delta T_{a-sur}(t)$ is less than 20 minutes. Another significant aspect is that the vertical soil temperature difference, $T_0 - T_s$ (with T_s taken at a depth of 2 cm) shows its peak before the maximum of T_0 is reached. Because of the evolution of $\nabla T_s(t)$, $G_0(t)$ precedes $Q^*(t)$. Consequently G_0/Q^* must vary with time which affects either the temporal variation of $\lambda E_{soil}/Q^*$ or H/Q^* .

Hence, $\lambda E_{soil}/Q^*$ is very unlikely to be constant and λE_{24} can hardly be estimated from a single $\lambda E_{soil}/Q^*$ estimation

Since the soil undergoes a delayed warming up during morning hours, due to thermal storage, and $\nabla T_s(t)$ precedes $K^l(t)$, Figure 5.4 shows that G_0/Q^* increases sharply during the morning. The immediate response of H to Q^* by rapid mixing of heat by eddy transport is held responsible for a rather constant H/Q^* allocation between 8³⁰ and 15³⁰ hour (Figure 5.4). Evidence that the quasi-constancy of H/Q^* is not a mere coincidence is presented in Annex 1. Annex 1 deals with values on $\delta T_{a-sur}(t)$ and $K^l(t)$ for different soil patches investigated during the entire 4th field expedition (see Table 4.2) and shows that the time lag between $\delta T_{a-sur}(t)$ and $K^l(t)$ is minimized. Besides $\delta T_{a-sur}(t)$, the $H(t)$ response is also governed by r_{ah} (see Eq. 3.6). The erratic windspeed on 17, 18 and 24 June is held responsible for some notable time shifts between the $\delta T_{a-sur}(t)$ and $K^l(t)$ behaviour on these days shown in Annex 1. The overall behaviour however illustrates

a close agreement in the dynamics with respect to $\delta T_{a-sur}(\hat{t})$ and $K^{\downarrow}(\hat{t})$. Holtslag and van Ulden (1983) used a surface heating coefficient to indicate the proportionality between δT_{a-sur} and Q^{\downarrow} for pastures in the Netherlands which reveals that H and Q^{\downarrow} are correlated for positive Q^{\downarrow} values. The same authors also studied δT_{a-sur} vs K^{\downarrow} and found close correlations for half hourly values over 4 summer days.

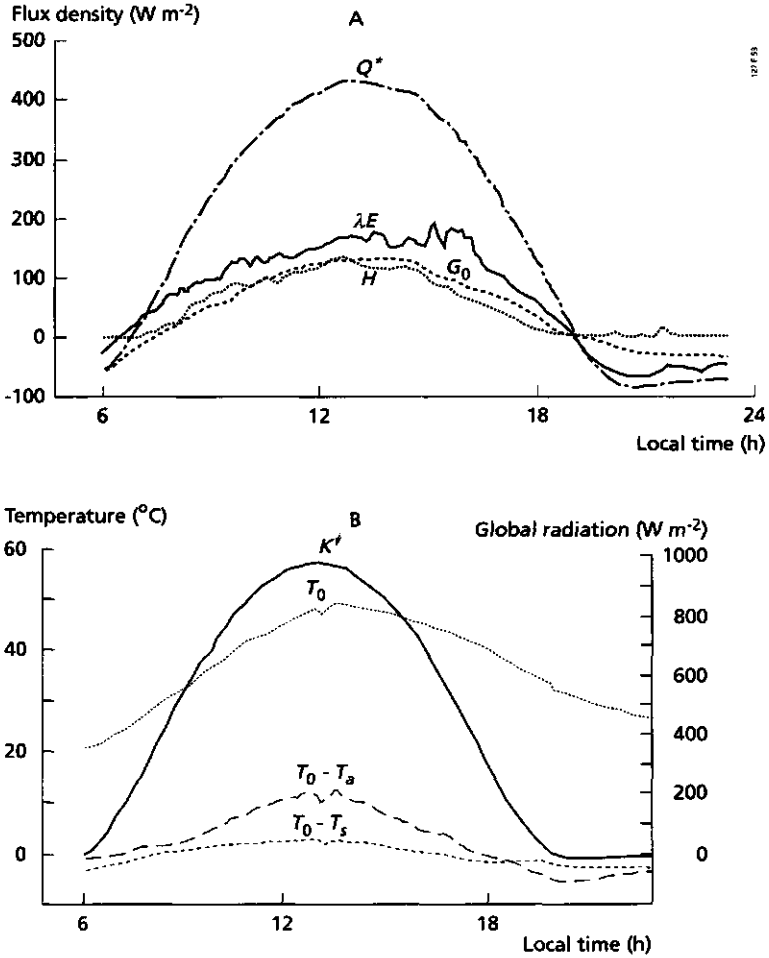


Fig. 5.3 (Part A) Typical diurnal surface flux densities at Bir Qifar-2, 15 June, 1988, Qattara Depression. (Part B) Incoming shortwave radiation K^{\downarrow} , surface temperature T_0 , vertical near-surface air temperature difference $\delta T_{a-sur} = T_0 - T_a$ and vertical near-surface soil temperature differences $T_0 - T_s$.

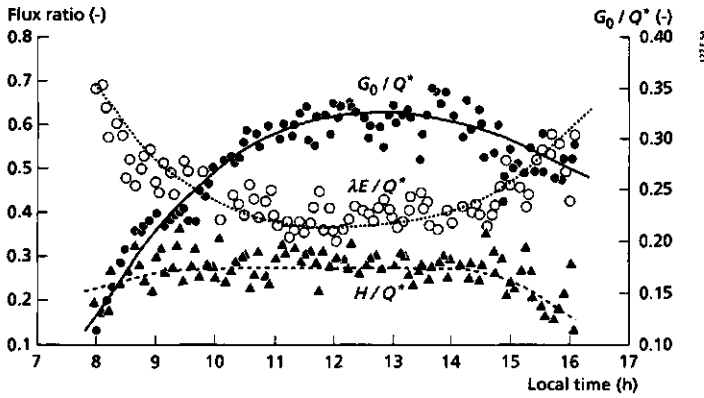


Fig. 5.4 Typical evolution of flux density ratio measurements at Bir Qifar-2, 15 June, 1988, Qattara Depression

The net effect of G_0/Q^* and H/Q^* is that $\lambda E_{soil}/Q^*$ must have a behaviour opposite to G_0/Q^* . Hence, experimental evidence is given that H/Q^* is rather stable and $\lambda E_{soil}/Q^*$ is concavely shaped to compensate for the convex G_0/Q^* feature (see Figure 5.4). The often published parabolically shaped diurnal variation of $\beta(t)$ (e.g. Avissar and Pielke, 1989; Diak, 1990) is thus explained. Figure 5.5 shows that β is more irregular than Λ and that a pronounced diurnal course of r_{soil} persists. A similar trend of r_{soil} was found by van de Griend and Owe at the bare soils of Tomelloso.

Since the inversely proportional symmetries of G_0/Q^* and $\lambda E/Q^*$ are compensated by the definition of Λ , it is expected that Λ will not change significantly with time. Shuttleworth et al. (1989) published the first indications that Λ is a fairly constant indicator of energy partitioning during daylight hours. Most surface types during the mesoscale First ISLSCP Field Experiment FIFE showed a typical flat $\Lambda(t)$ daytime behaviour (Brutsaert and Sugita, 1992; Crosson and Smith, 1992, Verma et al, 1992). More recently, the use of Λ also received support from other large scale field investigations such as HAPEX-MOBILHY (Nichols and Cuenca, 1993) and HAPEX-SAHEL (Gash et al., 1995). Due to $\Lambda(t)$ skewness at sunrise and sunset, a systematic difference can be found between Λ_{day} and Λ_{night} ; Λ is therefore quasi-constant during daytime only. Shuttleworth et al. (1989) compared midday Λ -values to all day Λ -average values for 4 days during FIFE. Because the largest contribution to λE_{24} is delivered during midday hours when Λ is constant at large radiation flux densities, the only difference was 1.5%. The temporal stability of Λ in heterogeneous terrain and at large scales was demonstrated in HAPEX-EFEDA by Bastiaanssen et al. (1995a): *The deviation between $\tilde{\Lambda}_{midday}$ and $\tilde{\Lambda}_{24}$ for a 10,000 km² large area was less than 5%.*

The proof of the quasi-constancy of moisture indicators can be given by investigating β , Λ , α and r_{soil} ($r_{soil} = r_g$) systematically for all available Qattara Depression energy

balance measurements. The data analysis comprises 42 daytime surface energy budgets over a period stretching from 1987 to 1989 (no β -measurements in 1986) and a total

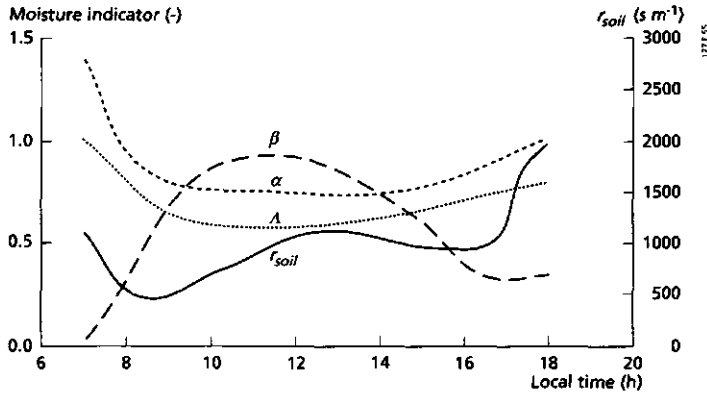


Fig. 5.5 Example of the daily evolution of the selected moisture indicators, Bowen ratio β , evaporative fraction Λ , Priestly and Taylor α , and surface resistance r_{soil} on 15 June, 1988, Bir Qifar-2, Qattara Depression

number of 16 study areas. The temporal stability of each moisture indicator is summarized in Table 5.2. The coefficient of variation was determined for the period between 9⁰⁰ to 16⁰⁰ hours local time when the land surface flux densities are most intensive. In addition, the results for the midday period between 10³⁰ and 14³⁰ hours are given.

On the basis of Table 5.2 it can be concluded that Λ is indeed optimal for describing the diurnal variation in energy dissipation (CV = 0.186, 0.128). All moisture indicators are more stable between 11³⁰ to 14³⁰ hours compared with the 10⁰⁰ to 16⁰⁰ hours time interval. The 5 to 7% difference between the CV of Λ and α is low and can be fully attributed to the daily variation of $(s_a + \gamma)/s_a$. It can be concluded that Λ and α have the smallest daytime variability. Table 5.2 further indicates that β is the most variable moisture indicator during daytime hours and is far from ideal for computing the daily integrated flux densities from an instantaneous β -estimation. The conclusions may not be extrapolated to time scales beyond one day, e.g. one week in which the overlying meteorology may change in terms of cloudiness, geostrophic windspeed, air temperature in the mixed layer etc., which may modulate the surface energy balance at the same status of soil moisture availability.

Table 5.2 Temporal stability of the moisture indicators analysed for 42 measurement days in the Qattara Depression spread across 16 study areas in the period 1987-1989. The mean coefficient of variation (CV) is given

Moisture indicator	CV (10 ⁰⁰ -16 ⁰⁰ hours)	CV (11 ³⁰ -14 ³⁰ hours)
Bowen ratio, β	0.613	0.387
Evaporative fraction, Λ	0.186	0.128
Priestley & Taylor, α	0.199	0.135
Surface resistance, r_{soil}	0.295	0.242

5.5 Understanding bare soil surface resistance using simulations with EVADES

The bare soil resistance r_{soil} hydrologically controls λE_{soil} and thus $\lambda E_{soil}/Q^*$. Although from the point of view of the temporal G_q/Q^* and H/Q^* behaviour it was tentatively concluded that $\lambda E_{soil}/Q^*$ must be concavely shaped, a clearcut soil physical interpretation has not been given. To better understand the diurnal behaviour of r_{soil} a decomposition into r_{sl} and r_{sv} needs to be made (Eq. 3.23). Since the Bowen-ratio surface energy balance method yields λE_{soil} rather than λE_r and λE_v , the Qattara Depression measurements were not specific enough to quantify r_{sv} and r_{sl} . The concept of r_{soil} , r_{sl} and r_{sv} is therefore tested by simulating the flow processes. This detailed knowledge of r_{sl} and r_{sv} can also be used to better interpret r_s which will appear from SEBAL.

The EVAporation in DEserts simulation model EVADES was developed and applied to compute the evaporation from the Qattara Depression (Bastiaanssen et al., 1989; 1990). More recently, the model formulation acquired a more general character, being based on the theory of moisture, vapour and heat flow presented in Chapter 2. EVADES solves iteratively $q_b, q_{bT}, q_v^F, q_v^K, q_v^D, q_v^{TUR}$ and q_{hc}, q_{ha} and relates these sub-surface flux densities to the surface radiation and energy balance. Annex 2 shows the outcome of a few calibration runs indicating that EVADES is a suitable model for analysing the physical land surface processes of a dry top-soil overlying a wet sub-soil in an hyper-arid environment. The EVADES executions carried out for the period June 14 to 16, 1988, resulted into the daytime evolution of $\lambda E_{soil}/Q^*$ depicted in Figure (5.6). Indeed, the pattern of $\lambda E_{soil}/Q^*$ corresponds to the expected shape.

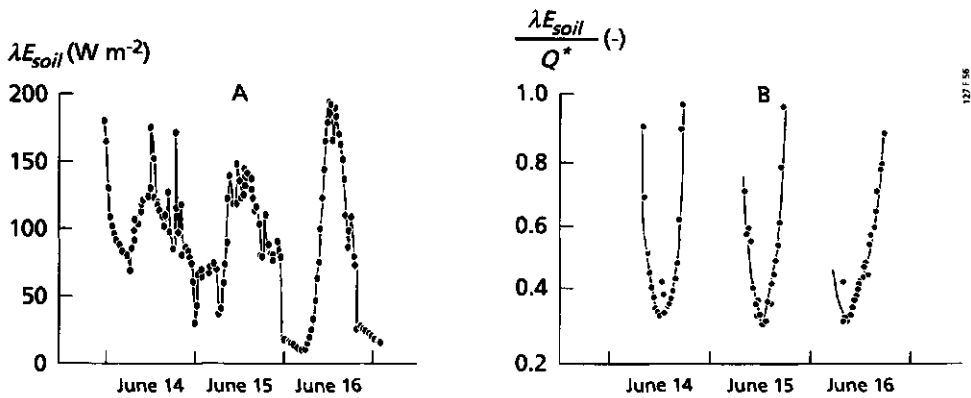


Fig. 5.6 (Part A) Simulated bare soil evaporation λE_{soil} with the EVADES model accounting for liquid, vapour and heat flow mechanisms including sub-surface latent heat exchanges and (Part B) the latent heat flux density/net radiation fraction $\lambda E_{soil} / Q^*$, 14 to 16 June, 1988, Qattara Depression

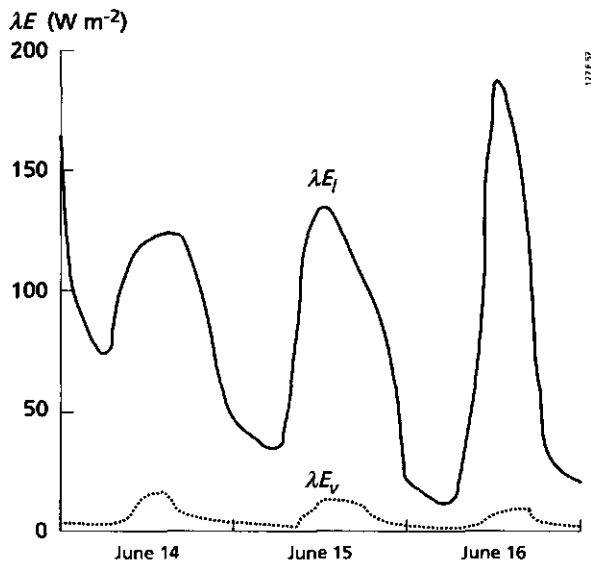


Fig. 5.7 Simulated daily (24h.) variation of surface λE_s and subsurface λE_v evaporation for three days between 14 to 16 June, 1988, Qattara Depression.

The air above the land surface did not reach saturation during these dry hot summer nights, which creates a suitable environment for night-time evaporation as well. The maximum instantaneous sub-surface evaporation λE_v did not exceed $12 W m^{-2}$ (June 14), whereas λE_s sometimes reaches values up to $180 W m^{-2}$ (June 16). For this

particular example, the simulations yielded an average $\lambda E_v/\lambda E_t$ fraction of 0.01 to 0.10 (see Figure 5.7). The daytime average of the ratio $[\int \lambda E_v dt]/[\int \lambda E_t dt]$ amounted to 0.05 on average (Table 5.3). For the June 15 simulations, the time integrated latent heat flux density λE_{24} gave a value of $7.19 \text{ MJ m}^{-2} \text{ d}^{-1}$ which is equivalent to 2.9 mm d^{-1} .

Table 5.3 Daily (24h.) integrated surface energy heat balances ($\text{MJ m}^{-2} \text{ d}^{-1}$) obtained from EVADES simulations for Bir Qifar-2, 14 to 16 June, 1988 Gattara Depression. The average computation time step is 15 seconds.

Term	June 14	June 15	June 16
Q'	8.41	8.62	8.32
G_0	+0.77	+0.59	+0.90
H	-0.19	+1.18	1.65
λE_t	7.95	6.84	5.80
λE_v	0.43	0.35	0.21

Dynamics in the bare soil resistance to liquid transfer, r_{sl} , can be observed from Figure 5.8. The pattern of r_{sl} encompasses a diurnal change with rather low values around noon. The average resistance becomes $r_{sl} \approx 3 \cdot 10^5 \text{ s m}^{-1}$ which must be equivalent to $D_0 = 3.33 \cdot 10^{-8} \text{ m}^2 \text{ s}^{-1}$, if $z_l = 0.01 \text{ m}$ (Eq. 3.19). The van Genuchten parameters used in the simulation process are $\theta_r = 0.01 \text{ cm}^3 \text{ cm}^{-3}$, $\theta_{sat} = 0.31 \text{ cm}^3 \text{ cm}^{-3}$, $\alpha = 0.01 \text{ cm}^{-1}$, $n = 1.5$, $l = -2.65$ and $k_{sat} = 0.5 \text{ cm d}^{-1}$ and were measured at the soil physical laboratory of the Staring Centre. On basis of the van Genuchten parameters, the iso-thermal liquid diffusivity at $\theta = 0.05 \text{ cm}^3 \text{ cm}^{-3}$ becomes $D_0 = 3.26 \cdot 10^{-8} \text{ m}^2 \text{ s}^{-1}$ (Eq. 2.31) which corresponds to z_l / r_{sl} .

The integration depth for vapour flow, z_0 , is taken as the depth at which q_v^{tot} is a pre-defined fraction of the at-surface value for q_v^{tot} . For a fraction of 0.30, this has led to $z_0 \approx 5 \text{ mm}$ most of the time. This does not mean that evaporation from $|z| > |z_0|$ does not occur. At moments with less dynamic vapour flow, $z_0 \approx 20 \text{ mm}$ was found. The diurnal fluctuations of r_{sv} can, besides of variations in z_0 , also be ascribed to the instability of D_v^{eff} . A diurnal range of three orders of magnitude could be found for D_v^{eff} , which could be entirely explained by the contribution of vapour diffusion and convection to the magnitude and direction of soil vapour flow. During time spells of several hours, q_v^{diff} and q_v^{conv} appeared to be moving in the opposite direction. A clearcut reason for that is the prevailing direction of heat flow, which most commonly coincides with the direction of q_v^{diff} . Notably during daytime, both heat and vapour flow downward and vapour will not be released into the atmosphere. Figure 5.9 reveals that $r_{sv} \sim 8000 \text{ s m}^{-1}$ corresponds to $D_v^{eff} = 6.3 \cdot 10^{-7} \text{ m}^2 \text{ s}^{-1}$ at 5 mm integration depth.

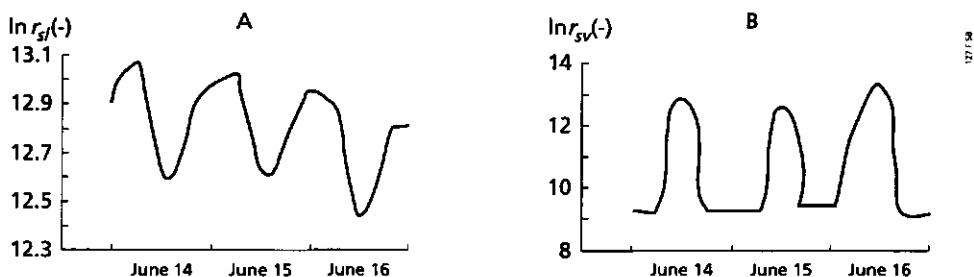


Fig. 5.8 (Part A) Simulated daily variation of the bare soil resistance, r_{sl} to liquid and (Part B) vapour, r_{sv} transport for three complete days between 14 to 16 June, 1988, Qattara Depression.

The conversion from r_{sv} and r_{sl} into r_{soil} can be achieved after quantifying firstly ω_6 and ω_7 :

$$\omega_6 = \frac{\rho_w(\theta_{zi} - \theta_0)}{\rho_v^{sat}(T_0) - \rho_{z0v}} \quad (-) \quad (5.10)$$

$$\omega_7 = \frac{\rho_v^{sat}(T_e) - \rho_{z0v}}{\rho_v^{sat}(T_0) - \rho_{z0v}} \quad (-) \quad (5.11)$$

so that Eq. (3.23) can alternatively be written as:

$$\frac{1}{r_{soil}} = \omega_6 \frac{1}{r_{sl}} + \omega_7 \frac{1}{r_{sv}} \quad (\text{m s}^{-1}) \quad (5.12)$$

Obviously, ω_7 is rather constant since the rate of increment of $\rho_v^{sat}(T_e) - \rho_{z0v}$ and $\rho_v^{sat}(T_0) - \rho_{z0v}$ is more or less similar during morning hours (Figure 5.9B). Apparently, these gradients in vapour density have the same rate of change in the afternoon. The more rapid increment of $\rho_v^{sat}(T_0) - \rho_{z0v}$ in relation to $\theta_{zi} - \theta_0$ manifests ω_6 with distinct fluctuations (Figure 5.9A). The value for ω_6 falls in the afternoon because of the gradual decrease of $\rho_v^{sat}(T_0) - \rho_{z0v}$.

According to Eq. (5.12), the ω_6 -pattern inversely affects $r_{soil}(t)$. Because ω_6 varies relatively more ($\omega_6 = 400-1600$) than r_{sl} ($\ln r_{sl} 12.5-13.1$), the diurnal variation of r_{soil} varies mainly with ω_6 . The resistance r_{soil} is approximately 200 s m^{-1} during the highest rates of evaporation whereafter it gradually rises to $400-800 \text{ s m}^{-1}$ during the afternoon.

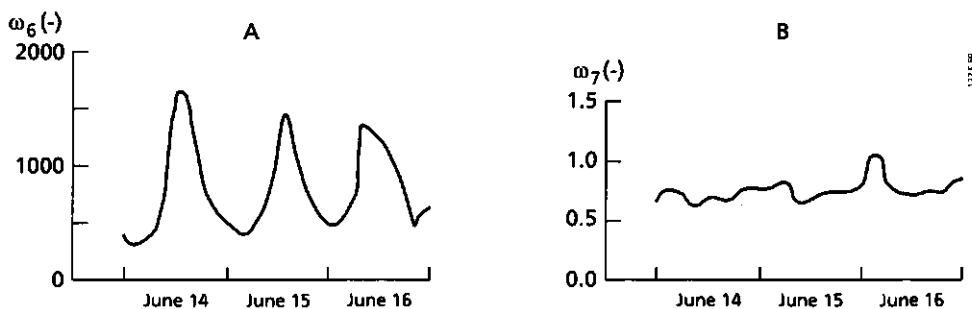


Fig. 5.9 Simulated daily variation of the weighting coefficients of (Part A) liquid ω_6 and (Part B) vapour ω_7 resistance to fluid transport for three days between 14 to 16 June, 1988, Qattara Depression.

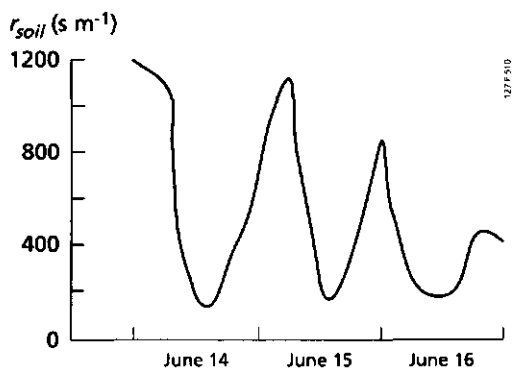


Fig. 5.10 Simulated daily variation of the total bare soil resistance to evaporation for three days between 14 to 16 June, 1988, Qattara Depression

These values are rather comparable with canopy resistances, r_c . Since the relative changes in Q^* are faster than $r_{soil} \lambda E_{soil} / Q^*$ increases in the afternoon. The appealing aspect of a physical description of $r_{soil}(t)$ becomes apparent from Figure 5.10 because the empirical $r_{soil}(\theta)$ -approaches such as mentioned in Table 2.2 are not suitable for describing the diurnal variation of r_{soil} .

5.6 Evaporative fraction and relative evaporation

Since Λ was experimentally justified as an adequate tool for describing surface energy partitioning for time scales of one day or less and daily integrated values for $Q^* - G_0$ can be determined with remote sensing data (e.g. van Oevelen et al., 1993; Kustas et al., 1994a), actual daily evaporation rates can be obtained as:

$$\lambda E_{24} = \Lambda(Q^* - G_0)_{24} \quad (\text{J m}^{-2} \text{ d}^{-1}) \quad (5.13)$$

Since on the basis of Siwa oasis measurements for a depth of the groundwater table of 30 cm the maximum Λ -value became $\Lambda_{max} \approx 1$, the impression exists that for those cases $Q^* - G_0 \approx \lambda E \approx \lambda E_p$ holds true. The generality of this hypothesis could be tested by evaporation measurements conducted at wet surfaces and under a variety of climates and types of land use which is beyond the scope of the current thesis. However, if the statement $\lambda E_p^{PM} \approx \lambda E_p$ is accepted as a suitable reference (if $\delta T_{a-sur} < 5 \text{ K}$, T_0 -iterations are executed and $T_a, \Delta e$ are measured above wet surfaces), the restriction under which condition $Q^* - G_0 = \lambda E_p^{PM} = \lambda E_p$ applies can be analytically explored as:

$$\lambda E_p^{PM} = \frac{(Q^* - G_0 + c_6)}{c_5} \quad (\text{W m}^{-2}) \quad (5.14)$$

where

$$c_5 = \frac{s_a + \gamma(1 + r_s^{min}/r_a)}{s_a} \quad (-) \quad (5.15)$$

$$c_6 = \frac{\rho_a c_p \Delta e / r_a}{s_a} \quad (\text{W m}^{-2}) \quad (5.16)$$

Hence for specific combinations of c_5 and c_6 , λE_p^{PM} exactly coincides with $Q^* - G_0$. The basic question is whether climatological values of r_a, s_a and Δe indeed show regularities in a way that the aerodynamic term is overruled by the radiation term in λE^{PM} . More specifically, the relationship between $Q^*, G_0, \Delta e$ and r_a can be expressed into c_7 according to:

$$Q^* - G_0 = \frac{\Delta e}{r_a} \frac{1}{c_7} \quad (\text{W m}^{-2}) \quad (5.17)$$

where

$$c_7 = \left[\frac{s_a + \gamma(1 + r_s^{min}/r_a)}{s_a} - 1 \right] \left(\frac{s_a}{\rho_a c_p} \right) \quad (\text{mbar m}^3 \text{ J}^{-1}) \quad (5.18)$$

Eq. (5.17) has very few exact solutions and it is more useful to elaborate under which conditions a 10% deviation applies. Then the following restriction needs to be tested:

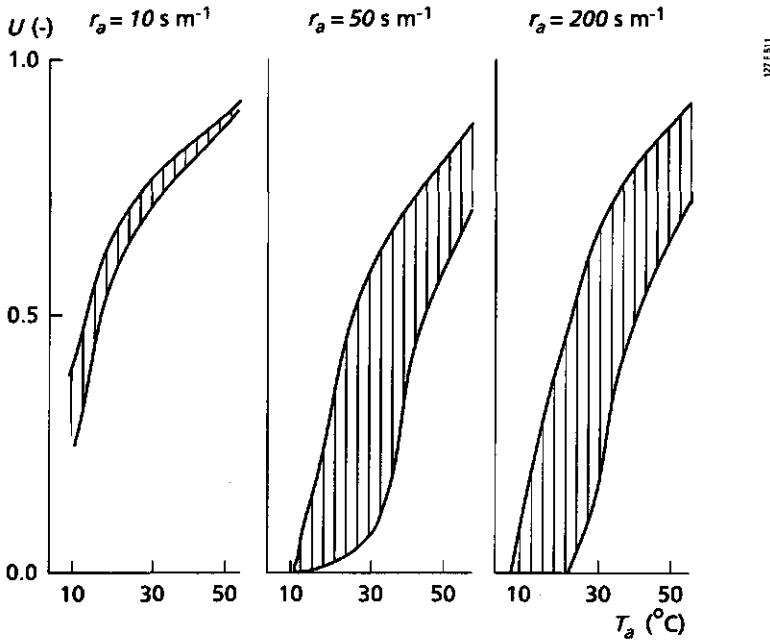


Fig. 5.11 Nomograph revealing the climatological conditions expressed as relative humidity U , vs. air temperature T_a for various values of the aerodynamic resistance r_a for which the net available energy ($Q^* - G_0$) deviates less than 10% from the potential evaporation established with the Penman-Monteith equation λE^{PM}

$$0.9 * \lambda E_p^{PM} < Q^* - G_0 < 1.1 * \lambda E_p^{PM} \quad (\text{W m}^{-2}) \quad (5.19)$$

Figure 5.11 shows the climatic requirements under which the difference between $Q^* - G_0$ and λE_p^{PM} is less than 10%. The fixed parameters in this exercise are $Q^* - G_0 = 300 \text{ W m}^{-2}$, $r_s^{min} = 40 \text{ s m}^{-1}$ and $\rho_a c_p = 1200 \text{ J m}^{-3} \text{ K}^{-1}$. It turns out that cold-dry, intermediate-humid and warm-humid climate systems often meet the conditions of $Q^* - G_0 \approx \lambda E_p^{PM}$. Since the aerodynamic contribution in λE_p^{PM} decreases at higher r_a -values, the agreement between $Q^* - G_0$ and λE_p^{PM} increases with r_a . The Mediterranean climates of Egypt and Spain with $T_a = 30^\circ\text{C}$ and $U = 0.50$ seem to be perfect situations to assume $\lambda E_p^{PM} \approx Q^* - G_0$. Hence, as a first approximation, $Q^* - G_0$ is a proper candidate for mapping out λE_p on a pixel-by-pixel basis and consistent with that, Λ is a suitable estimator for relative evaporation $\lambda E / \lambda E_p = \lambda E / (Q^* - G_0)$.

Jackson et al. (1981) and Moran et al. (1994) calculated the upper and lower limits of δT_{a-sur} by taking the extremes in surface resistance ($r_s = \infty$ and $r_s = 0$) using a surface energy balance combination equation. Menenti and Choudhury (1993) did the same but used T_a from the mixed layer. If instead, the transfer equations for H and λE are

substituted into the surface energy balance (which has the advantage that Δe and s_a can be omitted because $e_{sat}(T_0)$ can be directly solved) and $r_{ah} = r_{av}$ the formulation of δT_{a-sur} can be simplified into:

$$\delta T_{a-sur}(r_s=0) = \frac{Q^* r_a}{\rho_a c_p} - \frac{G_0 r_a}{\rho_a c_p} - \frac{1}{\gamma} [e_{sat}(T_0) - e] \quad (K) \quad (5.20)$$

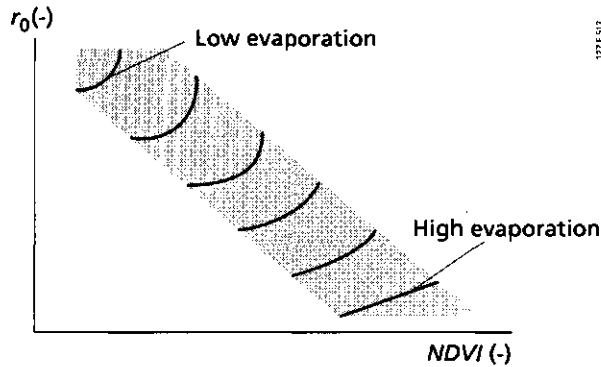


Fig. 5.12 Hypothetical isolines of potential evaporation according to radiation models as a function of surface reflectance r_0 and vegetation index NDVI

and

$$\delta T_a^{sur}(r_s=\infty) = \frac{Q^* r_a}{\rho_a c_p} - \frac{G_0 r_a}{\rho_a c_p} \quad (K) \quad (5.21)$$

Jackson's Crop Water Stress Deficit (CWSI), Moran's Water Deficit Index (WDI) are defined as:

$$\frac{\delta T_{a-sur} - \delta T_{a-sur}(r_s=0)}{\delta T_{a-sur}(r_s=\infty) - \delta T_{a-sur}(r_s=0)} = 1 - \frac{\lambda E}{\lambda E_p} \quad (-) \quad (5.22)$$

For environmental conditions where $\lambda E_p \approx Q^* - G_0$, CWSI and WDI become equal to $1 - \Lambda$, and it is suggested to compute the 'physical' limits of δT_{a-sur} according to Eqs. (5.20 and 5.21) using pixel-dependent $Q^* - G_0$, z_{om} (for r_a) and $e_{sat}(T_0)$ values. Menenti and Choudhury's Surface Energy Balance Index (SEBI) follows the same concept but will due to the difference in reference heights have some deviations of Eq. 5.22. Hence, Λ is a moisture indicator with similarity in definition to CWSI, WDI and SEBI.

Figure 5.12 shows a schematized nomograph of λE_p that would result from radiation type of expressions for λE_p , making surface reflectance and NDVI variable in the space

domain while keeping the other hydro-meteorological parameters such as K^d , L^d and T_a constant. Q^* decreases with increasing r_0 and G_0 decreases with increasing $NDVI$.

5.7 Concluding remarks

The diurnal variation of surface flux densities is significantly larger than that of moisture indicators. A moisture indicator expresses the local relative evaporation after identifying the local maximum evaporation. Potential evaporation is traditionally estimated with the Penman-Monteith model (Allen et al., 1995). Determination of λE_p on heterogeneous land surfaces with the λE_p^{PM} model is usually hampered by the assumption of areally constant hydro-meteorological parameters and their non-representativeness for wet conditions. Therefore, it is suggested to consider Q^*-G_0 as a suitable replacement for λE_p . Section 5.6 showed that several combinations of micro-meteorological conditions yield a situation in which Q^*-G_0 and λE_p^{PM} do not deviate more than 10%. Under these restrictions, $\Lambda \approx \lambda E/\lambda E_p$ and CWSI, WDI and SEBI become $\approx 1-\Lambda$. Bastiaanssen et al. (1995b) showed how Λ -maps can be used to diagnose crop stress and evaluate the performance of regional irrigation water management in the Nile Delta. It is suggested to improve the computation of the 'physical' limits of δT_{a-sur} by pixel-dependent Q^*-G_0 , $z_{0,m}$ and $e_{sa}(T_0)$ values without a surface energy balance combination equation (no Δe and s_a required).

Because of its quasi-constancy, the use of Λ makes the comparison of instantaneous remote sensing based flux densities, instantaneous aircraft flux density measurements, time-integrated ground-based flux densities and time-step model-based flux densities much simpler. The temporal behaviour of various moisture indicators was investigated with field measurements; Λ is tentatively chosen as superior because:

- Λ appeared to be the most stable during 42 daytime surface energy balances measured in the Qattara Depression between 11³⁰ to 14³⁰ hours (CV = 13%): The difference with α could be explained by daytime changes in s_a ;
- Λ has (after β) the simplest formulation, and can be computed from H and λE without any auxiliary data on s_a , $e_{sa}(T_0)$, e and r_{av} .

A physical explanation for the constancy of Λ was based on the convex G_0/Q^* diurnal shape. The largest $\nabla_z T_s$ -values occur prior to the peak of T_0 . It was observed that H/Q^* is rather flat and explained by the similarity between $\delta T_{a-sur}(t)$ and $K^d(t)$. As a result, $\lambda E/Q^*$ is a concave function of time which was confirmed by the EVADES simulations of $r_{soil}(t)$, at least for the bare soils in the Qattara Depression. The dynamics in the top-layer, notably the $\nabla_z \rho_v$ and $\nabla_z \theta$ gradients, explain that $r_{soil}(t)$ decreases in the morning and increases in the afternoon which results in concave $\lambda E/Q^*$ ratios.

The mathematical description of the diurnal variation of canopy resistance, $r_c(t)$, did receive considerable attention by modellers and bio-physicists. Despite the fact that most land surfaces are bare or partially covered on a global scale, a thorough description of $r_{soil}(t)$ received less attention in the international literature. The inclusion of Eq. (3.23) in land surface parameterization schemes improves the potential for predicting the latent heat flux density from bare and partially covered soil on a better physical basis, without modifying the complexity of model input parameters.

6 Derivation of empirical relationships between hydro-meteorological parameters and radiative properties of the land surface

6.1 Land surface radiative properties and exchange processes

The 'multi-step' Surface Energy Balance Algorithm for Land (SEBAL) uses hemispherical surface reflectance r_0 , vegetation index $NDVI$, surface temperature T_0 as well as their interrelationships to map land surface flux densities for a wide spectrum of land types. The moisture indicators dealt with in Chapter 5 can be derived from these land surface flux densities in combination with T_0 , T_a and r_{sh} data simultaneously obtained with the SEBAL computation procedure. A conceptual scheme of SEBAL is given in Figure 6.1.

Spaceborne radiometers measure spectrally reflected VISible and Near-InfraRed radiation, $K^{\uparrow}_{TOA}(\lambda)$, and emitted Thermal InfraRed radiation, $L^{\uparrow}_{TOA}(\lambda)$, at the Top Of the Atmosphere (TOA). The spectral intervals may be defined as 0.4 to 0.7 μm (VIS), 0.7 to 3.0 μm (NIR) and 3 to 14 μm (TIR). These radiance data can be converted into r_0 (Section 6.2), T_0 (see Section 6.3) and $NDVI$. The derivation of at-surface values for $NDVI$ has been extensively described elsewhere (e.g. Tucker, 1986) and will not receive much attention in this thesis.

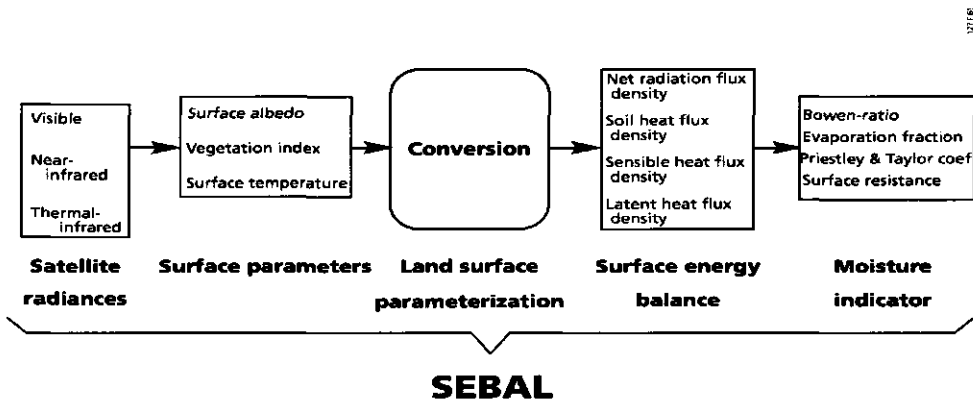


Fig. 6.1 Principal components of the Surface Energy Balance Algorithm for Land (SEBAL) which converts remotely measured, spectrally reflected and emitted radiances, into land surface flux densities and moisture indicators

Since SEBAL describes λE as the rest term of the surface energy balance, λE can be considered as a function f_1 of 12 variables s_1 to s_{12} :

$$\lambda E = f_1(r_0, L^\downarrow, \epsilon_0, T_0, K^\downarrow, \lambda'_s, T_s, z_{0m}, kB^{-1}, u_a, T_a, L) \quad (6.1)$$

The string s_1 to s_{12} is essentially similar to the ones in Eqs. (2.91) and (3.37). Areal variations in the values of the f_1 -function occur when the pixel resolution at which f_1 is estimated is small in comparison to the correlation length of the land-atmosphere exchange processes (see Section 1.1). Eq. (3.40) in Section 3.3 showed that for heterogeneous land surfaces, both the offset c_3 and the slope c_4 of the $T_0(\lambda E)$ relationship are not univocally defined. Although some classical $T_0(\lambda E)$ relationships for assessing evaporation with constant c_3 and c_4 value perform well at micro scale (e.g. Jackson et al, 1977), they are not designed nor suitable for composite terrain with distinct variations of all variables in the s_1 to s_{12} strings.

On composite terrain, the challenge is therefore to map distributed patterns of r_0 , L^\downarrow , ϵ_0 , T_0 , K^\downarrow , λ'_s , T_s , z_{0m} , kB^{-1} , u_a , T_a and L . Since r_0 and T_0 measurements are obtained for each pixel, it is preferable that the s_1 to s_{12} strings are determined at the same horizontal resolution. Such data demands cannot be met with synoptic meteorological stations, extended field observations, nor even from advanced HAPEX types of field experiments. Therefore several attempts were made by the remote sensing science community. Table 6.1 provides an impression of the extent to which f_1 can be derived from radiative properties of the land surface for cloud-free atmospheric conditions (see also Table 1.1). Apparently, not all s-strings can currently be related to a remote sensing observable and some new solutions need to be investigated.

The robustness of the various (semi-) empirical solutions posed in Table 6.1 varies for s_1 to s_{12} . For instance much research has been spent on methods to determine r_0 (being s_1) from space measurements of planetary reflectance r_p . Most of the solutions for r_0 are however based on physical atmospheric correction procedures which require atmospheric state conditions and spectral solar irradiance to be known exactly at the time of image acquisition. More simple procedures that are independent of the atmospheric measurements necessary to convert r_p into r_0 on the basis of a few known target r_0 -values are therefore tested in Section 6.2.

Procedures for obtaining T_0 are generally hampered by the water vapour absorption in the thermal infrared range. Although radiosoundings are standard solutions used to correct for these influences, their accuracy is not always ideal for the operational retrieval of T_0 on a regular basis and for large-scale land surfaces overlaid by an atmosphere with spatially variable state conditions. Section 6.3 deals with a simplified description on how to retrieve T_0 from thermal infrared measurements using a few anchor points.

Table 6.1 Hydro-meteorological parameters which can be derived from surface radiative properties. The correspondence between s_1 to s_{12} and the computation steps of the SEBAL algorithm are indicated

String	SEBAL step	Parameter	Remote sensing determinant	Source
s_1	8	r_o	r_p	Pinty and Ramond (1987), Arino et al. 1992
s_2	12	L^{\downarrow}	r_o, r_p	Bastiaanssen (1988a)
s_3	13	ε_o	NDVI	Van de Griend and Owe (1993)
s_4	14	T_o	T_{sat}	Wan and Dozier (1989); Becker and Li (1990)
s_5	15	K^{\downarrow}	n/N	Raschke et al., 1991
s_6	18	λ'_s	-	-
s_7	18	T_s	-	-
s_8	20	z_{om}	NDVI	Hatfield (1988); Moran (1990)
s_9	21	kB^{-1}	T_o	Kustas et al. (1989)
s_{10}	30	u	-	-
s_{11}	33	T_a	T_o	Chen et al. (1983); Davis and Tarpley (1983)
s_{12}	35	L	-	-

According to Table 6.1, techniques for identifying λ'_s and T_s from spaceborne determinants seems impossible. The need to determine T_s and λ'_s (or r_{sn}) is usually bypassed by considering the ratio of G_o over Q^* (e.g. Clothier et al., 1986). This G_o/Q^* fraction of vegetated surfaces can be a suitable proxy for λ'_s and T_s using indices for the presence of vegetation. Such a G_o/Q^* approach fails, however, in canopies with a low soil coverage because soil properties are not described by vegetation indices while G_o/Q^* is certainly affected by local characteristics. An improved version of G_o/Q^* -parameterization focusing on bare soils will be derived in Section 6.4.

Methods for estimating the momentum flux density by means of u (s_{10}) and L (s_{12}) are in their infancy. A new solution for finding large area aerodynamic characteristics from the negative slope between r_o and T_o as originally suggested by Menenti et al., (1989b) and Bastiaanssen (1991) will be further elaborated in Section 6.5.

Although the work of Chen et al. (1983) provides a good basis for mapping the regional patterns of T_a , a general accepted framework for the derivation of T_a from T_o does not exist and an alternative procedure is therefore worked out. Section 6.6 demonstrates that δT_{a-sur} is linearly related to T_o .

The remaining empirical relationships for s_2 , s_3 , s_5 , s_8 and s_9 being $L^{\downarrow}(r_o, r_p)$, $\varepsilon_o(NDVI)$, $K^{\downarrow}(n/N)$, $z_{om}(NDVI)$ and $kB^{-1}(T_o)$, respectively (Table 6.1) are sufficiently well documented and will not be critically reviewed with data from our Mediterranean study areas. They will be addressed in Chapter 7.

Table 6.2. Relationships between hydro-meteorological parameters and remote sensing observations which will receive more in-depth attention in this Chapter

String	Relationship	Solution for	Section
s_1	$r_0 (r_p)$	r_0	6.2
s_4	$T_0(T_{sat})$	T_0	6.3
s_6, s_7	$G_0/Q' (r_0, T_0, NDVI)$	λ'_{sr}, T_s	6.4
s_{10}, s_{12}	$T_0 (r_0)$	u, L	6.5
s_{11}	$\delta T_{a-sur} (T_0)$	T_a	6.6

6.2 Surface vs. planetary reflectance: $r_0(r_p)$ relationship

Formulations

Radiances observed by satellite sensors relate to a small field of view at the Top Of Atmosphere and are directional. The broadband planetary reflectance r_p required for land surface processes can be obtained after integration between 3 and 30 μm :

$$r_p = \frac{\int_{0.3}^{3.0} K_{TOA}^{\uparrow}(\lambda) d\lambda}{\int_{0.3}^{3.0} K_{TOA}^{\downarrow}(\lambda) d\lambda} \quad (-) \quad (6.2)$$

If no additional ground information on the surface roughness conditions are available and bi-directional surface reflectance models $r_0(\lambda, \phi_{sur}, \psi_{sur}, \phi'_{sur}, \psi'_{sur})$ cannot be applied, the surface target is usually assumed to be a Lambertian reflector. Then the spectrally integrated surface hemispherical reflectance r_0 may be obtained from the broadband planetary reflectance r_p in a simple and straightforward manner. Physically based numerical models that account for spectral atmospheric radiation transfer are available nowadays. These atmospheric correction methods are generally based on detailed information on the state of the atmosphere extracted from radiosoundings or spectral measurements of solar irradiance. An example of a simpler semi-empirical radiation transfer model is the one proposed by Arino et al. (1992) who used a different form of the radiation transfer equation presented in Eq. (2.8):

$$r_0 = \left[\frac{r_p - r_a}{\tau_{sw}'' + r_d(r_p - r_a)} \right] \quad (6.3)$$

where r_a is the atmospheric reflectance ($K_a^{\uparrow}/K_{TOA}^{\downarrow}$). The values for r_a , τ_{sw}'' and r_d changes with the atmospheric shortwave transmittance as a function of τ_{sw} and ϕ_{su} and can also be obtained empirically (Michels, 1989). In absence of sky diffuse radiance and

specularly reflected sunlight, i.e. $r_d = 0$, Eq. (6.3) can also be shaped in a linear form (Ahern et al., 1977; Koepke, 1985):

$$r_0 = \frac{r_p - r_a}{\tau_{sw}'} \quad (-) \quad (6.4)$$

The so-called 'dark object subtraction method' (Ahern et al., 1977) assumes r_0 of the darkest pixel (e.g. deep sea) to be zero. This approximation and Eq. (6.4) allows to find r_a as r_p of the darkest pixel.

Measurements

During the Egyptian field survey, r_0 was measured as the ratio of K^\uparrow over K^\downarrow from in-situ pyranometers on bare soil at the sites specified in Table 4.2. The measurements illustrated in Figure 6.2A indicate a diurnal variation in hemispherical surface reflectance $r_0(\phi_{su}, \psi_{su})$. Bastiaanssen (1988b) and Menenti et al. (1989a) also attributed this $r_0(\hat{t})$ behaviour to the fraction of diffuse radiation, surface roughness and dew formation.

Pelgrum (1992) applied Eq (6.3) for a number of separated METEOSAT images covering Lower Egypt, including part of the Mediterranean Sea, to generate a series of instantaneous r_0 -values from which $r_0(\hat{t})$ could be drawn at a significant larger resolution (5 km * 5 km) as compared to pyranometer (10 m * 10 m) (see Figure 6.2B). The values for r_p , r_a and τ_{sw} were different for each image and calculated according to the solar elevation-dependent shortwave transmittance, $\tau_{sw}(\phi_{su})$. Plots of this $r_0(\hat{t})$ -series of selected pixels confirms the trend which was surveyed in-situ. Hence single-direction measurements from a remote platform are able to describe the ϕ_{su} and ψ_{su} effects on spectrally integrated and hemispherical surface reflectance r_0 correctly through simple τ_{sw} field measurement

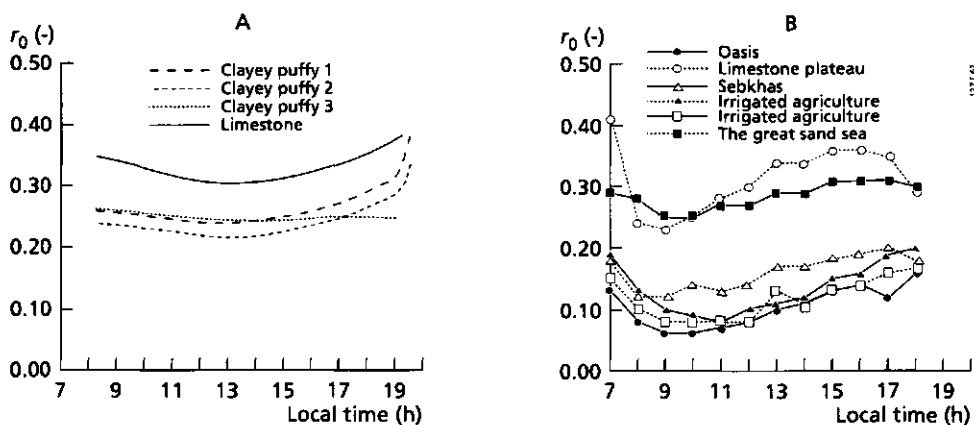


Fig. 6.2 (Part A) Diurnal trend of broadband hemispherical surface reflectance, r_0 measured at the Qattara Depression sebkhas on 20 June 1988; (Part B) r_0 estimated with METEOSAT spectral radiances measured over Lower Egypt on 5 August 1986 applying Eq. (6.3) (after Pelgrum, 1992)

Table 6.3 summarizes a few case studies conducted with Eq. 6.4. According to Table 6.3, the correlation coefficient is in the range $R^2 = 0.83$ to 0.96 when a linear conversion is applied. The root mean square error in estimating r_0 from r_p through Eq. (6.4) is $\Delta r_0 = 0.04$. Figure 6.3 illustrates a few cases with these linear transformations. Hence, Eq. (6.4) requires less ancillary data as compared to Eq. (6.3), while its performance is rather acceptable.

Table 6.3 Application studies with linear $r_0(r_p)$ relationships

Image and band selection	Date	Location	n	R^2	RMSE r_0
NS001-2,3,5,7,9,10	29 June, 1991	Castilla la Mancha, Spain	6	0.96	0.025
TM-1,2,3,4,5,7	2 April, 1987	Qattara Depression, Egypt	9	0.83	0.052
TM-1,2,3,4,5,7	27 July, 1987	Nile Delta, Egypt	4	0.95	0.044
TM-1,2,3,4,5,7	12 June, 1991	Castilla la Mancha, Spain	10	0.86	0.042
TM-1,2,3,4,5,7	9 July, 1991	HeiHe Basin, China	5	0.91	0.029
TM-1,2,3,4,5,7	18 Sept., 1992	HAPEX-Sahel, Niger	5	0.90	0.034

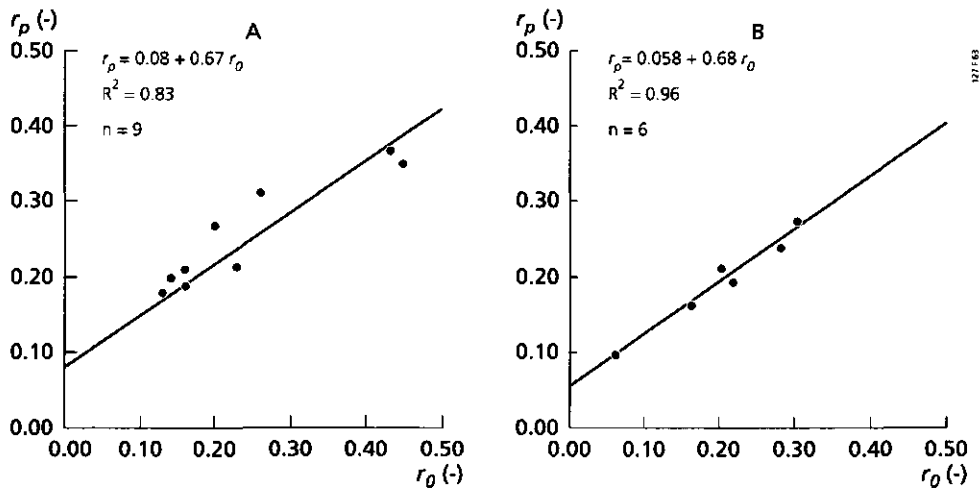


Fig. 6.3 Simplified linear relationships between broadband directional planetary reflectance, r_p , and broadband hemispherical surface reflectance, r_o . (Part A) Qattara Depression-Egypt, 2 April, 1987 (after Menenti et al., 1989a); (Part B) Castilla la Mancha-Spain, 29 June, 1991 (after Bastiaanssen et al., 1994a)

6.3 Surface vs. satellite temperature: $T_o(T_{sat})$ relationship

Longwave radiation can only be transmitted through the atmosphere in those ranges of the spectrum where the molecular absorption by water vapour, gases and suspended materials is minimized, i.e. atmospheric windows in the 8-14 μm spectral range. Thermal infrared radiometers have small bands in relative transparent parts of these spectrum. The wavelength dependent thermally emitted blackbody radiation from the land surface can be described by Planck's law (Eq. 2.2). Relative to water vapour, the scattering and absorption of other gases is small. Therefore, the transmittance is often related to the amount of precipitable water (e.g Becker and Li, 1991). Basically, the atmospheric correction consists of the following terms:

$$L_{TOA}^{\uparrow}(\lambda) = \underbrace{[\epsilon_{\lambda} L_{\lambda}(T_o)^{bb} + (1 - \epsilon_{\lambda}) L_{\lambda}^{\downarrow}]}_{L_{land}^{\uparrow}(\lambda)} \tau_{\lambda} + L_{atm}^{\uparrow}(\lambda) \quad (\text{W m}^{-2} \mu\text{m}^{-1}) \quad (6.5)$$

where $L_{atm}^{\uparrow}(\lambda)$ is the upwelling spectral radiance from atmospheric emission and scattering that reaches the sensor, L_{λ}^{\downarrow} is the downwelling spectral radiance from atmospheric emission incident upon the land surface and τ_{λ} is the spectral atmospheric transmission. Atmospheric correction schemes are indispensable and may vary from

highly sophisticated physically based radiative transfer models to simple empirical methods. LOWTRAN (Kneizys et al., 1988) is an atmospheric path radiance model which requires atmospheric vapour and temperature profiles to be known. The output of the model consists of τ_λ and $L_{atm}^\uparrow(\lambda)$. Split-window techniques have been developed to account for the differential water vapour absorption in the 10 to 13 μm range assuming the surface emissivity to be constant over the latter spectral region (Price, 1984). Alternatively, multiple in-situ installed thermal radiometers (yielding a set of $L_{land}^\uparrow(\lambda)$ -values) may be compared with the satellite based radiometers (yielding a second set of $L_{TOA}^\uparrow(\lambda)$ -values), from which τ_λ and $L_{atm}^\uparrow(\lambda)$ can be calibrated. This approach has a major advantage since the ground values of T_0 are anchored which is an advantage if thermal radiometers are erroneously calibrated. If physically correct τ_λ and $L_{atm}^\uparrow(\lambda)$ -data are taken, the error in $L_{TOA}^\uparrow(\lambda)$ will then be conveyed to $L_\lambda(T_0)^{bb}$ and T_0 will consequently be wrongly estimated. By merging ground data with satellite data, realistic surface temperature patterns can be more reliably obtained (although τ_λ and $L_{atm}^\uparrow(\lambda)$ may be physically useless).

The general form of Eqs. (6.5) has been applied for the studies listed in Table 6.3. Two particular examples are shown in Figure 6.4. The HAPEX-SAHEL large-scale field data collection programme study (Goutorbe et al., 1994) took place at long. 2 to 3°E and lat. 13 to 14°N to inspect the change of state of a Sahelian landscape in a dry-down period at the end of the rainy season during September 1992. The thermal infrared radiation in band 6 of Thematic Mapper at the land surface and at the top of the atmosphere are plotted for three field plots. A Thematic Mapper image of the HeiHe basin in the HEIFE study area, China (Mitsuta, 1994) has been included in part B of Figure 6.4 to demonstrate the accuracy of this approach over land surfaces with a significant thermal contrast between desert and oases with consequently non-homogeneous state conditions of the lower atmosphere. The 10 ground control points in HEIFE show a general error in estimating T_0 of ± 2 to 3 °C. The same accuracy was mentioned by Wan and Dozier (1989) and Choudhury (1991a) if accurate radiosounding data are used to obtain τ_λ and $L_{atm}^\uparrow(\lambda)$ which implies that this straightforward 'anchoring' approach is not less accurate than more sophisticated techniques. For both HAPEX and HEIFE cases, spectral radiance at the ground (broad band) was different from the spectral characteristics of the remote radiometer (narrow band). A correction on the difference of the spectral characteristics has been made by using Plancks law for the narrow band considering the temperature of the broad band. Figure 6.4B further exhibits the importance of having access to contrasting surface temperatures for land surface components with a size equal to the pixel scale. The accuracy of deriving T_0 from satellite platforms and high frequency acquisitions for e.g. climate monitoring can be improved if standard meteorological measurements would include surface temperature T_0 .

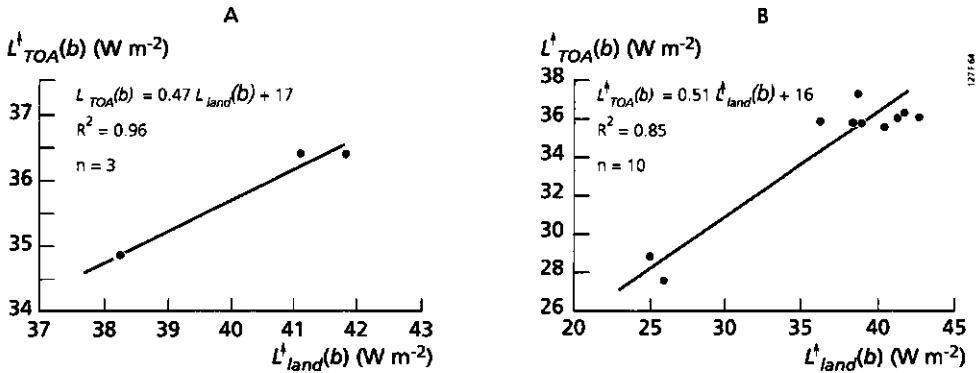


Fig. 6.4 General relationship between in-band radiances in the 10.45 to 12.42 μm spectral region at the top of the atmosphere $L_{TOA}^{\lambda}(b)$ measured by LANDSAT Thematic Mapper band 6 and in-situ radiometers (8-14 μm) $L_{land}^{\lambda}(b)$. A correction for the different spectral characteristics between radiometers have been applied. (Part A) HAPEX SAHEL and (Part B) HEIFE

Land surface temperature on the scale of a METEOSAT pixel is more difficult to validate. The large-scale thermal patterns at the Iberian Peninsula measured by METEOSAT on 29 June, 1991, were therefore calibrated with the surface temperatures of the Mediterranean Sea and the Atlantic Ocean. The validation on land was achieved by means of EFEDA data and using a high resolution thermal image of the NS001 radiometer: Surface radiative temperatures collected by radiometers installed at various locations spread over the experimental area are explored to calibrate the NS001 thermal image whereafter the NS001 thermal image is in turn applied to validate the METEOSAT thermal image. Table 6.4 was compiled to demonstrate the agreement between in-situ radiation temperature measurements and the NS001 estimates, as far as data were available at the moment of processing the NS001 image. In each case the minimum, mean and maximum surface radiation temperature has been extracted from the NS001 pixels for an area of 100 m * 100 m in the direct vicinity of the field observation point. The mean value has been obtained from linear averaging of the spectral radiances within the 100 m * 100 m grid.

Table 6.4 Validation of the NS001-based surface radiation temperature map ($^{\circ}\text{C}$).

Location	Site	In-situ	NS001 _{min}	NS001 _{mean}	NS001 _{max}
Tomelloso	Vineyard	40.0	40.4	42.2	44.4
Tomelloso	Vineyard	43.7	40.4	42.2	44.3
Tomelloso	Bare soil	45.3	39.9	42.3	44.9
Barrax	Irrigated corn	26.3	25.4	25.5	25.9

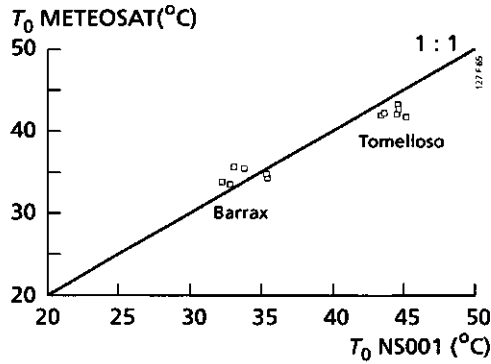


Fig. 6.5 Intercomparison between surface temperatures of 12 sub-areas, 4.1 by 3.9 km in size, obtained from NS001 and METEOSAT measurements in the EFEDA grid.

Considering the limited number of ground control points and the differences in footprint size between the in-situ thermal radiometers and NS001, the results of Table 6.4 should be seen as moderately good. Upscaling can be achieved by comparing the NS001 measurements with the METEOSAT measurements. The discrepancy in scale was solved by calculating the area-representative value for all NS001 pixels encompassed by a single METEOSAT pixel, again on the basis of averaging spectral radiances of 45,000 small NS001 pixels to meet the scale of one METEOSAT pixel. The radiation temperatures have been corrected for emissivity. A total number of 12 'giant' METEOSAT pixels has been considered (6 in Barrax and 6 in Tomelloso). Figure 6.5 shows the coherence in surface temperature T_0 from which it can be concluded that the differences are marginal (root mean square error = 1.8 °C) and that the thermal-infrared channel of METEOSAT describes large scale variations in T_0 appropriately.

6.4 Soil heat / net radiation flux density ratio: $G_0(Q)$ relationship

The soil heat flux density G_0 cannot directly be mapped from satellite observations. Many previous investigations have shown that the midday G_0/Q fraction is reasonably predictable from remote sensing determinants of vegetation characteristics such as vegetation indices and LAI (see Daughtry et al., 1990 for a review). However, the attenuation of radiative and conductive heat transfer in canopy and soil respectively changes significantly with soil cover, which suggests the need for the implicit inclusion of the soil thermal properties in these $G_0(Q)$ relationships if the soil coverage is low. The following comments with regard to the classical vegetation indices controlled G_0/Q fractions can therefore be made:

- effects of soil thermal properties ($\lambda_s', \rho_s c_s$) and soil water content (θ) on G_0/Q' are not accounted for;
- effects of the phase difference between G_0 and Q' arising from the diurnal variation of soil thermal storage and release of J_s are not accounted for.

Hence, a representation different from the standard G_0 one-layer resistance approach (Eq. 3.14) and based on remote sensing measurements which replaces T_s and r_{sh} needs to be developed. Eq. (6.6) is obtained by combining the G_0 -expression presented in Eq. (3.14) and the radiation balance Eq. (2.1), as a fraction G_0/Q' :

$$\Gamma = \frac{G_0}{Q'} = \frac{\rho_s c_s (T_0 - T_s)}{r_{sh} [(1 - r_0) K^\downarrow + L^*]} \quad (-) \quad (6.6)$$

so that the variables relevant for remote sensing are related to Γ as:

$$\Gamma = f_2(T_0, r_0, \frac{1}{K^\downarrow}) \quad (-) \quad (6.7)$$

where T_0 and r_0 are proportional to Γ and K^\downarrow is inversely proportional to Γ . The parameters of f_2 have in common that they can be determined from remote sensing (see Tables 1.1 and 6.1). Choudhury et al., (1987) introduced a *proportionality factor* Γ' to describe the conductive heat transfer in soil and an *extinction factor* Γ'' for the attenuation of radiation through canopies. Their parameterization of Γ consists of the product of two components:

$$\Gamma = \Gamma' \Gamma'' \quad (-) \quad (6.8)$$

Proportionality factor for bare soil, Γ'

In most previous remote sensing energy balance studies where G_0 was estimated through the G_0/Q' approach, Γ' was held areally constant whereas Γ'' was kept variable which may lead to an inaccurate assessment of G_0 over bare soils. In the framework of this thesis, field investigations on the proportionality factor Γ' were undertaken by burying heat flux density plates at very shallow depths (0.5-1.5 cm) in the bare soil sebkhas of the Qattara Depression. A net radiometer installed at 50 cm above the ground registered Q' . Totally, 25 complete daytime Γ' cycles were available to design a new parameterization of Γ' based on records collected during the summer and autumn of 1988 and 1989, respectively. Eight different locations have been included in the analysis and near-surface moisture conditions ranged between $\theta_0 = 0.01$ to $0.18 \text{ cm}^3 \text{ cm}^{-3}$. The average daytime Γ' value for the Qattara Depression varied between 0.092 and 0.355, which agrees well with previously published figures (e.g. Clothier et al., 1986; Choudhury et al., 1987). The proportionality factor

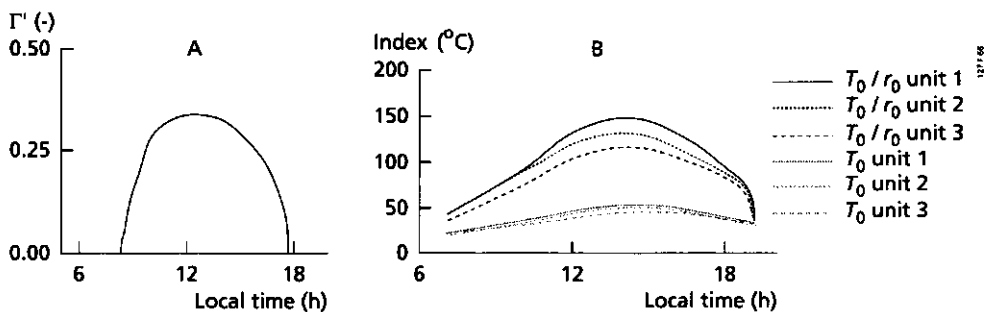


Fig. 6.6 (Part A) Typical diurnal trend of the soil heat / net radiation flux density ratio on bare soil, Γ' , taken from field measurements at Bir Qifar on 13 September 1989, (Part B) Daytime variation of the (T_0/r_0) index and T_0 exhibiting a trend in (T_0/r_0) being similar to Part A

Γ' , however, undergoes a diurnal cycle because the T_0 , T_s , r_{sh} , r_0 , K^d , L^* parameters enclosed in the formulation of Eq. (6.6) change continuously throughout the day. The diurnal shape of Γ' in Figure 6.6A can be described by a constant that is proportional to the energy partitioning whereas T_0/r_0 is proposed to describe the dynamic component of Γ' : Both T_0 and r_0 are included in f_2 . Chapter 5 described that Γ is in advance of T_0 . The (T_0/r_0) index compensates this time shift by the reduced r_0 -values around noon (Figure 6.2). Figure 6.6B shows the (T_0/r_0) and T_0 trends for three different sites, which emphasize the similarity between (T_0/r_0) and Γ' . Eq. (6.9) relates Γ' to T_0 and r_0 in agreement with the derivation made at Eq. (6.6):

$$\Gamma = \left(\frac{T_0}{r_0}\right) c_8 \quad (-) \quad (6.9)$$

The value for c_8 was calculated from the G_0 , Q^* , r_0 and T_0 field recordings as:

$$c_8 = \frac{1}{n} \sum_{i=1}^n \left(\frac{G_0 r_0}{Q^* T_0}\right)_i \quad (K^{-1}) \quad (6.10)$$

where T_0 is expressed in °C and n is the number of observations in the daytime period. According to Eq. (6.6), c_8 thus represents the soil thermal properties, $\rho_s c_s$ and r_{sh} . To meet the constraints with respect to the soil moisture dependency of Γ' , it was attempted to relate the variance of c_8 for the eight different locations investigated during 1988 and 1989 to θ_0 . For bare soils, r_0 can act as a substitute for θ_0 (see Figure 6.10) and the $c_8(r_0)$ relationship was for this reason further explored (Figure 6.7). An additional problem is that r_0 changes both with θ_0 and ϕ_{su} . The instantaneous r_0 -values were therefore integrated for the daytime observation period:

$$r_0^{avg} = \frac{\int_8^{16} K^\uparrow(t) dt}{\int_8^{16} K^\downarrow(t) dt} \quad (-) \quad (6.11)$$

The best fit ($R^2 = 0.67$) for c_8 based on the Qattara sebkhas then becomes:

$$c_8 = 0.0032r_0^{avg} + 0.0062(r_0^{avg})^2 \quad (-) \quad (6.12)$$

Extinction factor for canopies, Γ''

Because of interception of radiation, soil underneath vegetation will receive less radiation than bare soil and $T_0 - T_s$ will be significantly smaller. For regional energy balance studies, information to describe $T_0 - T_s$ is not available. Efforts in the formulation of Γ'' should therefore focus on remotely measurable vegetation parameters which control the attenuation of radiation. Choudhury et al. (1987) showed that the extinction coefficient Γ'' decreases in a non-linear fashion with increasing soil cover and LAI , while Kustas and Daughtry (1990) found a linear decrement between Γ'' and $NDVI$. In SEBAL, the $NDVI$ has been selected to describe the general effect of vegetation on land surface flux densities (see Figure 6.1).

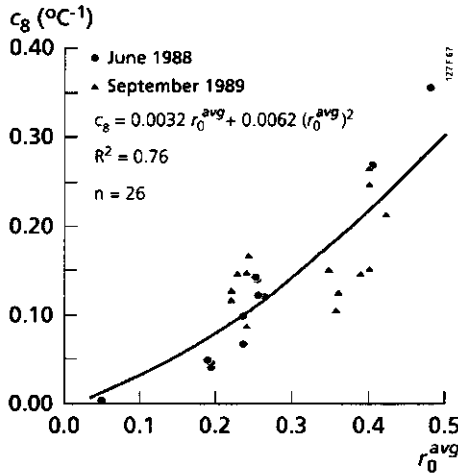


Fig. 6.7 Correlation between a factor c_8 (Eq. 6.9) and the daytime average hemispherical surface reflectance r_0^{avg} on the basis of field measurements at different types of sebkha collected during the summer and autumn of 1988 and 1989 respectively in the Qattara Depression

Since data on G_o/Q' in partially and completely vegetated surfaces were not routinely measured by the present author, Figure 6.8 is included based on measurements from Clothier et al. (1986), Choudhury et al. (1987), Kustas and Daughtry (1990) and van Oevelen (1991) (see Table 6.5). The best fit of the data shown in Figure 6.8 is:

$$\Gamma = 0.30 [1 - 0.98 (NDVI)^4] \quad (-) \quad (6.13)$$

Table 6.5 References of studies on the G_o/Q' ratio for partially closed canopies used to generate Figure 6.8. ND = Normalized Difference, LAI = Leaf Area Index

Source	Study area	Land cover	Vegetation	Soil moisture	Julian day number
Clothier et al, 1986	Phoenix, AZ	Alfalfa/stubble	ND	0.10-0.35	260-360
Choudhury et al., 1987	Phoenix, AZ	Bare/wheat	LAI	-	6-71
Kustas and Daughtry, 1990	Phoenix, AZ	Bare/alfalfa/cotton	ND, NDVI	0.03-0.25	162-165
Oevelen, van, 1991	Beltsville, MD	Bare/soybeans	NDVI	0.10-0.25	190-265

Figure 6.8 proves that the scatter in experimental Γ -values increases at decreasing $NDVI$, pinpointing the necessity to improve the description of Γ for sparse canopies. Γ , within the envelope of Figure 6.8 is gradually more influenced by Γ' when the soil cover

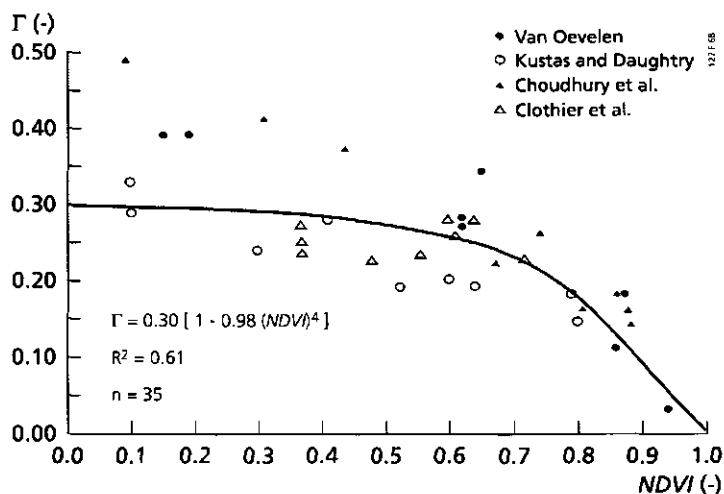


Fig. 6.8 Soil heat / net radiation flux density ratio, Γ , data for a variety of surface types and soil cover derived from the references listed in Table 6.5 to establish relationships between the extinction factor Γ versus the vegetation index $NDVI$

Table 6.6 Principal land use types related to the soil heat /net radiation flux density ratio sub-study conducted within the Central West Super site HAPEX SAHEL

Date	Site	Land use and attached symbol
03/09/1992	Degraded bushland	Herbs (A), Laterite-1 (B), Laterite-2 (C), Degraded bush (D), Millet (E)
05/09/1992	Fallow bush/grassland	Cleared bush (F), Bush/grassland (G), Sandplain (H), Old Millet (I)
08/09/1992	Fallow bush/grassland	Cleared bush (J), Bush/grassland (K), Bush-grass (L), Sandplain (M), Old millet (N)

decreases. The diversity in Γ (which can partly be explained by soil background interferences) can be accounted for by combining Eqs. (6.8), (6.12) and (6.13) leading to the final equation used in SEBAL:

$$\Gamma = \frac{T_0}{r_0} (0.0032 r_0^{avg} + 0.0062 r_0^{avg2}) [1 - 0.978 (NDVI)^4] \quad (6.14)$$

Eq. (6.14) was evaluated with independent field data selected from HAPEX Sahel. The Γ -values at the Central West supersite centered around Fandou Beri village (2°33'E, 13°13' N) were intensively observed on three different days. The principal land use types are specified in Table 6.6. The daytime average Γ_{avg} -values are presented in Figure 6.9.

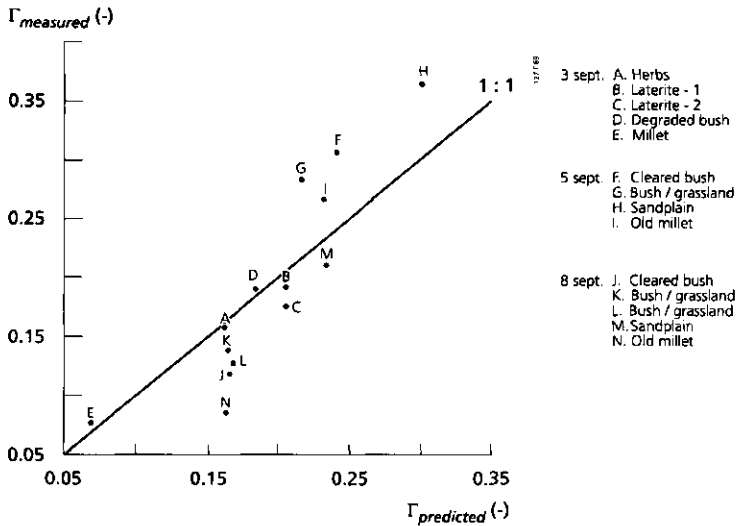


Fig. 6.9 Diagram of the daytime averaged soil heat / net radiation flux density ratio Γ in Niger calculated by means of Eq. (6.14), i.e. 'predicted', against field measurements.

Considering the wide differences in climate, soil and vegetation between Niger and Egypt, an encouraging result ($\Gamma(\text{RMSE}) = 0.04$) was obtained. Nevertheless, Figure 6.9 suggests a bias effect, emphasizing that the 0.0032 and 0.0062 calibration constants need to be refined when applied to other study areas.

6.5 Surface temperature vs. hemispherical surface reflectance: $T_0(r_0)$ relationship

6.5.1 Soil physical explanation

Since surface wetness θ_0 affects both r_0 and T_0 , an interrelationship between r_0 and T_0 can be expected as well. The interest in such a $T_0(r_0)$ relationship is that r_0 and T_0 are both components of the surface energy balance (and detectable from remote sensing data) which provides the opportunity to analytically relate them to each other and extract in that way additional information on large area aerodynamic properties (Menenti et al., 1989b; Bastiaanssen, 1991). The effect of θ_0 on r_0 will be explained first, then the impact of θ_0 on T_0 . The coupling between r_0 and T_0 and its significance for large-scale aerodynamic parameters will be explained afterwards.

The $r_0(\theta_0)$ relationship

If the soil is wet, its reflectance is lower than when it is dry (Graser and van Bavel, 1982). Figure 6.10 demonstrates the daytime averaged θ_0 -values for a range of soil types sampled from various spots in the Qattara Depression. The regression equation ($R^2 = 0.67$) reads as:

$$r_0^{avg} = 0.02 - 0.089 \ln \theta_0 \quad (-) \quad (6.15)$$

Eq. (6.15) applies to $0.01 < \theta_0 < 0.18 \text{ cm}^3 \text{ cm}^{-3}$. Deviations from the regression line in Figure 6.10 were attributed to variation in soil bulk properties. Figure 6.10 further demonstrates that under wet conditions, hemispherical surface reflectance is a factor 2 to 3 less than under dry conditions. This implies that Q^* must change significantly when going from wet to dry or dry to wet surfaces. Furthermore from the $r_s(\theta)$ coupling outlined in Section 3.2.2, it may be expected that the reflective behaviour through $r_0(\theta_0)$ is related to the partitioning between H and λE .

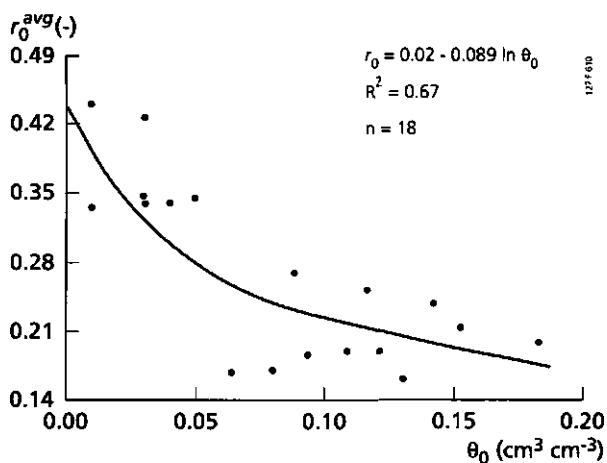


Fig. 6.10 Correlation between daytime averaged broad-band hemispherical surface reflectance, r_0^{avg} (Eq. 6.11), and surface soil water content, θ_0 , for a mixture of sebkha types in the Qattara Depression

The $T_0(\theta_0)$ relationship

The effect of θ_0 on T_0 is somewhat more entangled because T_0 is modulated by various other factors besides θ_0 (see Eq. 3.37). Mechanistic simulation models can be used to demonstrate the $T_0(\theta_0)$ behaviour for selected hydro-meteorological situations. The EVADES model has been used to derive the $T_0(\theta_0)$ relationship for a limited number of constant matric pressure heads, h_m , at different depths:

- Run I : Sandy soil, $h_m = -10$ cm 100 cm depth;
- Run II : Clay soil, $h_m = -10$ cm 100 cm depth;
- Run III : Sandy soil, $h_m = -10$ cm 200 cm depth;
- Run IV : Clay soil, $h_m = -10$ cm 200 cm depth;
- Run V : Sandy soil, $h_m = -1000$ cm 200 cm depth;
- Run VI : Clay soil, $h_m = -10$ cm 50 cm depth.

Independent of the sandy or clay soil type and the lower boundaries (Dirichlet condition) chosen, constant z_{om} and kB^{-1} surface characteristics have been considered for all six runs. The temperature at the lower boundary was held constant at 25 °C day and night. The climatological conditions measured in the Qattara Depression were used to specify the atmospheric demand. Table 6.7 shows the daily minima and maxima of T_a , U , u and K^d in September 1989. To create the possibility of extracting (θ_0, T_0, r_0) strings occurring at the same time and similar conditions in the overlying atmosphere, the diurnal cycles of T_a , U , u and K^d were held similar for the six runs and the 14-day simulation period of each run. The initialization of all $\theta(z)$ profiles (except run V and VI) was done according to the equilibrium soil water content profile $h_m = -h_g$. The soil temperature

profile $T_s(z)$ was initially set to an iso-thermal 25°C profile. The initialization of the soil vapour concentration profile $p_v(z)$ was done by assuming equilibrium with local θ and T_s values, applying Eq. (2.28). Run V and VI were made in addition to Run I to IV to demonstrate the $T_0(\theta_0)$ shape in extreme dry and wet cases, respectively. The soil physical data based on laboratory measurements are specified by means of the van Genuchten parameters θ_r , θ_{sat} , α , n , l and k_{sat} (van Genuchten, 1980) and added to Table 6.7. The $r_0(\theta)$ relationship shown in Figure 6.10 was used in EVADES for the radiative coupling between surface wetness and net shortwave radiation, K' .

Table 6.7 Specifications for the input data for the numerical experiment with the EVADES model to explore the coupling between soil moisture, surface temperature and hemispherical surface reflectance for dry and wet surfaces. The meteorological parameters are measured at a height of 2.0 metres

Run	θ_r	θ_{sat} (cm ³ cm ⁻³)	α (cm ⁻¹)	n (-)	l (-)	k_{sat} (cm d ⁻¹)	T_a (°C)		U (-)		u (m s ⁻¹)		K' (W m ⁻²)	
							min	max	min	max	min	max	min	max
I	0.043	0.347	0.022	2.13	-1.37	0.96	15-35	0.2-0.8	2-3	0-815				
II	0.000	0.496	0.120	1.22	-6.48	9.12	15-35	0.2-0.8	2-3	0-815				
III	0.043	0.347	0.022	2.13	-1.37	0.96	15-35	0.2-0.8	2-3	0-815				
IV	0.000	0.496	0.120	1.22	-6.48	9.12	15-35	0.2-0.8	2-3	0-815				
V	0.000	0.347	0.022	3.50	+0.50	9.60	15-35	0.2-0.8	2-3	0-815				
VI	0.000	0.530	0.022	1.60	-7.50	5.00	15-35	0.2-0.8	2-3	0-815				
day 180-194			$z_{0m} = 0.01$ m		$z_{0m}/z_{0n} = 10$		latitude 30°30' N							

First, T_0 , r_0 and θ_0 were computed for 14 sequential days under the conditions described above. Thereafter, all instantaneous T_0, r_0, θ_0 12⁰⁰ hour values were extracted from the simulations and treated as if they all happened simultaneously in 6*14 parallel reservoirs (weather conditions are equal). Figure 6.11A demonstrates the simulated $T_0(\theta_0)$ relationship proving that soil water content controls T_0 . A drawback of the $T_0(\theta_0)$ relationship is that the shape of the function changes continuously throughout the day according to the unsteady character of $T_0(t)$. Hence, $T_0(\theta)$ expressions are strictly location and time-dependent and cannot be used to compile a map of soil moisture.

The $T_0(r_0)$ relationship

Combination of $T_0(\theta_0)$ and $r_0(\theta_0)$, suggests a correlation among T_0 and r_0 which is illustrated in Figure 6.11B. The advantage of Figure 6.11B is that it can be compiled from all platforms with synergistic visible and thermal infrared channels. Obviously, T_0 increases with r_0 until moisture is depleted and a critical matric pressure head is reached. Remaining soil moisture is retained at low pressure head and T_0 will be controlled by other factors.

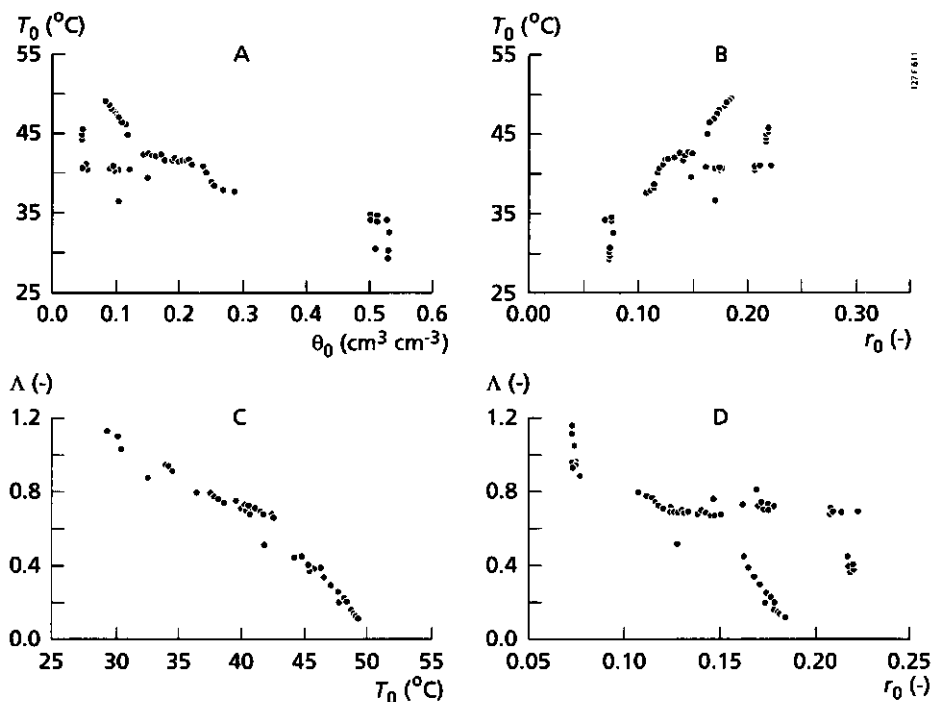


Fig. 6.11 (Part A) The shape of the $T_0(\theta_0)$ relationship simulated with the EVADES model for run I to VI considering different bare soils exposed to various moisture conditions. (Part B) The $T_0(r_0)$ relationship combines $r_0(\theta_0)$ and $T_0(\theta_0)$. (Part C) The evaporative fraction Λ is compared with surface temperature T_0 . (Part D) Evaporative fraction Λ and hemispherical surface reflectance r_0

According to Figure 6.11B, a positive correlation exhibits between T_0 and r_0 on wet to intermediately dry land ($r_0 < 0.20$, $\theta_0 > 0.05 \text{ cm}^3 \text{ cm}^{-3}$, $T_0 < 45^{\circ}\text{C}$). Figure 6.11C and 6.11D have been added to illustrate how T_0 and r_0 affects energy partitioning in terms of Λ . An evaporative fraction of $\Lambda \sim 1$ turns to appear at $r_0 < 0.08$, $\theta_0 > 0.35 \text{ cm}^3 \text{ cm}^{-3}$ and $T_0 < 33^{\circ}\text{C}$. These land surface elements are wet surfaces where water vapour is released at a rate according to the atmospheric demand and δT_{a-sur} is confined to a minimum. A downward sensible heat flux density is produced to the ground if evaporation cools down the air temperature, i.e. 'advection entrainment' (McNaughton, 1976). Kalma and Jupp (1990), Gay and Bernhofer (1991) and Wang et al. (1994b) showed by taking measurements above wet surfaces under arid conditions that during daytime T_a can exceed T_0 by several degrees. Except at the edges between wet and dry surfaces (Blyth et al., 1993), this enhancement of Λ however rarely exceeds 1.2. A general statement of $\Lambda \approx 1.0$ at wet surface is therefore a proper first approximation.

When land dries out, both r_0 and T_0 increase. Values for $\Lambda = 0$ were found in Figure 6.11 if $r_0 > 0.25$, $\theta_0 < 0.03$ and $T_0 > 52^\circ\text{C}$. Although these values have an indicative value only, it is demonstrated that the extremes in Λ can be appraised on the basis of the $T_0(r_0)$ relationship. It may therefore be tentatively concluded that the availability of T_0 and r_0 information of land surfaces with extremes in hydrological conditions can be applied to allocate spots with $\Lambda = 0$ and $\Lambda = 1$ geographically. This statement will be justified later and may be crucial for detecting extremes in regional surface energy balances (sub-areas with $H \approx 0$; $\lambda E \approx 0$). Its potential will be demonstrated for Egypt and Spain in Chapter 8.

The slope of the (T_0, r_0) datapoints depicted in Figure 6.11B was predicted by the physical laws of the EVADES model. The $\partial_{T_0} r_0$ slope can be explored to determine an area-effective resistance r_{ah}^{dry} . Namely coupling of the radiation and energy balance yields:

$$K^\downarrow - r_0 K^\downarrow + L^* = G_0 + H + \lambda E \quad (\text{W m}^{-2}) \quad (6.16)$$

which after expressing in r_0 gives:

$$r_0 = \frac{1}{K^\downarrow} (K^\downarrow + L^* - G_0 - H - \lambda E) \quad (-) \quad (6.17)$$

Differentiation of Eq. (6.17) with respect to T_0 gives the coupling between the slope of the $T_0(r_0)$ relationship and how surface flux density changes at regional scale with surface temperature (Bastiaanssen, 1991):

$$\partial_{T_0} r_0 = \frac{1}{K^\downarrow} (\partial_{T_0} L^* - \partial_{T_0} G_0 - \partial_{T_0} H - \partial_{T_0} \lambda E) \quad (\text{K}^{-1}) \quad (6.18)$$

The hyperbolic trend of the $T_0(r_0)$ relationship noticed in Figure 6.11B can now be physically interpreted from Eq. (6.18) because $\partial_{T_0} r_0$ varies with the first derivatives of the surface flux densities. Although the magnitude of $\partial_{T_0} L^*$, $\partial_{T_0} G_0$, $\partial_{T_0} H$ and $\partial_{T_0} \lambda E$ change with land wetness, land cover and land use, their signs are fixed. The value for $\partial_{T_0} r_0$ remains positive as long as:

$$|\partial_{T_0} L^* - \partial_{T_0} G_0 - \partial_{T_0} H| > |\partial_{T_0} \lambda E| \quad (\text{W m}^{-2} \text{K}^{-1}) \quad (6.19)$$

Because $\partial_{T_0} r_0$ is positive at wet and negative at dry surfaces, $|\partial_{T_0} \lambda E|$ at wet surfaces must be relatively small. Because $\partial_{T_0} r_0$ is mainly governed by $\partial_{T_0} \lambda E$, the positive slope between r_0 and T_0 is referred to as the 'evaporation controlled branch' of the $T_0(r_0)$ relationship. The negative $\partial_{T_0} r_0$ slope can be referred to as the 'radiation controlled branch' of the $T_0(r_0)$ relationship because the decrement of $Q^* - G_0$ for a fixed interval δr_0 (which forces T_0 to fall at constant λE) is stronger than the decrement of λE (which forces T_0 to rise at constant $Q^* - G_0$). The value for $|\partial_{T_0} \lambda E|$ can be illustrated by means of Figure 6.12 being based on the data shown in Figure 6.11B. Figure 6.11 has shown

that a negative slope of $\partial_{T_0} r_0$ arises at approximately $T_0 = 45^\circ\text{C}$ which implies that $|\partial_{T_0} \lambda E|$ is larger than the left hand side of Eq. (6.19). According to Figure 6.12, $|\partial_{T_0} \lambda E| \neq 0$ at $T_0 = 45^\circ\text{C}$ and has a fairly constant slope until $\lambda E = 0$. Consequently $\partial_{T_0} \lambda E = 0$ if evaporation is eliminated, i.e. $\lambda E = 0$. Since Figure 6.12 demonstrates that $\partial_{T_0} \lambda E$ is not necessarily zero at T_0^{max} , T_0^{max} is not a perfect determinant for allocating dry land surfaces. Additional insights can be gained from Figure 6.11D, which shows that Δ decreases at increasing reflectance r_0 . Hence, $\partial_{T_0} \lambda E \approx 0$ occurs from elements with a high temperature **and** a high hemispherical surface reflectance. The surface reflectance at which $\partial_{T_0} \lambda E \approx 0$ holds true, can be mathematically found as the reflectance to which the negative linearized slope between T_0 and r_0 is associated. At this negative 'radiation-controlled branch', Eq. (6.18) turns into:

$$\partial_{T_0} r_0 = \frac{1}{K^{\downarrow}} (\partial_{T_0} L^* - \partial_{T_0} G_0 - \partial_{T_0} H) \quad (\text{K}^{-1}) \quad (6.20)$$

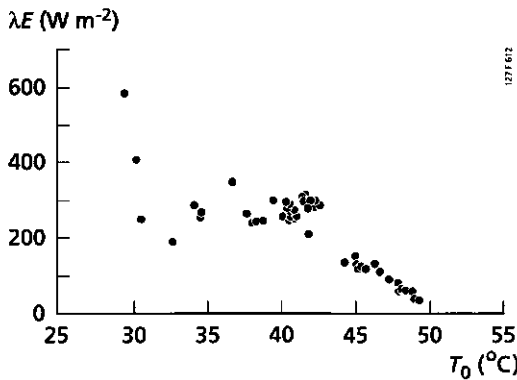


Fig. 6.12 Areal pattern of latent heat flux density, λE as a function of surface temperature, T_0 based on run I to VI depicted in Figure 6.11

The vantage point of Eq. (6.20) is that $\partial_{T_0} H$ can be approximated from the relative easily measurable parameters r_0 and T_0 (if a negative slope between r_0 and T_0 is observed). Solutions for $\partial_{T_0} G_0$ and $\partial_{T_0} L^*$ are simple and will be addressed in Chapter 7. As a first approximation, we may consider:

$$\partial_{T_0} H \approx \frac{\rho_a C_p}{r_{ah}^{dry}} \quad (\text{W m}^{-2} \text{ K}^{-1}) \quad (6.21)$$

which enables us to assess the areal effective aerodynamic resistance r_{ah}^{dry} for dry land surface elements fulfilling the condition $\partial_{T_0} \lambda E \approx 0$. The method proposed to obtain r_{ah}^{dry} was validated from a few patches in the Qattara Depression using local $\partial_{T_0} r_0$ observations at pockets of dry soil whereafter Eq (6.21) was inferred to quantify r_{ah}^{dry} . Together with local measurements of Q^* , G_0 , T_0 and T_a , H was calculated using r_{ah}^{dry} . After calculating λE as the balance residue, a comparison with λE -values obtained with the Bowen-ratio surface energy balance method was made. As shown in Figure 6.13, the agreement is quite good and the deviations are within the error range of obtaining λE by means of the Bowen-ratio surface energy balance technique (being approximately 20 to 30%, Sinclair et al., 1975).

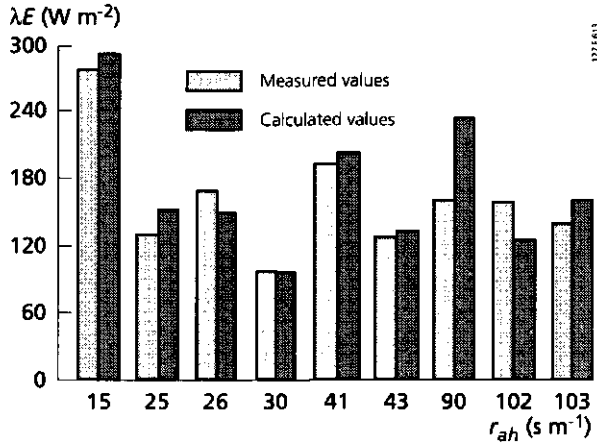


Fig. 6.13 Comparison of actual evaporation in units of latent heat flux density λE estimated with Eq. (6.21) and with the Bowen-ratio surface energy balance method for various values of the aerodynamic resistance, r_{ah} , at Bir Qifar, Qattara Depression

6.5.2 Experimental evidence of regional $T_0(r_0)$ relationships

Remote sensing research in the last decade has shown that the $T_0(r_0)$ relationship is not just an occasional feature for sebkha soils in arid regions. Table 6.8 demonstrates that the dual $T_0(r_0)$ branches were measured on various scales and for various land

surface types. The r_0 -values at T_0^{max} are also included in Table 6.8 and range between 0.20 to 0.33. Note that these values are not equal to r_0^{thresh} .

A Thematic Mapper image acquired on 7 August, 1986 at the Eastern Qattara Depression on 9^{5h} local time will be discussed to explain the $T_0(r_0)$ relationship measured from space. Colour Plate 1 shows r_0 while Colour Plate 2 provides the corresponding areal T_0 -patterns. The diversity in surface hydrological conditions, encompassing wet sebkhas and deserts, generates a wide range of (T_0, r_0) values. The dry areas (sand dunes and limestone plateaux; groundwater is deep) outside the depression in the direction of the South, contain the warmest spots with $T_0 = 312$ to 320 K and $r_0 = 0.22$ to 0.30. The coldest land surface elements are inside the depression where $r_0 = 0.10$ and $T_0 = 302$ K being marked as marshlands.

A fitting function through the (T_0, r_0) -pixel values of Colour Plates 1 and 2 has been drawn to describe the overall $T_0(r_0)$ behaviour (Menenti and Bastiaanssen, 1993). The positive slope between T_0 and r_0 applies for $r_0 < 0.24$ (see Figure 6.14A). Pixels with $r_0 > 0.24$ belonging to the negative slope are located inside the eolian eroded ridges oriented in the Southwest direction. The linearized slope of the radiation controlled branch yielded $-0.019 K^{-1}$ which, according to the overall $T_0(r_0)$ function, occurs at $r_0^{thresh} = 0.276$. Pixels

Table 6.8 Overview of observed correlations between hemispherical surface reflectance r_0 and surface temperature T_0

Source	Country	Total area (km ²)	Resolution (m)	Positive $\partial r_0 / \partial T_0$	Negative $\partial r_0 / \partial T_0$	$r_0(T_0^{max})$
Menenti (1984)	Libya	2 10 ⁴	500	yes	yes	0.33
Goward et al. (1985)	USA	4 10 ²	500	no	yes	0.30
Gebhardt (1986)	Germany	5 10 ³	20	no	yes	-
Vukovich (1987)	Senegal	6 10 ²	1000	yes	no	-
Seguin et al. (1989)	Senegal	1 10 ⁶	1000	yes	yes	0.30
Menenti et al. (1989a)	Egypt	1 10 ¹	5	yes	yes	0.23
Cure et al. (1989)	USA	1 10 ⁰	1	yes	yes	0.33
Smith and Choudhury (1990a)	USA	5 10 ²	1000	yes	no	-
Rosema and Fiselier (1990)	Mali	5 10 ³	5000	yes	yes	-
Bastiaanssen (1991)	Egypt	8 10 ³	120	yes	yes	0.31
Pelgrum (1992)	Egypt	4 10 ⁵	6000	yes	yes	0.2-0.25
Wal, van der (1992)	Egypt	8 10 ³	120	yes	yes	0.33
Bastiaanssen et al. (1994a)	Spain	2 10 ²	20	yes	yes	0.28
Bastiaanssen et al. (1994a)	Spain	2 10 ²	20	no	yes	0.20
Roerink (1994)	Argentina	3 10 ³	120	yes	yes	0.21
Wang et al. (1995)	China	1 10 ⁴	120	yes	yes	0.24
Roerink (1995)	Niger	1 10 ⁴	120	yes	yes	0.29

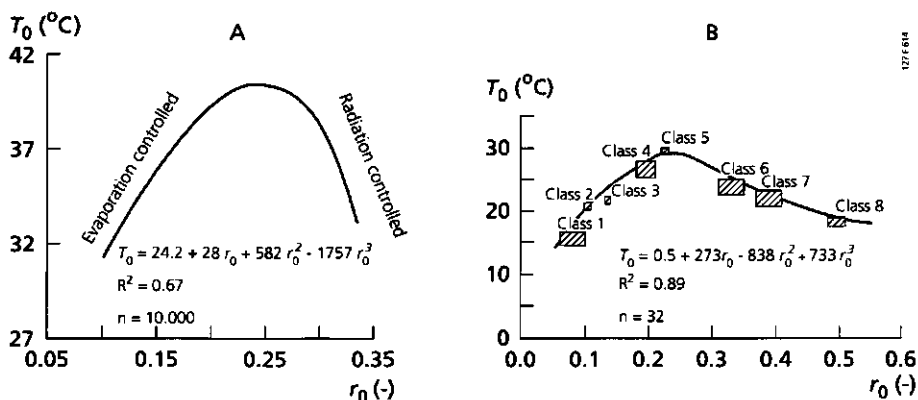


Fig. 6.14 Observed relationships between instantaneous surface temperatures, T_0 , and hemispherical surface reflectances, r_0 , derived from Thematic Mapper measurements. (Part A) Eastern Qattara Depression (path/row 178/39 acquired on 7 August, 1986), (Part B) Western Qattara Depression, (path/row 179/39 acquired on 13 November, 1987)

with $r_0 > 0.276$ are situated in the desert where $\partial_{T_0} \lambda E \approx 0$ and $\lambda E = 0$ are acceptable conditions confirming the proposed procedure to allocate pixels with $\partial_{T_0} \lambda E = 0$ from remote sensing determinants.

The pixels situated in sub-grid 13, 14 and 15 at the bottom of the Colour Plates 1 and 2 gave three different sets of (T_0, r_0) . Eqs. (6.20) and (6.21) were applied to determine the linearized slope $\partial_{T_0} r_0$ of each set and relate it to r_{ah}^{dry} (Table 6.10). Eq. (6.22) has been applied to explain the differences in r_{ah}^{dry} found from $\partial_{T_0} r_0$. For the sake of simplicity, Eq. (6.22) does not consider ψ_h or ψ_m -corrections and is just meant to demonstrate the physical significance of $\partial_{T_0} r_0$ and how that relates to r_{ah}^{dry} . A value of $kB^{-1} = 2.3$ has been applied. The presence of dune ridges in sub-grid 15 explains the lowest r_{ah}^{dry} -values noticed as being caused by enhanced surface roughness (see Colour Plates 1 and 2). Although, in the absence of meso scale field measurements, no evidence exists on the reliability of these regional effective r_{ah}^{dry} -values, the obtained trends between \tilde{z}_{0m} and the relief of sand dunes agrees with the expectations: Higher roughness coincides with a higher density of dune ridges.

$$r_{ah}^{dry} \approx \frac{1}{k^2 U_{100}} \ln\left(\frac{100}{\tilde{z}_{0h}}\right) \ln\left(\frac{100}{\tilde{z}_{0m}}\right) \quad (\text{s m}^{-1}) \quad (6.22)$$

A classification was carried out for a different Thematic Mapper scene in the Western Part of the Qattara Depression near Qara oasis using T_0 and r_0 as attributes. A number of eight land clusters were discriminated, with five clusters appearing on the positive $T_0(r_0)$ branch and three clusters on the negative $T_0(r_0)$ branch. Figure 6.14B shows the standard deviations of T_0 and r_0 for each land cluster identified. According to a photo-

Table 6.10 Aerodynamic behaviour of desert surfaces with different roughnesses as interpreted from surface albedo and surface temperature measurements on August 5, 1986 (See Colour Plates 1 and 2)

Sub-grid Colour Plates 1,2	$\partial_{T_0} r_0$ (K ⁻¹)	r_{ah}^{dry} (s m ⁻¹)	U_{100} (m s ⁻¹)	z_{om} (m)
13	-0.0266	70	10	0.0045
14	-0.0272	68	10	0.0050
15	-0.0312	56	10	0.0170

geological-vegetation map of the area, the sub-grid areas reflect open water (Class 1), wet sebkha (Class 2), sebkha covered with rippled sand (Class 3), dry sebkha (Class 4) and sandy soft clay (Class 5). The dry land area composes of Qifar sand formation (Class 6), Moghra limestone formation (Class 7) and gravel plain (Class 8). Pixels with $r_0 > 0.24$ represent negative $\partial_{T_0} r_0$ -values. The linearized slope is remarkably close to the Eastern Qattara, $\partial_{T_0} r_0 = -0.053 \text{ K}^{-1}$. The open water evaporation at Class 1 can be assumed to take place at the maximum rate, i.e. $\Lambda \approx 1.0$. The sebkhas of class 2 to 5 have a reduced evaporation rate in comparison to open water. Classes 6,7 and 8 are dry desert surfaces fulfilling $\partial_{T_0} \lambda E = 0$. The treshhold reflectance where $r_0^{tresh} = 0.268$ applies is suitable for distinguishing sub-areas with $\partial_{T_0} \lambda E = 0$, $\lambda E = 0$ and $\Lambda = 0$ from the remaining sub-areas.

In conclusion we can state that the $T_0(r_0)$ relationship provides a unique opportunity without further ground information to extract the following information:

- the allocation of wet ($\Lambda \approx 1$) and dry ($\Lambda \approx 0$) land surface elements without having access to additional field information (if the area has sufficient hydrological contrast);
- the threshold hemispherical surface reflectance r_0^{tresh} above which $\partial_{T_0} \lambda E = 0$ applies;
- the first derivative of sensible heat flux density versus temperature, $\partial_{T_0} H$ for deriving r_{ah}^{dry} which is an area-effective value;

It will be shown in Chapter 7 how these aspects are merged in SEBAL to derive area-effective momentum flux densities and land surface energy balances with a minimum of ground data.

6.6 Near-surface vertical air temperature differences vs. surface temperature: $\delta T_{a-sur}(T_0)$ relationship

The main difficulty in determining surface energy budgets from satellite based K^\uparrow and L^\uparrow measurements, is a proper estimation of the energy partitioning between H and λE . Chapters 2 and 3 have shown that the number of parameters affecting r_{ah} in one-layer

schemes is less than r_s , and it is for this reason preferred to solve λE after having estimated H .

Sensible heat flux density is traditionally estimated by inferring $T_{z_{0h}}$ from remote sensing data (assuming $T_{z_{0h}} = T_0$, after adjusting kB^1), T_a and u obtained from synoptic measurements and the surface roughnesses z_{0m} and z_{0h} based on vegetation heights and/or land cover type (see Choudhury, 1989 for a review). The evidence that $T_{z_{0h}}$ can be treated as T_0 was given in Section 3.3. The basic question which remains is:

How can the regional distribution of T_a -data be determined in the absence or incompleteness of synoptic stations ?

Approach

Derivation of T_a patterns from satellite thermal infrared data was carried out by Chen et al. (1983) who investigated the capability of geostationary GOES thermal infrared data to infer T_a . A value of $R^2 = 0.76$ was found by linear regressing T_0 vs. 1.5 meter high shelter T_a -values. The standard deviation from the regression line was 1.3-2.0°C. Davis and Tarpley (1983) reported from NOAA temperature data also a standard linear trend between T_0 and T_a over a large area of North America with standard deviations of 1.6-2.6 K. Horiguchi et al. (1992) did a regression analysis between clusters of 1.5 meter height T_a -values gathered from a meteorological observation network and T_0 obtained from geostationary thermal infrared data. Their work brought forward that the error on deriving T_a is $\approx 1-1.7$ K.

Linear fitting between T_0 and T_a for a number of land surface elements i yields a constant offset. The offset of a regional $T_a(T_0)$ relationship theoretically implies that $c_9 \approx 1$ and $c_{10} \approx \delta \tilde{T}_{a-sur}$:

$$T_{a-i} = c_9 T_{0-i} - c_{10} \quad (^\circ\text{C}) \quad (6.23)$$

where i represents a particular land surface element. The linearity between T_{0-i} and T_{a-i} posed in Eq. (6.23) may however not be generally applied because δT_{a-sur} is not constant. For instance, Otle et al., 1989 showed that δT_{a-sur} changes because of crop stress, which basically contradicts a linear $T_0(T_a)$ relationship such as presented at Eq.(6.23). Although T_{a-i} is certainly not constant, the dynamic range of T_{a-i} is reduced compared to the areal variability of δT_{a-sur} . It is therefore preferred to consider δT_{a-sur} instead of T_{a-i} :

$$\delta T_{a-sur-i} = T_{0-i} - \tilde{T}_a \quad (^\circ\text{C}) \quad (6.24)$$

For a set of land surface elements, the following perturbation equation can be tentatively proposed:

$$\delta T_{a-sur-i} = c_{11} T_{0-i} - c_{12} \quad (^{\circ}C) \quad (6.25)$$

where c_{11} and c_{12} are the linear regression coefficients. The perturbation method is applied to tentatively derive an expression similar to Eq. (6.24), but using an unknown offset c_{12} and slope c_{11} . Perturbations from Eq. (6.24) are small if $c_{11} \approx 1.0$ and $c_{12} \approx \tilde{T}_a$. When c_{11} deviates from 1.0, \tilde{T}_a can be more generally calculated from c_{11} and c_{12} :

$$\tilde{T}_a = (1 - c_{11}) \tilde{T}_0 + c_{12} \quad (^{\circ}C) \quad (6.26)$$

Table 6.11 *Field observations performed during HAPEX-SAHEL in Niger at the Central West Supersite to prove the suggested linearity between near-surface vertical air temperature difference, δT_{a-sur} and surface temperature, T_0 at Eq. (6.25).*

Day	Location	Hour	n	R ² ([∘] C)	Intercept c_9 ([∘] C [∘] C ⁻¹)	Slope c_{10} ([∘] C)	$T_0(\delta T_{a-sur} = 0)$
03/09/93	Degraded bush	9 ⁰⁰	5	0.93	33.9	1.24	27.3
		10 ⁰⁰	5	0.94	27.6	0.98	28.2
		11 ⁰⁰	5	0.98	30.3	1.01	30.0
		12 ⁰⁰	5	0.98	27.4	0.91	30.1
		13 ⁰⁰	5	0.98	29.8	0.95	31.3
05/09/93	Fallow bush/ grassland	9 ⁰⁰	4	0.89	30.4	1.08	28.1
		10 ⁰⁰	4	0.98	28.3	0.99	28.6
		11 ⁰⁰	4	0.99	30.4	1.01	30.1
		12 ⁰⁰	4	0.99	31.4	0.99	31.7
		13 ⁰⁰	4	0.98	34.9	1.04	33.6
		14 ⁰⁰	4	0.95	38.2	1.09	35.0
		15 ⁰⁰	4	0.99	40.9	1.14	35.9
08/09/93	Fallow bush/ grassland	9 ⁰⁰	5	0.97	43.0	1.45	29.7
		10 ⁰⁰	5	0.97	32.7	1.08	30.3
		11 ⁰⁰	5	0.98	28.4	0.92	30.9
		12 ⁰⁰	5	0.99	28.5	0.89	32.0
		13 ⁰⁰	5	0.99	30.7	0.93	33.0
		14 ⁰⁰	5	0.99	33.0	0.98	33.7
		15 ⁰⁰	5	0.99	33.4	0.98	34.1
		16 ⁰⁰	5	0.98	35.6	0.98	36.3

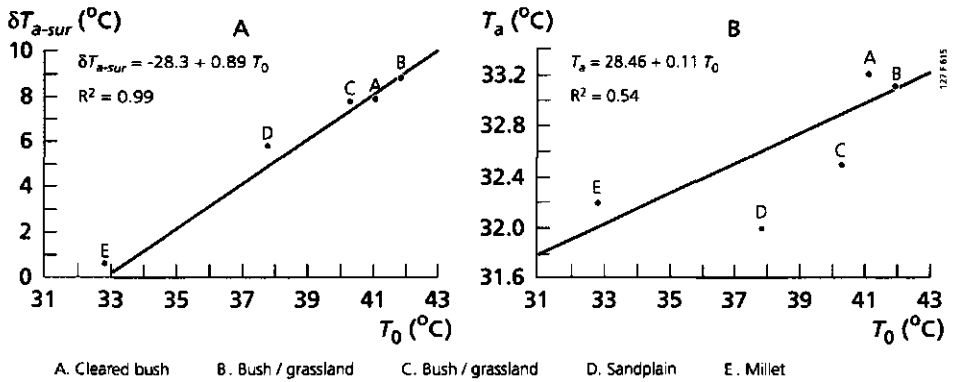


Fig. 6.15 Linearity of air temperature T_a , vertical air temperature differences δT_{a-sur} and surface temperature T_0 measured at the West Central super site during HAPEX SAHEL, September 1992, (Part A) $\delta T_{a-sur}(T_0)$ relationship, (Part B) $T_a(T_0)$ relationship

A deeper investigation of the shape of the $\delta T_{a-sur}(T_0)$ relationship is required to check the generality of Eq. (6.25). In the next section, an attempt will be initiated to study c_{11} and c_{12} in composite terrain using in-situ observations of T_{0-i} and $\delta T_{a-sur-r}$. Data collected in Niger, Egypt and China has been used.

Niger

During the Special Observation Period of HAPEX-SAHEL, T_{a-i} was recorded at 3 m. elevation at several sites. The surface temperature T_{0-i} was measured with a handheld thermal infrared radiometer operating in the 8 to 14 μm spectral region and the radiation temperature T_{0-i}^R has been corrected for emissivity. $\delta T_{a-sur-i}$ was calculated as the difference in T_{0-i} and T_{a-i} . The four to five land units were located on a 2 km transect and were specified in Table 6.6. The results are presented in Table 6.11. The correlation coefficient is unexpectedly high for *all* readings. The graph presented in Figure 6.15A indicate $\delta T_{a-sur}(T_0)$ to be basically linear. The regression coefficients were rather similar with a mean intercept being $c_{12} = 32.7^{\circ}\text{C}$ and a mean slope of $c_{11} = 0.98^{\circ}\text{C}^{\circ}\text{C}^{-1}$. Hence, the slope is indeed very close to one which proves the correctness of Eq. (6.25) and $c_{12} \approx \bar{T}_a$.

The $\delta T_{a-sur}(T_0)$ relationship in Figure 6.15A shows more coherence than the $T_a(T_0)$ relationship of Figure 6.15B. The $\delta T_{a-sur}(T_0)$ curve fitting also provides the opportunity to allocate sub-areas where advection entrainment occurs ($T_{a-sur} > T_0$; $H < 0$). These temperature values have been added in the far right-hand column of Table 6.9. This trigger value of surface temperature for stable conditions ($\delta T_{a-sur} < 0$) has a diurnal pattern and ranges between 27 to 36 $^{\circ}\text{C}$.

Egypt

During the 5th Qattara Depression field expedition, three ($\delta T_{a-sur}(T_0)$) parallel pairs were measured continuously with a 5' sampling interval. The observation height for T_{a-i} was 200 cm. Figure 6.16 depict the R^2 values between δT_{a-sur} and T_0 for days with observations between 9⁰⁰ and 18⁰⁰ hours.

The offset in the $\delta T_{a-sur}(T_0)$ function shows a diurnal pattern (Figure 6.17B) whereas the shape is fairly constant at $c_{11} \approx 1.0$. The diurnal variation of c_{12} has a trend that is similar to $T_a(t)$ with warming up in the morning and a plateau in the afternoon. It can be concluded that c_{12} is broadly speaking constant with time when strong heat releases from the land surface occur and the PBL grows. The sudden decrease of $c_{12} \approx 35^\circ\text{C}$ at 20⁰⁰ hours to $c_{12} \approx 20^\circ\text{C}$ at 21⁰⁰ hours is most probably associated with the inversion of the $T_p(z)$ profiles. The average slope for the wet saline sebkhas in the Qattara Depression is $c_{11} = 1.09 \text{ K K}^{-1}$ and the intercept of $c_{12} = 37.1^\circ\text{C}$. Figure 6.18 shows the mean slopes and offsets for the days investigated. Although the correlation coefficient was high, it seems that c_{11} exhibits fluctuations: on September 17, the average gain plus the standard deviation is almost 1.4 which implies that $c_{12} \neq \tilde{T}_a$.

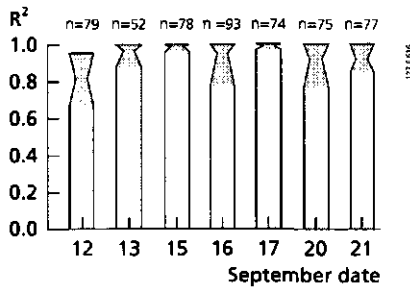


Fig. 6.16 Mean daytime R^2 of near-surface vertical air temperature differences, δT_{a-sur} vs. surface temperature, T_0 , measured at sebkhas in the Qattara Depression, September 1989. The standard deviation of the average R^2 is indicated

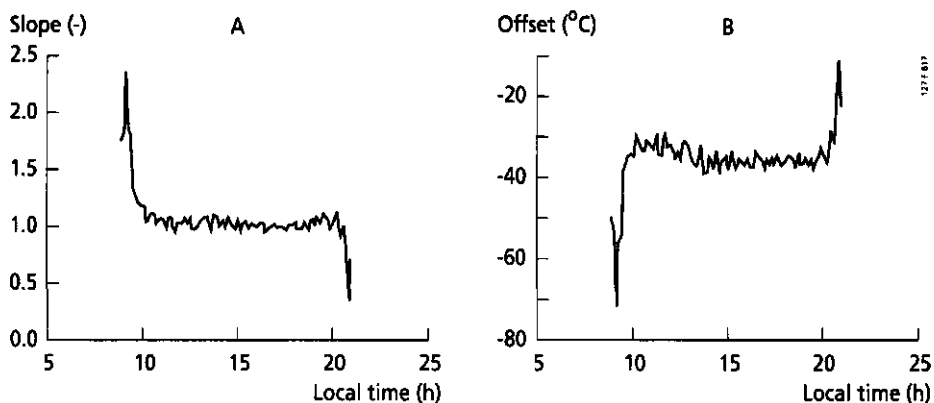


Fig. 6.17 (Part A) Diurnal variation of the slope c_{11} in the linear relationship between near-surface vertical air temperature differences δT_{a-sur} and surface temperature T_0 , (Part B) Offset c_{12} of the same relationship based on field measurements on 15 September, 1989, Qattara Depression

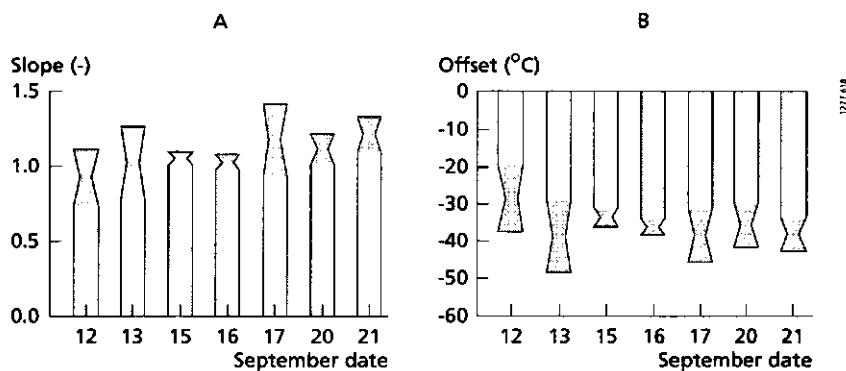


Fig. 6.18 Average and standard deviations of slopes and offsets during daytime at the sebkhias in the Quattara Depression, September 1989

China

Data from the HEIFE experiment in Central China (Wang et al., 1994a) has been considered to analyse the $\delta T_{a-sur}(T_0)$ relationship for landscapes where extremes in physiography and hydrology exists. The study area encompasses the Gobi desert,

irrigated oases near the towns of Zhan Ye and Linzhe and mountainous hillslopes (lat 39°N, long. 101°E). The distance between the most far away measurement points was approximately 50 km. Figure 6.18 shows the observed $\delta T_{a-sur}(T_0)$ trends at 11⁰⁰ hours local time for T_0 , T_a and δT_{a-sur} . At this time, the lowest air temperature was $T_a = 26^\circ\text{C}$ while at the hot spots a temperature of 31°C at the same elevation above the land surface was already measured. The $T_a(T_0)$ relationship depicted in Figure 6.18A expresses much scatter with significant standard deviations from the regression line. On the contrary, the $\delta T_{a-sur}(T_0)$ trend of Figure 6B has a much reduced scatter. The expected linear trend for the δT_{a-sur} relationship was confirmed for the arid conditions of the HeiHe basin for several days with an average slope of $c_{11} = 0.97^\circ\text{C } ^\circ\text{C}^{-1}$ and an average offset of $c_{12} = 27.8^\circ\text{C}$.

The experimental evidence of the $\delta T_{a-sur}(T_0)$ relationship can be summarized in the following conclusions:

- The linear $\delta T_{a-sur}(T_0)$ hypothesis for heterogeneous terrain conditions has been experimentally proved and the perturbations from Eq. (6.25) are small, which means that the slope lies close to one (Niger 0.98, Egypt 1.09, China 0.97) and the offset equals approximately the area-effective air temperature;
- δT_{a-sur} can be spatially interpolated using a T_0 -image if c_{11} and c_{12} for that particular image and moment of acquisition are determined. If T_0 can be accurately interpreted from remote radiances, this implies that T_a may be mapped for composite terrain;
- The areal effective air temperature \bar{T}_a at observation height can be found from the $\delta T_{a-sur}(T_0)$ relationship using the general form of Eq. (6.26);

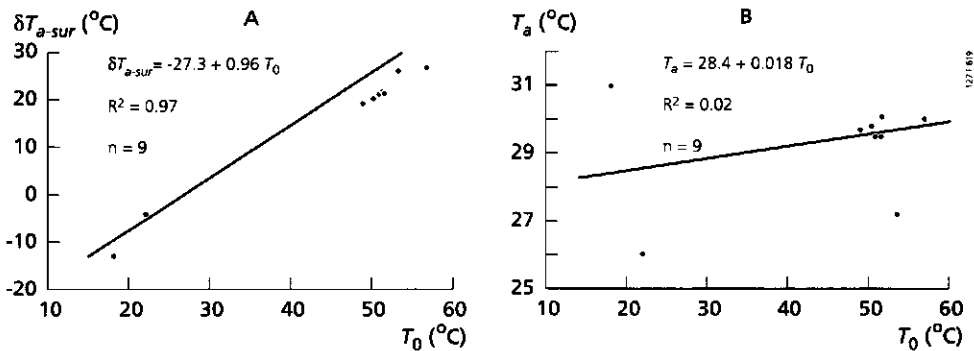


Fig. 6.19 Observed behaviour of near-surface vertical air temperature differences, δT_{a-sur} and surface temperature, T_0 , in the HeiHe basin with distinct land surface types such as desert, oases and mountains along a 50 km transect, 9 July, 1991. (Part A) $\delta T_{a-sur}(T_0)$ relationship and (Part B) $T_a(T_0)$ relationship

The similar magnitudes of $T_0(\delta T_{a-sur} = 0)$ in Niger (33.4 °C), the Qattara Depression ($T_0(\delta T_{a-sur} = 0) = 34^\circ\text{C}$) and a somewhat lower value of the HeiHe basin ($T_0(\delta T_{a-sur} = 0) = 27.8^\circ\text{C}$) can be tested with the Priestley and Taylor's equation. The condition of $\delta T_{a-sur} \approx 0$ above wet land surfaces according to λE_p^{PT} can be theoretically calculated for $\alpha = 1.26$ from:

$$\lambda E_p^{PT} = Q^* - G_0 \quad (H=0) \quad (\text{W m}^{-2}) \quad (6.27)$$

or

$$Q^* - G_0 = 1.26(Q^* - G_0) \frac{s_a}{s_a + \gamma} \quad (\text{W m}^{-2}) \quad (6.28)$$

The solution for Eq. (6.28) is $s_a = 2.57 \text{ mbar K}^{-1}$ which corresponds to a temperature of $T_a = 31^\circ$. Note that $T_a = 31^\circ\text{C}$ agrees perfectly well with the T_0 -range between $T_0 = 27\text{-}36^\circ\text{C}$ derived from the slope of the $\delta T_{a-sur}(T_0)$ descriptive functions. Hence, an upperbound for the air temperature above wet land surfaces in arid regions is estimated and vertical advection emerges if the surface temperature is lower as being controlled by evaporation.

6.7 Concluding remarks

The following simplified relationships were derived and/or experimentally tested before using them into the SEBAL procedure:

- r_0 (r_p) relationship;
- T_0 (T_{sat}) relationship;
- Γ (r_0, T_0, NDVI) relationship;
- T_0 (r_0) relationship;
- δT_{a-sur} (T_0) relationship;

The experimental evidence of these relationships indicate something important: *variability due to complex physical processes can average out to simple relationships.*

Net radiation flux density

An accurate determination of r_0 from r_p does not require radiosoundings if the image is acquired under clear skies with a relatively low level of diffuse radiation. At best, a series of r_0 -values from dark and bright targets should be made available from in-situ observations at several 'homogeneous' land surface targets, whereafter a (non-) linear

$r_p \rightarrow r_0$ transformation can be established. Instead of r_0 -observations, field measurements on τ_{sw} can also be used since τ_{sw} is a suitable basis for obtaining the two-way transmittance τ_{sw}'' to solve the $r_0(r_p)$ relationship. To ensure realistic land surface temperatures, it is preferred to perform a similar procedure for T_0 : A linear regression analysis between spectral radiance at the top of the atmosphere and at the land surface is proposed and has been indicated to perform well.

Soil heat flux density

It was shown that Γ can be separated into a proportionality factor Γ' and an extinction factor Γ'' and that remote sensing data can be used to determine Γ' and Γ'' separately. Although *NDVI* is a suitable parameter for areally recognizing attenuation effects, *NDVI* is not suitable for predicting Γ over sparse canopies and vast terrains with variation in Γ' . Moreover, soil heat storage effects on the $\Gamma(\hat{t})$ relationship are more essential in partial canopies, which needs ample attention when images with different acquisition times are applied. A new solution was designed which describes Γ under sparse canopies empirically both in space and time, thereby opening the way to applications with low and high resolution operational satellite systems from which diurnal variations in G_0 for large areas can be assessed.

Sensible heat flux density

The key-issue in evaporation estimations with remote sensing data is an adequate description of sensible heat flux density. Kustas et al. (1994b) concluded that for remote sensing studies, the utility of *H*-mapping is limited by the spatial extrapolation of synoptic T_a and u observations. The problem of u is solved by considering the areal patterns of u . instead and r_{ah}^{dry} will be used for that (Chap. 7). The coherence between r_0 and T_0 over composite terrain was explained by field observations in Qattara Depression and a sound physical interpretation could be given by means of the EVADES model. It was shown that the radiation-controlled branch of the $T_0(r_0)$ function provides important information from which pixels with $\partial_{\tau_0} \lambda E \approx 0$ can be extracted. A zero slope of the first derivative of λE may be associated to $\lambda E = 0$. Pairs of T_0 and r_0 are therefore suitable for rapidly distinguishing between dry and wet zones. Areas with $r_0 < 0.10$ and assigned to low T_0 -values showed evaporative fractions in the range $\Lambda \approx 1.0$. Areas with $r_0 > 0.30$ assigned to high T_0 -values showed $\Lambda \approx 0$. It was concluded that T_0, r_0 over dry land surface elements can be used to establish an area-effective aerodynamic resistance r_{ah}^{dry} and that T_0, r_0 measurements of undulating terrain in the Western Desert of Egypt agrees theoretically with variations in surface roughness.

One other serious concern in *H*-mapping is the large horizontal variability of near-surface air temperature. Strictly speaking, δT_{a-sur} should be estimated for *H* rather than T_a . Considering the large total number of regression analyses of individual $\delta T_{a-sur}(T_0)$ data pairs (Niger: 21, Egypt: 528, China: 9), the conclusion arises that the $\delta T_{a-sur}(T_0)$ curves are linear and more universal than expected. Hence, δT_{a-sur} can be regionally interpolated in a simple manner from T_0 using linear transformations with an effective slope and offset

for heterogeneous environments. The differences of $\delta T_{a-sur} = T_0 - T_{a-sur}$ from the $\delta T_{a-sur} = c_{11} T_0 - c_{12}$ linear regression model were found to be small in composite terrain which justifies retrieving the areal average \tilde{T}_a from the fitted offset. If δT_{a-sur} will be derived from the inversion of H at specific elements where $\Lambda \approx 0$ and $\Lambda \approx 1$ applies, the need for T_a synoptic data will be eliminated. This approach will hereafter be referred to as the 'evaporative fraction-vertical air temperature difference' method.

The correctness of the $T_{sat} \rightarrow T_0^R$, $T_0^R \rightarrow T_0$ conversions using atmospheric and emissivity corrections and the $T_0 = T_{20h}$ assumption by adjusting kB^1 becomes to a certain extent irrelevant because the physical limits of H are internally calibrated by adjusting δT_{a-sur} in an inverse manner at pixels with a predefined Λ value. This is a step forward because the absolute T_0 value is not longer explicitly needed which implies that kB^1 doesn't need to be spatially interpreted for heterogenous land surfaces.

7 SEBAL parameterization for distributed land surface flux densities

7.1 General schematization

SEBAL solves the surface energy balance (Eq. 1.1) pixel-by-pixel and on an instantaneous time basis. Net radiation is obtained from distributed hemispherical surface reflectance and surface radiation temperature data in combination with spatially variable zenith angles for the determination of the clear sky incoming shortwave solar radiation. The incoming longwave radiation is held areally constant. Soil heat flux density is obtained from the new empirical soil heat /net radiation flux density fraction derived at Section 6.4. The area-effective momentum flux density is computed from the area-effective aerodynamic resistance for dry land surface elements using the slope between surface temperature and surface hemispherical reflectance (Section 6.5). The vertical near-surface air temperature difference is coupled linearly to surface temperature (Section 6.6). The vertical difference between two horizontal layers of different air temperature is obtained by an inversion of the equation for sensible heat transfer at specific partial areas corresponding with two extreme conditions: One where $H \approx 0$ (wet) and one where $\lambda E \approx 0$ (dry). These partial areas can be allocated by means of the $T_o(r_o)$ relationship. The momentum and sensible heat flux densities are based on the resistance version of the flux-profile relationships. For each pixel (which may encompass a mixture of landscape elements), a one-layer resistance scheme for τ and H will be applied (Section 3.3). Finally latent heat flux density is obtained as the residue of the land surface energy balance.

The land surface flux densities are calculated in a specific sequential order:

- Net radiation flux density, $Q^*(x,y)$ Section 7.3
- Soil heat flux density, $G_o(x,y)$ Section 7.4
- Momentum flux density, $\tau(x,y)$ Section 7.5
- Sensible heat flux density, $H(x,y)$ Section 7.6
- Latent heat flux density, $\lambda E(x,y)$ Section 7.7

The (x,y) notation denotes that a certain parameter is variable in the horizontal space domain with a resolution equal to the size of a pixel. If the (x,y) notation is not specifically mentioned, that particular parameter is taken spatially constant. Since SEBAL aims to solve local flux densities in order to make a comparison with in-situ flux densities and soil water content feasible, the height for z_{sur} will be kept small being approximately 10% of the pixel size (Eq. 3.40). Because horizontal advection of heat is not included in Eq. (1.1), the physical processes can only be realistically schematized to be strictly vertical

if and $z = z_{sur}$ is kept adjacent to the land surface (Figure 7.1). Blending of flux density profiles is schematized to begin at $z = z_{sur}$. At the blending height ($z = z_B$), horizontal flux densities have smoothed at-surface variability of wind speed, air potential temperature and humidity. Consequently, the flow domain between $z = z_{sur}$ and $z = z_B$ should have a two-dimensional character (Figure 7.1). The area-effective momentum flux density τ at height $z = z_B$ is taken as the momentum flux density from dry land surface elements, τ^{dry} so that $\tilde{\tau} \approx \tau^{dry}$. The momentum flux density τ should be disaggregated into local vertical momentum flux densities between height $z = z_{0m}$ and $z = z_{sur}$. After having achieved this (Section 7.5), vertical $H(x,y)$ flux densities will be calculated on the basis of $\tau(x,y)$, surface roughness $z_{0h}(x,y)$, aerodynamic resistance $r_{ah}(x,y)$ and $\delta T_{a-sur}(x,y)$ (Section 7.6).

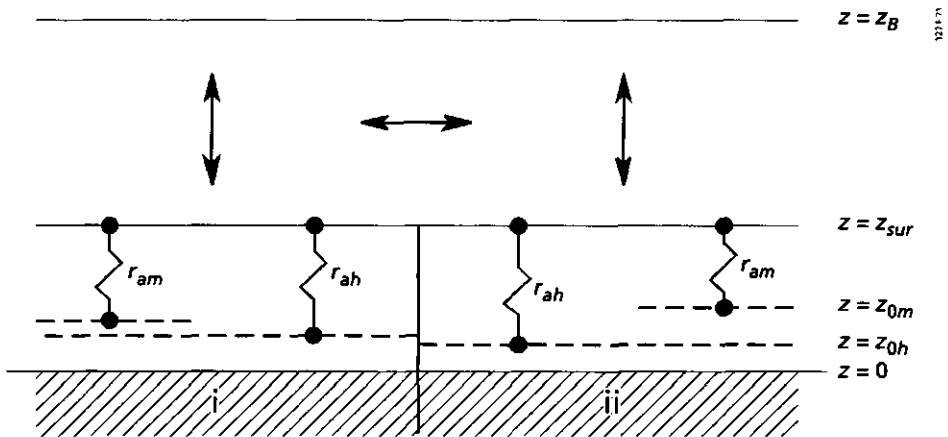


Fig. 7.1 SEBAL schematization of momentum, heat and vapour flow in the surface layer for two neighbouring pixels, *i* and *ii*

Table 7.1 summarizes SEBAL's calculation scheme. The right-hand side of Table 7.1 establishes the link to the data strings s_1 to s_{12} of all hydro-meteorological parameters listed in Table 6.1. The relationships investigated in-depth from Table 6.2 are indicated by their Section number.

The incorporation of the Monin-Obukhov similarity hypothesis makes the estimation of $H(x,y)$ and $\tau(x,y)$ more complex due to the implicit character of H and u , being included in L (see Eq. 2.68). Three iterative procedures therefore need to be worked out:

- Iteration I : regional $\tilde{\tau}$ flux density for \tilde{u} and \tilde{L}
- Iteration II : local $\tau(x,y)$ flux density for $u(x,y)$ in $L(x,y)$
- Iteration III : local $\tau(x,y)$ and $H(x,y)$ flux density for $u(x,y)$ and $H(x,y)$ in $L(x,y)$

Table 7.1 Summary of the SEBAL calculation scheme. The bold parameters in the column input data have to be made available from supplementary sources

Computation step and description	Equation	Variable/constant	Input data	String
Retrieval procedures				
1. Spectral radiances, $K_{TOA}^{\lambda}, L_{\lambda}^{TOA}$	7.1	x,y	DN	
2. Solar declination, δ	7.2	-	J	
3. Solar angle hour, ω_s	7.3	x	<i>t',long</i>	
4. Solar zenith angle, ϕ_{su}	7.5	x,y	δ, ω_s, lat	
5. Earth-sun distance, d_s	7.6	-	J	
6. In-band planetary reflectance, $r_p(b)$	7.7	x,y	$K_{TOA}^{\lambda}(b), d_s, K_{atm}^{\lambda}(b)$	
7. Planetary reflectance, r_p	7.9	x,y	$r_p(b), c(b)$	
8. Hemispherical surface reflectance, r_o	6.4	x,y	r_p, τ_{sw} or r_p	s ₁₁ , Section 6.2
9. Normalized Difference Vegetation Index, NDVI	7.10	x,y	$r_o(\lambda)$	
10. Shortwave clear sky transmittance, τ_{sw}	7.11	-	r_p, τ_{sw} or r_o	
11. Apparent emissivity, ϵ_2'	7.14	-	τ_{sw}^{avg}	
12. Incoming longwave radiation, L^{\downarrow}	7.15	-	ϵ_2', T_a^*	S ₂
13. Thermal infrared surface emissivity, ϵ_o	7.16	x,y	NDVI	S ₃
14. Surface temperature, T_o	7.19	x,y	$\tau_{\lambda}(b), L_{atm}^{\downarrow}(b)$ or $T_o, L_{\lambda}^{TOA}(b)$	S ₄ , Section 6.3
Net radiation flux density				
15. Incoming global radiation, K^{\downarrow}	7.20	x,y	$\tau_{sw}, K_{TOA}^{\lambda}$	S ₅
16. Outgoing longwave radiation, L^{\uparrow}	7.21	-	ϵ_o, T_o	
17. Net radiation, Q^{\downarrow}	2.8	x,y	$r_o, K^{\downarrow}, L^{\downarrow}, L^{\uparrow}$	
Soil heat flux density				
18. Soil heat net radiation flux density ratio, Γ	6.14	x,y	$T_o, r_o, NDVI$	S _{61, S7} , Section 6.4
19. Soil heat flux density, G_o	7.22	x,y	Γ, Q^{\downarrow}	
Momentum flux density				
20. Roughness momentum, z_{om}	7.27	x,y	NDVI, <i>h_v</i>, LAI or z_{om}	S ₈
21. Roughness heat, z_{oh}	7.28	x,y	z_{om}, kB^{-1}	S ₉
22. Effective roughness heat, z_{oh}	7.31	-	z_{oh}, T_o, T_a	
23. Longwave radiation-temperature, $\partial L^{\downarrow} / \partial T_o$	7.36	-	ϵ_o^*, T_o^{*dy}	
24. Soil heat flux density-temperature, $\partial G_o / \partial T_o$	7.38	-	T_o, G_o	
25. Reflectance-temperature, $\partial r_o / \partial T_o$	7.41	-	T_o, r_o	Section 6.5
26. Aerodynamic resistance above dry land, r_{ah}^{*dy}	7.44	-	$\partial T_o / \partial T_a, \partial T_o / \partial z, \partial T_o / \partial G_o, \rho_a c_p$	
27. Sensible heat flux density above dry land, H^{*dy}	7.45	-	Q^{*dy}, G_o^{*dy}	
28. Effective Monin Obukhov length, L^{*dy}	7.46	-	$H^{*dy}, T_o^{*dy}, T_a^{*dy}, z_{oh}^{*dy}, r_{ah}^{*dy}, \partial T_o / \partial z$	
29. Effective wind speed, $u(z_{sur})$	7.49	-	Ψ_m, z_{om}, u	
30. Friction velocity, u	7.51	x,y	$u(z_{sur}), z_{om}, \Psi_m$	S ₁₀
31. Momentum flux density τ	7.53	x,y	u, ρ_a	
Sensible heat flux density				
32. Aerodynamic resistance, r_{ah-sur}	7.55	x,y	u, z_{oh}, Ψ_{h-sur}	
33. Surface to air temperature difference, δT_{a-sur}	7.58	x,y	$T_o, Q^{\downarrow}, G_o, r_{ah-sur}$	S ₁₁ , Section 6.6
34. Sensible heat flux density, H	7.59	x,y	$\delta T_{a-sur}, r_{ah-sur}, \rho_a c_p$	
35. Monin Obukhov length, L	7.60	x,y	u, T_o, H	S ₁₂
Latent heat flux density				
36. Latent heat flux density, λE	7.61	x,y	Q^{\downarrow}, G_o, H	

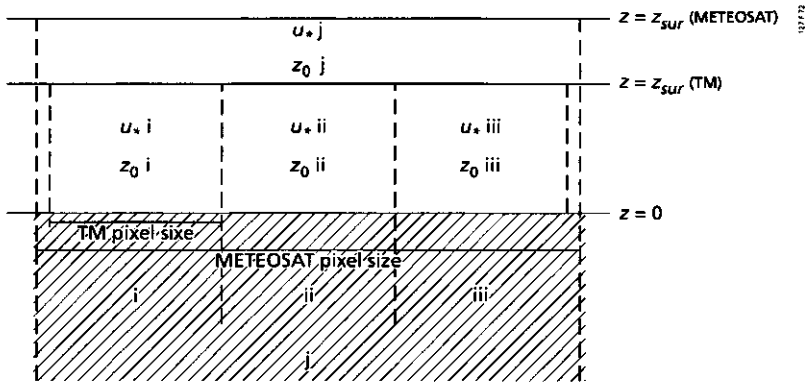


Fig. 7.2 Integration height for near-surface turbulent flux densities z_{sur} for pixels with different dimensions. Codes i to iii apply to Thematic Mapper and j to METEOSAT pixel resolutions

Iteration I applies to $\tilde{\tau}$ at $z = z_B$. Iteration II is necessary to let $u_*(x,y)$ imbedded in $\psi_m(x,y)$ equilibrate with $\tau(x,y)$ between $z=z_{0m}$ and $z=z_{sur}$. Iteration III establishes local $H(x,y)$ flux densities with $H(x,y)$ implicitly present in $\psi_h(x,y)$. A further explanation of these iterations will be given in the appropriate Sections.

According to the theory provided in Figure 3.8, z_{sur} can be pixel dependent. Since u_* is not known in advance, z_{sur} cannot be computed locally at the primary phase of the computation procedure so that z_{sur} should be initially kept similar for all pixels (Figure 7.2) and based on the minimum of all z_{sur} values considering a minimum u_* value and x as half a pixel size. The integration limit z_{sur} therefore differs for pixels with different dimensions.

7.2 Determination of surface radiative properties

Step 1. Spectral radiances in the visible and infrared regions, $K^{\uparrow}_{TOA(\lambda)_{x,y}}$, $L^{\uparrow}_{TOA(\lambda)_{x,y}}$
 Remotely measured spectral radiances in the visible and near-infrared, $K^{\uparrow}_{TOA(\lambda)}$, and thermal infrared $L^{\uparrow}_{TOA(\lambda)}$ range are represented in binary digital satellite image products by means of Digital Numbers, DN, which are radiance values in arbitrary units. In the case of LANDSAT Thematic Mapper, to convert DN values to radiances, a simple linear interpolation is applied (Markham and Barker, 1987):

$$K_{TOA}^{\uparrow}(\lambda)_{x,y} = c_{13} + \frac{c_{14} - c_{13}}{255} DN(x,y) \quad (W \text{ m}^{-2} \text{ sr}^{-1} \mu\text{m}^{-1}) \quad (7.1)$$

where $K_{TOA}^{\uparrow}(\lambda)$ ($W \text{ m}^{-2} \text{ sr}^{-1} \mu\text{m}^{-1}$) is the bi-directional spectral radiance at the sensor and c_{13} and c_{14} are the calibration parameters with c_{13} being the spectral radiance at $DN=0$ and c_{14} the spectral radiance at $DN=255$. The values for c_{13} and c_{14} vary for each reflectance band. The calibration of the spectrally emitted radiance $L_{TOA}^{\uparrow}(\lambda)$ and DN is non-linear.

Step 2. Solar declination, δ

The solar declination, δ , is the angular height of the sun above the astronomical equatorial plane. δ changes throughout the year according to (e.g. Duffie and Beckman, 1980):

$$\delta = 0.409 * \sin(0.0172J - 1.39) \quad (\text{rad}) \quad (7.2)$$

where J is the Julian day number (January 1 is day 1).

Step 3. Solar angle hour, $\omega_a(x)$

The longitude dependent solar angle hour, $\omega_a(x)$, reads as:

$$\omega_a(x) = \pi \left[\frac{t(x) - 12}{12} \right] \quad (\text{rad}) \quad (7.3)$$

where $t(x)$ (decimal hours) is the local longitude time which can be obtained from the Greenwich Mean Time t' at 0° longitude according to the following correction:

$$t(x) = t' + \text{min}/60 + \text{long}(x) \frac{12}{\pi} \quad (\text{h}) \quad (7.4)$$

where long (rad) is the longitude.

Step 4. Solar zenith angle, $\phi_{su}(x,y)$

The solar zenith angle is the angle between a line normal to a particular point at a horizontal land surface and a line through the solar centre. Iqbal (1983) gave a simplified goniometric function to describe ϕ_{su} :

$$\cos \phi_{su}(x,y) = \sin(\delta) \sin[lat(y)] + \cos(\delta) \cos[lat(y)] \cos[\omega_a(x)] \quad (\text{rad}) \quad (7.5)$$

where lat (rad) is the latitude. The combination of Eqs. (7.2) to (7.5) can be used to determine, besides $\phi_{su}(x,y)$, the timings of sunset and sunrise, the maximum number of sunshine hours and maximum zenith angle for any horizontal surface and any selected moment.

Step 5. Earth-Sun distance, d_s

The earth-sun distance changes because of the elliptical orbit of the earth around the sun. Accordingly, the solar radiation is affected by a variable path. The earth-sun distance reaches its minimum value at the beginning of January while the beginning of June is marked by the farthest distance among these celestial bodies. The motion of the earth-sun distance can be approximated by the function:

$$d_s = 1 + 0.0167 \sin\left[\frac{2\pi(J-93.5)}{365}\right] \quad (\text{AU}) \quad (7.6)$$

where d_s (-) is the relative Earth-Sun distance in astronomical units (AUs). The absolute value of 1 AU is 1.496×10^8 km.

Step 6. In-band spectral clear sky shortwave hemispherical planetary reflectance, $r_p(b)(x,y)$

Values for in-band spectral reflectance $r_p(b)$ can be computed from incoming and outgoing in-band radiances at the top of the atmosphere. In SEBAL, the nature of the reflecting surface is assumed to be isotropic (Lambertian reflector for azimuth and zenith effects), as models for the bi-directional reflectance without a detailed surface description at the regional scale cannot be applied. The in-band outgoing radiance $K_{TOA}^\uparrow(b)$ was obtained by multiplying $K_{TOA}^\uparrow(\lambda)$ from computation step 1 by its bandwidth b . Integration of $K_{TOA}^\uparrow(b)$ over zenith and azimuth angles gives the hemispherical radiance, $\pi K_{TOA}^\uparrow(b)$, which yields the in-band hemispherical reflectance at the top of the atmosphere as:

$$r_p(b)(x,y) = \frac{\pi K_{TOA}^\uparrow(b)}{K_{TOA}^\downarrow(b)} \quad (-) \quad (7.7)$$

and

$$K_{TOA}^\downarrow(b) = \frac{K_{exo}^\downarrow(b) \cos(\phi_{su})(x,y)}{d_s^2} \quad (\text{W m}^{-2}) \quad (7.8)$$

where $K_{exo}^\downarrow(b)$ (W m^{-2}) is the mean in-band solar exo-atmospheric irradiance undisturbed by the atmosphere at $\phi_{su}=0^\circ$. The value of $K_{exo}^\downarrow(b)$ used in Eq. (7.8) is corrected for the sensor spectral response for consistency with $K_{TOA}^\uparrow(b)$.

Step 7. Integrated clear sky shortwave hemispherical planetary reflectance, $r_p(x,y)$

The spectrally integrated planetary reflectance, r_p , is derived by performing a narrow-band to broad-band integration covering all reflectance bands in the visible and near-infrared region. The results should be approximately similar to $\int_{0.3}^{3.0} r_p(\lambda) d\lambda$. The weighing factor, $c(b)$ accounts for the uneven distribution of $K_{exo}^{\downarrow}(\lambda)$ in spectral bands of a specific sensor:

$$r_p(x,y) = \int_{0.3}^{3.0} r_p(\lambda) d\lambda \approx \sum_{i=1}^n c(b)_i r_p(b)_i \quad (-) \quad (7.9)$$

where n represents the total number of spectral bands i of the radiometer defined in the 0.3 and 3.0 μm zone. The sum of the weighing factors $\sum c(b)_i$ should be equal to one. Because of the inclusion of a wider spectral range, measurements with larger band widths are generally preferred to assess $r_p(x,y)$. For example Pinty et al (1985) argued that METEOSAT measurements of $r_p(b)$ in the 0.4-1.1 μm are rather suitable for assessing r_p .

Step 8. Integrated clear sky shortwave hemispherical surface reflectance, $r_0(x,y)$

The opportunity to determine r_0 from satellite observations in the visible and near-infrared range derives from the fact that under clear sky conditions r_p and r_0 are evidently linked (Figure 6.3). SEBAL computes r_0 according to the retrieval procedure depicted in Figure 7.3. Alternative ways of quantifying r_0 are included. The choice of solution depends on the amount and quality of available ground data. If r_0 is measured at a few specific land surface elements in the study area, τ_{sw} can be obtained by combining r_p from remote sensing measurements and r_0 from these in-situ measurements. If τ_{sw} is measured, r_0

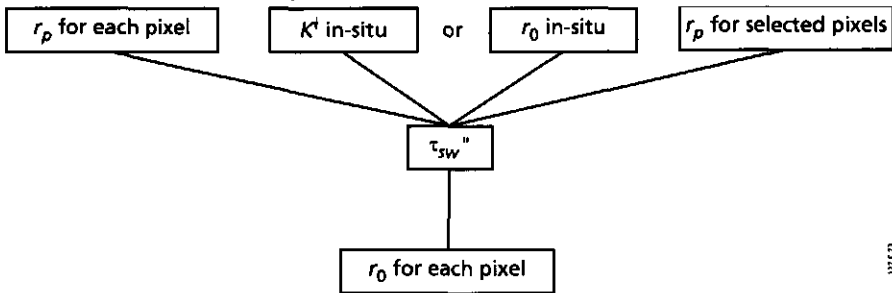


Fig. 7.3 Alternative procedures for converting the hemispherical planetary reflectance, r_p , into hemispherical surface reflectance r_0 on the basis of Eq. (6.4)

can be derived from r_p and τ_{sw} directly. Because it ensures realistic r_0 values, it is preferred to the practical $r_0(r_p)$ procedure which corrects for several effects.

Chapter 6 has shown that for low diffuse radiation levels and minor scattering effects from land surface elements, r_0 may be linearly related to r_p :

$$r_0 = \frac{r_p - r_a}{\tau_{sw}''} \quad (6.4)$$

Step 9. Normalized Difference Vegetation Index, $NDVI(x,y)$

Because chlorophyll has a strong spectral absorption in the visible region at 0.475 and 0.65 μm (Tucker, 1986), land surface spectral reflectances $r_0(\lambda)$ provide information on the presence of chlorophyll and thus on surface vegetation conditions. This information can be utilized to compute the $NDVI$ for each pixel (x,y) from the radiances in the red and infrared channels as:

$$NDVI(x,y) = \frac{r_0(\text{infrared})(x,y) - r_0(\text{red})(x,y)}{r_0(\text{infrared})(x,y) + r_0(\text{red})(x,y)} \quad (-) \quad (7.10)$$

Vegetation indices such as the $NDVI$ respond to the density of plant canopies, colour and the different stages of soil wetness and cultivation practices (Huete and Warrick, 1990). $NDVI$ becomes meaningless where there are sparse canopies and bare soil conditions. Huete and Tucker (1991) showed that $NDVI$ -values for bare soil lie generally between 0.05-0.3. Because of the variable optical properties of the soil, a strict range for bare soils cannot be given.

Step 10. Area-effective shortwave atmospheric clear sky transmission factor, τ_{sw}

The atmospheric clear sky transmission factor τ_{sw} is established by the attenuation of K_{TOA}^l along its path. In the absence of data on K^l or degree of cloudiness to find τ_{sw} from local measurements, the two-way transmittance τ_{sw}'' of Eq. (6.6) is suggested as a solution to determine τ_{sw} . The latter solution is only feasible if τ_{sw}'' was derived from a limited number of r_0 measurements at step 8:

$$\tau_{sw} = \tau_{sw}''^{0.5} = \left(\frac{r_p(x,y) - r_a}{r_0(x,y)} \right)^{0.5} \quad (-) \quad (7.11)$$

Step 11. Area-effective apparent emissivity of the atmosphere, ϵ'_2

Atmospheric thermal radiation from water vapour, aerosols, CO_2 and O_3 is emitted both in an upward and downward direction (Eq. 6.5). Atmospheric water vapour and aerosols also play an important role in the establishment of the shortwave transmittance discussed in the previous computation step. It was therefore attempted to interrelate the apparent emissivity at 2.0 elevation ϵ'_2 and τ_{sw} . Bastiaanssen (1988b) used data from the Qattara Depression of field expeditions 2,3 and 4 (Table 4.2) to relate ϵ_2^{avg} to τ_{sw}^{avg} . The formulations applied were:

$$\tau_{sw}^{avg} = \frac{\int_8^{17} K^{\downarrow}(t) dt}{\int_8^{17} K_{TOA}^{\downarrow}(t) dt} \quad (-) \quad (7.12)$$

$$\varepsilon_2^{avg} = -\sum_i^n \frac{Q_i^* - K_i + L_i^{\uparrow}}{\sigma T_{a-i}^4} \quad (-) \quad (7.13)$$

where n (-) represents the number of observations performed during 8⁰⁰ A.M. and 5⁰⁰ P.M. and T_a is measured at 2.0 m. height. The integration limits in Eq. (7.12) are sunrise and sunset. The following strictly empirical relationship was established:

$$\varepsilon_2^{avg} = 1.08(-\ln \tau_{sw}^{avg})^{0.265} \quad (-) \quad (7.14)$$

The permitted range to which 1.08 and 0.265 apply is $\tau_{sw}^{avg} = 0.55$ to 0.82.

Step 12. At-surface incoming longwave radiation, L^{\downarrow}

The value for L^{\downarrow} can be estimated from ε_2^{avg} and T_a . In this stage of the computation, T_a has not yet been quantified. However, T_a can be inferred from climatic records and denoted further as T_a^* .

$$L^{\downarrow} = \varepsilon_2^{avg} \sigma T_a^{*4} \quad (W \ m^{-2}) \quad (7.15)$$

If field measurements of L^{\downarrow} are available beforehand, it is recommended to use L^{\downarrow} directly, rather than Eq. (7.15).

Step 13. Broad-band thermal infrared surface emissivity, $\varepsilon_0(x,y)$

Van de Griend and Owe (1993) used an emissivity box together with radiometers to measure simultaneously $NDVI$ and ε_0 in the savannah environment of Botswana. A broad-band emissivity ε_0 for the 8 to 14 μm spectral range could be predicted by means of NOAA-AVHRR's $NDVI$ spectral definitions according to the following empirical type of function:

$$\varepsilon_0(x,y) = 1.009 + 0.047 \ln NDVI(x,y) \quad (-) \quad (7.16)$$

The application of Eq. (7.16) is restricted to measurements conducted in the range of $NDVI = 0.16-0.74$. Eq. (7.16) has also been tested with data from the Tomelloso super site in EFEDA. Owe (1992) concluded that the regression coefficients do not need adaption. It should be noted that Eq. (7.16) is not valid for water bodies with a low $NDVI$

and high emissivity ($\epsilon_0=0.99$ to 1.0). Since ϵ_0 changes with wavelength, Eq. (7.16) cannot be applied to other wavelengths such as is required by ϵ_λ in Eq. (6.5).

Step 14. Land surface temperature, $T_0(x,y)$

The relationship between $L_{land}^\uparrow(b)$ and $L_{TOA}^\uparrow(b)$ for a homogeneous atmosphere reads as:

$$L_{TOA}^\uparrow(b)_{x,y} = \tau_\lambda(b)L_{land}^\uparrow(b)_{x,y} + L_{atm}^\uparrow(b) \quad (\text{W m}^{-2}) \quad (7.17)$$

where $L_{land}^\uparrow(b)$ comprises ϵ_λ , $L_\lambda(T_0)^{bb}$ and L_λ^\downarrow of Eq. (6.5). $L_\lambda(T_0)^{bb}$ values necessary to solve T_0 are obtained from an inversion of Eq. (6.5):

$$L_\lambda(T_0)^{bb}_{x,y} = \left\{ \frac{[L_{TOA}^\uparrow(b)_{x,y} - L_{atm}^\uparrow(b)]}{\tau_\lambda(b)} - (1 - \epsilon_\lambda)L_\lambda^\downarrow \right\} \epsilon_\lambda^{-1} \quad (\text{W m}^{-2}) \quad (7.18)$$

whereafter $T_0(x,y)$ can be obtained by inversion of the Planck function:

$$T_0(x,y) = \left[\frac{L_\lambda(T_0)^{bb}_{x,y}}{c_{15}} \right]^{(c_{16})^{-1}} \quad (\text{K}) \quad (7.19)$$

where c_{15} and c_{16} are wavelength-dependent conversion constants. Wukelic et al. (1989) demonstrated that if non-local and non-coincident radiosounding data were used to derive the unknown $\tau_\lambda(b)$ and $L_{atm}^\uparrow(b)$ parameters in Eq. (7.17), the error might approach (or even exceed) the error made if no correction of $L_{TOA}^\uparrow(b)$ is made at all. The absence of accurate data on the atmospheric composition to compute $L_{atm}^\uparrow(b)$ and $\tau_\lambda(b)$ at the moment of satellite overpass must be considered a norm, rather than an exception. It is therefore proposed in SEBAL to derive $\tau_\lambda(b)$ and $L_{atm}^\uparrow(b)$ from field observations of T_0 applying Planck's law which enables the computation of $L_{land}^\uparrow(b)$ at a few specific land surface elements simultaneously with narrow band $L_{TOA}^\uparrow(b)$ satellite measurements of the same targets. A curve fitting according to Eq. (7.17) can then be established. It should be noted that T_0 is obtained from in-situ thermal infrared radiometers which usually have spectral characteristics that are different from the remotely operation radiometers. Comparison of radiances with different spectral definitions can be prevented by correcting the surface temperature T_0 of the in-situ measurements with ϵ_λ in the band of the remote radiometer. In the 8 to 14 μm spectral range, Eq. (7.16) may be applied. If this minimal field investigation on some $T_0(x,y)$ pairs for practical reasons cannot be met, it is suggested to calibrate $\tau_\lambda(b)$ and $L_{atm}^\uparrow(b)$ from large open water bodies with a known temperature ($\epsilon_\lambda = 1.0$).

7.3 Net radiation flux density

Step 15. Incoming global radiation, $K^\downarrow(x,y)$

The integrated radiation over the entire solar spectrum that reaches a horizontal flat land surface can be calculated as:

$$K^\downarrow(x,y) = K_{TOA}^\downarrow(x,y)\tau_{sw} \quad (\text{W m}^{-2}) \quad (7.20)$$

The areal variation of $K_{TOA}^\downarrow(x,y)$, being a spectrally integrated form of $K_{TOA}^\downarrow(b)$ in Eq. (7.8), only has practical significance if the area under consideration is sufficiently large such that spatial variation of $\cos \phi_{su}$ is evident. τ_{sw} is estimated as described under Eq. (7.11).

Step 16. Outgoing longwave radiation, $L^\uparrow(x,y)$

According to the law of Stefan Boltzmann (Eq. 2.4), the total area under the Planck curve for a given temperature T , $\int L_\lambda(T)d\lambda$, is proportional to T^4 :

$$L^\uparrow(x,y) = \int L_\lambda(T)d\lambda = \epsilon_0\sigma(x,y)T_0^4(x,y) \quad (\text{W m}^{-2}) \quad (7.21)$$

where ϵ_0 can be taken from Eq. (7.16).

Step 17. Net radiation, $Q^\uparrow(x,y)$

The four components of radiation described in the previous computation steps must be combined to yield Q^\uparrow :

$$Q^\uparrow(x,y) = K^\downarrow(x,y) - r_0(x,y)K^\downarrow(x,y) + L^\downarrow - L^\uparrow(x,y) \quad (2.8)$$

where $K^\downarrow(x,y)$, $r_0(x,y)$ and $L^\uparrow(x,y)$ are determined with a spatial resolution of one pixel. Eq. (2.8) implies that L^\downarrow is constant over the image.

7.4 Soil heat flux density

Step 18. Soil heat /net radiation flux density ratio, $\Gamma(x,y)$

Since $Q^\uparrow - G_0$ represents the available energy for H and λE , mapping of $Q^\uparrow - G_0$ has to be done prior to estimating H and λE . The ratio of soil heat /net radiation flux density, Γ , is estimated according to Eq. (6.14):

$$\Gamma(t) = \frac{T_0(t)}{r_0(t)} (0.0032 r_0^{avg} + 0.0062 r_0^{avg^2}) [1 - 0.978 (NDVI)^4] \quad (6.14)$$

where T_0 is expressed in °C.

Step 19. Soil heat flux density, $G_0(x,y)$

After independent estimation of $\Gamma(x,y)$ and $Q'(x,y)$, it is feasible to map G_0 pixelwise:

$$G_0(x,y) = \Gamma(x,y)Q'(x,y) \quad (\text{W m}^{-2}) \quad (7.22)$$

Since Q' decreases with increasing r_0 , and Γ increases with increasing r_0^{avg} , the spatial variation of G_0 in heterogeneous land surfaces will tend to level off. Significant differences in G_0 only occurs when sites with low T_0 , high $NDVI$ are alternated with sites that have a high T_0 , low $NDVI$, e.g. warm pockets of bare soil and cold agricultural fields. The physical explanation for a uniform G_0 pattern on the basis of Eq. (3.14) is that wet land with a relatively high λ_s' -value (say $1.5 \text{ W m}^{-1} \text{ K}^{-1}$) usually has a low near-surface vertical soil temperature gradient, $\nabla_z T_s$, since T_0 is controlled by evaporation. At dry lands where λ_s' is low (say $0.5 \text{ W m}^{-1} \text{ K}^{-1}$), $\nabla_z T_s$ for both cases will for both cases then tend to be large since the surface is not cooled down by evaporation. The product of λ_s' and ∇T_s will then tend to become similar in the two cases.

7.5 Momentum flux density

In SEBAL the height $z=z_B$ will be used to compute the area-average momentum flux density from the bulk aerodynamic resistance to heat transport r_{ah-B}^{dry} (see computation steps 26 and 29 for more details). The area-average momentum flux density is defined as:

$$\langle \tau \rangle = \frac{1}{A} \int_A \tau(a) da, \quad (\text{N m}^{-2}) \quad (7.23)$$

and will be estimated in SEBAL as an area-effective flux density:

$$\langle \tau \rangle = \tilde{\tau} = \rho_a \frac{\tilde{u}_B}{r_{am-B}^{dry}} \quad (\text{N m}^{-2}) \quad (7.24)$$

where \tilde{r}_{am-B} is related to \tilde{r}_{ah-B} according to:

$$\tilde{r}_{ah-B} = \tilde{r}_{am-B} + \frac{k\tilde{B}^{-1}}{k\tilde{u}_*} \quad (\text{s m}^{-1}) \quad (7.25)$$

where τ_{ah-B} will be determined from the slope between T_0 and r_0 (see Eq. 6.22). The disaggregation of $\tilde{\tau}$ into $\tau(x,y)$, is complicated by the fact that the flux density layer above heterogeneous land surfaces will be perturbed by lateral exchanges (see Figure 7.1) and per definition not reach $z=z_B$ (u is only constant with height for $z < z_{sur}$). The latter implies that, neither u nor u' is constant with height between $z_{sur} < z < z_B$. More precisely, r_{am-B} can be defined by splitting $r_{am-B}(x,y)$ into two segments: One with a local $u(x,y)$ valid for $z < z_{sur}$ and a 'regionalized' u' between z_{sur} and z_B :

$$r_{am-B}(x,y) = \int_{z_{0m}}^{z_{sur}} \frac{\phi_m(z_{sur}, L)}{ku(x,y)z} dz + \int_{z_{sur}}^{z_0} \frac{\phi_m(z_B, L)}{ku'z} dz \quad (\text{s m}^{-1}) \quad (7.26)$$

Figure 7.4A was compiled to demonstrate the relative contribution of the second term on the right-hand side of Eq. (7.26) on $r_{am-B}(x,y)$. Typical integration limits are $z_{sur}=5$ m (10% of a Thematic Mapper 120m wide pixel) and $z_B=100$ m (Mason, 1988). To study the combination of the first and second term on $r_{am-B}(x,y)$ i.e the effects of the integration limits, $u \approx u'$ has been considered (Figure 7.4A). Obviously, $r_{am-B}(x,y)$ is only rather sensitive to the second term in Eq. (7.26) for rougher surfaces ($z_{0m} > 0.1$ m). Figure 7.4B has been drawn to evaluate the hypothesis $u' \approx u$. A 50% increase and decrease in u has been considered for u' and the conclusion can be drawn that especially $u' < u$ needs ample attention. The latter implies that the second term in Eq. (7.26) is only crucial for the dis-aggregation of $\tilde{\tau}$ for rough surfaces and low friction velocities.

Although not physically correct, a possible way to describe u' is by assuming that $u(x,y)$ is constant with height; With locally variable surface roughnesses $z_{0m}(x,y)$ neighbouring $u(z)$ -profiles will then tend to blend and that all local $u(z)$ profiles give the same value of u at $z = z_B$ (Andre and Blondin, 1986). Figure 7.5A illustrates this approach. The $u(z)$ profiles of Figure 7.5A were computed with the 1D-flux-profile relationship of Eq. (2.79). For $z > z_B$, u and z_{0m} apply. Consequently, a kink in the wind profile arises at $z=z_B$.

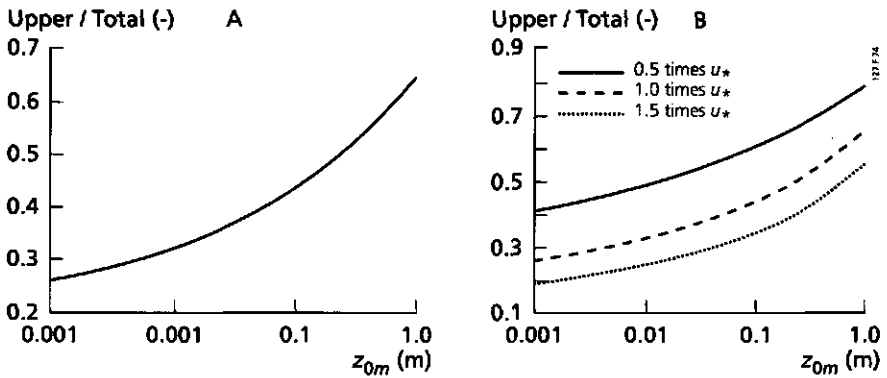


Fig. 7.4 (Part A) Effects of local surface roughness on the contribution of the upper air layer ($z_{sur} < z < z_B$) on the aerodynamic resistance to momentum transfer between $z_{0m} < z < z_B$ using Eq. (7.26), (Part B) Effect of the friction velocity between ($z_{sur} < z < z_B$) on the aerodynamic resistance to momentum transfer between $z_{0m} < z < z_B$

Over against that, Fiedler and Panofsky (1972) used a near-surface wind speed, say $u(z_{sur})$, to define z_{0m} as that roughness length which produces $\bar{\tau}$ correctly. We may assume that $\bar{\tau}$ at $z = z_B$ is equal to $\bar{\tau}$ at $z = z_{sur}$ with the major difference that at $z = z_{sur}$ τ is spatially variable and not blended with the neighbouring flux density. The 1D-flux-profile relationship of Eq. (2.79) can then also be invoked to decompose $\bar{\tau}$ into $\tau(x,y)$ for $z < z_{sur}$. Following Fiedler and Panofsky, the wind speed $u(z_{sur})$ can be applied to find $u(x,y)$ for $z < z_{sur}$. Figure 7.5B shows the wind profile if $u(z_{sur})$ and $z_{0m}(x,y)$ are considered for $z < z_{sur}$ and \tilde{u} and \tilde{z}_{0m} for the range $z \geq z_{sur}$. Consequently, the kink arises now at $z = z_{sur}$. This approach is thought to be more consistent because u only remains constant with height for $z < z_{sur}$. The latter solution will be applied in the SEBAL computation steps that follow.

Step 20. Distributed surface roughness length for momentum transfer, $z_{0m}(x,y)$

It was argued at computation step 9 that classes of vegetation density can be related to NDVI. Pierce et al. (1992) showed that even LAI can be obtained from NDVI for various biome types. Hanan et al. (1991) provided a methodology for retrieving fractional vegetation cover from NDVI. Asrar et al. (1992) showed by means of physical models that LAI, NDVI and groundcover are interrelated. Since z_{0m}/h_v changes with LAI (Section 2.3, Eqs. (2.83) to (2.85)), a direct relationship between NDVI, z_{0m} and h_v may be expected. Hatfield (1988) confirmed by means of field measurements in cotton with temporal vegetation density variations that spectral measurements in the red and near-infrared region can be used to estimate surface roughness z_{0m} and displacement height d . A different proof was given by Moran (1990) who used functions relating NIR/red ratio or NDVI to z_{0m} during an alfalfa growing season. In SEBAL it is without further investigations assumed that these relationships can also be applied for heterogenous land surfaces:

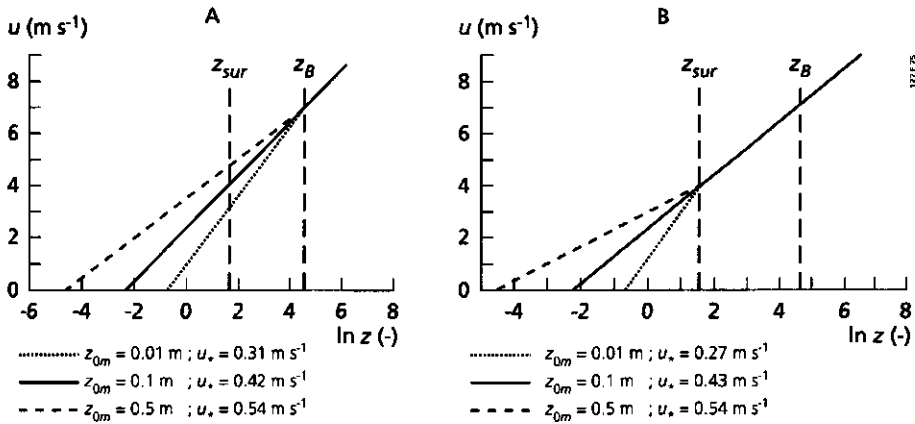


Fig. 7.5 Vertical profiles of horizontal wind speed $u(z)$ above three land surface elements with different surface roughness, z_{0m} . The assumptions of vertical variations in momentum flux density differ. (Part A) u is constant with height between z_{0m} and z_B ; for $z > z_B$, \tilde{u} is considered. (Part B) u is constant with height for $z < z_{sur}$ and for $z > z_{sur}$. u is taken

$$z_{0m}(x,y) = \exp(c_{17} + c_{18} \text{NDVI}(x,y)) \quad (\text{m}) \quad (7.27)$$

The aerodynamic effects of sheltering leaves is not very well described by Eq. (7.27). For conditions of natural vegetation with dispersed shrubs and trees, z_{0m} depends on the spacing, shape, size, distribution and density of these obstacles which is too complicated to relate to NDVI . In the present author's opinion, Eq. (7.27) is therefore especially useful to describe the role of fractional vegetation cover on surface roughness, rather than aiming to solve the roughness for different sparse canopies structures. The workability of Eq. (7.27) will be tested with EFEDA field data and this is described in Chapter 8. The impact of Eq. (7.27) on flux densities is demonstrated by means of an uncertainty analysis in Chapter 9. New techniques for retrieving z_{0m} and LAI remotely by laser beam techniques are in progress (Menenti and Ritchie, 1994) and form a promising alternative to Eq. (7.27).

At least some data should be made available from in-situ measurements to get c_{17} and c_{18} calibrated for several field conditions encountered within the study area. Measurements of z_{0m} , h_v and LAI are especially desirable at the extremes of NDVI ($\text{NDVI}_{min} \approx 0.2$; $\text{NDVI}_{max} \approx 0.8$) in order to retrieve the study area-dependent c_{17} and c_{18} coefficients.

Step 21. Distributed surface roughness length for heat transfer, $z_{0h}(x,y)$

The ratio between z_{0m} and z_{0h} changes with scale and surface type, as described in Chapter 3. Therefore kB^{-1} needs to be calibrated against local τ and H -flux densities, which is hardly feasible except in the HAPEX type of experiments at meso scale. However, kB^{-1} and δT_{a-sur} are related because T_0 increases with kB^{-1} which directly affects δT_{a-sur} ($\delta T_{a-sur} = T_0 - T_a$). In other words, an increased resistance r_{ah} by an increase of kB^{-1} should be compensated by an increased δT_{a-sur} to maintain a certain H -flux density. On similar grounds, Kustas et al. (1989) found that kB^{-1} can be related to δT_{a-sur} and u . They calibrated kB^{-1} and extrapolated $kB^{-1}(t)$ in the time domain using $T_0(t)$. Their semi-operational model for kB^{-1} is:

$$kB^{-1}(x,y) = c_{19} u(x,y) \delta T_a(x,y) \quad (-) \quad (7.28)$$

where the empirical slope c_{19} remains between 0.13 and 0.17. If no information on kB^{-1} is available, $kB^{-1}=2.3$ may be taken (Choudhury, 1989).

Considering the results of Section 6.6 showing the potential for extrapolating δT_{a-sur} regionally for a wide range of surface types and climate conditions and the difficulties of predicting the spatial distribution of kB^{-1} in complex terrain (Dolman and Blyth, 1995), it is preferable to calibrate δT_{a-sur} rather than kB^{-1} . Then kB^{-1} should be areally fixed and δT_{a-sur} will be solved pixelwise according to Eq. (6.25).

Hence, the non-uniqueness of kB^{-1} is a crucial problem for the application of one-layer resistance parameterization schemes in composite terrain and although $T_{z_{0h}} = T_0$ is usually assumed, erroneous H -flux densities will result if kB^{-1} values are not adjusted to the local $T_{z_{0h}}$ values (Lhomme et al., 1994).

Step 22. Effective surface roughness length for heat transfer, \tilde{z}_{0h}

The effective roughness length z_{0h} is a value that by using boundary layer similarity theory over a given landscape structure and topography yields the correct area-average $\langle H \rangle$ -value which is defined as:

$$\langle H \rangle = \frac{1}{A} \int_A H(a_i) da_i \quad (\text{W m}^{-2}) \quad (7.29)$$

One possible solution is to inversely derive the effective surface roughness \tilde{z}_{0h} from areally aggregated land surface flux densities at composite patches using numerical PBL models (Diak, 1990). A solution with simulation models is too sophisticated for vast regions in the absence of data and simpler aggregation rules need to be developed (Blyth et al., 1993). A logarithmic relationship between r_{ah} and z_{0h} follows immediately from Eq. (3.4). If flux densities can be lineary averaged and are proportional to resistance, i.e. $H \sim r_{ah}^{-1} \sim \ln z_{0h}$, it is mathematically consistent to obtain \tilde{z}_{0h} :

$$\bar{z}_{0h} = \exp\left[\frac{1}{n}\left(\sum_{i=1}^n \ln z_{0h-i}\right)\right] \quad (m) \quad (7.30)$$

where n is the number of land surface elements. Noilhan and Lacarrere (1995) used this logarithmic averaging procedure for the HAPEX-MOBILHY area (Andre et al., 1986) and applied Eq. (7.30) to obtain grid-square average values for surface roughness. The comparison of predictions in soil water content and evaporation made by the French Weather Service mesoscale model PERIDOT with local ground values for a 25-day simulation period was encouraging.

Eq. (7.29) basically explains that local land surface elements with $H(x,y) \geq \langle H \rangle$ have a larger contribution to $\langle H \rangle$ than elements with $H(x,y) < \langle H \rangle$. Eq. (7.30) does not account for this effect and all surfaces that are similar in roughness will give the same contribution to $\langle H \rangle$ which, considering an heterogeneous energy partitioning, is an over-simplified concept. Using the opportunity demonstrated in Section 6.6 to retrieve δT_{a-sur} from T_o and the dominant control of $\delta T_{a-sur}(x,y)$ on $H(x,y)$, an upgraded version of Eq. (7.30) is proposed:

$$\bar{z}_{0h} = \exp\left\{\frac{1}{n}\left[\sum_{i=1}^n \frac{T_{o-i}(x,y)}{T_o} \ln z_{0h-i}(x,y)\right]\right\} \quad (m) \quad (7.31)$$

which assigns more weight to the roughness of warmer land surface elements than to those elements with a low H value. For this, $T_o(x,y)$ needs to be areally aggregated to obtain \bar{T}_o from all pixels. The aggregation of $T_o(x,y)$ should be realized through the spatial integration of flux density $L^\uparrow(x,y)$ from the surface radiation balance that is calculated from $T_o(x,y)$ and $\epsilon_o(x,y)$ using Stefan Boltzmann's law:

$$\bar{T}_o = \frac{\frac{1}{n}\sum_{i=1}^n L_i^\uparrow(x,y)}{\bar{\epsilon}_o \sigma} \quad (K) \quad (7.32)$$

Application of Eq. (7.32) requires an *a priori* quantification of $\bar{\epsilon}_o$. A weighted average for ϵ_o can be obtained from the frequency distribution of ϵ_{o-i} obtained under computation step 13:

$$\varepsilon_0^{dry} = \sum_{i=1}^n [\omega \varepsilon_0(x,y)]_i \quad (-) \quad (7.33)$$

where the weighing coefficients ω_i are frequencies of each $\varepsilon_{0,i}$ value.

Step 23. Partial derivative of net longwave radiation with respect to surface temperature above dry land, $\partial L^* / \partial T_0$

Due to variations in the thermal emittance of the land surface, the variation of net longwave radiation in composite terrain under clear skies with a constant atmospheric emittance reads as:

$$L^*(x,y) = L^\downarrow - L^\uparrow(x,y) \quad (\text{W m}^{-2}) \quad (7.34)$$

so that:

$$\frac{\partial L^*}{\partial T_0} = -\frac{\partial L^\uparrow}{\partial T_0} \quad (\text{W m}^{-2} \text{ K}^{-1}) \quad (7.35)$$

Eq. (6.20) requires the quantification of $\partial_{T_0} L^*$ for land surface elements with zero evaporation; By differentiating Eq. (7.21) we get for areas with $\partial_{T_0} \lambda E = 0$:

$$\frac{\partial L^*}{\partial T_0} = -4\varepsilon_0^{dry} \sigma T_0^{dry^3} \quad (\text{W m}^{-2} \text{ K}^{-1}) \quad (7.36)$$

where ε_0^{dry} and T_0^{dry} represent area-effective values for land surface elements with zero evaporation. The allocation of pixels with zero evaporation will be explained below.

Step 24. Partial derivative of soil heat flux density with respect to surface temperature above dry land, $\partial G_0 / \partial T_0$

The slope between G_0 and T_0 needs to be quantified for Eq. (6.20) as well. This first derivative of G_0 with respect to T_0 is:

$$\frac{\partial G_0}{\partial T_0} = \frac{\lambda'_s}{z} \left(1 - \frac{\partial T_s}{\partial T_0}\right) \quad (\text{W m}^{-2} \text{ K}^{-1}) \quad (7.37)$$

Since λ'_s and z are unknown for a heterogeneous landscape and $\partial_{T_s} T_0$ changes with z , Eq. (7.37) cannot be solved. Because G_0 changes rather linearly with T_0 (Pelgrum and Bastiaanssen, 1995a; Roerink, 1995), the easiest way is to apply a linear regression analysis between (G_0, T_0) data pairs yielding an effective slope c_{21} as:

$$G_0(x, y) = c_{20} + c_{21}T_0(x, y) \quad (\text{W m}^{-2}) \quad (7.38)$$

The case studies which will be presented in Chapter 8 show that there is indeed a linear regional relationship between G_0 and T_0 which are determined at steps 19 and 14 respectively. If the trend between G_0 and T_0 has a non-linear character, the regression analysis should be restricted to the high range of T_0 -values where $\partial_{T_0}\lambda E \approx 0$ applies.

Step 25. Partial derivative of hemispherical surface reflectance with respect to surface temperature above dry land, $\partial r_0/\partial T_0$

If the slope $\partial_{T_0}r_0$ can be retrieved from the $T_0(r_0)$ relationship with sufficient precision, the $T_0(r_0)$ relationship provides the opportunity to derive r_{ah}^{dry} (Eq. 6.21). The $T_0(r_0)$ relationship can be estimated by means of 3rd order polynomial fitting functions (Bastiaanssen, 1991) from which the 2nd order function for $\partial_{T_0}r_0$ can be derived:

$$\frac{\partial r_0}{\partial T_0} = \left(\frac{\partial T_0}{\partial r_0}\right)^{-1} = (c_{22} + 2c_{23}r_0 + 3c_{24}r_0^2)^{-1} \quad (\text{K}^{-1}) \quad (7.39)$$

The hemispherical surface reflectance at which the negative 'radiation controlled' $T_0(r_0)$ branch emerges (if the r_0 -range permits) can be obtained from $\partial_{T_0}r_0 = 0$ and be referred to as $r_0(T_0^{\max})$:

$$c_{22} + 2c_{23}r_0(T_0^{\max}) + 3c_{24}r_0(T_0^{\max})^2 = 0 \quad (7.40)$$

The negative linearized slope c_{26}^{-1} for all pixels that fulfil the condition $r_0 > r_0(T_0^{\max})$ can be obtained from linear curve fitting of all (T_0, r_0) pixel pairs belonging to this category:

$$T_0 = c_{25} + c_{26}r_0 \quad \text{for } r_0 > r_0(T_0^{\max}) \quad (7.41)$$

where c_{26}^{-1} represents the negative linearized slope at which $\partial_{T_0}\lambda E \approx 0$, $\lambda E \approx 0$ and $\Lambda \approx 0$ apply. The threshold reflectance r_0^{thresh} associated to c_{24}^{-1} can be obtained according to:

$$c_{26}^{-1} = c_{22} + 2c_{23}r_0^{\text{thresh}} + 3c_{24}(r_0^{\text{thresh}})^2 \quad (7.42)$$

If r_0^{thresh} is determined according to Eq. (7.42), pixels with $\lambda E \approx 0$ can be assigned as $r_0 \geq r_0^{\text{thresh}}$. A $T_0(r_0)$ relationship drawn on the basis of pixel based (T_0, r_0) -values exhibits a natural scatter between r_0 and T_0 , because T_0 is in addition to r_0 also governed by c_1 , c_2 , K^{\downarrow} , ϵ_0 , L^{\downarrow} and λE (see Eq. 3.37). A marked improvement in the correlation coefficient between r_0 and T_0 can be accomplished if the average (r_0, T_0) values of land units are considered, rather than individual pixel values (compare also Figs. 6.14A and 6.14B).

Step 26. Air resistance to heat transport above dry land, r_{ah-B}^{dry}

Menenti et al. (1989b) and Bastiaanssen (1991) used $\partial_{T_0} H$ to find r_{ah}^{dry} regardless of the availability of field data. The values for K^{\downarrow} (Eq. 7.20), $\partial_{T_0} L^*$ (Eq. 7.36), $\partial_{T_0} G_0$ (Eq. 7.38) and $\partial_{T_0} r_0$ (Eq. 7.41) for dry land surfaces with $\partial_{T_0} \lambda E = 0$ were quantified as described above. Substituting these values in Eq. (6.20), yields $\partial_{T_0} H$:

$$\frac{\partial H}{\partial T_0} = -K^{\downarrow} \frac{\partial r_0}{\partial T_0} + \frac{\partial L^*}{\partial T_0} - \frac{\partial G_0}{\partial T_0} \quad (\text{W m}^{-2} \text{ K}^{-1}) \quad (7.43)$$

Because the Monin Obukhov length L is a function of temperature, a more physically correct version of Eq. (6.21) to obtain r_{ah-B}^{dry} reads as:

$$\frac{\partial H}{\partial T_0} = \frac{\rho_a c_p}{r_{ah-B}^{dry}} + \rho_a c_p \frac{\partial}{\partial T_0} \left(\frac{1}{r_{ah-B}^{dry}} \right) T_0 \quad (\text{W m}^{-2} \text{ K}^{-1}) \quad (7.44)$$

Since $\partial_{T_p} T_0$ is not considered in Eq. (7.44), it implies that T_p applies to a height such that T_p is not affected by T_0 , i.e. $z > z_B$. If no data are available, z_B for flat land surfaces can be set to 100 m height, being sufficiently high to assume T_p to be regionally constant. In a later phase, it will be demonstrated with examples that the determination of the area-effective momentum flux density is rather insensitive to the selection of z_B .

Unfortunately, the second term on the right hand side of Eq. (7.44) cannot be solved analytically. A numerical differentiation is feasible when the Monin Obukhov length L is solved at different T_0 -values (see Eq. 2.67). Therefore, ψ_h^{dry} imbedded in r_{ah-B}^{dry} has to be quantified first. A solution for ψ_h requires estimates of H , as described in the next computation step.

Although ρ_a in Eq. (7.44) most commonly ranges between 1.15 and 1.25 kg m⁻³ at sea-level pressures, ρ_a can be calculated for any atmospheric pressure from ideal gas laws (Eq. 2.48). If climatological mean humidity data to fix ρ_a are applied, the range between 1.15 and 1.25 kg m⁻³ can be substantially narrowed.

Step 27. Sensible heat flux density above dry land, H^{dry}

Without further field investigations, $r_0 > r_0^{thresh}$ may be used to establish for which pixels it may be assessed that $\lambda E \approx 0$. A simple summation of the surface flux densities is feasible under restricted physical conditions (Shuttleworth, 1988). Since the landscape structure in arid zones is often disorganized, the area-effective H -value at these dry land surface elements can be simply obtained by linearly averaging the distributed H -flux densities:

$$H^{dry} = \frac{1}{n} \left\{ \sum_{i=1}^n [Q^*(x,y) - G_0(x,y)] \right\} \quad \text{for } r_0 > r_0^{thresh} \quad (\text{W m}^{-2}) \quad (7.45)$$

Step 28. Area-effective Monin Obukhov length above dry land, L^{dry}

The buoyancy effect above these dry land surface elements can be accounted for by means of L^{dry} .

$$L^{dry} = -\frac{\rho_a c_p (u_*^{dry})^3 T'^{dry}}{kgH^{dry}} \quad \text{for } r_0 > r_0^{thresh} \quad (m) \quad (7.46)$$

where T'^{dry} represents the mean value of T_0^{dry} and T_{p-B} ($(T_0^{dry} + T_{p-B}) * 0.5$); T_{p-B} is the air potential temperature at height z_B . The value for T_{p-B} could be estimated from H^{dry} obtained with Eq. (7.45) and T_0^{dry} calculated from L^{dry} for all pixels fulfilling the condition $r_0 > r_0^{thresh}$, using the classical ohm-type expression for H :

$$T_{p-B} = T_0^{dry} - \frac{r_{ah-B}^{dry} H^{dry}}{\rho_a c_p} \quad (K) \quad (7.47)$$

in which r_{ah-B}^{dry} is the value looked for in Eq. (7.44). Since u_*^{dry} is not known, L^{dry} of Eq. (7.46) cannot be solved yet. However, u_*^{dry} is imbedded in r_{ah-B}^{dry} and L^{dry} . Iteration I in Fig 7.6 is designed to obtain u_*^{dry} . Holtslag and van Ulden (1983) estimated u using a similar numerical procedure but for local τ -flux densities at pastures first at neutral atmospheric conditions (making ψ_h and ψ_m tentatively zero) whereafter consecutive improvements in u could be obtained. The same procedure is followed in the SEBAL scheme. The first approximation of u will stem from Eq. (6.21) where $\partial_{\tau_0} r_{ah} = 0$. Thereafter, L^{dry} can be computed from the first u estimation which opens the possibility of solving $\partial_{\tau_0} r_{ah}$. Subsequent estimates of u_*^{dry} , L^{dry} , ψ_{h-B}^{dry} , r_{ah-B}^{dry} , T_{p-B}^{dry} and T'^{dry} need to be made in successive iterative computation steps until a single u_*^{dry} -value matches $\partial_{\tau_0} H$ according to Eq. (7.44) and H^{dry} in Eq. (7.45). The input parameters for Iteration I are H^{dry} , z_{0h}^{dry} and T_0^{dry} and they are kept unchanged during Iteration I until the calculated value for $\partial_{\tau_0} H$ matches the 'observed' value from Eq. (7.44) through remote sensing.

The solution of Iteration I yields an area-effective u_*^{dry} value. Since the area-effective momentum flux density $\tilde{\tau}$ is approximately similar for wet and dry land surface elements (some differences due to stability corrections persists), $u_*^{dry} = \tilde{u}$ is reasonable and $\tilde{\tau}$ can be obtained as:

$$\tilde{\tau} = \rho_a (u_*^{dry})^2 \quad (N \ m^{-2}) \quad (7.48)$$

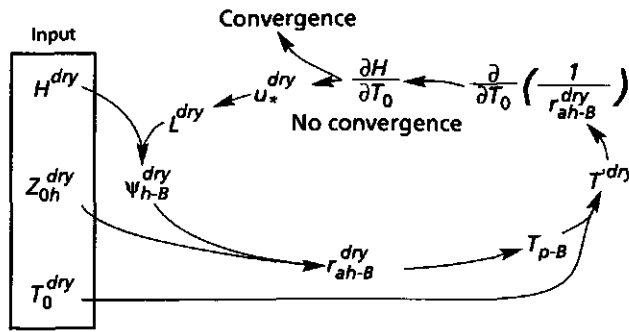


Fig. 7.6 Iteration cycle I of u_*^{dry} required to let $\partial_{T_0}H$ be consistent with H^{dry} , z_{0h}^{dry} and T_0^{dry} on the basis of flux-profile relationships for heterogeneous areas. The value of u_*^{dry} is used to obtain $\tilde{\tau}$.

A brief sensitivity analysis on the effect of choosing different z_B -values on $\tilde{\tau}$ can now be given by repeating computation steps 26 to 28 for 25, 50, 100, 200 and 500 m altitude. The hypothetical land surfaces are defined as $z_{0m}=0.001, 0.01$ and 0.20 m, $T_0^{dry}=300$ K, $z_{0h}^{dry}=0.001$ m, $z_{0m}^{dry}=0.05$ m, $\partial_{T_0}H = 20$ W m⁻¹K⁻¹, $H^{dry}=350$ W m⁻², and $\rho_a c_p=1155$ J m⁻³ K⁻¹. The selection of z_B at which $\partial_{T_0}H$ and H^{dry} apply seems to be fairly irrelevant since the \tilde{u} and $\tilde{\tau}$ variations found are negligible and seems to stabilize when $z_B \geq 100$ m

Table 7.2 Sensitivity of the area-average momentum-flux density $\tilde{\tau}$ to changes/errors in the regionally constant blending height z_B for momentum and heat transfer according to the procedure outlined in computation steps 26 to 28

Blending height z_B (m)	\tilde{u} (m s ⁻¹)	L_{dry} (m)	r_{ah-B}^{dry} (s m ⁻¹)	Ψ_{m-B} (-)	u_B (m s ⁻¹)	$\tilde{\tau}$ (Nm ²)
25	0.33	-8.8	54.1	2.7	2.8	0.125
50	0.34	-9.5	54.0	3.2	3.1	0.133
100	0.35	-9.9	53.9	3.9	3.2	0.141
200	0.35	-10.2	54.0	4.5	3.2	0.141
500	0.35	-10.5	53.9	5.3	3.3	0.141

Step 29. Near-surface area-effective wind speed, $u(z_{sur})$

The wind profile expression (Eq. 2.79) can be used to determine the near-surface windspeed at $z=z_{sur}$ (Figure 7.5B) using the area-effective momentum flux density and roughness:

$$\tilde{u}(z_{sur}) = \frac{\tilde{u}_*}{k} \left[\ln \frac{z_{sur}}{z_{0m}} - \Psi_m(z_{sur}, L') \right] \quad (\text{m s}^{-1}) \quad (7.49)$$

where $\tilde{u}_* \approx u_*^{dry}$. The value for z_{0m} can be computed in the same manner as was done for z_{0h}^{dry} (Eq. 7.30). The quantification of z_{sur} is performed according to the theory

presented in Section 3.5. The value for $\psi_m(z_{sur}, L')$ was determined on the basis of Eq. (7.50) using a first estimate of \tilde{H} as 50% of H^{dry} :

$$L' = -\frac{\rho_a c_p (\tilde{u}_*)^3 T''}{kgH^{dry} 0.5} \quad (m) \quad (7.50)$$

A new temperature T'' was introduced at this stage to better describe the effective temperature of the heterogeneous landscape with dry and wet surface elements. T'' was for this purpose computed as the mean of \tilde{T}_0 and T_a using Eq. (6.26).

Step 30. Distributed friction velocity, $u_*(x,y)$

The SEBAL schematization is based on the Fiedler and Panofsky definition of a near-surface area-effective wind speed, $\tilde{u}(z_{sur})$. For $z < z_{sur}$, \tilde{u} can be disaggregated into $u_*(x,y)$ as:

$$u_*(x,y) = \left\{ \frac{1}{k\tilde{u}(z_{sur})} \left[\ln \frac{z_{sur}}{z_{0,m}(x,y)} - \psi'_m(x,y) \right] \right\}^{-1} \quad (m \ s^{-1}) \quad (7.51)$$

For each pixel $z_{0,m}(x,y)$ was computed from $NDVI(x,y)$ at computation step 20. The stability correction $\psi'_m(x,y)$ is based on the following version of Monin-Obukhov length:

$$L(x,y) = -\frac{\rho_a c_p [u_*^3(x,y)] T_0(x,y)}{kgH^{dry} 0.5} \quad (m) \quad (7.52)$$

where $T_0(x,y)$ is included to account for the spatial thermal patterns. Since $u_*(x,y)$ is implicitly present in $\psi'_m(x,y)$, improved estimates of $u_*(x,y)$ can be made by modifying $\psi'_m(x,y)$ with the outcome of Eq. (7.51) and hence an iterative procedure II is needed to use Eqs. (7.51) and (7.52) (see Figure 7.8).

Step 31. Distributed momentum flux density, $\tau(x,y)$

After convergence of the procedure outlined in computation step 30, the local momentum flux densities become:

$$\tau(x,y) = \rho_a u_*^2(x,y) \quad (N \ m^{-2}) \quad (7.53)$$

7.6 Sensible heat flux density

Step 32. Distributed air resistance to heat transport, $r_{ah-sur}(x,y)$

Since $u(x,y)$, $z_{0h}(x,y)$ and $L(x,y)$ are identified for the air layer between $z_{0h} < z < z_{sur}$, $\psi_h(x,y)$ can be assessed as:

$$\psi_{h-sur}(x,y) = f_3(z_{sur} L(x,y)) \quad (-) \quad (7.54)$$

which can be solved if Eq. (2.90) is used. The resistance for the heat exchange between soil, plant and atmosphere valid for the layer between z_{0h} and z_{sur} then changes spatially according to:

$$r_{ah-sur}(x,y) = \frac{1}{ku_a(x,y)} \left[\ln\left(\frac{z_{sur}}{z_{0h}(x,y)}\right) - \psi_{h-sur}(x,y) \right] \quad (\text{s m}^{-1}) \quad (7.55)$$

Step 33. Near-surface vertical air temperature difference, $\delta T_{a-sur}(x,y)$

The linearity of the $\delta T_{a-sur}(T_0)$ relationship was experimentally justified in Section 6.5. Image-dependent regional coefficients for the $\delta T_{a-sur}(T_0)$ relationship may be determined if $(\delta T_{a-sur}, T_0)$ -pairs can be estimated for wet and dry surfaces. Pixels with $r_0 > r_0^{thresh}$ ($\Lambda = 0$) and $r_0 < 0.10$, $\Lambda = 1.0$ (see Section 6.5) will for this purpose be applied.

Upper bound of sensible heat flux density: $\Lambda \approx 0.0 \rightarrow H \approx Q^* - G_0$

The upper bound of H applies to non-evaporating land surfaces, where $H \approx Q^* - G_0$. The role of $u(x,y)$, $z_{0h}(x,y)$ and $\psi_h(x,y)$ should be incorporated in the establishment of the regional maximum vertical air temperature difference δT_a^{dry} because rough-dry and smooth-dry sites may co-exist and have different δT_{a-sur} values. Since for pixels with $r_0 > r_0^{thresh}$, $Q^*(x,y) - G_0(x,y)$ and $r_{ah-sur}(x,y)$ are known from respectively computation steps 17, 19 and 32, the formulation of Eq. (7.56) can be applied to find $\delta T_a^{dry}(x,y)$:

$$\delta T_a^{dry}(x,y) = \frac{Q^*(x,y) - G_0(x,y)}{\rho_a c_p} r_{ah-sur}(x,y) \quad \text{for } r_0 > r_0^{thresh}, z = z_{sur} \quad (^\circ\text{C}) \quad (7.56)$$

A range of $\delta T_a^{dry}(x,y)$ -values will result from (Eq. 7.56). As a first approximation the 95% percentile of the distribution of $\delta T_a^{dry}(x,y)$ -values obtained via Eq. (7.56) can act as the regionally representative δT_a^{dry} value. If this 95% percentile finally results in negative $\lambda E(x,y)$ values, when $\lambda E = Q^* - G_0 - H$ is applied later for each pixel, $H(x,y)$ must have been overestimated and δT_a^{dry} should be reduced. The 95% level can be adjusted until less than 1% of the pixels fulfil the condition $\lambda E < 0$. The latter procedure is an internal calibration procedure designed to prevent unrealistic negative λE values arising during daytime (condensation is not likely to occur).

Lower bound of sensible heat flux density: $\Lambda \approx 1.0 \rightarrow H \approx 0$

Chapter 6 has revealed that the land surface cluster that meets the assumption $\Lambda \approx 1$ can be characterized by $r_0 < 0.10$ and minimum T_0 -values. If $\Lambda \approx 1.0$, δT_a^{wet} will tend to zero:

$$\delta T_a^{wet} = 0 \quad \text{for } r_0 < 0.10, z = z_{sur} \quad (^\circ\text{C}) \quad (7.57)$$

Combining the $(\delta T_a^{wet}, T_0^{wet})$ and $(\delta T_a^{dry}, T_0^{dry})$ data pairs displayed in Figure 7.7 creates the possibility to internally calibrate the $\delta T_{a-sur}(T_0)$ relationship:

$$\delta T_{a-sur}(x, y) = c_{27} + c_{28} T_0(x, y) \quad (\text{K}) \quad (7.58)$$

where c_{28} presents $\delta T_a^{dry} / (T_0^{dry} - T_0^{wet})$ and $c_{27} = -c_{28} * T_0^{wet}$. In this way, the range of H values is ensured by means of extremes in the $(T_0, r_0, \Lambda, \delta T_{a-sur})$ space. Problems originating from poorly-quantified z_{0m} , kB^1 and u . values may lead to a mis-estimation of r_{ah} but do not longer drastically affect H .

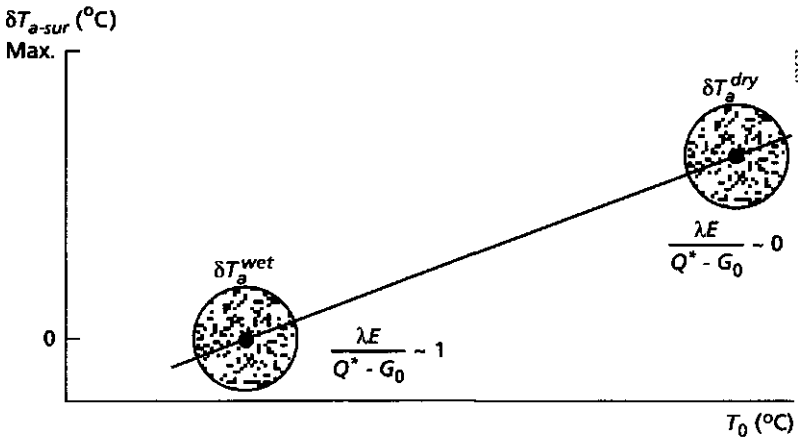


Fig. 7.7 A new procedure for estimating the near-surface vertical air temperature difference δT_{a-sur} from surface temperature T_0 using special cases of the evaporative fraction Λ and the sensible heat transfer equation, i.e. the 'evaporative fraction-vertical air temperature difference' method.

Hence, kB^1 has either to be tuned with T_0 remote sensing or with δT_{a-sur} when kB^1 is fixed antecedently. The latter approach is followed in SEBAL because δT_{a-sur} is easier to extrapolate regionally than kB^1 .

Hence, the whole discussion on the accuracy that can be obtained when deriving $T_0 - T_a$ from combined remote sensing and in-situ measurements can be by-passed if δT_{a-sur} is derived from inversion of the transfer equation for sensible heat flux density in combination with Eq. (7.58), i.e. the *evaporative fraction-vertical air temperature difference* method.

Step 34. Sensible heat flux density, $H(x,y)$

Since the transport resistance $r_{ah-sur}(x,y)$ and the driving force $\delta T_{a-sur}(x,y)$ are mapped in computation steps 32 and 33, respectively and care has been taken that the extremes of H are physically sound, H can be found as:

$$H(x,y) = \frac{\rho_a c_p}{r_{ah-sur}(x,y)} \delta T_{a-sur}(x,y) \quad (\text{W m}^{-2}) \quad (7.59)$$

Step 35. Distributed Monin-Obukhov length

The first estimates of $H(x,y)$ at computation step 34 can be used to improve the first assessment of the local $u(x,y)$ and Monin Obukhov length $L(x,y)$ values by replacing $H^{dry*}0.5$ with $H(x,y)$ (Iteration II and III, Figure 7.8).

$$L(x,y) = - \frac{\rho_a c_p u_*^3(x,y) T_0(x,y)}{kgH(x,y)} \quad (\text{m}) \quad (7.60)$$

The example in Table 7.3 shows that the first round of iteration III of ψ_h will give on average a 7 % change in H while the 3rd iteration gave less than a 1 % change in H . SEBAL therefore considers only three cycles as a standard option for iteration III.

Table 7.3 Impact of the distributed sensible heat flux density H on the ψ_h -correction for three different land surface types which are different in δT_{a-sur} $z_{sur}=5$ m and $H^{dry}=350$ W m^{-2} .

Land surface type	δT_{a-sur} (K) reference	z_{0h} (m)	u_* (ms^{-1})	H (Wm^{-2})	1 st iteration			3 rd iteration		
					ψ_h^{sur} -	r_{ah}^{sur} (s m^{-1})	H (W m^{-2})	ψ_h^{sur} -	r_{ah}^{sur} (s m^{-1})	H (W m^{-2})
1	20	0.001	0.24	175	1.67	96	332	2.21	64	360
2	10	0.01	0.32	175	1.10	39	296	1.48	36	320
3	1	0.20	0.55	175	0.37	13	69	0.21	13	87

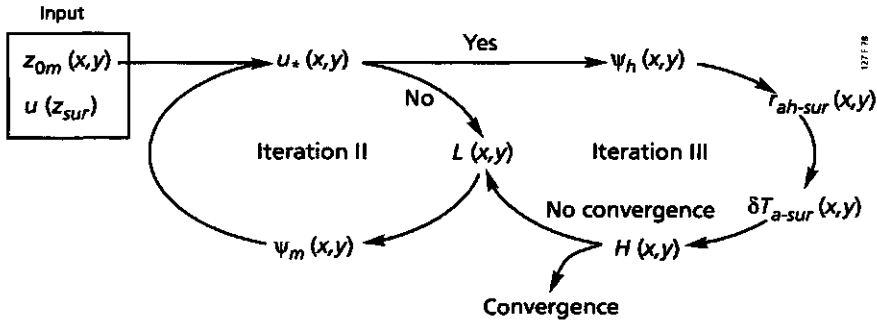


Fig. 7.8 Iterations II and III for the inclusion of distributed friction velocities u_* and sensible heat flux densities H in the distributed Monin-Obukhov lengths, L

7.7 Latent heat flux density

Step 36. Latent heat flux density, $\lambda E(x,y)$

For conditions of zero horizontal advection at $z < z_{sur}$, λE can be obtained as the residual of the energy budget theorem:

$$\lambda E(x,y) = Q^*(x,y) - G_0(x,y) - H(x,y) \quad (\text{W m}^{-2}) \quad (7.61)$$

Alternatively, it would have been possible to calculate λE on the basis of Eq. (3.40) because all ingredients for quantifying c_3 and c_4 already have been discussed. It should yield exactly the same results as Eq. (7.61).

According to the theory presented in Chapter 3, the $\lambda E(x,y)$ values should have a link with the surface resistance r_s of one-layer schemes. The long route in obtaining λE from Q^* , G_0 and H was necessary because a direct mapping of actual r_s values by alternative means is currently impossible and r_s determines the actual evaporation rate. At this stage however, r_s can be obtained by inversion of Eq. (3.33) (see also Section 5.2). It is recommended to do this for a few wet and dry land surface elements in order to check the consistency between vapour flux density λE , vapour gradient $e_{sat}(T_0) - e$, aerodynamic resistance r_{av} , surface resistance r_s , and soil water content θ variations. For wet surfaces, r_s should be approximately $0-70 \text{ s m}^{-1}$ (Monteith, 1994), whereas for dry surfaces $r_s > 500 \text{ s m}^{-1}$ holds.

7.8 Concluding remarks

The research aims stated in Chapter 1 included establishing the semivariograms and the probability density functions of the various land surface flux densities and associated moisture indicators at a scale where natural variations are evident. SEBAL is based on the flux-profile relationships in combination with the Monin-Obukhov similarity hypothesis to correct the non-uniqueness between flux density and gradient in combination with a surface energy budget, which makes the algorithm *generally applicable*. Nevertheless, several intermediate steps have a semi-empirical character which may be improved in future if more sophisticated sensors become operational and more land surface physical attributes mentioned in Table 1.1 can be measured directly.

The high accuracy of T_0 to be used in sensible heat flux density estimations (error ≤ 0.5 K: Brutsaert et al., 1993) is no longer required: δT_{a-sur} is solved from H , rather than from T_0 and T_a separated. Although T_0 is still needed to spatially interpolate δT_{a-sur} , the standard error of T_0 becomes to a certain extent irrelevant (it only affects c_{27} and c_{28} , not H). Also the role of kB^{-1} is less critical because the maximum value for H is purely established by $Q^* - G_0$ and δT_a^{max} will be adapted according to a predefined value for kB^{-1} .

A flow chart version of Table 7.1 is presented in Figure 7.9. The computation step numbers of the algorithm are indicated in succession for the entire calculation procedure. At the current stage of investigation, it has not been fully explored whether the individual empirical solutions at specific computation steps are universally applicable or not. The semi-empirical expressions are of two different types: (i) the ground-to-ground regression curves with fixed regression coefficients and (ii) the image-to-ground regression curves with coefficients varying from image to image. The relationships of category (i) consists of:

- ε'_2 = $f(\tau_{sw})$ computation step 11
- $\varepsilon_0(x,y)$ = $f(NDVI(x,y))$ computation step 13
- $\Gamma(x,y)$ = $f(r_0(x,y), T_0(x,y), NDVI(x,y))$ computation step 18

Category (ii) comprises:

- $r_0(x,y)$ = $f(r_p(x,y), \tau_{sw}^n, r_a)$ computation step 8
- $T_0(x,y)$ = $f(T_{sat}(x,y), \tau_\lambda, L_{atm}^\uparrow)$ computation step 14
- $z_{0m}(x,y)$ = $f(NDVI(x,y))$ computation step 20
- $\delta T_{a-sur}(x,y)$ = $f(T_0(x,y))$ computation step 33

Although category (ii) is semi-empirical in character, its regression coefficients are determined for each image and they therefore are not bound to specific land surface and climate systems to which they are originally derived such as in category (i). The

application of category (i) therefore requires always due attention and category (ii) requires except the $\delta T_{a-sur}(T_0)$ relationship, access to ground data.

The advantage of SEBAL is that in comparison to other flux algorithms less ancillary ground data are needed. The volume of ground information is significantly reduced in comparison to for instance Kustas et al., (1994b) who used ground conventional measurements of u , K^d , T_a , U , z_{om} and d from the MONSOON database to apply their remote sensing algorithm. The necessity of conventional measurements can be categorized into 'minimal' and 'desirable' (Table 7.4). The parameters enumerated as 'minimal' should be measured in-situ *per se*. With 'desirable' is meant that these data are not strictly essential for the operation of SEBAL, but can be used if they are available.

Table 7.4 Necessity of ground measurements for use in the SEBAL package

Computation step	Minimal	Computation step	Desirable
8	τ_{sw} or r_0	12	L^d
12	T_a	20	z_{om}
14	T_0	21	kB^{-1}
20	h_v , LAI		

The suggestion to explore the extremes in H first by assigning pixels with $\Lambda \approx 0$ and $\Lambda \approx 1$ according to their position on the $T_0(r_0)$ relationship whereafter the dynamic range of δT_{a-sur} can be established by inversion, is considered to be an improvement in assessing H . Records with T_a are no longer needed and the accuracy of T_0 has less impact on the reliability of H . Moreover, a land use classification to assist the evaporation mapping (e.g. Thunnissen and Nieuwenhuis, 1985; Sucksdorff and Oettle, 1990), which is difficult to perform in arid regions because of low soil coverage (e.g. Azzali et al., 1990), is not required.

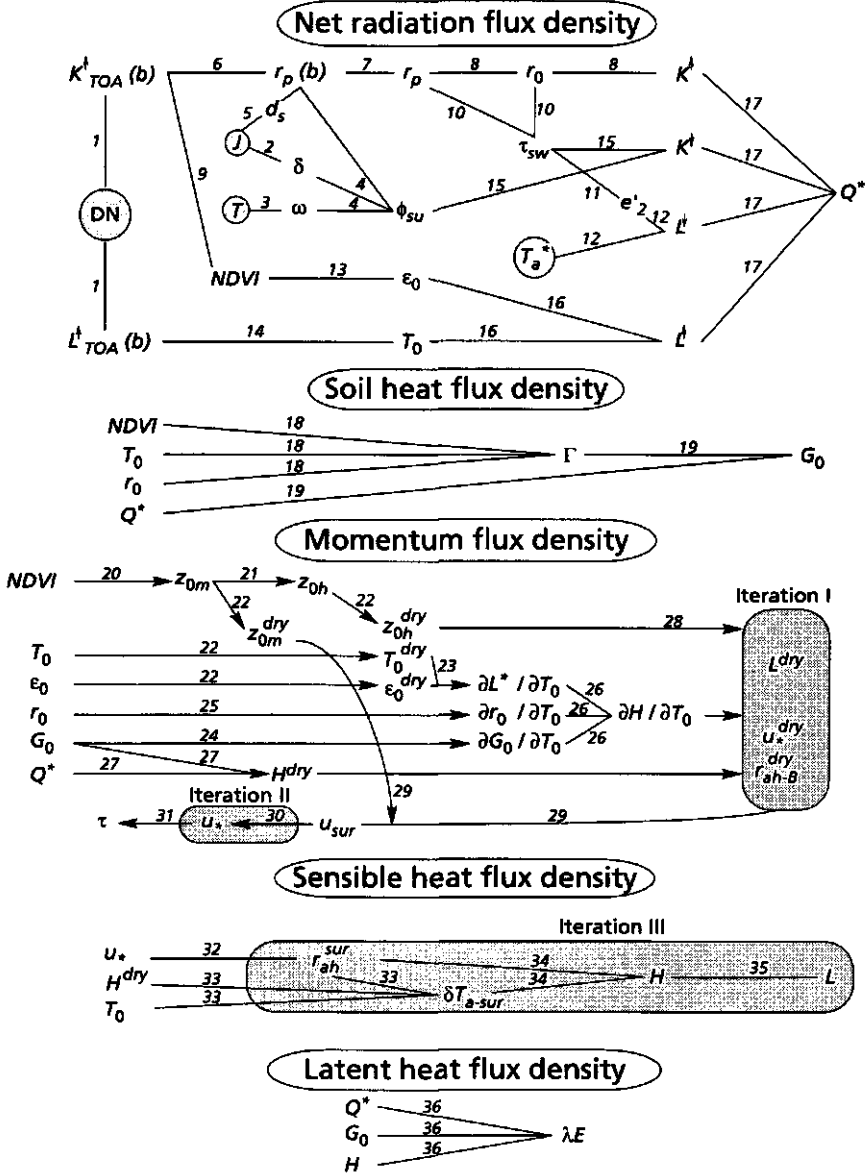


Fig. 7.9 Flowchart of the SEBAL procedure

The following assumptions are imbedded in the model formulation:

- The (semi-) empirical relationships between $r_0(r_p)$, $T_0(T_{sat})$, $\Gamma(r_0, NDVI, T_0)$, $T_0(r_0)$, $\delta T_{a-sur}(T_0)$, $\epsilon'(\tau_{sw})$, $\epsilon_0(NDVI)$ and $z_{0m}(NDVI)$ are valid to describe the environmental

- conditions. The latter does not imply that the coefficients in these relationships are the same for each area, for each acquisition time and for each length scale;
- Pixels with $r_0 < 0.10$ and a relative low T_0 -value on the T_0 -frequency distribution fulfill the condition $\Lambda \approx 1$ (which implies $\delta T_{a-sur} \approx 0$);
 - Pixels situated on the negative branch of the $T_0(r_0)$ relationship and $r_0 > r_0^{thresh}$ have zero evaporation and fulfill the condition $\partial_{\tau_0} \lambda E \approx 0$, $\lambda E \approx 0$ and $\Lambda \approx 0$;
 - Near-surface horizontal advection between the roughness length and the reference level z_{sur} chosen adjacent to the land surface can be eliminated from the surface energy budget if z_{sur} is restricted to less than 5% of the horizontal pixel size;
 - The area-representative momentum flux density above dry and variable moist land surfaces are approximately similar;
 - Area aggregation of land surface flux densities can be done by arithmetic mean procedures assuming that the edge effect between two land surface types does not seriously affect the regional representative flux density;
 - Atmospheric concentrations of dust, aerosols and gases are well mixed at meso scale allowing r_0 , NDVI and T_0 to be corrected for atmospheric perturbations uniformly;
 - The momentum flux density above dry land surfaces at 10% of the PBL height ($z = z_B$) is horizontally constant and is independent of surface features;
 - The Monin-Obukhov similarity hypothesis applies over heterogeneous terrain;
 - The surface roughness values for momentum and heat transport z_{om} and z_{oh} are lognormally distributed in heterogeneous landscapes;
 - Land surfaces behave as Lambertian reflectors;
 - Condensation does not occur during daytime, ($\lambda E \geq 0$);
 - The displacement height correction factor over large composite surfaces with sparse canopies is a complex phenomenon but may be ignored if $z_{sur} \gg d$ and flow is semi-smooth (distance between obstacles > 15 obstacle height);
 - The moist air density between the land surface and the reference height z_{sur} is constant over composite terrain;

In summary, the advantages and disadvantages can be evaluated as:

Advantages

- minimal collateral data required
- physical concept, and therefore applicable for various climates
- no need for land use classification
- no need to involve data demanding SVAT type of simulation models
- provision of semivariograms and probability density functions of the most relevant hydro-meteorological parameters involved in one-layer resistance schemes
- method is suitable for all visible, near-infrared and thermal-infrared radiometers, which implies that it can be applied at different spatial and temporal resolutions (which does not mean that a high accuracy is guaranteed for all combinations of scale and resolution)

- for high resolution images, the results can be verified with in-situ flux densities and local soil water content measurements
- modular approach

Disadvantages

- cloud-free conditions required
- presence of *drylands* ($\Lambda \approx 0$) and *wetlands* ($\Lambda \approx 1$) required
- surface roughness is poorly described
- only suitable for flat terrain

8 Surface flux densities and moisture indicators estimated with SEBAL: Validation, spatial variability and length scales

8.1 Validation of surface flux densities and moisture indicators

8.1.1 Validation strategy of surface flux densities

Due to the limited areal extent to which the natural variation of flux densities over heterogeneous land surfaces can be obtained from in-situ measurements, the flux densities estimated by remote sensing algorithms are usually difficult to validate. The availability of HAPEX type data however should be considered to be optimal for verifying the regional surface energy balance estimated from remote sensing data. Field measurements of turbulent flux densities by means of instrumented towers are representative for relatively small source areas, i.e. the footprint in the upwind direction which contributes to the establishment of a certain flux density. The orientation and length of this footprint in the upwind direction to which the measured flux density relates changes with surface parameters such as roughness length, displacement height and wind variables such as speed and direction (e.g. Itier et al., 1994). Schuepp et al. (1990) showed analytically that the contribution to the measured flux density from land surface elements adjacent to the tower is significantly higher than from land surface elements located at a distance x further away. The cumulative contribution as a function of distance x upwind to the flux density measurement F_{meas} at height z_{meas} reads as:

$$\frac{\int_0^x F_0(x) dx}{F_{meas}} = \exp\left(-\frac{u_{avg} z_{meas}}{u_* kx}\right) \quad (-) \quad (8.1)$$

where $x=0$ represents the position of the mast and u_{avg} is the average windspeed of the $u(z)$ profile between z_{0m} and z_{meas} to which u_* applies (Schuepp et al. 1990):

$$u_{avg} = u_* \frac{\ln(z_{meas}/z_{0m}) - 1 + z_{0m}z_{meas}}{k(1 - z_{0m}/z_{meas})} \quad (\text{ms}^{-1}) \quad (8.2)$$

According to Eq. (8.1), the cumulative flux density increases in a non-linear fashion with the distance x to the flux density measurement F_{meas} at $x = 0$ and $z = z_{meas}$. Unless the landscape is strictly uniform, the exact orientation of the source areas is crucial for validating the surface flux density maps based on remote sensing measurements. A

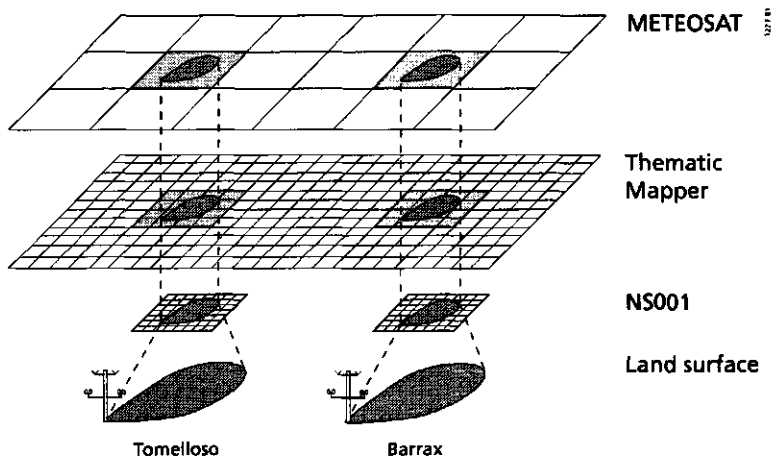


Fig. 8.1 Multi-scale validation procedure required for the verification of remote sensing-based surface flux density maps with different spatial resolutions. The NS001 is a Daedalus AAD1268 twelve channel multi-spectral scanner mounted on an aircraft

Table 8.1 Images and their spatial resolution used for flux density mapping in the Castilla la Mancha area during EFEDA. The Universal Transfer Mercator (UTM) coordinates refer to the upper left corner of each image

image	Super-site	Date of acquisition	Pixel resolution (m * m)	Number of pixels	UTM x	UTM y
Landsat-TM	Barrax	June 12	30*30 (120*120)	254700	568245.2	4333005.0
Landsat-TM	Tomelloso	June 12	30*30 (120*120)	254700	496408.5	4341615.0
Landsat-TM	Rado de Haro	June 12	30*30 (120*120)	254700	527309.5	4387130.0
Landsat-TM	la Mancha	June 12	30*30 (120*120)	12008668	439280.0	466739.5
NS001	Barrax	June 29	18.5*18.5	669774	568245.2	4333005.0
NS001	Tomelloso	June 29	18.5*18.5	669774	496408.5	4341615.0
METEOSAT	la Mancha	June 29	3933*4109	595	465312.0	4396503.0
METEOSAT	Iberia	June 29	3933*4109	50688	-97107.0	4877256.0

comparison of pixel-based flux densities against tower-based flux densities in composite terrain is only feasible if the pixel size is small compared to the size of the source area because Eq. (8.1) basically implies that the weighing coefficient is variable within the footprint and that small sized surface elements should be considered. Consequently, the validation of low resolution flux density-maps with pixels larger than the footprint, requires a nested calibration procedure between tower-based flux densities starting from high resolution flux density maps to low resolution flux density maps (Figure 8.1). Low resolution flux density maps may not be directly compared against turbulent heat flux densities measured in heterogeneous terrain. The latter validation philosophy has been

followed in this Chapter using data from different remotely operating radiometers. Different satellite resolutions and acquisition dates have been chosen to compute the surface flux densities for a range of areas (Table 8.1).

8.1.2 Validation of surface flux densities with NS001 data

Distributed hydro-meteorological parameters

The (semi-) empirical relationships on which SEBAL is based are presented in Table 8.2 with their local regression coefficients. The data reflect the mission NS001 flown during EFADA. The computation steps mentioned in Table 8.2 correspond with the codes used in Table 7.1. A 5 m level for z_{sur} was selected in this case study whereas the blending height was $z_B=100m$. The z_{om}/z_{oh} ratio was arbitrarily taken to be 10 ($kB^1=2.3$) and regionally constant.

Table 8.2 Conversion equations used in the SEBAL parameterization for the Tomelloso and Barrax sub-regions acquired with NS001 data on 29 June, 1991, at 10 21' GMT. The computation steps relate to Table 7.1

Computation step	Unit	Tomelloso sub-region	Barrax sub-region
8	$r_o(x,y)$	-	$-0.085+1.47r_o(x,y)$
13	$\epsilon_o(x,y)$	-	$1.009+0.047\ln[NDVI(x,y)]$
14	$T_o(x,y)$	K	$[T_{sat}(x,y)^4/0.91]^{0.25}$
15	$K^4(x,y)$	W m ⁻²	$1358*0.66*cos\phi_{sat}(x,y)/1.016^2$
18	$\Gamma(x,y)$	-	$T_o(x,y)/r_o(x,y) [0.32r_o^{*0.9}(x,y)+0.62r_o^{*0.9}(x,y)] [1-0.98NDVI^4(x,y)] 10^{-2}$
19	$G_o(x,y)$	W m ⁻²	$49.0+1.23T_o(x,y)$
20	$z_{om}(x,y)$	m	$\exp[-5.5+5.8 NDVI(x,y)]$
21	$z_{oh}(x,y)$	m	$0.01*z_{om}(x,y)$
25	$T_o(x,y)$	K	$292+305r_o-1160r_o^2+1330r_o^3$
30	$u(x,y)$	m s ⁻¹	$\{[(0.41 2.5)^{-1} \ln(5.0/z_{om}(x,y))-2.01]\}^{-1}$
30	$L(x,y)$	m	$\{[(0.41 8.5)^{-1} \ln(5.0/z_{om}(x,y))-0.43]\}^{-1}$
30	$L(x,y)$	m	$-[1175 u_o^3(x,y) T_o(x,y)]/[k g 151]$
32	$r_{oh-sur}(x,y)$	s m ⁻¹	$-[1175 u_o^3(x,y) T_o(x,y)]/[k g 167]$
32	$r_{oh-sur}(x,y)$	s m ⁻¹	$[0.41 u(x,y)]^{-1} \{ \ln[5.0/z_{oh}(x,y)] - \psi_h \}$
33	$\delta T_{e-sur}(x,y)$	°C	$-19.0+0.73T_o(x,y)$
33	$\delta T_{e-sur}(x,y)$	°C	$-13.3+0.61T_o(x,y)$

The linearized slope $\partial_{\tau_o} r_o$ of the 'radiation controlled' branch of Figure 8.11A could be obtained by linear curve fitting of the (r_o^{dry}, T_o^{dry}) data string, being selected by means of r_o^{trash} yielding $-0.0412 K^{-1}$ for Tomelloso and $-0.0768 K^{-1}$ for Barrax (Table 8.3). The average windspeed at the blending height after iteration 1 outlined at computation steps 26 to 28 became $4.5 m s^{-1}$ at 100 m elevation. The wind speed extrapolated from the Staring Centre tower near Casa de las Carrascas using a logarithmic profile with $z_{om}=0.033$ and a measured value of $u_{2.4}=2.2 m s^{-1}$ from the tower yielded $u_{100}=4.5 m s^{-1}$, which supports the concept of using the 'radiation controlled' branch of the $T_o(r_o)$ relationship to determine τ_B and \bar{u}_B . A similar procedure has been applied for the Barrax

sub-scene. The extremely flat $\partial_{T_0} r_0 = -0.0768 \text{ K}^{-1}$ slope for Barrax yielded to $r_{ah-B}^{dry} = 23.2 \text{ s m}^{-1}$, which is only feasible when the geostrophic wind speed is high ($u_{100} = 15 \text{ m s}^{-1}$ if $\bar{z}_{0m} = 0.04 \text{ m}$). Radiosoundings at the moment of the NS001 overpass were not available but the wind speed in the Blancarves Viejos area along the Gineta road was 5 m s^{-1} at a height of 1 metre, which confirms a significant momentum flux density at this place and time of image acquisition.

Table 8.3 Values of the first order derivatives of surface albedo r_0 and the surface flux densities L^\uparrow , G_0 , H , and λE with respect to surface temperature on the dry-lands of the Tomelloso and Barrax super-sites on 29 June, 1991 at 10 21' GMT

Slope	Unit	Tomelloso sub-scene	Barrax sub-scene
$\partial r_0 / \partial T_0^{dry}$	K^{-1}	-0.0412	-0.0768
$\partial L^\uparrow / \partial T_0^{dry}$	$\text{W m}^{-2} \text{ K}^{-1}$	-6.85	-6.45
$\partial G_0 / \partial T_0^{dry}$	$\text{W m}^{-2} \text{ K}^{-1}$	1.23	2.64
$\partial H / \partial T_0^{dry}$	$\text{W m}^{-2} \text{ K}^{-1}$	22.4	48.1
$\partial \lambda E / \partial T_0^{dry}$	$\text{W m}^{-2} \text{ K}^{-1}$	0.0	0.0

Colour Plates 3 and 4 exhibit the spatial structure of λE for the Tomelloso and Barrax super-sites respectively after applying the equations mentioned in Table 8.2. A validation is presented in Figure 8.2. A calibration against one or more observed flux densities was not performed. It was just assumed that low r_0 and low T_0 pixels fulfil the condition $\Lambda = 1$ and $\Lambda = 0$ holds true for $r_0 > r_0^{fresh}$. This allocation procedure of 'dry' and 'wet' pixels was repeated for both sub-scenes. A total of 13 individual flux density towers were used for validation. Most of these control points (10) were situated at 5-15 km east of Tomelloso in the centre of Colour Plate 3. The Barrax data (3) were collected at La Gineta at 5 km east of the Barrax village.

The in-situ measured H and λE flux densities by the EFEDA participants had different integration times varying between 5 to 60 minutes so that a direct comparison with instantaneous SEBAL-flux densities was impossible to perform. To overcome these temporal inconsistencies, relative flux densities were estimated by means of Λ values (Table 8.4) so that the bias forthcoming from different time integrations is excluded. The original flux density data delivered by the EFEDA community is enumerated in Annex 3.

The turbulent flux densities were measured with eddy correlation, Bowen-ratio and flux density profile-energy budget methods (Moene, 1992); Experimental errors on these measurements have to be taken into account. According to the technique applied to measure H and λE , the Λ -error stemming from field measurements has been computed for each tower separately. Error bounds of 5% to the ground-based H -flux densities for eddy correlation, 10% for profile relationships measurements and 15% for Bowen-ratio's were assigned. The estimation of λE resulted in an error of 5% for the eddy correlation method, 15% for the Bowen-ratio method and 25% for energy budget residuals

(misinterpretations from Q' , G_o and H all affects λE). With this information, the absolute standard error of Λ measurements was calculated as:

$$|\Lambda - \text{error}| = \frac{\Delta \lambda E}{\lambda E + H} + \lambda E \frac{\Delta(\lambda E + H)}{(\lambda E + H)^2} \quad (-) \quad (8.3)$$

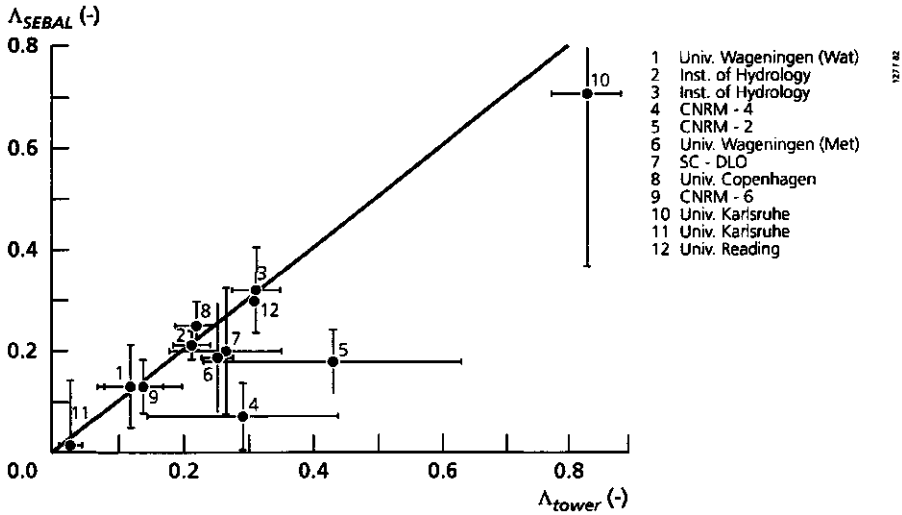


Fig. 8.2 Validation of the SEBAL derived evaporative fractions, Λ_{SEBAL} , using NS001 data against tower measurements of evaporative fractions, Λ_{tower} for 29 June 1991 in Tomelloso and Barrax at 10 21' GMT. The error bars are indicated according to the values presented in Table 8.4. The EFEDA participants are indicated by number. The footprint of each flux density tower is $92.5 \times 92.5 \text{ m}^2$ (after Bastiaanssen et al., 1995a)

where the $\Delta(\lambda E + H)$ error can be approximated according to:

$$\Delta(\lambda E + H) = \sqrt{\left[\left(\frac{\Delta H}{H} \right)^2 + \left(\frac{\Delta \lambda E}{\lambda E} \right)^2 \right]} (\lambda E + H) \quad (W \text{ m}^{-2}) \quad (8.4)$$

Each pixel on the upwind trajectory of a tower will leave a flux density signature in the air moving above it. The allocation of the pixels which needs to be areally aggregated and the weight of each individual pixel can be computed according to Eq. (8.1). Due to incomplete field data of the 13 individual stations on June 29, this procedure with pixel-dependent contributions to the measured flux density ($\int F_o(x) dx / F_{meas}$) could for this case unfortunately not be worked out and a more simple approach was followed: Two rectangular integration regions of (i) 5×5 and (ii) 7×13 pixels were chosen in the upwind direction and all pixels were given equal weight (i.e. the homogenous area approach). One times the standard deviation of the flux densities inside the integration regions was

Table 8.4 Data on evaporative fraction estimated with the SEBAL parameterization and in-situ tower measurements collected by various EFEDA participants during the Special Observation Period (see also Figure 8.2). The values between brackets are the standard deviations of the areally integrated at-pixel values (in the case of SEBAL) or standard measurement errors calculated with Eq. (8.3) (in the case of tower data), 29 June, 1991 at 10 21' GMT. Flux density stations 9, 10 and 11 are situated in **Barrax**, the other stations in **Tomelloso**

Flux density station	Institution	Land use	Coordinates	Ground-based	SEBAL	SEBAL
			UTM	Λ values	25 pixels	91 pixels
1	Univ. Wageningen (Wat)	Fallow	508919.50, 4333460.00	0.12 (0.06)	0.14 (0.08)	0.17 (0.09)
2	Inst. of Hydrology	Vetch	504440.39, 4333523.69	0.21 (0.03)	0.22 (0.04)	0.20 (0.06)
3	Inst. of Hydrology	Vineyard	509309.50, 4333010.00	0.31 (0.04)	0.33 (0.08)	0.30 (0.13)
4	CNRM-4	Vetch	504089.50, 4333580.00	0.29 (0.15)	0.08 (0.07)	0.17 (0.24)
5	CNRM-2	Vineyard	506309.50, 4332350.00	0.43 (0.21)	0.19 (0.06)	0.17 (0.07)
6	Univ. Wageningen (Met)	Vineyard	506009.50, 4332290.00	0.25 (0.03)	0.20 (0.11)	0.21 (0.10)
7	SC-DLO	Vineyard	505859.50, 4332320.00	0.26 (0.09)	0.21 (0.12)	0.20 (0.11)
8	Univ. Copenhagen [^]	Vineyard	506399.50, 4330940.00	0.22 (0.03)	0.26 (0.05)	0.25 (0.06)
9	CNRM-6	Fallow	576989.50, 4325240.00	0.14 (0.07)	0.14 (0.05)	0.14 (0.05)
10	Univ. Karlsruhe	Maize	575129.50, 4324070.00	0.82 (0.10)	0.72 (0.36)	0.54 (0.44)
11	Univ. Karlsruhe	Fallow	575039.50, 4324460.00	0.03 (0.01)	0.02 (0.13)	0.09 (0.13)
12	Univ. Reading [^]	Vineyard	509249.50, 4333250.00	0.31 (-)	0.31 (-)	0.31 (-)
13	Univ. Reading [^]	Vetch	504299.50, 4333580.00	0.28 (-)	0.25 (-)	0.25 (-)

[^]) data taken at June 28 from Bolle and Streckenbach, 1992

considered to be acceptable and a function of (i) the incorrect treatment of footprint contributions, (ii) the SEBAL error and (iii) the spatial variability.

It was concluded that all the data points in Figure 8.2 lie within the envelope of each point measurement. When the centre of each error bar is considered, the root mean square error between Λ_{tower} and Λ_{SEBAL} for the 13 observation points becomes

$\Lambda(\text{RMSE})=0.10$. The slope of the fitted line for a squared footprint of 25 pixels was 0.997 ($R^2=0.79$) while the rectangular footprint of 91 pixels induced a clearcut shift in the slope being 1.488 ($R^2=0.76$). From Table 8.4 we can see that the selection of the size of the footprint (25 or 91 pixels) mainly has consequences for flux density stations 4 and 10. The significant deviation from the 1:1 line of station 4 is therefore related to the selection of the integration pixels (station 4: 25 pixels $\Lambda_{\text{SEBAL}}=0.08$, 91 pixels $\Lambda_{\text{SEBAL}}=0.17$). Λ_{SEBAL} of CNRM-2 tends to have a poor performance at station 5 independently of the selected footprint. The wide error range of Λ_{tower} for station 5 in Figure 8.2 exhibits the difficulties of mapping λE over dry surfaces using the flux density-profile energy budget method. The vineyard measurements of stations 6, 7, 8 and 12 reveal that Λ_{tower} lies between 0.22 and 0.31. Since station 5 was separated not further than 1 km from stations 6, 7 and 8 and vegetation coverage did not differ from the other vineyards, the impression exists that at station 5 the evaporation rate has been over-estimated ($\Lambda_{\text{tower}}=0.43$). Although no generality is claimed, the examples illustrate the tendency to consider small integration areas when the same weight is given to all pixels (<100 m in horizontal length scale) for a measurement height of approximately 20 m. Latter statement agrees with Eq. (8.1) indicating that the main source area is found close to the tower.

8.1.3 Validation of moisture indicators with NS001 data

Besides ground observations of surface flux densities, a soil moisture monitoring program was executed (Droogers et al., 1993). The energy partitioning in arid conditions relates primarily to the available soil water storage (see Chap. 5). A comparison between the four defined moisture indicators β , Λ , α and r_s vs. near-surface soil water content is therefore a different yardstick that can be used to check the reliability of Colour Plates 3 and 4. Colour Plate 5 illustrates the Λ patterns in Barrax. An overlay of NS001 pixels with soil moisture plots can be directly made because footprint calculations are not needed which theoretically implies that validation can be focussed on one single pixel. Over 46 plots and 15 test fields (some fields were equipped with more plots), soil moisture was monitored at several standard depths between 5 and 50 cm. Six different test fields were located in the Tomelloso area (vineyard, vetch, bare soil). The Barrax area contained nine test fields (maize, fallow, barley, alfalfa). The incorporation of moisture data in Barrax is especially valuable, since the surface flux densities in Barrax could only be checked for three locations (see Table 8.4).

The field-averaged moisture conditions at 10 cm depth, θ_{10} , are plotted against the moisture indicators of that particular field and they compare well (Figure 8.3). Evidently, r_s shows the best relationship with θ_{10} . This finding can be explained by the dominant role of r_{soil} on r_s for partially covered soils and the dependency of r_{soil} on r_{sl} and D_0^{eff} (see Table 3.2 and Eq. (3.19)). The non-linearity between r_{soil} and θ but also r_c and θ for homogeneous bare soil and homogeneous canopy surfaces, respectively is widely

known. From Figure 8.3 the conclusion can be drawn that the non-linearity between a bulk surface resistance r_s and soil water content also holds for *heterogeneous* landscapes (vineyard, vetch, bare soil, maize, barley and alfalfa at different development stages, different soil types and different moisture depletion phases merged in one single graph). The relationship between β and θ_{10} is much weaker than for r_s and θ_{10} because β only considers λE , which includes besides r_s , also effects from $e_{sat}(T_0)-e$, and r_{av} . The same comment applies to Λ and α which do not depend on $e_{sat}(T_0)-e$ and r_{av} either. Surfaces with variations in $e_{sat}(T_0)-e$ but which are constant with respect to θ_{10} , respond with different λE (and consequently have different α , Λ and α values) at the same moisture content, which explains the large scatter in the $\beta(\theta)$, $\Lambda(\theta)$ and $\alpha(\theta)$ relationships. Furthermore it has to be remarked that g_1 in Eq. (3.17) and \bar{D}_0 in Eq. (3.19) are seemingly dominant over g_2 to g_5 because variation in r_s can be attributed to variations in θ_{10} .

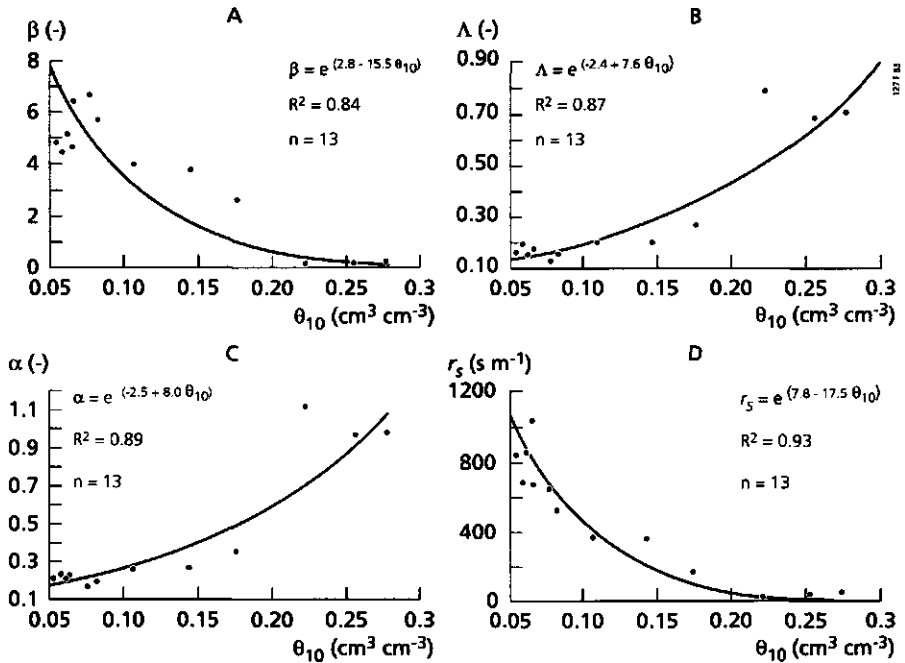


Fig. 8.3 The non-linear trend between the moisture indicators and volumetric soil water content at 10 cm depth (θ_{10}) for **Tomelloso and Barrax** enclosing a range of surfaces (vineyard, vetch, bare soil, maize, barley, alfalfa) and soils (reddish sandy loam, loamy sand, limestone) with different soil moisture conditions ($0.05 - 0.30 \text{ cm}^3 \text{cm}^{-3}$). (Part A) Bowen ratio β , (Part B) evaporative fraction Λ , (Part C) Priestley and Taylor α , and (Part D) bulk surface resistance r_s , 29 June 1991 at 10 21' GMT

8.1.4 Validation of surface flux densities with Thematic Mapper data

EFEDA's ultimate goal was to develop techniques to assess the bulk surface energy balance for a grid square that is typically 100 km * 100 km in size. It therefore remains necessary to deal with the entire EFEDA area, rather than studying separated fragments such as was done with the NS001 images and the super-sites in the previous sections. Terrain elements composed of agricultural crops and natural vegetation which have not been subjected to intensive research during the SOP should be considered in the regional surface energy balance. Colour Plate 7 and Figure (4.7) provide the boundaries of the TM image. The equations used to transfer the primary remote sensing data obtained from the Thematic Mapper measurements on June 12 into hydro-meteorological parameters are summarized in Table 8.5. The surface flux density map was validated against in-situ flux density data (Figure 8.4). Again, 13 flux density towers could be included in the comparison study, although they were not the same towers as were used in Figure 8.2. The original flux density data retrieved from the EFEDA flux density database of June 12 are reported in Annex 4 while a summary is provided in Table 8.6. The calculation of the footprints of the measured flux densities for the integration of the pixel-flux densities was done according to the model presented in Eq. (8.1) (Pelgrum and Bastiaanssen, 1995a). The

Table 8.5 Conversion equations applied in the SEBAL parameterization for the **Castilla la Mancha** region using TM data on 12 June, 1991, at 10 12' GMT. The computation steps relate to Table 7.1

Computation step	Parameter	Unit	Equation Unit
8	$r_o(x,y)$	-	$-0.062+1.61r_o(x,y)$
9	$NDVI(x,y)$	-	$-0.043+1.008 NDVI^{TOA}$
13	$\epsilon_o(x,y)$	-	$1.009+0.047\ln[NDVI(x,y)]$
14	$T_o^R(x,y)$	K	$[1.05T_{sat}(x,y)^4-50.3/\sigma]^{0.25}$
15	$K^k(x,y)$	W m ²	$1367*0.72* \cos\phi_{su}(x,y) 0.969$
18	$\Gamma(x,y)$	-	$\{T_o(x,y)/r_o(x,y)$ $[0.32r_o^{avg}(x,y)+0.62r_o^{avg}(x,y)]\}$ $[1-0.98NDVI^R(x,y)] 10^{-2}$
19	$G_o(x,y)$	W m ²	$-18+2.02T_o(x,y)$
20	$z_{om}(x,y)$	m	$\exp[-6.7+6.4 NDVI(x,y)]$
21	$z_{oh}(x,y)$	m	$0.01 * z_{om}(x,y)$
25	$T_o(x,y)$	°C	$19.2+44.1r_o+341r_o^2-762r_o^3$
30	$u_s(x,y)$	m s ⁻¹	$\{(0.41 3.2)^{-1} [\ln[5.0/z_{om}(x,y)]-\psi_n]\}^{-1}$
30	$L(x,y)$	m	$-[1230 u_s^3(x,y) T_o(x,y)]/[k g 100]$
32	$r_{ah-sur}(x,y)$	s m ⁻¹	$[k u_s(x,y)]^{-1} \{\ln[5.0/z_{oh}(x,y)]-\psi_n\}$
33	$\delta T_{a-sur}(x,y)$	°C	$-5.0+0.24T_o(x,y)$

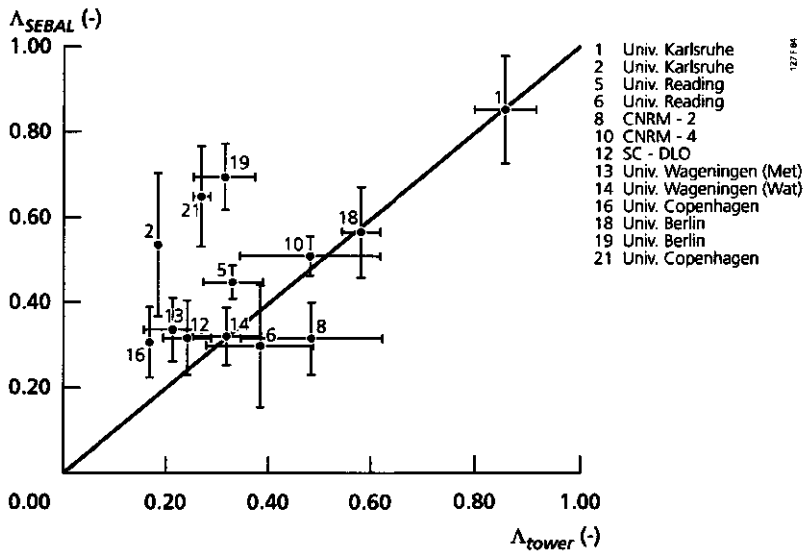


Fig. 8.4 Validation of the SEBAL derived evaporative fractions Λ_{SEBAL} against tower measurements of evaporative fractions Λ_{tower} for 12 June 1991 in **Castilla la Mancha**, at 10 12' GMT, (Landsat Thematic Mapper). The responsible institutes are indicated by number, are explained in Table 8.6 (after Bastiaanssen et al., 1995a)

total horizontal distance in the upwind direction from which approximately 100 % of measured flux density originates was at 1425 m and $z_{meas} = 15$ m. The required $z_{0m}(x,y)$ and $u(x,y)$ values to compute $\int F_0(x)dx/F_{meas}$ were taken from the z_{0m} and u -map as a result of computation step 20 and 30, respectively.

For reasons being similar as the NS001 study, the evaporative fraction was chosen to validate SEBAL-flux densities. From the total amount of 13 stations, 4 stations fell outside the envelope based on one times the standard deviation (68% probability level). As such, the performance is not as good as it was for the NS001 sub-scenes. The root mean square error with respect to the centre of the error bar is also much larger $\Lambda(RMSE)=0.19$. The mean Λ of all fields equipped with turbulent flux density measurements was $\Lambda_{tower}=0.45$ while SEBAL gave $\Lambda_{SEBAL}=0.49$ indicating that the overall SEBAL performance for an ensemble of land units is rather encouraging. Flux density stations 19 and 21, both located at Rada de Haro deviate the most from the 1:1 line. Λ_{SEBAL} is for these station unrealistically large for hillslopes cultivated in matoral and sunflower. Colour Plate 7 shows that the Rada de Haro super site has a striped pattern of r_s . It is not unlikely that the coordinates of stations 19 and 21 are more inaccurate than the remaining stations because the present author is not familiar with the field situation around Rada de Haro and accurate field maps were not available. One plausible reason of a different nature is a mis-quantification of r_{ah-sur} by SEBAL because z_{0m} in Table-8.5 is based on the crops grown in the flat Tomelloso and Barrax regions. The

undulating terrain of Rada de Haro induces however a geographical roughness which needs to be superimposed on the roughness for vegetation which was not accounted for. This leads to an underestimation of the actual z_{om} value, whereafter low H -flux densities and large λE -flux densities will emerge.

Table 8.6 Data on evaporative fraction estimated with the SEBAL parameterization and in-situ tower measurements collected by various EFEDA participants during the Special Observation Period (see also Figure 8.4). The values between brackets are the allowed deviations of the area-integrated SEBAL values or standard measurement errors calculated with Eq. (8.3) (in case of tower data), Landsat Thematic Mapper 12 June, 1991, at 10 12' GMT, 12 June, 1991. Flux density stations 1 and 2 were near Barrax, 18,19 and 21 at Rada de Haro and the remaining stations were set up at the Tomelloso super-site.

Flux density station	Institution	Land use	Coordinates UTM	Ground-based	SEBAL
1	Univ. Karlsruhe	Maize	575129.50, 4324070.00	0.86 (0.10)	0.85 (0.57)
2	Univ. Karlsruhe	Fallow	575039.50, 4324460.00	0.19 (0.02)	0.54 (0.23)
5	Univ. Reading	Vetch	504299.50, 4333580.00	0.33 (0.11)	0.45 (0.07)
6	Univ. Reading	Vineyard	509249.50, 4333250.00	0.39 (0.20)	0.30 (0.22)
8	CNRM-2	Vineyard	506309.50, 4332350.00	0.48 (0.25)	0.32 (0.19)
10	CNRM-4	Vetch	504089.50, 4333580.00	0.48 (0.25)	0.51 (0.05)
12	SC-DLO	Vineyard	505859.50, 4332320.00	0.24 (0.07)	0.32 (0.10)
13	Univ. Wageningen (Meteorology)	Vineyard	506009.50, 4332290.00	0.21 (0.11)	0.34 (0.08)
14	Univ. Wageningen (Water Resources)	Fallow	508919.50, 4333460.00	0.32 (0.12)	0.32 (0.08)
16	Univ. Copenhagen	Vineyard	506399.50, 4330940.00	0.17 (0.02)	0.31 (0.12)
18	Univ. Berlin	Field 2	533189.50, 4380680.00	0.58 (0.07)	0.56 (0.28)
19	Univ. Berlin	Field 3	533369.50, 4380560.00	0.32 (0.12)	0.69 (0.16)
21	Univ. Copenhagen	Sunfl.	534149.50, 4378490.00	0.27 (0.03)	0.65 (0.13)

8.1.5 Validation of moisture indicators with Thematic Mapper data

The relationship between soil moisture and soil moisture indicators was again established using the data of Droogers et al. (1993). The data presented in Figure 8.5 reflect the Tomelloso and Barrax super-sites. The more intensive regional vegetation activities on June 12 can be hold responsible for higher Λ values at the same soil water content as June 29: More water is extracted from the sub-layers by more intense rooting activities which enhances Λ . The obtained results of Figures 8.3 and 8.5 can be summarized as:

- The presence of soil moisture is of overriding importance for the energy partitioning in composited semi-arid terrain;
- Topsoil water content in sparse canopies can be obtained from visible and infrared (high and low resolution) images using the concept of moisture indicators and surface resistance in particular;
- The relationships between moisture indicators and near-surface soil moisture are time dependent which demands image dependent calibration lines;
- The fractional vegetation coverage affects the $r_s(\theta)$ relationship because of water uptake by roots from deeper layers.

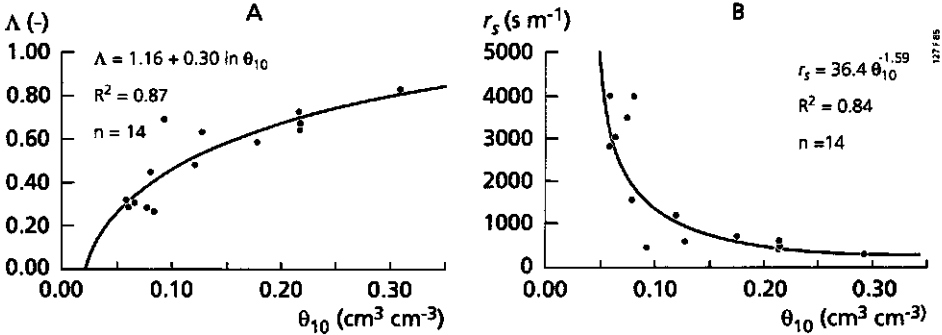
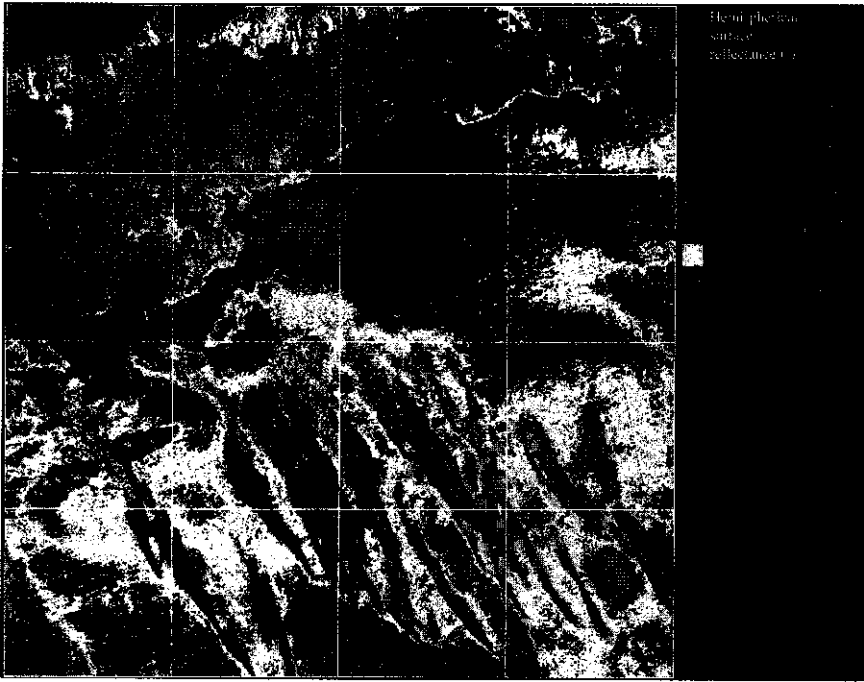


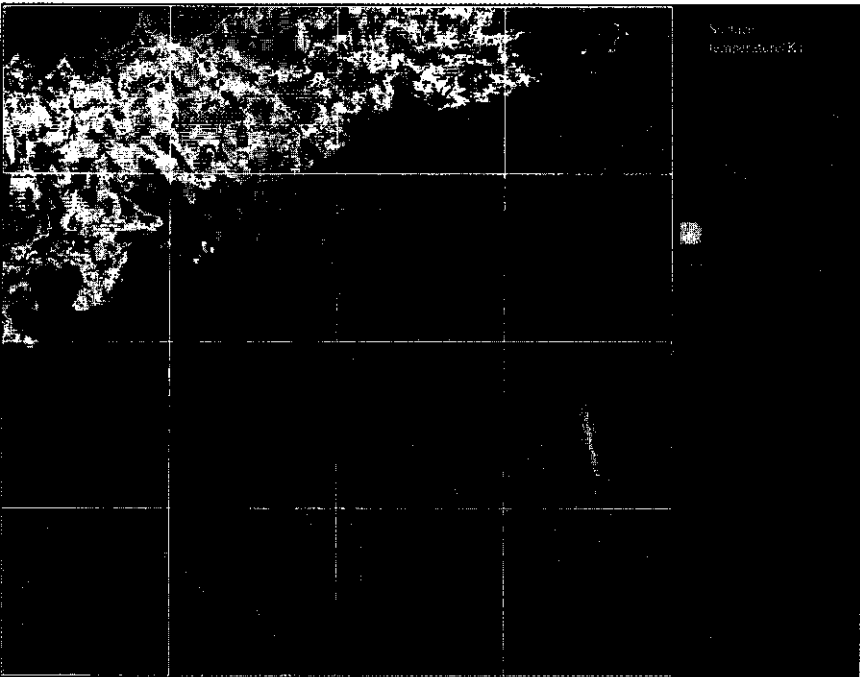
Fig. 8.5 Thematic Mapper based moisture indicators and volumetric soil water content at 10 cm depth, θ_{10} , across the entire EFEDA grid for a range of surfaces (vineyard, vetch, bare soil, maize, barley, alfafa) and soils with different soil moisture conditions (Part A) Evaporative fraction Λ , (Part B) bulk surface resistance r_s , 12 June, 1991 at 10 12' GMT, (after Pelgrum and Bastiaanssen, 1995b).

8.1.6 Low resolution observations in Egypt

A general shortcoming of the validation procedures discussed in Sections 8.1 to 8.5 is that only a small number of selected point observations, which represent a minor fraction of the total study area, could be involved in the validation study. An alternative way to obtain regional evaporation rates is by studying the water balance for closed systems



Colour Plate 1



Colour Plate 2



such as watersheds and deltas. Examples of these closed-basin types of hydrological studies in Egypt using numerical water balance models are the Qattara Depression FEMSATS model study performed by Bastiaanssen and Menenti (1990) and the Eastern Nile Delta SIWARE model study performed by Abdel Gawad et al. (1991). Since the latter case study had a more extensive data set with respect to evaporation and to condense the discussion, only the Nile Delta evaporation will be discussed shortly hereafter.

An area situated between longitude $26^\circ - 34^\circ$ East and latitude $26^\circ - 32^\circ$ North on 5 August 1986 was originally selected to estimate the evaporation of Lower Egypt (Pelgrum, 1992). It was attempted to solve the surface energy balance at each daytime hour using METEOSAT- based r_0 and T_0 data. The $T_0(r_0)$ relationship was investigated by considering 115×150 large sized pixels encompassing the Nile Delta, Western Desert and Mediterranean Sea .

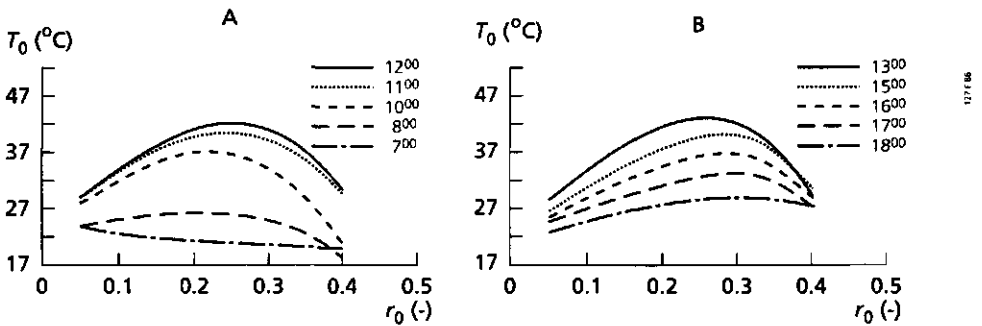


Fig. 8.6 Course of the fitted $T_0(r_0)$ characteristic throughout the day in an area between longitude $26^\circ - 34^\circ$ East and latitude $26^\circ - 32^\circ$ North in Lower Egypt based on METEOSAT measurements, 5 August, 1986

The typical half-moon shape between T_0 and r_0 appears between 10 00' and 16 00' hour when the thermal contrast between pixels is most evident (Figure 8.6). At a lower solar altitude, the $T_0(r_0)$ lines are less concave and F^2 becomes less than 0.40. The accuracy of determining the linearized $\partial_{T_0} r_0$ slope in the early morning and late afternoon to estimate $r_{ah-\theta}^{dry}$, u_B and τ is therefore low. Nevertheless, the SEBAL procedure has been repeated for each hourly image during daylight (12 images), yielding a set of $12 \times 115 \times 150$ instantaneous surface energy balances between 7 00' AM and 6 00' PM. Time integration of λE into E_{24} was achieved by combining all 12 instantaneous λE values for each individual pixel. The nighttime evaporation was set to zero. The 24 hour SEBAL evaporation rates obtained from low resolution METEOSAT study were compared with the 24-hour evaporation figures obtained from the SIWARE water balance simulation model of the Eastern Nile Delta (Abdel Gawad et al., 1991). The year 1986 was selected because SIWARE's water balance has been calibrated against discharge measurements

in the canal network for this period. The SIWARE model consists of a regional irrigation and drainage infrastructure and simulates agricultural water management practices within land elements attached to the surface water network. The actual evaporation is

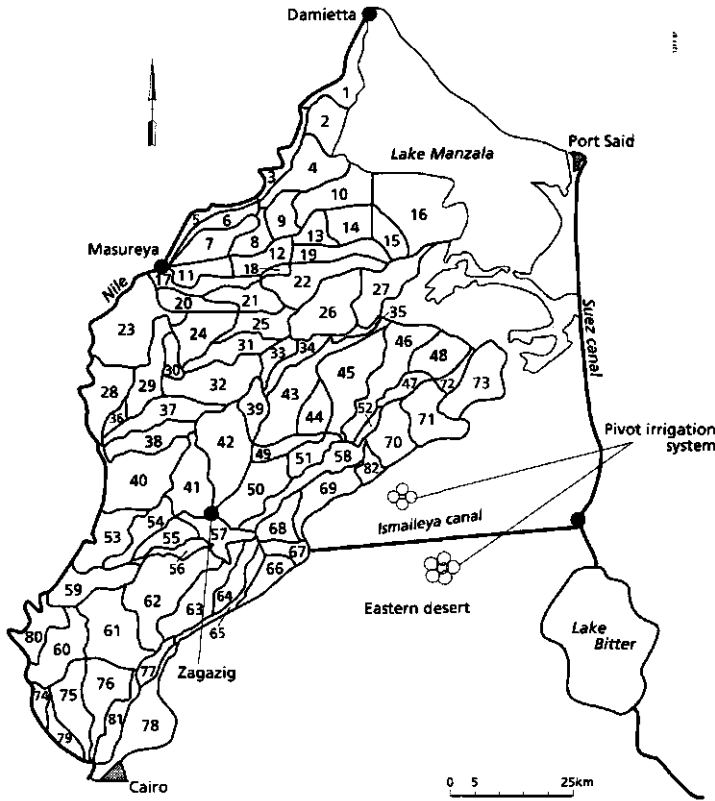


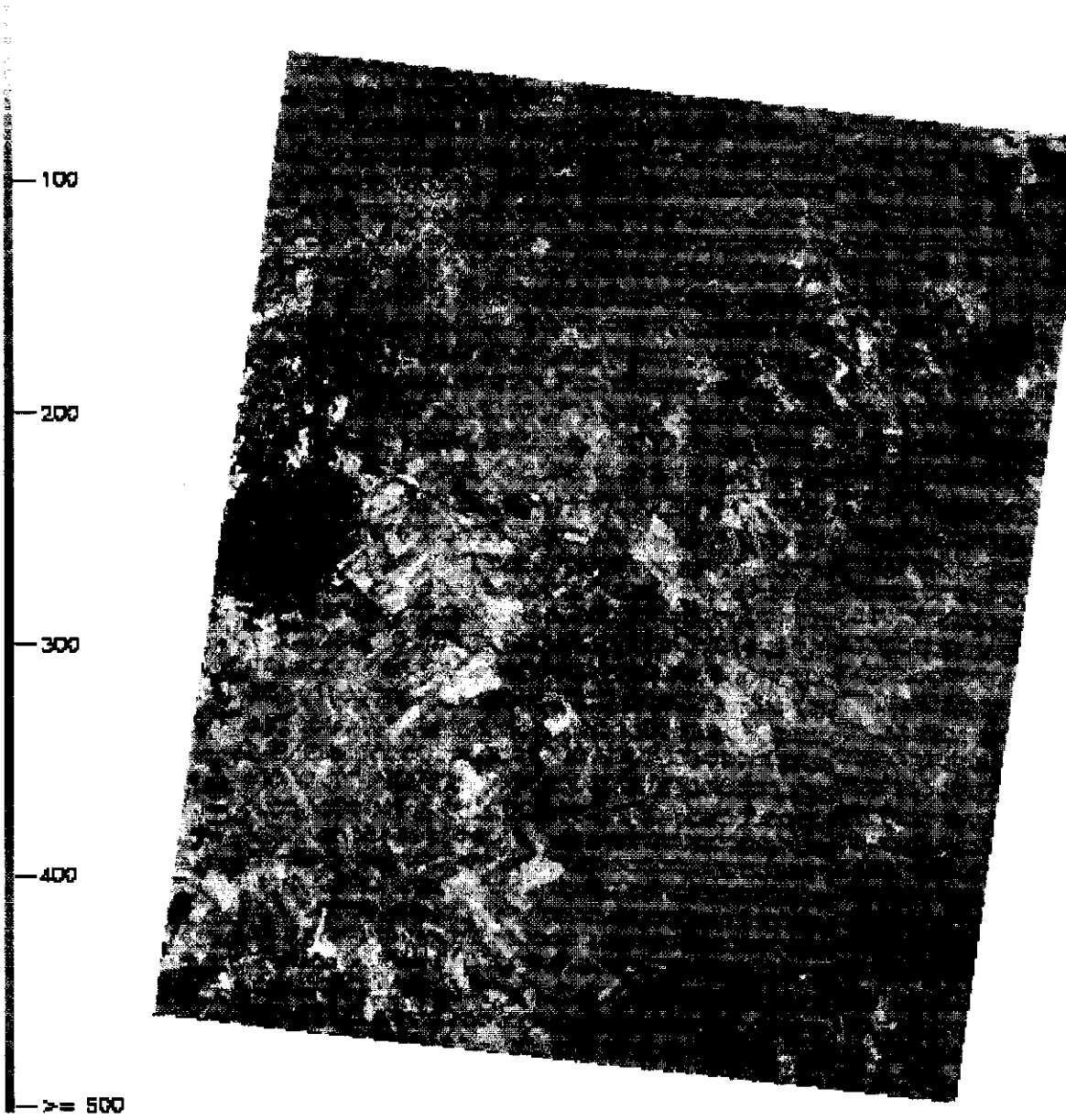
Fig. 8.7 Elements distinguished in the **Eastern Nile Delta** with indications of the main irrigation command areas (adapted after Abdel Gawad et al, 1991)

calculated for each land use category within each model element. The SIWARE network in the Eastern Nile Delta distinguishes 82 elements (Figure 8.7). The total gross irrigated area covered by the 82 elements is about 700,000 ha. A crude distinction was made between three small command areas in the southern part of the Eastern Nile Delta, namely Bassoseya, Abu Managa, and Sharqaweya, covering 14% of the gross area. The remaining 86% of the gross area is covered by Ismaileya, Rayah Tawfiki, and Mansureya (see Figure 4.4).

Colour Plate 6 shows the E_{24} -patterns according to SEBAL and SIWARE. Not surprisingly, the highest SEBAL evaporation rate arose, at Lake Manzalah and its surrounding swamps (6.0 mm d^{-1}). The evaporation from the Mediterranean Sea was

Latent heat flux density (W m^{-2})
Tomelloso, 29 June 1991

$\leftarrow \leq 0$



Colour Plate 3

0 5 km

Latent heat flux density (W m^{-2})
Barrax, 29 June 1991

- <= 0

- 100

- 200

- 300

- 400

- >= 500



Colour Plate 4



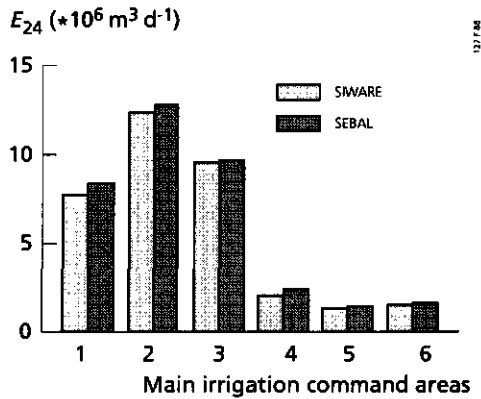


Fig. 8.8 The relative deviation of daily evaporation between SIWARE and SEBAL for the six main irrigation command areas. The numbers represents the (1) Ismaileya, (2) Rayah Tawfiki, (3) Mansureya, (4) Sharqaweya, (5) Bassoseya and (6) Abu Managa area (after Bastiaanssen et al., 1992)

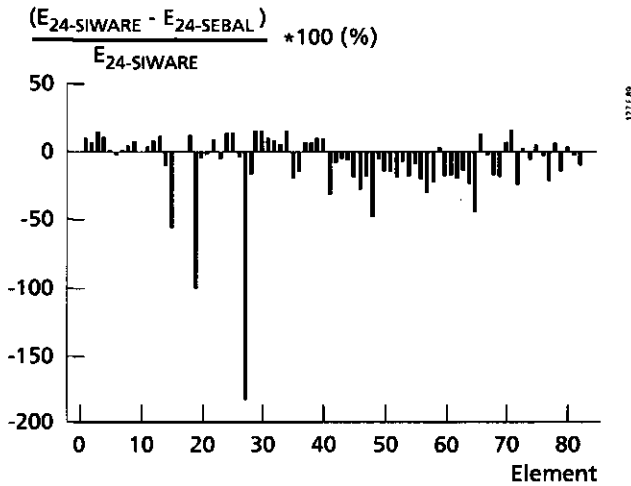


Fig. 8.9 Determination of the relative deviation of 24 hour evaporation values $\Delta E_{24}/E_{24} * 100$ for each of the 82 elements of SIWARE on August 5, 1986. The average value turned out to be $\Delta E_{24}/E_{24} * 100\% = -8\% \pm 26\%$ (after Bastiaanssen et al., 1992)

found to be slightly higher (7.0 mm d⁻¹). At irrigated land with spatial resolutions of 5 by 5 km, the maximum evaporation was found to be 5.1 mm d⁻¹. SIWARE predicted 5.9 mm d⁻¹ for element 40 which is adjacent to this place. Both SEBAL and SIWARE showed remarkably reduced E_{24} values just North of Cairo (elements 79,81). Again the agreement is acceptable with values around 5.0 mm d⁻¹ for SEBAL and from 5.1 to 5.5 mm d⁻¹ for SIWARE. Furthermore, SEBAL showed a significant areal evaporation gradient in the West-East direction along the desert fringe area from 5.7 mm d⁻¹ in the ancient irrigated

lands to 2.7 mm d^{-1} in the desert reclamation areas. SIWARE also shows a change of 5.8 to 2.7 mm d^{-1} for this transect.

For the 700,000 ha as a total, daily values of SEBAL appeared to be 5.1 % higher than the SIWARE predictions. A 5.1 % deviation is within the allowable range of the SIWARE model accuracy (which is 10% on an annual basis). The validation procedure can be further down-scaled to the level of a command area (Figure 8.8). The relative error at the level of command areas $\Delta E_{24}/E_{24}$ appeared to be surprisingly good with the mean of the six cases at $\Delta E_{24}/E_{24} * 100\% = -8\%$ (SD=6%). Notably Mansureya, Bassoseya and Abu Managa command areas show a nice agreement. A further down-scaling allows for extending the comparison study to the level of each element. The average deviations for the separated elements between SEBAL and SIWARE was $\Delta E_{24}/E_{24} * 100\% = -8\%$ (SD = 26%). With the exception of units 15, 19 and 27, the results are encouraging (see Figure 8.9). The findings for units 15, 19 and 27 could be attributed to a misallocation of the irrigation water delivery schedule in SIWARE after the summer crops were harvested and they should actually not have been included in the comparison study. Hence, the relative error increases when going from composite regions (5.1 %) and command areas ($8\% \pm 6\%$) to isolated elements ($8\% \pm 26\%$).

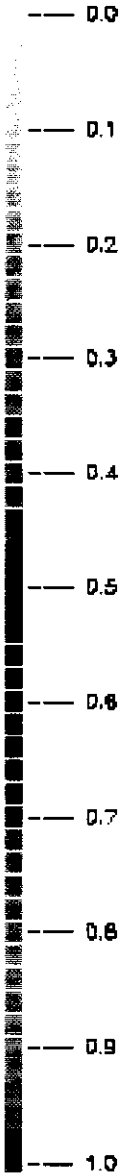
8.2 Spatial variability

8.2.1 Spatial variability of surface hemispherical reflectance, vegetation Index and surface temperature

During the NS001 mission, visible and infrared measurements were taken at flying altitude. Two pilot areas were chosen by the present author from the original E-F flight line illustrated in Figure 4.7, covering the super-sites with intensive field measurements in Tomelloso and Barrax. Table 8.7 shows the extent of ground data which has been consulted to interpret the NS001 spectral data into radiative properties of the land surface.

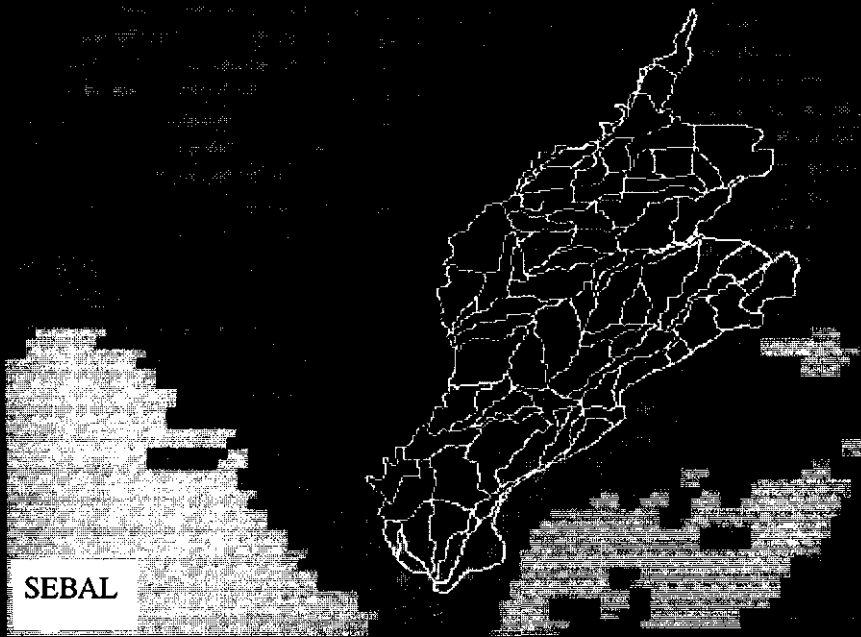
A consequence of irrigation practices in the Barrax region is a patchy type of agriculture with rainfed and irrigated parcels intermixed. The presence of wet-land farming ($r_0=0.10$ to 0.20, $NDVI=0.40$ to 0.77) and dry-land farming ($r_0=0.25$ to 0.35, $NDVI=0.26$ to 0.40) is evident on Figures 8.10A and 8.10B. The occurrence of r_0 values in the range

Evaporative fraction (-)
Barrax, 29 June 1991

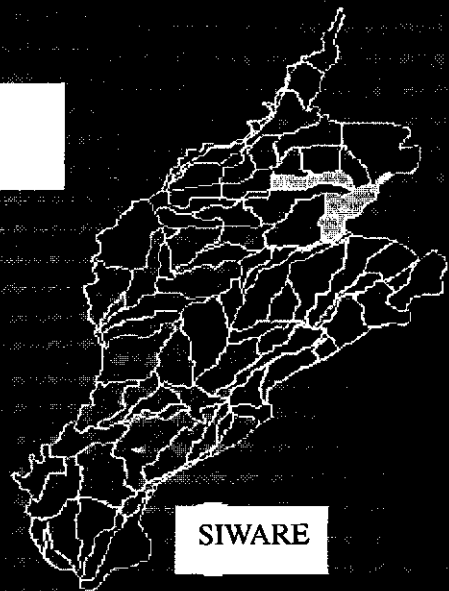


Colour Plate 5





5 August 1986
Evaporation (mm day⁻¹)



Colour Plate 6

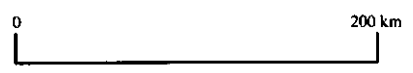


Table 8.7 In-situ measurements collected from the **Tomelloso** and **Barrax** super-sites used in the **SEBAL** parameterization for the **NS001** flight on 29 June, 1991.

Symbol	Unit	Tomelloso	Barrax	Source
τ_{sw}	-	0.66	-	SC-DLO
τ_{lw}	-	0.91	-	SC-DLO
L^{\downarrow}	W m ⁻²	470	-	SC-DLO
L^{\uparrow}	W m ⁻²	621	-	Various
r_o	-	0.20,0.22,0.28,0.30	0.06,0.16	Bolle and Streckenbach.,92
h	cm	20,48,58,59	60,76,80,82,86	Bolle and Streckenbach.,92

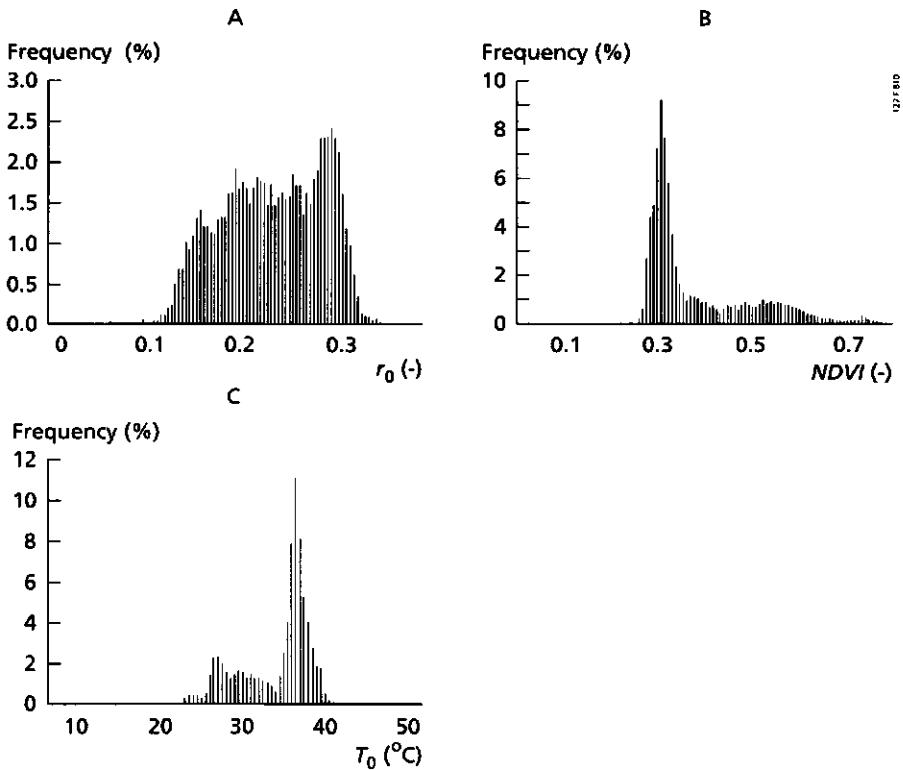


Fig. 8.10 NS001-based frequency distributions of (Part A) hemispherical surface reflectance r_o , (Part B) NDVI and (Part C) surface temperature T_o measurements of the **Barrax** super site on 29 June, 1991 at 10 21' GMT.

0.15-0.25 is related to the presence of vegetation with variable fractional cover and variable moisture deficit conditions. At dry-land patches, T_o was higher than at the irrigated patches. The lower T_o -range coincides with higher NDVI and lower r_o values (Figure 8.11). According to Carlson et al. (1990), the $T_o(NDVI)$ relationship is crop and

moisture dependent (see also Nemani and Running, 1989). The *NDVI* was significantly correlated with T_0 ($R^2 = 0.86$). Eq. (3.40) has shown that low T_0 values occur at intensive evaporation rates. Therefore Figure 8.11B has a diagnostic value in determining the canopy contribution to the latent heat flux density.

The $T_0(r_0)$ relationship of Barrax has an evident 'evaporation-controlled' branch with reduced T_0 values at low r_0 values (Figure 8.11A). Since pixels fulfilling the condition $r_0 \approx 0.10$ occur, these land surface elements should, according to the theory presented in Chapter 6, have a large evaporative fraction ($\Lambda \approx 1$). The transition from evaporation to radiation-controlled processes can be mathematically identified from the curve fitting shown in Figure 8.11A and lies at $r_0(\partial_{T_0} r_0 = 0) = 0.28$. The threshold hemispherical surface reflectance at which $\partial_{\lambda E} T_0 \approx 0$, $\lambda E \approx 0$ and $\Lambda \approx 0$ can be derived as $r_0^{thresh} = 0.30$. The latter value lies close to the r_0^{thresh} values found for the Egyptian deserts (Chapter 6).

The extensive viticulture practices around Tomelloso show less variation in the *NDVI*- r_0 - T_0 diagrams because the spatial variation in land use, land coverage and soil moisture status is in this specific area at the start of the summer season less developed (Bastiaanssen et al., 1994a).

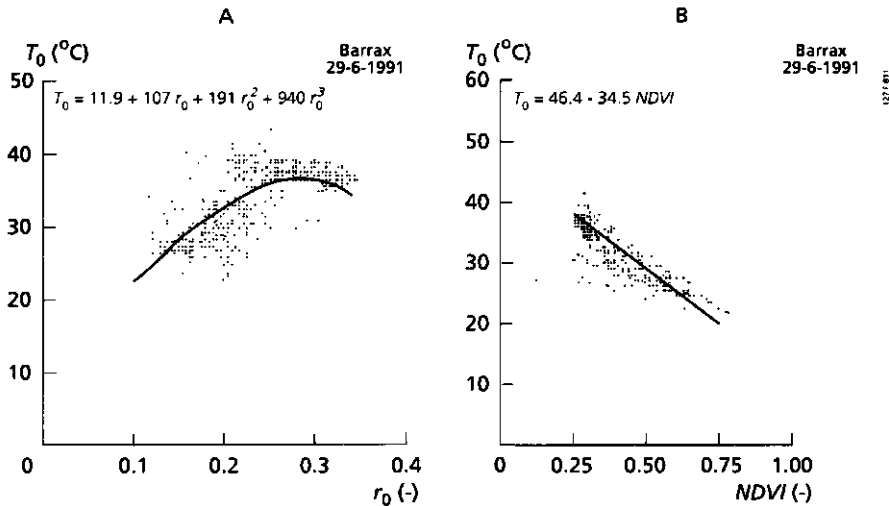
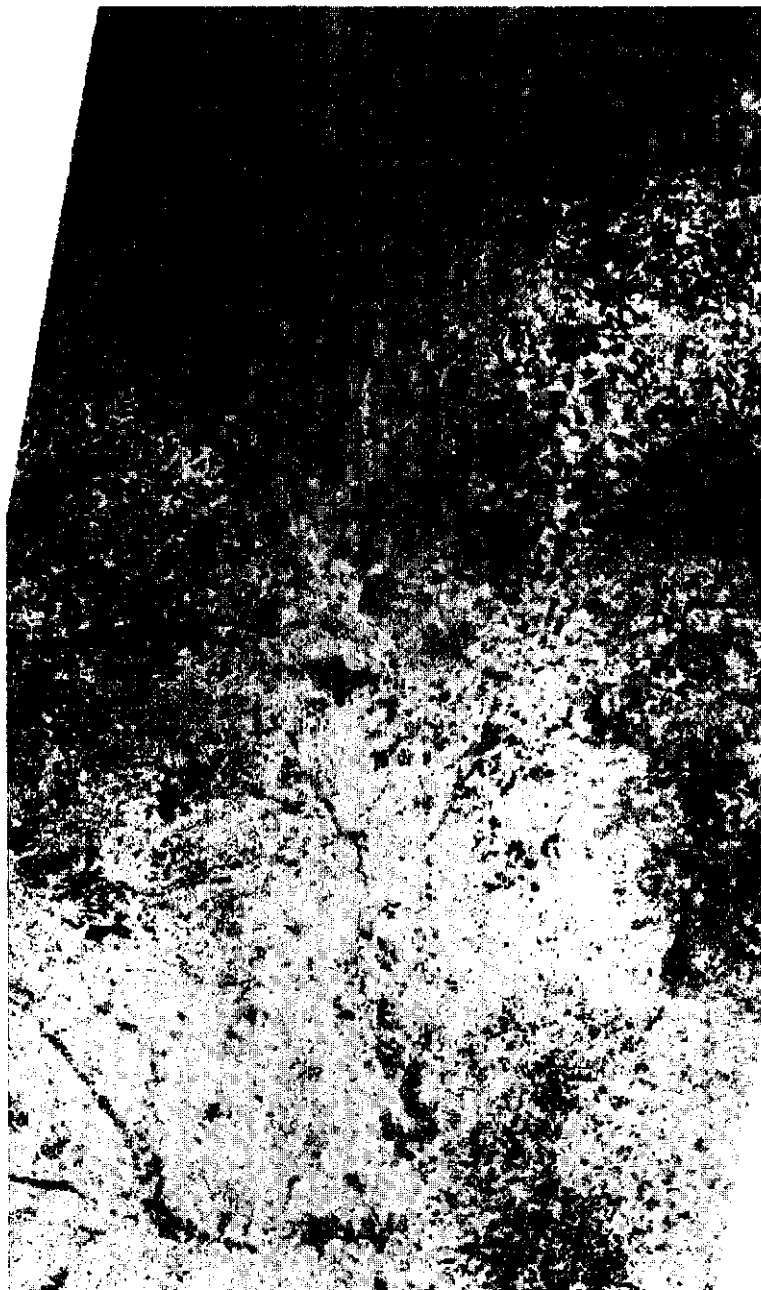


Fig. 8.11 (Part A) The $T_0(r_0)$ relationship to indicate wet and dry surfaces. (Part B) The $T_0(\text{NDVI})$ relationship to indicate the contribution of canopies to the regional evaporation, NS001, Barrax sub-region, 29 June, 1991, 10 21' GMT (after Bastiaanssen et al., 1994a)

Bulk surface resistance to evaporation ($s\ m^{-1}$)
Castilla la Mancha, 12 June 1991

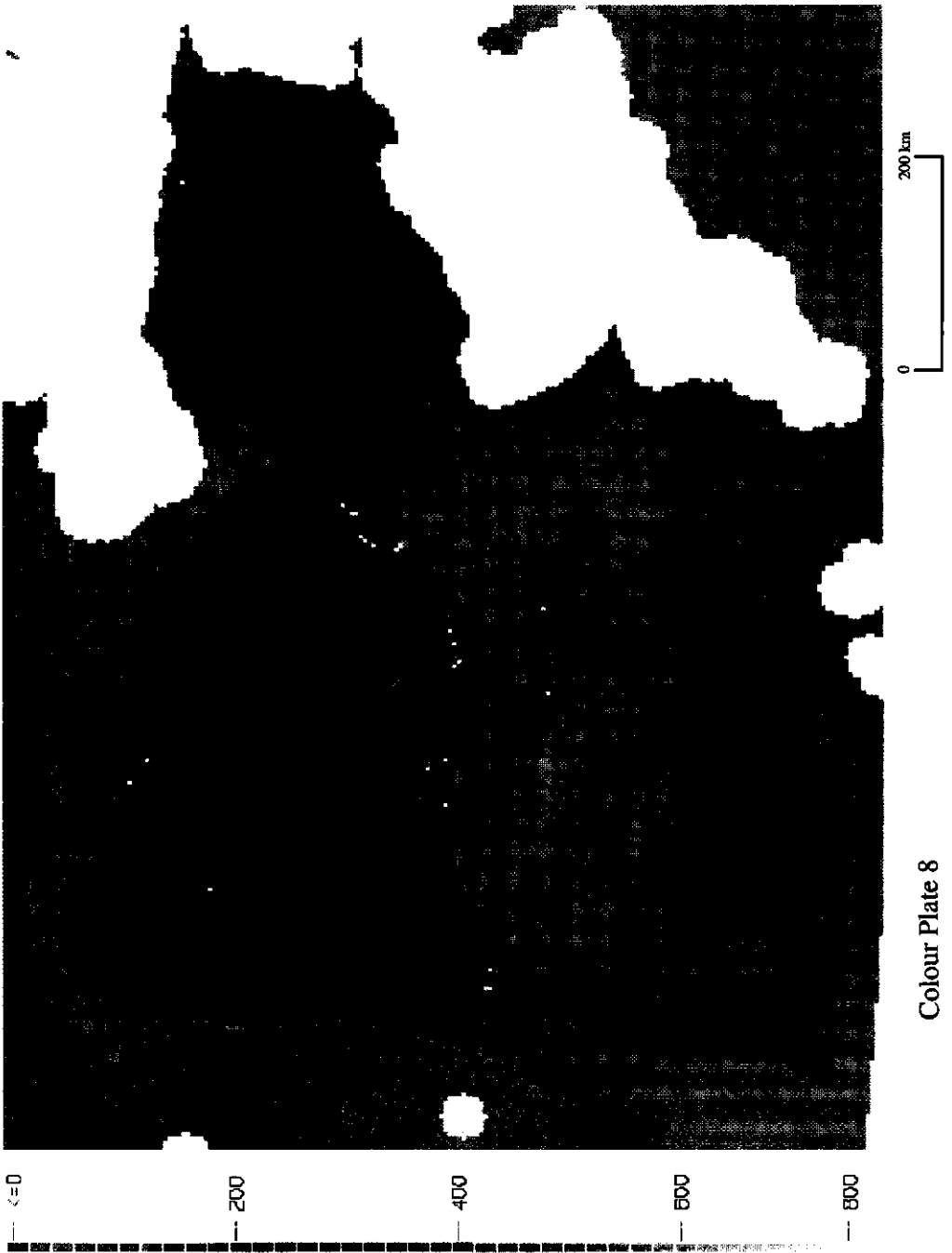


- 0
- 100
- 200
- 300
- 400
- 500
- 600
- 700
- 800
- 900
- >1000

0 30 km

Colour Plate 7

Bulk surface resistance to evaporation ($s\ m^{-1}$)
Iberian Peninsula, 29 June 1991



8.2.2 Length scale of land surface flux densities

The validated Λ -maps can be explored to study the semi-variograms on energy partitioning as introduced in Eq. (1.2). A number of 6 transects have been selected (3 North-South; 3 West-East) for each of the Barrax and Tomelloso NS001 sub-scenes. An example of the variogram of Barrax is given in Figure 8.12. Table 8.8 summarizes the sills and ranges of the twelve selected transects. On the basis of Table 8.8, it may be concluded that the semi-variance at sill-level in Barrax is larger than for Tomelloso, which can be confirmed from the large dynamic range of Λ due to more dispersed agricultural activities (compare Figs. 8.19 and 8.20 further on). Surprisingly, *the average correlation length of Barrax (3293 m) is smaller than the 3900 m found for Tomelloso*, which implies that the geometry of energy partitioning in Barrax is more regular than for Tomelloso, viz. wet and dry spots are regularly spread over the image. The latter finding can be verified with the aid of Colour Plates 3 and 4 which show indeed that some fields with large evaporation rates are located on the Northern part of the Tomelloso sub-scene and that natural vegetation around the Ruinera area are clustered in the Southern part. *Hence, the correlation length provides a suitable basis for understanding the effect of shifting from high to low resolution images on the areal distribution of surface flux densities and moisture indicators as was suggested at Figure 1.3.*

Table 8.8 Semi-variogram statistics on evaporative fraction with 18.5 m being the smallest sampling size (resolution NS001).

	Transect	Sill (-)	Range (m)		Transect	Sill (-)	Range (m)
Tomelloso	1	$1.8 \cdot 10^{-2}$	2500	Barrax	1	$1.8 \cdot 10^{-2}$	4000
Tomelloso	2	$1.2 \cdot 10^{-2}$	3000	Barrax	2	$2.5 \cdot 10^{-2}$	1400
Tomelloso	3	$1.3 \cdot 10^{-2}$	4000	Barrax	3	$1.5 \cdot 10^{-2}$	5000
Tomelloso	4	$1.2 \cdot 10^{-2}$	4500	Barrax	4	$1.2 \cdot 10^{-2}$	2000
Tomelloso	5	$1.5 \cdot 10^{-2}$	5500	Barrax	5	$1.6 \cdot 10^{-2}$	2000
Tomelloso	6	$1.2 \cdot 10^{-2}$	4000	Barrax	6	$3.0 \cdot 10^{-2}$	5000
Average		$1.4 \cdot 10^{-2}$	3900			$1.9 \cdot 10^{-2}$	3293

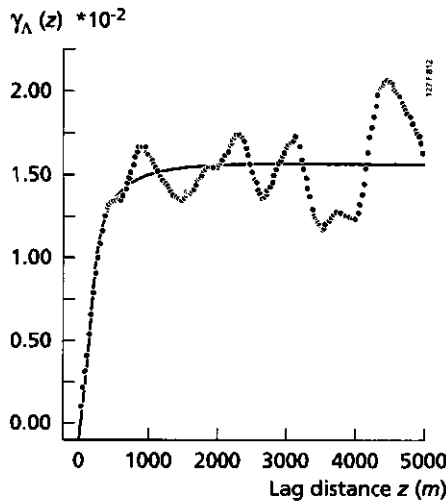


Fig. 8.12 Semi-variogram on evaporative fraction $\gamma_{\Lambda}(z)$ for a transect on the **Barrax** NS001 sub-scene, 29 June, 1991

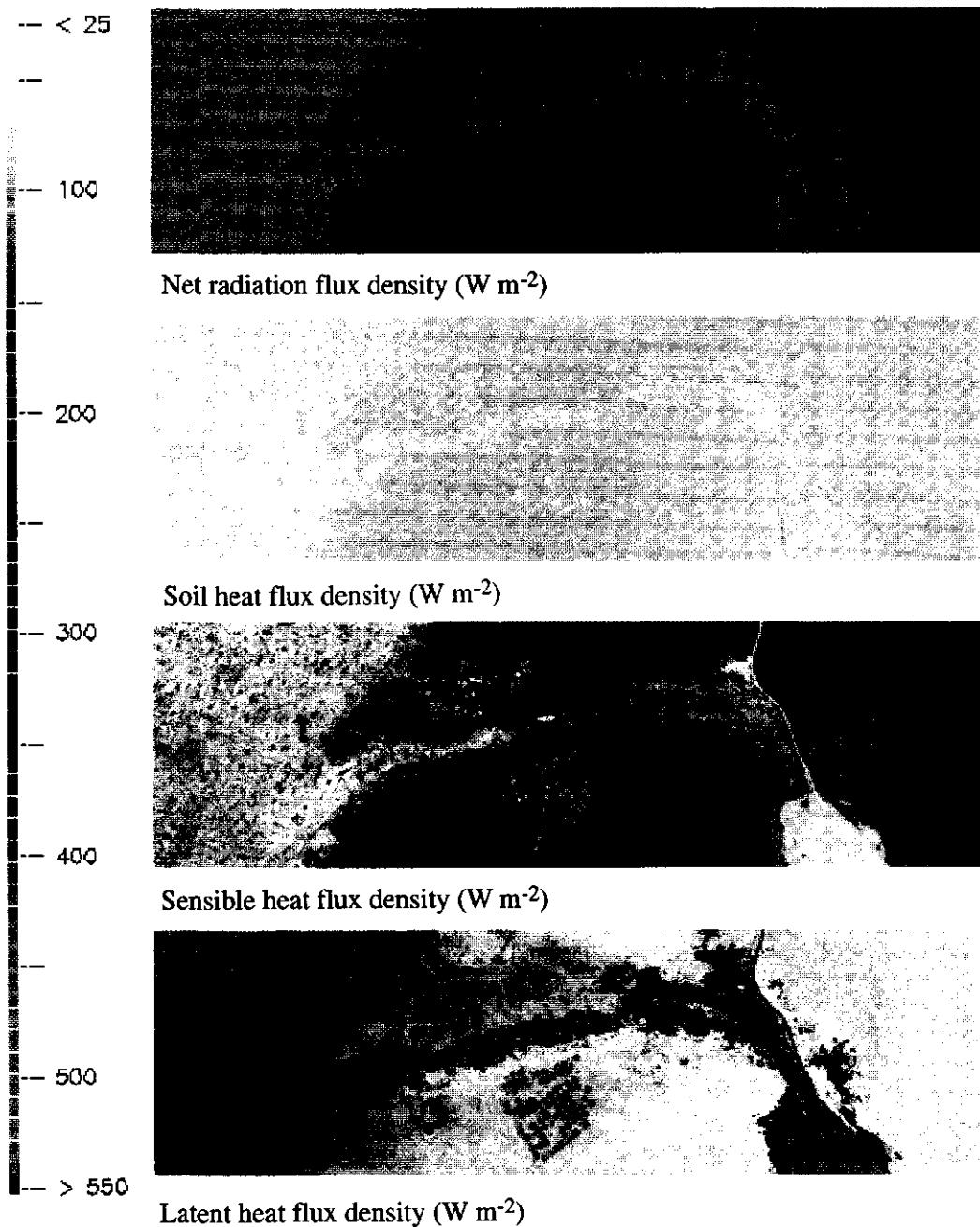
8.2.3 Multi-resolution land surface flux densities

A description of macro-scale surface energy balances, including the whole Iberian Peninsula, was obtained by considering $NDVI$ from NOAA-AVHRR and r_0 , T_0 from METEOSAT. On heterogeneous land surfaces, flux density F_0 is non-linearly related to r_0 (e.g. Eq. 6.12), $NDVI$ (e.g. Eqs. 6.13, 7.27) and T_0 (e.g. Eqs. 7.21, 7.50). Consequently, it is not self-evident that the true area-average \tilde{F}_0 can be estimated using the same remote sensing algorithm applied to \tilde{r}_0 , \tilde{NDVI} , \tilde{T}_0 :

$$\langle (F_{0-SEBAL}(r_0, NDVI, T_0))(x, y) \rangle \neq \tilde{F}_{0-SEBAL}(\tilde{r}_0, \tilde{NDVI}, \tilde{T}_0) \quad (-) \quad (8.5)$$

The value of \tilde{F}_0 obtained from \tilde{r}_0 , \tilde{NDVI} and \tilde{T}_0 with SEBAL can be validated both on the scale of one large sized pixel and a set of them. As stated before, the METEOSAT flux density maps cannot be compared with field measurements directly (pixel size larger than footprint size, see Table 8.8) and an intercomparison with the NS001 Λ -map was made (Figure 8.13). The agreement for Tomelloso was better than for Barrax which might be related to the large semi-variance of Λ_{Barrax} . Since \tilde{T}_0 METEOSAT covers a length of almost 4 km, each of the 'giant' pixels of Barrax encompasses an evident spatial variability (Figure 8.14). Since 4 km exceeds the average correlation length of 3293 m, $\Lambda_{Meteosat}$ for the Barrax pixels is entirely constant. *The larger correlation length of*

Eastern Nile delta, 27 July 1987



Colour Plate 9

Tomelloso that is approximately 4 km (note that it ranges between 2500 to 5500 m for the different transects) explains the larger scatter of $\Lambda_{\text{Tomelloso}}$ in Figure 8.13.

Hence, the reliability of a flux density determined from a single METEOSAT pixel varies with the degree of small-scale variability in land surface processes expressed by means of the semi-variance (sill level). The lower sill of Tomelloso as compared to Barrax (Table 8.8) explains the better agreement for the Tomelloso super site in Figure 8.13. If a set of METEOSAT pixels is considered, the error will tend to level off. The six full sized METEOSAT pixels of June 29 yielded at 10 00' GMT $\tilde{\Lambda}=0.46$ and $\tilde{\Lambda}=0.19$ for Barrax and Tomelloso whereas NS001 gave $\tilde{\Lambda}=0.34$ and $\tilde{\Lambda}=0.21$, respectively at approximately the same moment of acquisition. This reduces the error ($\delta\Lambda/\Lambda$) for Tomelloso to $0.02/0.21=10\%$ and Barrax to $0.12/0.34=35\%$. A completely different explanation for the differences noticed between $\tilde{\Lambda}_{\text{NS001}}$ and $\tilde{\Lambda}_{\text{Meteosat}}$ is the difference in areal coverage (see Figure 8.14). The calculations of Λ_{NS001} are based on the full NS001 scenes whereas the six METEOSAT pixels only cover the latter sub-scene by approximately 70%. In general it may be stated that the accuracy of SEBAL changes with the semi-variance, correlation length and the pixel size.

The DLR Falcon 20 aircraft was flown on June 19, 21, 25 and 28 and measured the turbulent flux densities at cruising altitude. This independent data source was used to validate a larger set of 595 METEOSAT pixels. The flight pattern on June 28 consisted of parallel legs to obtain the horizontal variability of the near-surface flux densities at 350 m height across the full EFEDA domain (Jochum et al., 1993a). The average evaporative fraction calculated according to Eq. (8.12) considering leg ML1, ML2, ML4, ML6 and ML7 gave $\tilde{\Lambda}=0.24$. A number of 595 METEOSAT pixels for an area of approximately 85 km * 125 km covering almost the entire EFEDA grid gave an average of $\Lambda=0.21$. Figure 8.15 illustrates the Λ -contour map from SEBAL calculations. Although there is a time span of 17 days between them, the general shape of Figure 8.15 with predominant East-West gradients can also be recognized on Colour Plate 7. Simulation results with the Peridot model, in which the land surface parameterization scheme of Noilhan and Planton (1989) is incorporated, also gave similar East-West gradients (Noilhan et al. 1995).

The upper right corner of Figure 8.15 shows gaps in the contour lines caused by clouds. Since this zone around the Embalse de Alarcon reservoir contributes significantly to $\langle \lambda E \rangle$ but could not be included in the spatial integration of $\lambda E(x,y)$ because of clouds, the actual METEOSAT- based $\tilde{\Lambda}$ -value should be slightly higher approaching the Falcon $\tilde{\Lambda}=0.24$ value rather well ($\Lambda_{\text{Meteosat}}-\Lambda_{\text{Falcon}} \approx 0.0$ to 0.02). A full comparison on a pixel-by-pixel basis with the Falcon flux densities could not be established, because the aircraft flew above the constant flux density layer at an altitude where the land surface flux densities are perturbed by sea breeze effects.

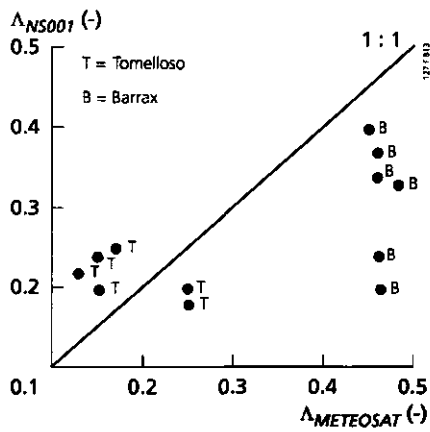


Fig. 8.13 Effects of image resolution (NS001 and METEOSAT) on the estimation of evaporative fraction Δ where T refers to Tomelloso and B to Barrax pixels, 29 June, 10 21', 1991 (after Bastiaanssen et al., 1995a)

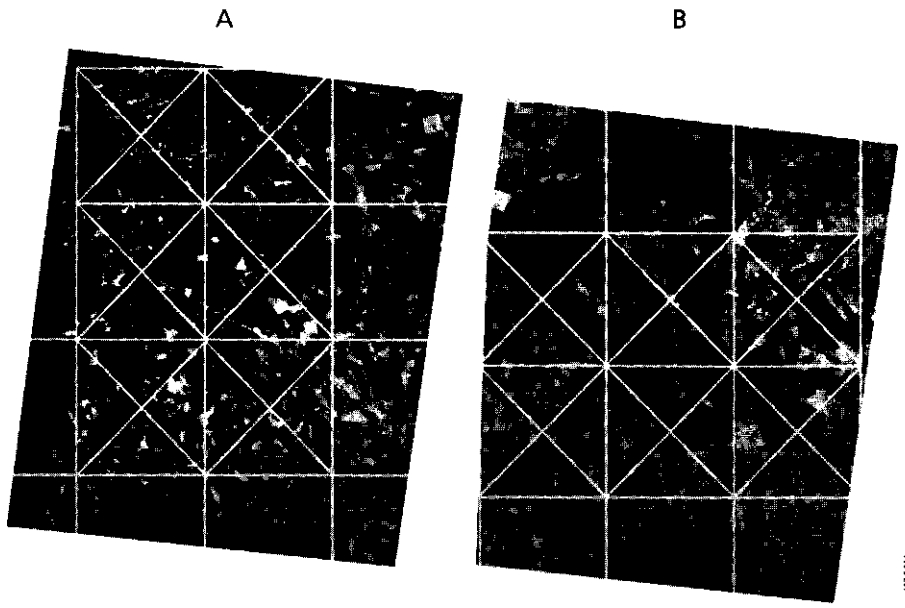
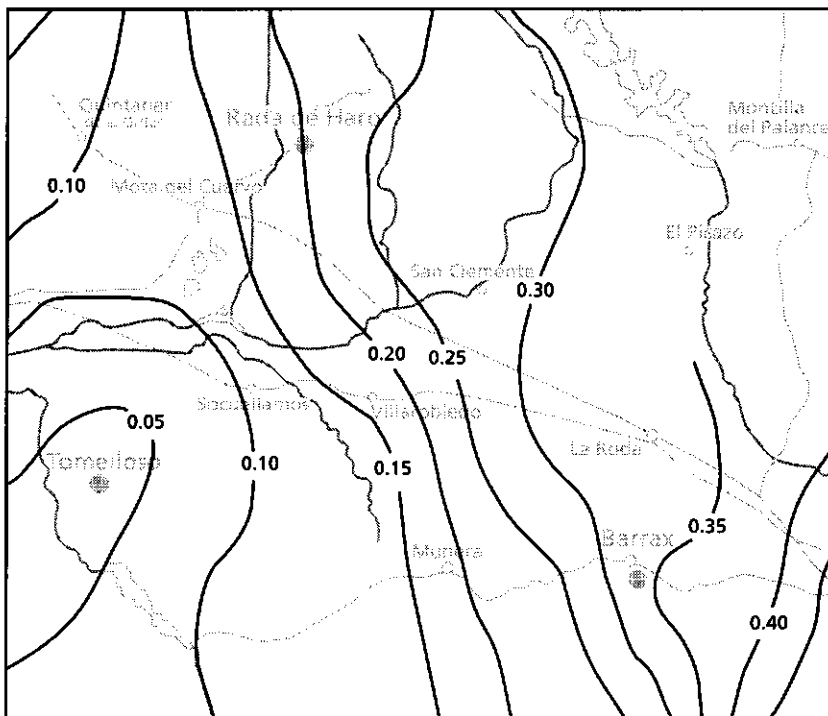


Fig. 8.14 Overlay of the METEOSAT and NS001 images (Part A) Tomelloso and (Part B) Barrax (after Pelgrum and Bastiaanssen, 1995a)



127/015

Fig. 8.15 SEBAL-based contour map of the evaporative fraction Δ interpreted from METEOSAT and NOAA-AVHRR measurements covering the entire EFEDA grid, 29 June, 10 00' GMT, 1991 (after Bastiaanssen et al., 1995a)

8.3 Space and time integration of surface flux densities and moisture indicators

8.3.1 Spatial integration in Castilla la Mancha

Whereas ground measurements are especially valuable for understanding the *temporal variation* of surface flux densities, the benefit of remote sensing lies in its ability to determine the *spatial variation* of the surface flux densities. The frequency distributions of Q' and λE could be compiled from the 862×777 individual balances for the validated Tomelloso super site (Figure 8.16).

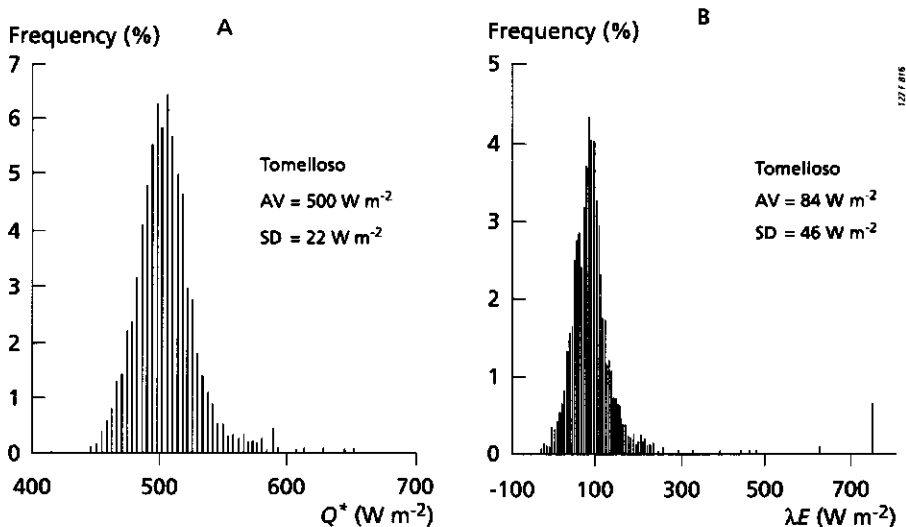


Fig. 8.16 Frequency distributions of (Part A) net radiation Q^* and (Part B) latent heat flux density λE for **Tomelloso** based on NS001 measurements on 29 June, 1991 at 10 21' GMT (after Bastiaanssen and Roebeling, 1993).

Since the r_0 , $NDVI$ and T_0 data array represents SEBAL's primary data source, the pdfs of Q^* , G_0 , H and λE should somehow reflect them: Q^* mainly follows the normal distribution of r_0 , G_0 relates to T_0 and $NDVI$ and H reflects T_0 . As a consequence of the residue approach, the feature of the λE pdf overlaps the pdf of all primary input data.

If the landscape exhibits disorganized variability on horizontal scales less than 10 km, the effects of convective transport can be disregarded (Type A, Shuttleworth, 1988). Under these conditions, surface flux densities can be mathematical averaged. The area-averaged surface flux densities can be used to find, in an inverse manner, the effective values of the resistances involved:

$$\langle Q^* \rangle = \frac{1}{n} \sum_{i=1}^n Q_i^*(x, y) \quad (\text{W m}^{-2}) \quad (8.6)$$

$$\langle H \rangle = \frac{1}{n} \sum_{i=1}^n H_i(x, y) \quad (\text{W m}^{-2}) \quad (8.7)$$

$$\langle \lambda E \rangle = \frac{1}{n} \sum_{i=1}^n \lambda E_i(x, y) \quad (\text{W m}^{-2}) \quad (8.8)$$

$$\tilde{T}_a = (1 - c_{11}) \tilde{T}_0 + c_{12} \quad (^\circ\text{C}) \quad (6.26)$$

$$\tilde{r}_{ah-sur} = \rho_a c_p \frac{\tilde{T}_0 - \tilde{T}_a}{\langle H \rangle} \quad (\text{s m}^{-1}) \quad (8.9)$$

$$\tilde{e}_{sat} = \frac{1}{n} \sum_{i=1}^n e_{sat}[T_0(x, y)] \quad (\text{mbar}) \quad (8.10)$$

$$\tilde{r}_s = \rho_a c_p \left(\frac{\tilde{e}_{sat} - e_{act}}{\gamma \langle \lambda E \rangle} \right) - \tilde{r}_{ah-sur} \quad (\text{s m}^{-1}) \quad (8.11)$$

$$\tilde{\Lambda} = \frac{\langle \lambda E \rangle}{\langle Q \rangle + \langle G_0 \rangle} = \frac{\langle \lambda E \rangle}{\langle \lambda E \rangle + \langle H \rangle} \quad (-) \quad (8.12)$$

With respect to the Tomelloso data, the Q' values appeared to be normally distributed with a mean value of $\langle Q' \rangle = 500 \text{ W m}^{-2}$ and a standard deviation of $\text{SD } 22 \text{ W m}^{-2}$ (Bastiaanssen and Roebeling, 1993). With $\langle r_0 \rangle = 0.22$ (see Figure 8.10A) and $\langle K^{\downarrow} \rangle = 740 \text{ W m}^{-2}$, $\langle L' \rangle$ becomes -77 W m^{-2} . Taking $\langle L' \rangle$ to be -77 W m^{-2} and $L^{\downarrow} = 470 \text{ W m}^{-2}$, it was feasible to find L^{\uparrow} as 547 W m^{-2} being equivalent to $T_0^R = 40.3 \text{ }^\circ\text{C}$. The $\lambda E(x, y)$ values showed a normal distribution which can be characterized by $\langle \lambda E \rangle = 84 \text{ W m}^{-2}$ and $\text{SD} = 46 \text{ W m}^{-2}$. Low λE values relate to harvested cereals and vetch pastures. The Tomelloso precipitation records during the SOP showed a monthly value of less than 20 mm so that the at-surface bare soil evaporation λE_i had become negligible. A latent heat flux density of 84 W m^{-2} at 10 21' GMT yields a daily integrated value of $2.86 \text{ MJ m}^{-2} \text{ d}^{-1}$ if the temporally stable Λ -approach is used (see Eq. 5.13), which is equal to 1.17 mm d^{-1} at 25°C .

The Q' patterns of Barrax showed more diversity than those of Tomelloso (Figure 8.17: $\langle Q' \rangle = 544 \text{ W m}^{-2}$; $\text{SD} = 15 \text{ W m}^{-2}$). Dry-land in Barrax has however a significant higher albedo ($r_0 = 0.28$) than the dry farmed ferro soils of Tomelloso ($r_0 = 0.23$). The lower reflectance in Tomelloso can be explained by the higher concentration of iron

conglomerates. The Q^* classes with the highest frequency are for Tomelloso and Barrax almost similar and these areas are the traditionally cultivated areas. Consequently, the available energy ($Q^* - G_0$) will be larger in Tomelloso which affects the maximum possible evaporation rate. The normal distribution of $\lambda E(x,y)$ below 180 W m^{-2} looks similar to the distribution identified at Tomelloso, revealing that the *evaporation statistics of dry-land farming are to a certain extent similar*. Since a large group of pixels also contributed to λE above 180 W m^{-2} , the overall evaporation was significantly higher ($\langle \lambda E \rangle = 158 \text{ W m}^{-2}$; $\text{SD} = 136 \text{ W m}^{-2}$) as compared to Tomelloso. The $\langle \lambda E \rangle$ -value can be converted by means of Λ into a 24-hour value of $5.37 \text{ MJ m}^{-2} \text{ d}^{-1}$ which is equivalent to 2.20 mm d^{-1} at 25°C .

The areal distribution of r_s is recognized as a means to describe variability in the water balance of watersheds (e.g. Hofstee et al., 1993). Colour Plate 7 shows the r_s -map for the entire EFEDA grid. The same patchy structure of r_s was also mentioned by Brunet et al. (1994) on the basis of field measurements. Figure 8.18 shows the frequency distribution of Λ and r_s . The class of pixels with $\Lambda > 0.6$ represents irrigated maize, wheat, alfalfa and berseem. Figure 8.18B shows that the bulk of the r_s -pixels lie between $20\text{-}150 \text{ s m}^{-1}$ which are favourable conditions for crop growth. According to the definition of Eq. (8.11), the Barrax area-representative value for \tilde{r}_s becomes 468 s m^{-1} and $\tilde{\Lambda} = 0.34$.

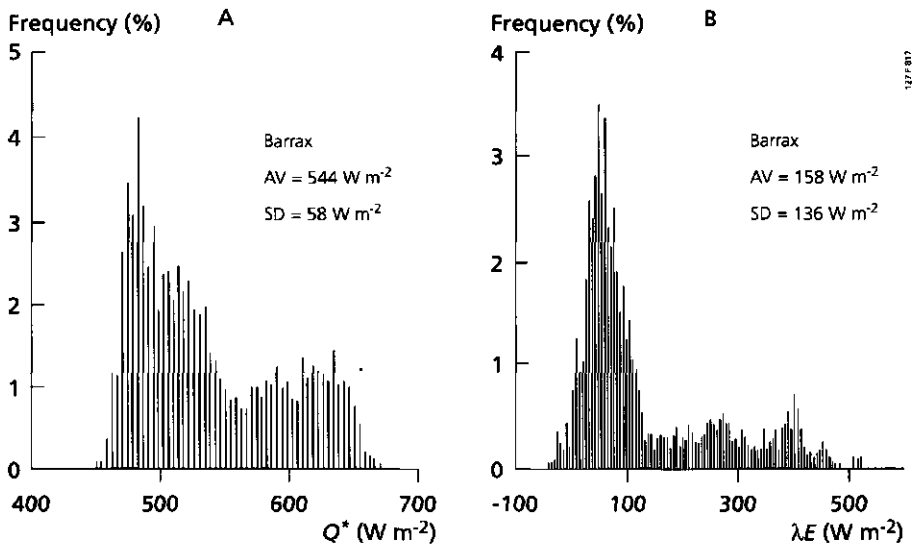


Fig. 8.17 Frequency distribution of (Part A) net radiation flux density Q^* and (Part B) latent heat flux density λE for Barrax based on NS001 measurements on 29 June, 1991 at 10 21' GMT (after Bastiaanssen and Roebeling, 1993)

The frequency distribution of the moisture indicators for Tomelloso are displayed in Figure 8.19. The traditional rainfed agricultural zones, representing the main part of the area, have a strongly reduced evaporation for this summer image with r_s ranging from 200-2500 $s\ m^{-1}$. The Barrax area-effective value for Tomelloso is $\tilde{r}_s=1541\ s\ m^{-1}$ and $\tilde{\Lambda} = 0.21$.

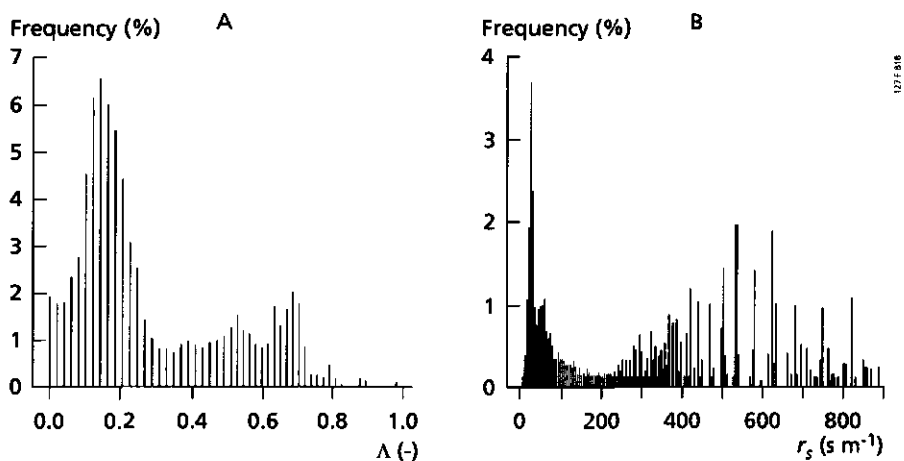


Fig. 8.18 Frequency distributions of (Part A) the evaporative fraction Λ and (Part B) the bulk surface resistance r_s for **Barrax**-based on 862×777 pixels with a size of 18.5×18.5 m each, NS001 (flight line E-F), 29 June 1991, at 10 21' GMT

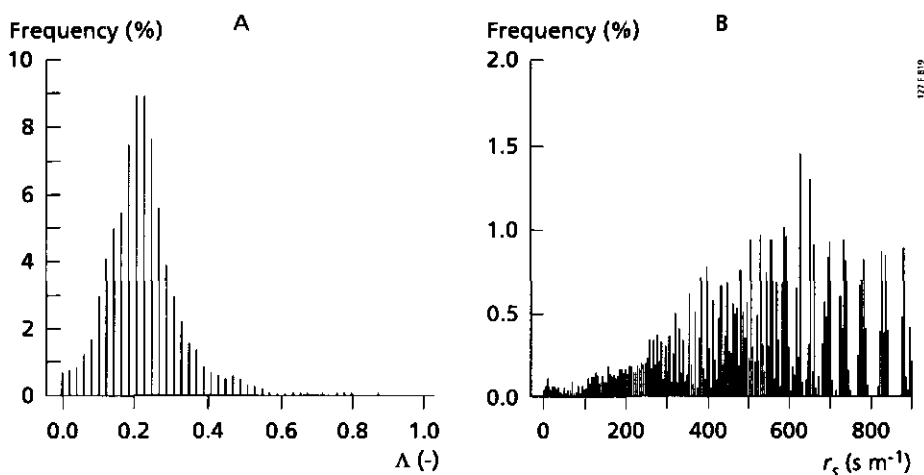


Fig. 8.19 Frequency distribution of (Part A) the evaporative fraction Λ and (part B) the bulk surface resistance r_s for **Tomelloso** based on 862×777 pixels with a size of 18.5×18.5 m², NS001 flight line E-F, 29 June 1991, at 10 21' GMT

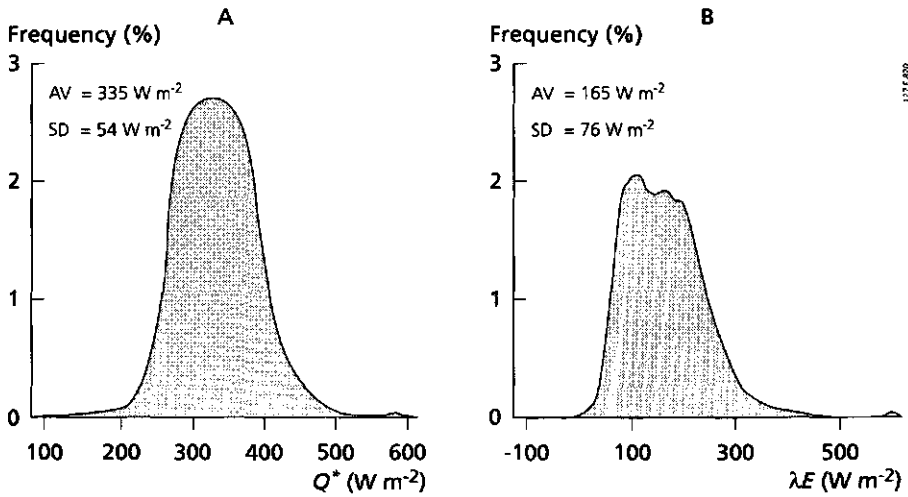


Fig. 8.20 Frequency distributions of (Part A) the net radiation flux density Q^* and latent heat flux density λE (Part B) for the entire EFEDA-grid based on 2668 * 4501 pixels with a size of 30 * 30 m each, TM, 12 June 1991, at 10 12' GMT (after Pelgrum and Bastiaanssen, 1995a)

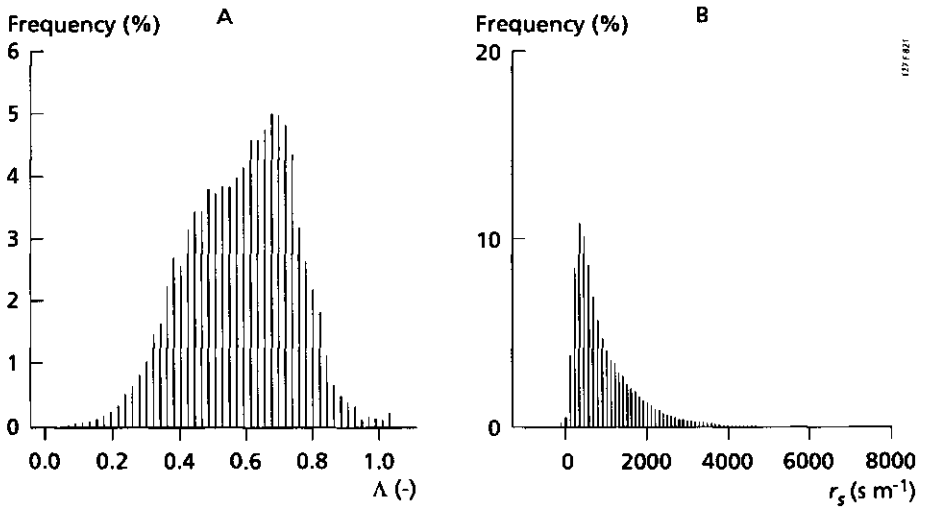


Fig. 8.21 (Part A) Frequency distribution of the evaporative fraction Λ and (Part B) the bulk surface resistance r_s for the entire EFEDA grid, with a resolution of 30 * 30 m² (120 * 120 m² for thermal infrared), Thematic Mapper, 12 June 1991 at 10 12' GMT, (after Pelgrum and Bastiaanssen, 1995a)

Merging all $\lambda E(x,y)$ pixels of the entire EFEDA grid based on the Thematic Mapper study of June 12 yields Figure (8.20). Three peaks may be noticed in the λE -pdf, which reflect the natural areas (170 W m^{-2}), the dry-land agriculture (100 W m^{-2}) and irrigated agricultural areas (210 W m^{-2}). Intermediate forms of land use lie in the range between $\lambda E=70$ to 220 W m^{-2} and cause a rather smoothed contribution of local evaporation to the regional evaporation. Figure 8.21 depicts Λ and r_s for the whole EFEDA grid. Obviously, June 12 shows higher Λ and lower r_s values as compared to the NS001 study on June 29 (Figures 8.18 and 8.19), indicating that a considerably dry-down phenomenon took place during the SOP. A direct comparison is only feasible for the Barrax and Tomelloso sub-areas.

Figure 8.22 shows the diurnal evolution of $\langle \lambda E \rangle$, $\langle H \rangle$ and $\langle \Lambda \rangle$ for the whole EFEDA area where $\tilde{\Lambda}$ is established according to Eq. (8.12) using the available $H(x,y,t), \lambda E(x,y,t)$ information of the 10×595 METEOSAT pixels (10 daytime slots on June 29, 1991). The latent heat flux density shows a remarkably flat behaviour throughout the course of day, which was also noted from the individual λE field flux density measurements at arable sites and vineyards (Bolle et al., 1993). The trajectory of $\tilde{\Lambda}$ between 10 00' and 15 00' coincides with the time range found for Λ to behave constant for the Qattara Depression bare soil conditions (Chap. 5). The area-averaged, time-averaged $\tilde{\Lambda}_{24}$ -value computed according to Eq. (8.13) became $\tilde{\Lambda}_{24}=0.21$. The latter value is rather similar to the midday $\tilde{\Lambda}$ -value for the same ensemble of pixels ($\tilde{\Lambda}_{24}=0.21$ and $\tilde{\Lambda}=0.20$, see Figure 8.22) which implies that one image acquired in the period between 10 00' and 15 00' is sufficient to compute $\lambda \tilde{E}_{24}$ according to Eq. (8.14), being a version of Eq. (5.13) applicable to heterogeneous land surfaces:

$$\tilde{\Lambda}_{24} = \frac{\sum_1^{n,m} \lambda E_{ij}(a_p, t_j)}{\sum_1^{n,m} \lambda E_{ij}(a_p, t_j) + \sum_1^{n,m} H_{ij}(a_p, t_j)} \quad (8.13)$$

$$\lambda \tilde{E}_{24} = \tilde{\Lambda} (\tilde{Q}_{24}^* - \tilde{G}_{0,24}) \quad (\text{J m}^{-2} \text{ d}^{-1}) \quad (8.14)$$

where $n=595$ pixels, $m=10$ image, a_i is the areal size of one METEOSAT pixel and t_j is the instantaneous time.

A summary of the flux densities for the areas specified in Table 8.1 is worked out in Table 8.9. *The standard deviations show that λE has the largest spatial variability of all the surface flux densities considered (CV(λE)=0.43 on average).* This finding supports

the comments addressed in the concluding remarks of Chapter 2 emphasizing that $\lambda E(x,y)$ depends on several bio-physical parameters and of Chapter 3 stating that of the other surface flux densities, λE is the most difficult term to determine. The CV of latent heat flux densities changes with pixel resolution (NS001: CV = 0.70, METEOSAT: CV = 0.16 for Tomelloso and Barrax on June 29), which is logical considering the semi-variogram in Figure 8.5. $\langle \lambda E \rangle_{\text{Barrax}}$ is 2.3 times $\langle \lambda E \rangle_{\text{Tomelloso}}$ on average, while approximately only 35% of the Barrax area is irrigated. Hence, small irregularities in soil moisture supply immediately affect the regional bulk evaporation rate. $\lambda E_{\text{Rada de Haro}}$ is 1.8 times $\lambda E_{\text{Tomelloso}}$ on average. The regional evaporation of the total EFEDA area ($\langle \lambda E \rangle = 164 \text{ W m}^{-2}$) is best represented by the Barrax super site on June 12 ($\langle \lambda E \rangle = 192 \text{ W m}^{-2}$). The Tomelloso super site is more suitable to reveal the regional situation for June 29, which emphasizes the fact that the dynamics of land surface flux densities changes with land use.

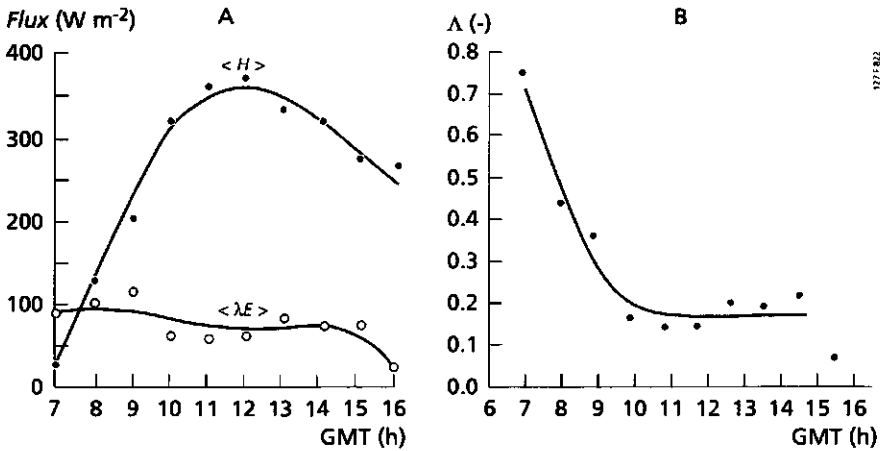


Fig. 8.22 Daily course of (Part A) the latent λE and sensible heat H flux densities and (Part B) evaporative fraction for 595 METEOSAT pixels covering the entire EFEDA grid with an area of nearly 9,000 km², 29 June, 1991 (after Bastiaanssen et al., 1995a).

It should be noted that the arithmetic mean of a small sample does not provide a good estimate of the regional λE . For example the arithmetic mean of the three super site $\langle \lambda E \rangle$ values (71, 194, 98 W m^{-2}) on the basis of the June 29 METEOSAT measurements is $\langle \lambda E \rangle = 121 \text{ W m}^{-2}$ while the 595 METEOSAT pixels covering the total EFEDA grid yields to $\langle \lambda E \rangle = 73 \text{ W m}^{-2}$. A simple arithmetic mean of all tower flux densities is therefore a strongly oversimplified approach for obtaining the area-averaged surface flux density from the SOP flux density database. Pelgrum and Bastiaanssen (1995b) elaborated different remote sensing techniques to weight the tower flux densities in a more advanced manner.

Although field measurements in the developing grapes at Tomelloso have shown a slight increase of λE throughout the SOP, Table 8.9 indicates that $\lambda E_{\text{Tomelloso}}$ is fairly constant

throughout the SOP with $\langle \lambda E \rangle = 71, 84, 84 \text{ W m}^{-2}$. Rada de Haro undergoes a sharp dry-down between June 12 and 29 ($194 \rightarrow 98 \text{ W m}^{-2}$) while Barrax exhibits a more gradual dry-down effect ($194, 192, 158 \text{ W m}^{-2}$) by man-controlled water supply facilities.

Table 8.9 Area-averaged instantaneous surface flux densities (W m^{-2}) calculated for the various (sub-) regions during EFEDA, June 1991. The values between brackets represent the standard deviations.

Platform	Date	Time	Symbol	Tomelloso	Barrax	Rado de Haro	EFEDA
TM	June 12	10 12'	$\langle Q \rangle$	280 (30)	348 (49)	358 (46)	339 (54)
TM	June 12	10 12'	$\langle G_p \rangle$	69 (5)	66 (8)	65 (5)	66 (5)
TM	June 12	10 12'	$\langle H \rangle$	127 (13)	90 (25)	98 (17)	103 (24)
TM	June 12	10 12'	$\langle \lambda E \rangle$	84 (36)	192 (76)	194 (57)	164 (76)
NS001	June 29	10 21'	$\langle Q \rangle$	500 (22)	544 (58)	-	-
NS001	June 29	10 21'	$\langle G_p \rangle$	105 (3)	83 (12)	-	-
NS001	June 29	10 21'	$\langle H \rangle$	312 (33)	302 (75)	-	-
NS001	June 29	10 21'	$\langle \lambda E \rangle$	84 (46)	158 (136)	-	-
METEOSAT	June 29	10 00'	$\langle Q \rangle$	468 (14)	497 (8)	470 (12)	464 (16)
METEOSAT	June 29	10 00'	$\langle G_p \rangle$	85 (1)	81 (2)	76 (1)	77 (2)
METEOSAT	June 29	10 00'	$\langle H \rangle$	312 (7)	225 (5)	296 (8)	314 (36)
METEOSAT	June 29	10 00'	$\langle \lambda E \rangle$	71 (21)	194 (4)	98 (33)	73 (49)

Figure 8.23 summarizes the temporal integration of energy partitioning by means of Λ for the whole EFEDA grid. The work of Bolle et al. (1993) suggested an average energy partitioning value for the whole EFEDA grid between June 11 to 28 of $\bar{\Lambda}_{24} = 0.23$. Comparing this value with the data displayed in Figure 8.23 indicates that *the in-situ flux densities are underestimating the regional patterns in energy partitioning* most probably due to the non-representativeness of the selected sites. The June 19 Falcon aircraft flight yielded an average evaporative fraction for leg L1, L4 and L8 of $\bar{\Lambda} = 0.42$ (Jochum et al., 1993b) which is consistent with the dry-down phase noticed between June 12 ($\bar{\Lambda}_{TM} = 0.61$) and June 29 ($\bar{\Lambda}_{Meteosat} = 0.19$). A double box flux density flight made on June 20 by the Dornier 128 aircraft estimated $\bar{\Lambda} = 0.35$ and a L-pattern flight on June 23 gave $\bar{\Lambda} = 0.31$ falling well in the expected change in meso-scale energy partitioning (Bolle and Streckenbach, 1993). A comprehensive overview of the moisture indicators is presented in Table 8.10.

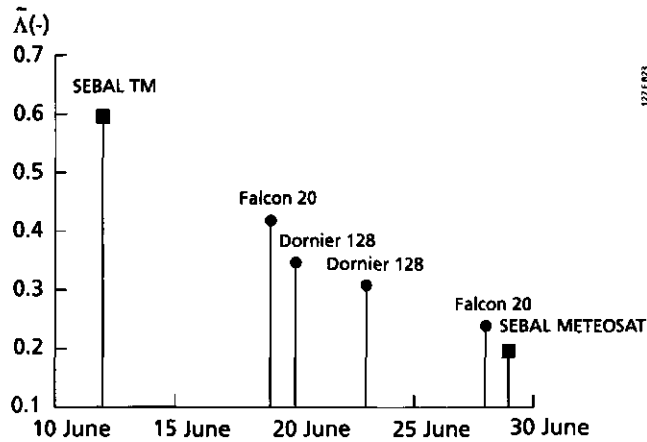


Fig. 8.23 Temporal behaviour of the aggregated evaporative fraction $\tilde{\Lambda}$ for the entire 9,000 km² EFEDA grid according to SEBAL and aircraft flux density measurements made by Falcon 20 and Dornier 128

Table 8.10 Area-effective instantaneous moisture indicators β , Λ , α , r_s , calculated for the various (sub-) regions during EFEDA, June 1991. Except for the bulk surface resistance r_s (s m⁻¹), all moisture indicators are dimensionless.

Platform	Date	Time	Symbol	Tomelloso	Barrax	Rada de Haro	EFEDA
TM	June 12	10 12'	β	1.51	0.47	0.51	0.63
TM	June 12	10 12'	$\tilde{\Lambda}$	0.40	0.68	0.66	0.61
TM	June 12	10 12'	$\tilde{\alpha}$	0.50	0.86	0.82	0.74
TM	June 12	10 12'	\tilde{r}_s	1842	486	432	661
NS001	June 29	10 21'	$\tilde{\beta}$	3.71	1.91	-	-
NS001	June 29	10 21'	$\tilde{\Lambda}$	0.21	0.34	-	-
NS001	June 29	10 21'	$\tilde{\alpha}$	0.27	0.45	-	-
NS001	June 29	10 21'	\tilde{r}_s	1541	468	-	-
METEOSAT	June 29	10 00'	$\tilde{\beta}$	4.39	1.16	3.02	4.30
METEOSAT	June 29	10 00'	$\tilde{\Lambda}$	0.19	0.46	0.25	0.19
METEOSAT	June 29	10 00'	$\tilde{\alpha}$	0.26	0.64	0.34	0.26
METEOSAT	June 29	10 00'	\tilde{r}_s	1584	308	763	1166

The value for $\tilde{\Lambda}_{EFEDA}$ on June 12 was systematically higher (0.61) than observed for the June 29 METEOSAT studies (0.19). This dry-down phenomenon during June is most probably a typically recurrent seasonal rootzone moisture depletion effect and may not

be related to abnormal atmospheric circulation and desertification. Multi-temporal analysis of *NDVI* images confirms that the *NDVI* in Central Spain decreases during the summer (Bolle et al., 1993). By the end of spring, the natural vegetation tends to reduce its stomatal aperture under high summer evaporative demands and soil moisture deficit conditions. In particular, this can be observed for Rada de Haro $\tilde{r}_s=432 \rightarrow 763 \text{ s m}^{-1}$. The ripening and harvest of wheat and barley in Barrax is probably responsible for the collapse of $\tilde{\Lambda}=0.68$ to $\tilde{\Lambda}=0.46$. Although $\langle \lambda E \rangle$ for Tomelloso was found to be quasi-constant, $\tilde{\Lambda}$ decreases from 0.40 to 0.19 because the summer solar exposures increased $Q^* - G_0$. The bulk surface resistance tends to be stabler for Tomelloso (1842 \rightarrow 1541 and 1584 s m^{-1}) which emphasizes that soil water content remained more or less similar (θ_{10} is already low on June 12 and rainfall is small). The resistance for Barrax was also fairly stable (486, 468, 308 s m^{-1}) so the Λ_{Barrax} also has to be attributed to some extent to changes in $Q^* - G_0$ (not entirely however, because λE decreases as well). Hence, $\tilde{\Lambda}$ is suitable to describe the daytime evolution of the surface energy partitioning but is less suitable to derive the hydrological situation for larger time scales at which the net available energy changes.

The $r_s(\theta_{10})$ relationships of Figs. 8.6 and 8.8 were used to infer θ_{10} -maps from r_s -maps. The area-average $\langle \theta_{10} \rangle$ values obtained via $\theta_{10}(x,y)$ are summarized in Table 8.11. The absence of rainfall causes a significant dry-down in Rada de Haro (0.23 \rightarrow 0.07 $\text{ cm}^3 \text{ cm}^{-3}$). Supplementary irrigation in Barrax is hold responsible for a delayed dry-down (0.22 \rightarrow 0.15 $\text{ cm}^3 \text{ cm}^{-3}$). The soil moisture extraction by perennials is mainly from 100 cm depth which explains a relatively constant θ_{10} value at shallow depth for the Tomelloso sub-region. *The soil moisture behaviour of the entire EFEDA grid changed from 0.16 to 0.10 $\text{ cm}^3 \text{ cm}^{-3}$ which can be utilized to validate large-scale atmospheric models.* Colour Plate 8 shows that r_s at macro-scale can be determined which can be applied to verify / initialize land surface parameterization schemes at this scale.

Table 8.11 Area-representative near-surface soil water content $\tilde{\theta}_{10}$ calculated for the various (sub-) regions during EFEDA, June 1991

Platform	Soil water content at 10 cm ($\text{ cm}^3 \text{ cm}^{-3}$)	Date	Time	Tomelloso	Barrax	Rada de Haro	EFEDA
TM	$\tilde{\theta}_{10}$	June 12	10 12'	0.08	0.22	0.23	0.16
NS001	$\tilde{\theta}_{10}$	June 29	10 21'	0.08	0.15	-	-
METEOSAT	$\tilde{\theta}_{10}$	June 29	10 00'	-	0.10	0.07	0.10

With NOAA/AVHRR and METEOSAT data, the possibility arises to estimate actual evaporation for the whole Iberian Peninsula, including the shores of the Mediterranean Sea and the Atlantic Ocean (Figure 8.24). Ten METEOSAT slots with an hourly interval

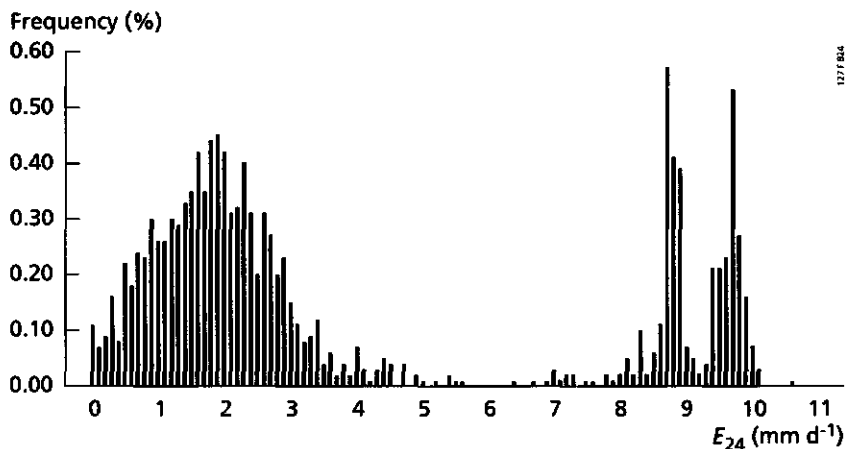


Fig. 8.24 Spatial distribution of actual evaporation rates E_{24} on the Iberian Peninsula and parts of the surrounding seas, 29 June, 1991 (after Bastiaanssen et al., 1995a)

acquired on June 29 have been selected and λE was computed for each image and each pixel by repeated application of SEBAL. A daytime aggregation procedure of the 10 different $\lambda E(t)$ -pairs for each pixel was performed to arrive at the daily actual evaporation rate. The nighttime latent heat flux density was set to zero. Holtslag and de Bruin (1988) experimentally showed that some evaporation may occur but field measurements carried out in the Tomelloso vineyard, on June 29 indicated $\lambda E = -1.7 \text{ W m}^{-2}$. The area-average daily-total actual evaporation of the pixels situated on land was established in this manner to be approximately 1.75 mm d^{-1} .

8.3.2 Lower Egypt

The area-effective energy balance of the whole of Lower Egypt (long: 26-34 E; lat. 26-32 N) was calculated. The numerical error in the closure of the energy budget is 1 to 2% of \bar{Q} , which is rather acceptable considering the extremes of desert and sea manifested within the same image. The possibility arises to assess the area-average - daily total evaporation in the same way as was done for the Iberian Peninsula. The cumulative amount of vapour release during daytime (6^{00} and 18^{00}) added up to a value of $\int \langle \lambda E \rangle dt = 6.5 \text{ MJ m}^{-2}$ (Figure 8.25) which is equivalent to 2.6 mm d^{-1} at 25°C ambient temperature if nighttime latent heat exchanges are ignored. Latent heat flux density may be negative during nighttime which reduces $\langle E_{24} \rangle$ slightly. The cumulative amount of sensible heat was found to be $\int \langle H \rangle dt = 7.3 \text{ MJ m}^{-2}$. The height of the PBL can be computed from the daytime evolution of $\langle H \rangle(t)$ (e.g. Raupach, 1991).

Figure 8.25 demonstrates that $\tilde{\beta}$ ($\text{CV } \tilde{\beta} = 0.14$) contains more fluctuation than $\tilde{\Lambda}$ ($\text{CV } \tilde{\Lambda} = 0.08$). As in the la Mancha case study, $\tilde{\Lambda}$ is stable throughout daylight hours. The

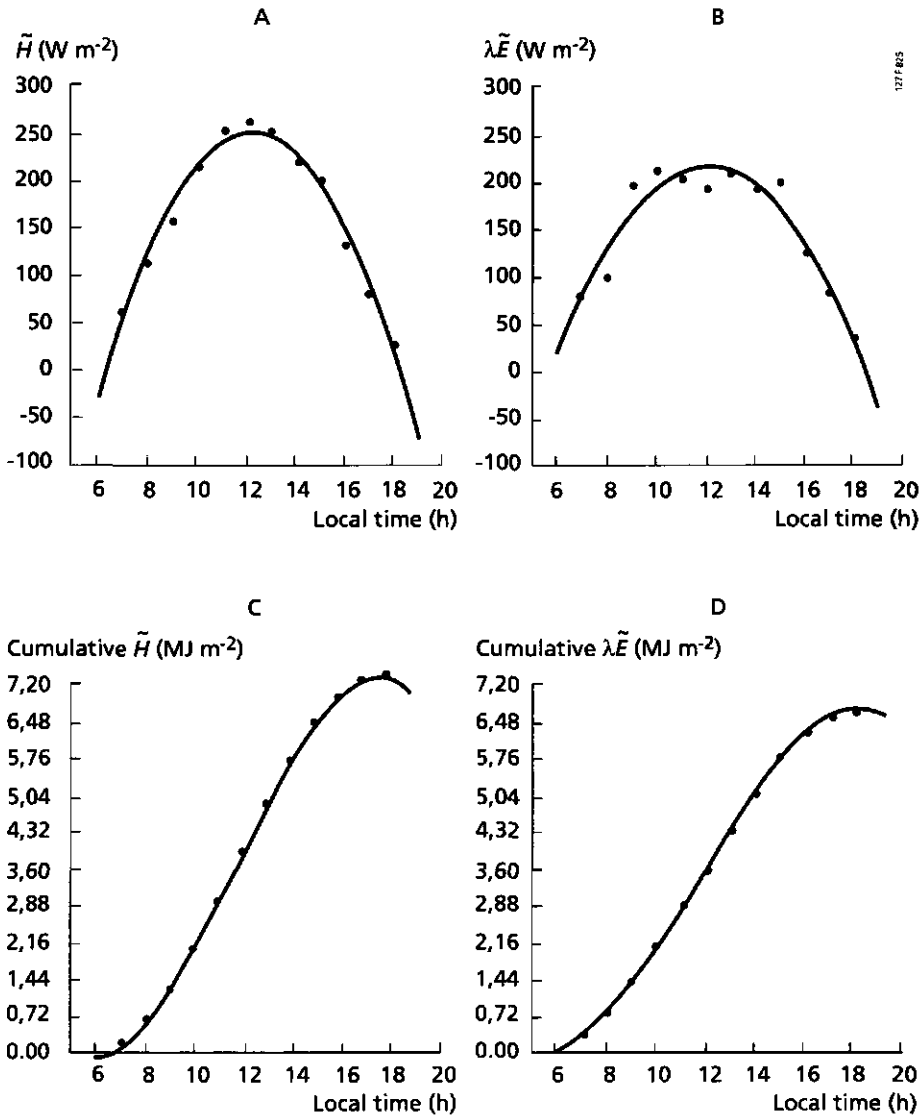


Fig. 8.25 (Part A) Daily evolution of the area-average sensible heat flux density $\langle H \rangle$ and (Part B) latent heat $\langle \lambda E \rangle$ over Lower Egypt and part of the Mediterranean Sea on 5 August, 1986. The dots denote instantaneous area-average cumulative surface flux densities while the line is the best approximation through the points. Part C and D depict the cumulative values (after Feddes et al., 1993)

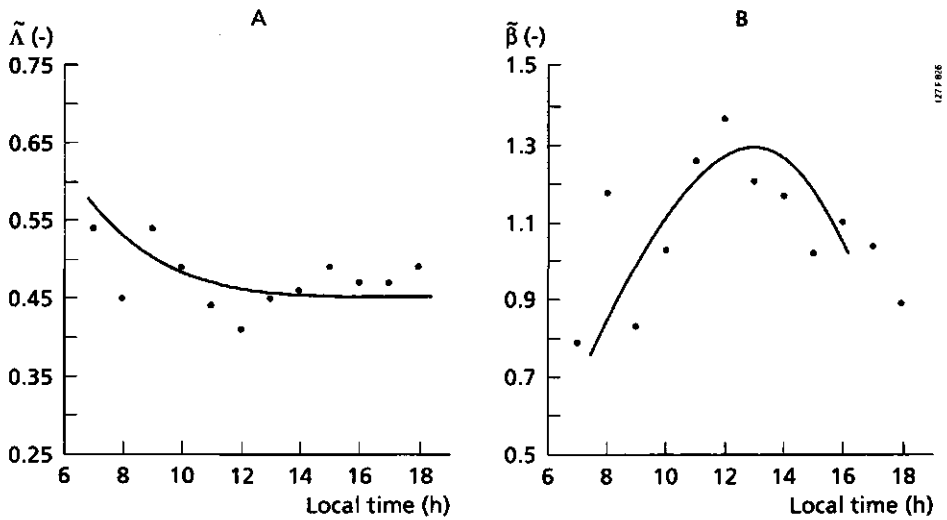


Fig. 8.26 (Part A) Diurnal course of areal effective Bowen-ratio $\tilde{\beta}$ and (Part B) evaporative fraction $\tilde{\Lambda}$ for a $620 \times 825 \text{ km}^2$ vast region in Lower Egypt; computed with METEOSAT-based reflectance and temperature data on 5 August, 1986

$\tilde{\Lambda}$ -value became stable after 11⁰⁰ local time and remained as such until 18⁰⁰ hours local time. Hence, the daytime behaviour of macro-scale $\tilde{\Lambda}$ values for land systems can be as smooth as for micro scale wet desert surfaces (see Figure 6.3). The number of 12 images can be substantially reduced without reducing the accuracy of the integrated daily flux densities using Eq. (8.14).

8.4 Concluding remarks

The surface flux densities predicted with SEBAL were validated against flux density data retrieved from the EFEDA database. An accurate intercomparison of flux densities appears to be complicated by combined effects of measurement errors of the in-situ flux densities, their footprint, the exact location of the tower ($x=0$) and the integration time of the in-situ measurements. Nevertheless, an attempt was made to compare the evaporative fractions for a number of small footprints. Approximately 85 % of the selected footprints on June 12 and 29 fall within the error boundaries of the SEBAL and in-situ flux densities. The root mean square error between tower-based and remote sensing-based Λ -data was found to lie between 0.10 to 0.19, depending on the day chosen. The error is substantially reduced if all the footprints are considered together ($\Delta\tilde{\Lambda}=0.04$, relative error is 10%) or on the spatial scale at which the bulk aircraft flux densities are meaningful such as for Castilla la Mancha (1,000,000 ha: $\Delta\tilde{\Lambda} \approx 0.01$). Moreover, the error

changes with the spatial sampling resolution: the results of a single METEOSAT pixel in Barrax with a high sill level were poor, whereas the results for the same area but sampled with NS001 were much more satisfactory. The EFEDA case study has indicated that SEBAL can be used for multi-resolution data sets as long as a number of say 20 pixels can be averaged. *Large-scale field experiments should pay attention to an exact determination of the footprint orientation and length* in order to calculate the fractional contribution of land surface elements to the total flux density measured by towers at a given elevation.

A regional validation study on 700,000 ha of irrigated land in the Eastern Nile Delta revealed that the remote sensing parameterization of dial (24-hour) evaporation was within the confidence limits of the calibrated SIWARE regional water balance model. By downscaling from 100 km (all SIWARE element) to a few km (one SIWARE element), likewise the Spanish case study, the Λ -deviation increases. At the level of an irrigation unit, the deviation was 8% on average, which is still fairly acceptable.

Multi-temporal SEBAL studies demonstrated that a considerable change in energy partitioning occurred during EFEDA's SOP in June 1991 (Tomelloso $\Lambda=0.40 \rightarrow \Lambda=0.19$; Barrax $\Lambda=0.68 \rightarrow \Lambda=0.46$; Rada de Haro $\Lambda=0.60 \rightarrow \Lambda=0.25$) which could not be understood from the limited in-situ flux densities measurements. The changes in energy partitioning could be attributed to changes in net available energy Q^*-G_0 and soil moisture θ_{10} (Tomelloso $0.08 \rightarrow 0.08 \text{ cm}^3 \text{ cm}^{-3}$; Barrax $0.22 \rightarrow 0.15 \text{ cm}^3 \text{ cm}^{-3}$; Rado de Haro $0.23 \rightarrow 0.09 \text{ cm}^3 \text{ cm}^{-3}$). The mapping of near-surface soil moisture can best be done by utilizing r_s data. The regression functions between r_s and θ_{10} are however time and resolution-dependent.

To by-pass the problems associated with averaging of resistances to coarser scales (Eq. 8.9) which requires the involvement of \tilde{e}_{sat} , or Priestley and Taylor α -parameters, which requires s_a , it was concluded to consider flux density ratios like the evaporative fraction or the classical Bowen ratio.

The evaporative fraction was found to be superior because:

- it is stabler than α , β and r_s during daylight hours, even at heterogeneous large-scale land surfaces such as the EFEDA grid and Lower Egypt (CV = 0.20); *this implies that one midday image of surface reflectance and surface temperature suffices to compute the daily evaporation*;
- it is retrievable from remote sensing algorithms, field flux density measurements, aircraft flux density measurements and model simulations, creating a suitable environment for intercomparison of the different Λ values;
- it is easy to aggregate to coarser scales;

Intercomparison of energy partitioning for larger time frames (weekly and longer) can best be achieved with r_s . The bulk surface resistance both theoretically (Eqs. 3.17 and

3.19) and practically (Figs. 8.6 and 8.8) reflects best the hydrological situation. The regional distributed patterns of surface hemispherical reflectance, surface temperature, NDVI, emissivity, solar radiation, surface roughness, near-surface vertical air temperature difference, friction velocity, Monin-Obukhov length, aerodynamic resistance and bulk surface resistance could be obtained through the (semi-) empirical steps included in the SEBAL parameterization. Although programs such as EFEDA were not sufficient to assess the reliability of these intermediate products, the pdfs of these products may contribute to stochastic-dynamic model approaches (e.g. Avissar, 1991; Famiglietti and Wood, 1994).

The ultimate thermal-infrared remote sensing results are in direct contrast with the FIFE investigations (Hall et al., 1992). It was concluded that substitution of $T_0 - T_a$ by δT_{a-sur} and the inversion of δT_{a-sur} from H^{phy} improves the potential of using thermal infrared remote sensing for environmental studies. Especially it has been demonstrated that the $T_0(r_0)$ relationship of heterogeneous land scapes allows the allocation of dry and wet areas with specific solutions of the surface energy balance: Land surface elements with $r_0 < 0.10$ and a relative low T_0 value may be considered to fulfil $\Lambda \approx 1.0$. Although SEBAL has some empirical steps to estimate hydro-meteorological parameters such as surface roughness length for momentum, this does not hamper the flux density estimations. Hence, SEBAL seems to be a reasonable trade-off between physical complexity and data demand with respect to availability of in-situ measurements.

It may finally be concluded that the design of large-scale field surveys with the aim of establishing regional evaporation should be made after processing existing satellite images. Then the usefulness of field work on the $H-\lambda E$ patterns can be improved by installing towers at crucial points in the H and λE frequency distributions (average, 10% tails etc.) which facilitates the validation of remote sensing based flux density maps and the monitoring of bulk energy partitioning.

9 Parameter variability and impact on surface flux densities and moisture indicators

9.1 Approach

Surface flux densities and moisture indicators obtained by applying the 36-step SEBAL procedure comprise deficiencies and failures on (i) radiometer calibration, (ii) atmospheric correction, (iii) empirical relationships, (iv) spatial variability of hydro-meteorological parameters (v) simplified energy budgets, etc. The various model parameters of SEBAL are, without exception, all directly or indirectly estimated from spectral radiances and therefore associated with more or less uncertainty and results should be termed 'estimations'. The effects of parameter variability on these estimations have not been addressed so far. Chapter 8 has given indications of the deviation of SEBAL flux densities if a sample window is considered. This chapter is meant to describe the role of parameter variability on the SEBAL estimation more intensively following the concepts given by Bastiaanssen et al. (1994b). The following approaches will be applied:

- *Sensitivity*. A numerical estimation of the first derivative of a certain model parameter on a certain output parameter. All relevant model parameters will be considered one by one, while keeping the other parameters constant according to the values for the reference situation. The relative importance of each independent model parameter on the surface flux densities and moisture indicators will appear from this analysis. The discussion of the model output variables will be restricted to H , λE , Λ and r_s . Section 9.3 addresses the sensitivity study;
- *Uncertainty*. A numerical estimation of the combined effect of exposing all relevant model parameters simultaneously to a predefined stochastic deviation; This gives the pdf of the deviation of estimated H , λE , Λ and r_s -values from the mean value. To this end, a Monte Carlo simulation approach is applied. Section 9.4 addresses the uncertainty study;

A number of 4 dependent SEBAL output variables H , λE , Λ , r_s , for a homogeneous land surface will be considered which is more generally expressed as Y_k with $k=1,2,\dots,4$. Each Y_k is related through the SEBAL model to the independent variables x_i with $i=1,2,\dots,12$:

$$Y_k = f_k(x_1 \dots x_i \dots x_n) \quad (9.1)$$

The sensitivity describes the effect of a change dx of x_i on Y_k . The relative sensitivity can be expressed as dY_k/dx_i . A set of reference input parameters of x_i , called r_i , can be determined from accurate field estimations rather than from remote sensing estimations which give as a result the reference value of Y_k hereafter called R_k :

$$R_k = f_k(r_1 \dots r_p \dots r_{12}) \quad (9.2)$$

R_k can in the case of H and λE also be measured directly, which does not require the involvement of r_p . The latter does not hold however for Λ and r_s . For natural land surfaces with spatial variation in surface energy budgets, the spatially distributed random variables are given for $j = 1, 2, \dots, 20$ land use types:

$$Y_{k,var} = f_k(Y_{k,1} \dots Y_{k,j} \dots Y_{k,20}) \quad (9.3)$$

which after areal integration of $j = 1, 20$ land surface clusters leads to:

$$Z_k = \frac{1}{A} \int_A^{20} Y_{k,j} da_j \quad (9.4)$$

and if C_k represents the reference value of Z_k it can be defined as:

$$C_k = \frac{1}{A} \int_A^{20} R_{k,j} da_j \quad (9.5)$$

where C_k can for instance be obtained from aircraft flux densities directly or areal integration of H and λE to obtain \tilde{H} and $\tilde{\lambda E}$. It should be noted that the integration of Λ and r_s for obtaining Z_k and C_k should be established alternatively by means of Eqs. (8.12) and (8.11) respectively and that C_Λ and C_{r_s} cannot be measured directly. An overview of a three-dimensional array of model parameters (x_j), model output (Y_k) and land surface types is illustrated in Figure 9.1.

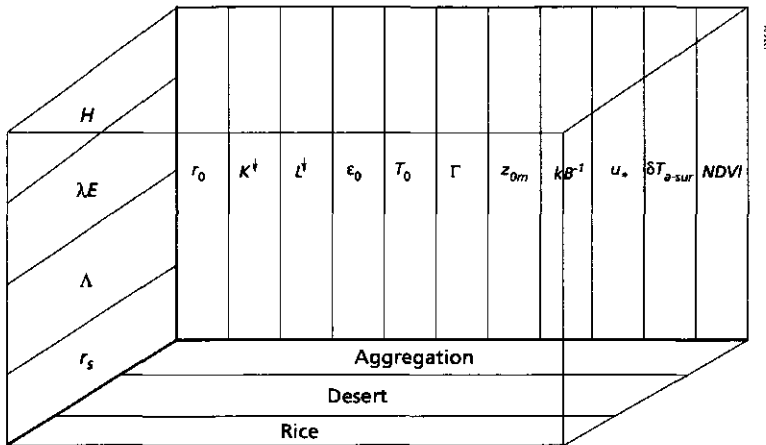


Fig. 9.1 Design of a parameter variability study for homogeneous (desert and rice) and heterogeneous land surfaces (aggregation) in terms of the SEBAL model input and output parameters

The main interest is to find to which extent $Y_{k,j}$ and Z_k are realistically estimated by SEBAL and how the $(Y_{k,j}-R_{k,j})$ and (Z_k-C_k) deviations behave. A large number of repetitions of $Y_{j,k}$ and Z_k estimations are necessary to perform a probability analysis. One of the important conditions is that the number of realizations should be large enough for the statistics to become constant. For H , λE , Λ and r_s , 3000 samples in the case study followed hereafter appeared to be necessary: The mean value and standard deviation became stable when more samples were taken. The simulation method described above is generally known as a Monte-Carlo method.

The R_k and C_k values should be obtained using accurate turbulent flux density measurements (in-situ for R_k , aircraft for C_k). In the absence of these data (for instance when $Y_{j,k}=r_s$ or $C_k=\tilde{r}_s$ which cannot be measured) or if no reference measurements are available, model results are used and the *accuracy analysis* becomes an *uncertainty analysis*. The results of Section 9.4 should therefore **not** be conceived as the attainable accuracy. Then the overall deviation of Y_k for a homogeneous land surface from the arithmetic mean of Y_k , $Y_{k,mean}$, can be explored to calculate the cumulative probability density function of the absolute deviations. If a total of m random samples are taken, the error of estimates S_e for a *patch* can be calculated with:

$$S_e = \sqrt{\frac{1}{m} \sum_{i=1}^m (Y_k - R_k)^2} \quad (9.6)$$

and the same evaluation applies for *heterogenous regional landscapes* with j land surface elements:

$$S_e = \sqrt{\frac{1}{m} \sum_{i=1}^m (Z_k - C_k)^2} \quad (9.7)$$

The input parameters x_1 to x_n are assumed to be independent and the error for each parameter can be considered separately.

9.2 Physical characteristics of the selected land surfaces

Land surface conditions

Satellite radiances acquired from the Landsat Thematic Mapper overpassing the Nile Delta on 27 July, 1987 were used to perform the parameter variability analysis and its effect on the surface flux densities and moisture indicators. The study with the reference data was performed by van der Wal (1992). The position of the TM image is indicated

in Figure 4.4. The area is characterized by large clusters of irrigated and desert land. Because of the need to expand Egypt's agricultural production, desert reclamation schemes are underway and partly in operation along the desert fringes. An example of the reference calculated distributed surface energy balance terms is provided in Colour Plate 9. This study area was selected because it encompasses a wide diversity in hydrological, agricultural and meteorological conditions.

The datapoints on the $T_0(r_0)$ and $T_0(NDVI)$ relationships of Figure 9.2 represent the average values of 20 sub-grid areas identified by a clustering technique using r_0 , $NDVI$ and T_0 as attributes. The numerical assignment of r_0 , T_0 and $NDVI$ for each sub-grid is shown in Annex 5. The $T_0(r_0)$ relationship indicates that a wide range of land wetnesses is present. Class 1 of the (T_0, r_0) relationship represents the open water bodies of Lake Bitter, the Suez Canal and the Nile river. The low T_0 values of class 3 are observed in the green rice areas east of Mansureya. Class 5 and 6 are the intensively cultivated lands along the 31°N latitude. Classes 10, 11 and 12 represent the irrigation districts just north of Cairo, where maize is the dominant crop. Not surprisingly, the desert showed the highest r_0 values (Classes 19-20) being located on the 'radiation controlled' branch of the $T_0(r_0)$ relationship. Figure 9.2B shows that, except class 1, T_0 is mainly controlled by the density of crops. The area-average surface flux densities and moisture indicators can be obtained after linear averaging of the flux densities of the 20 separated land use clusters. Since the areal size of each cluster is irrelevant for the parameter variability study, it is assumed that all 20 clusters are equal in occurrence (Figure 9.3). The geographical position is also irrelevant for Z_k . The clusters in Figure 9.3 are therefore presented in a sequential order rather than according their geographical position and areal size. The values for $\tilde{\Lambda}$ and \tilde{r}_s were obtained using equations (8.6) to (8.12).

Wet and dry homogeneous land units: unit 3 (rice) and unit 20 (desert) respectively, were selected to study the effects of x_i -model parameter uncertainty on Y_k . The SEBAL output of the reference run, Y_k^{ref} , without considering any parameter variability, is presented in Table 9.1. The aggregated values for all 20 land units Z_1 to Z_4 are displayed under the header 'aggregated'. The areal constant parameters used to compile Table 9.1 are displayed in Table 9.2.

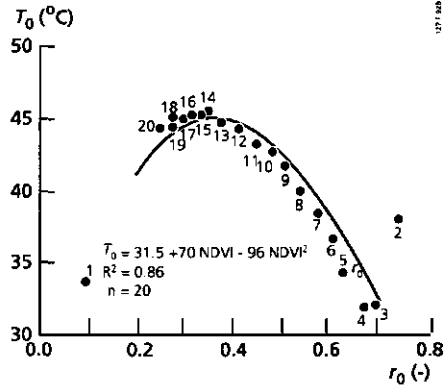
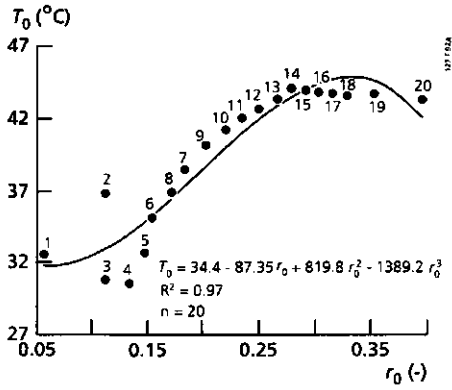


Fig. 9.2 (Part A) The $T_o(r_o)$ relationship of the Eastern Nile Delta and Eastern Desert obtained from TM measurements on path/row 176/39; 176/140, acquired on July 27, 1987 (after van der Wal 1992) and (Part B) the $T_o(NDVI)$ relationship

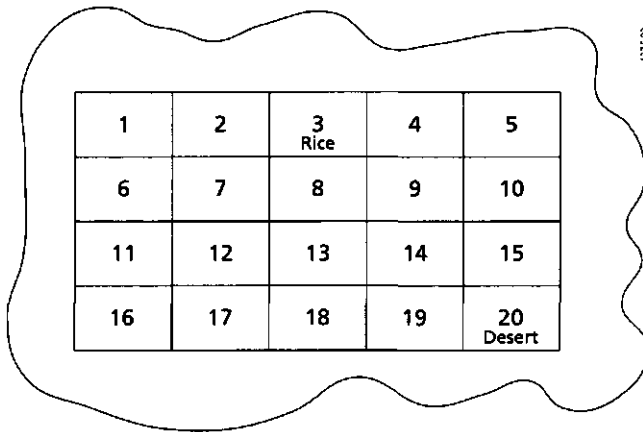


Fig. 9.3 Schematic representation of the 20 land use clusters in the Eastern Nile Delta and adjacent Eastern Desert distinguished on the basis of hemispherical surface reflectance r_o , NDVI and surface temperature T_o .

Table 9.1 Surface flux densities and moisture indicators as computed with SEBAL for homogeneous rice and desert areas respectively, as well as the aggregated behaviour of all 20 units, indicated as 'Aggregated'. The large surface resistance is related to the low latent heat flux density and does not have an infinite value because the latent heat flux density in desert unit no. 20 is not entirely zero ($\Lambda \neq 0$)

Parameter	Unit	Rice	Desert	Aggregated
		$Y_{k,3}^{ref}$	$Y_{k,20}^{ref}$	Z_k^{ref}
Sensible heat flux density	$W m^{-2}$	27	224	235
Latent heat flux density	$W m^{-2}$	623	10	202
Surface resistance	$s m^{-1}$	61	12351	415
Evaporative fraction	-	0.96	0.04	0.46

Table 9.2 Values of hydro-meteorological parameters applied for analysis of the surface flux densities in the Eastern Nile Delta and Eastern Desert. A link to the computation steps and the equations used is included

Computation step	Equation	Symbol	Unit	Reference value
2.	7.2	δ	rad	0.334
5.	7.6	d_s	AU	1.015
8.	6.6	r_a	-	0.046
10.	7.11	τ_{sw}''	-	0.83
12.	7.15	L^{\downarrow}	$W m^{-2}$	310
14.	7.17	$\tau_{\lambda}(b)$	-	1.12
21.	-	kB^1	-	2.3
26.	2.48	$\rho_a c_p$	$J m^{-3} K^{-1}$	1179
28.	7.47	T_{p-B}	$^{\circ}C$	22.7
-	3.33	$e(z)$	mbar	20.5

According to the 'evaporative fraction-vertical air temperature difference' method, out of all land clusters two extremes should always be selected to quantify δT_a^{dry} and δT_a^{wet} . The open water bodies of sub-grid 1 are assumed to meet the condition $\Lambda \approx 1.0$ ($r_0 = 0.056$). Given the conditions of negligible H values, the near-surface vertical air temperature difference ($\delta T_a^{wet} \approx 0.0^{\circ}C$) under all circumstances of possible parameter variabilities was assigned to Lake Bitter. The assessment of δT_a^{dry} has to be tuned with the $(Q^* - G_0)$ and (T_0, r_{ah}) -data of the desert pixels that have an albedo larger than r_0^{thresh} . Sub-grid area 18 was assigned as the area with $\Lambda = 0.0$. Inherent to the parameterization chosen, Λ of units 1 and 18 are fixed, independent of the variability of other SEBAL model parameters.

9.3 Sensitivity analysis of surface flux densities and moisture indicators

The 12-dimensional parameter string s_1 to s_{12} of Eq. (6.1) controls the pixel-dependent surface energy budget. Since SEBAL substitutes Γ for λ'_s and T_s and the Monin Obukhov length L and u_s do not need to be studied separately as $L=f(u_s)$, the sensitivity analysis on surface flux densities and moisture indicators can be reduced from 12 to 10 parameter strings. Although *NDVI* is not a direct hydro-meteorological parameter in the SEBAL procedure (but is included in the description of $z_{0,m}$, ϵ_0 and Γ), *NDVI* was added to the sensitivity analysis to better understand the importance of correctly accounting for the effects of atmospheric interferences on *NDVI*.

The sensitivity analysis is based on a fixed 25% change in the 11 model parameters (x_i) with respect to their values of the standard run, while keeping all other parameters unchanged. Care has been taken to ensure that the 25% change does not exceed the physical limits of its x_i -parameters. For instance, it is very unlikely that $\tau_{sw}>0.95$ occurs. The results are presented in Figure 9.4, where the relative sensitivities are illustrated as fractional differences:

$$\frac{Y_k - Y_k^{ref}}{Y_k^{ref}} \quad (-) \quad (9.8)$$

The results of the fixed 25% increase of x_i are shown first, whereafter for the same x_i and Y_k the results of a 25% decrease in x_i are presented. The results are presented Y_k -wise and only for $j=3$ (rice) and $j=20$ (desert). Figure 9.5 demonstrates Z_k for all 20 clusters.

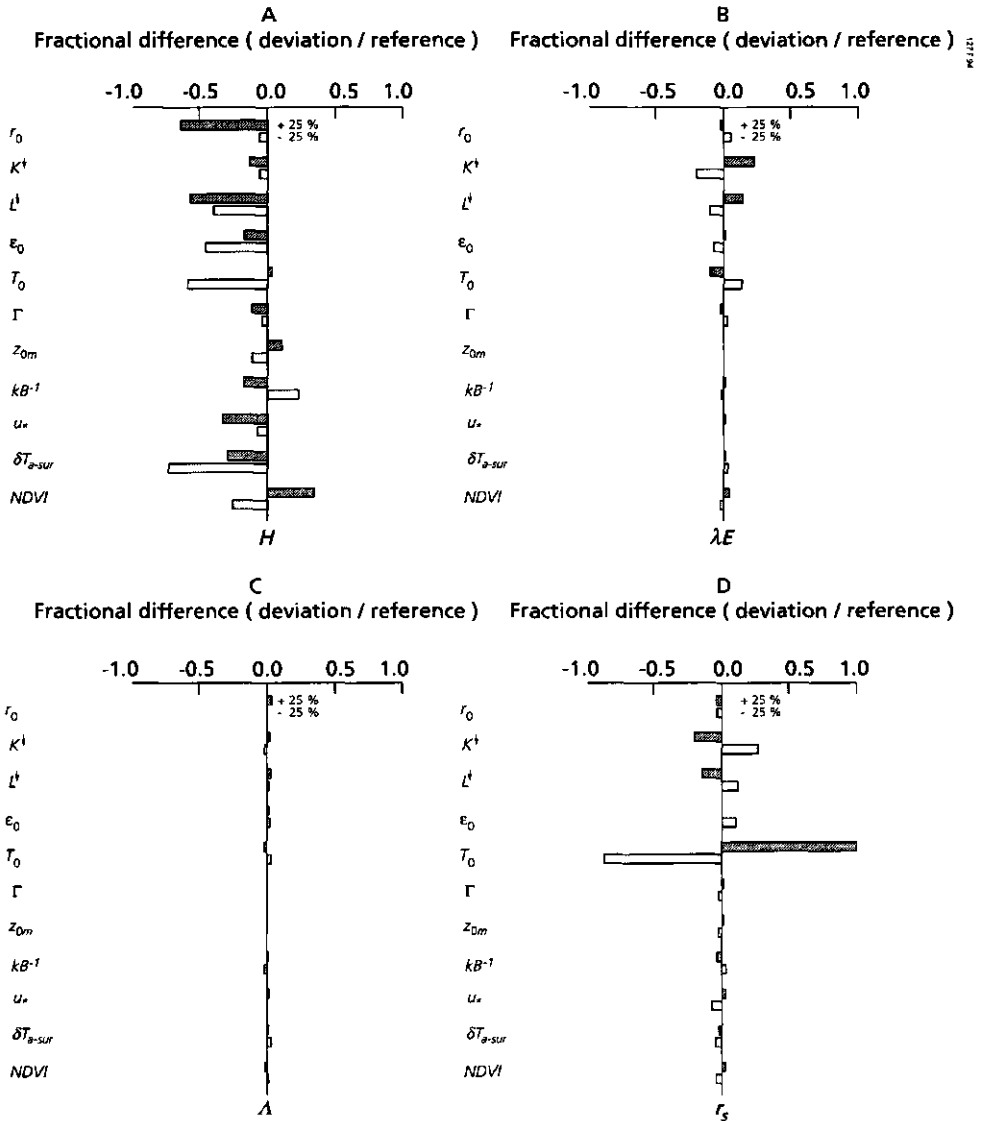


Fig. 9.4 Results of the sensitivity analysis of selected surface flux densities and moisture indicators for the **homogeneous rice area** ($j=3$) with 25% positive (first bar) and 25% negative (second bar) changes of SEBAL model parameters x_i . (Part A) Sensible heat flux density H , (Part B) latent heat flux density λE , (Part C) evaporative fraction Λ and (Part D) surface resistance, r_s

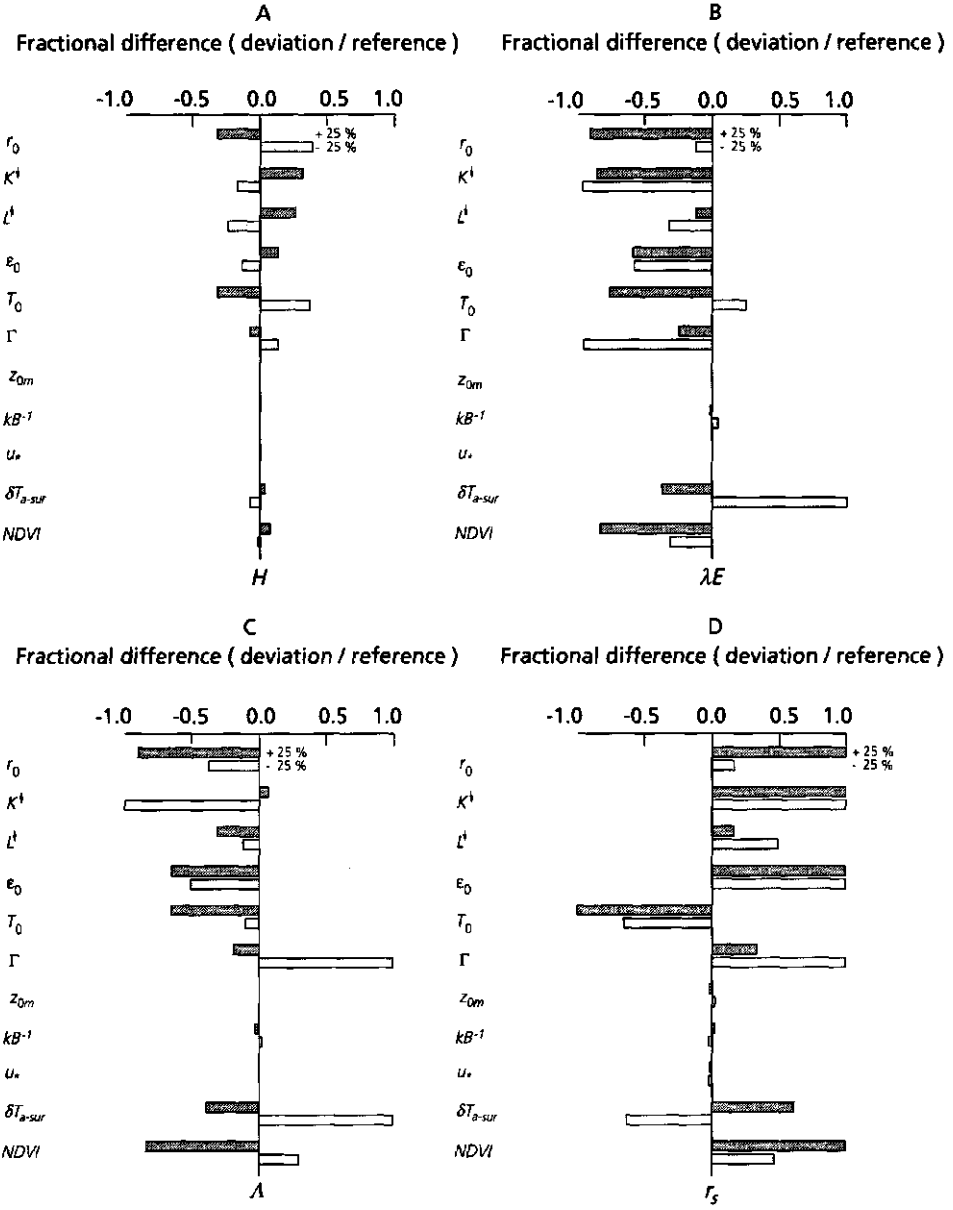


Fig. 9.5 Results of the sensitivity analysis of selected surface flux densities and moisture indicators for the **homogeneous desert area** ($j=20$) with 25% positive (first bar) and negative (second bar) changes of SEBAL model parameters x_i , (Part A) Sensible heat flux density H , (Part B) latent heat flux density λE , (Part C) evaporative fraction Λ and (Part D) surface resistance, r_s

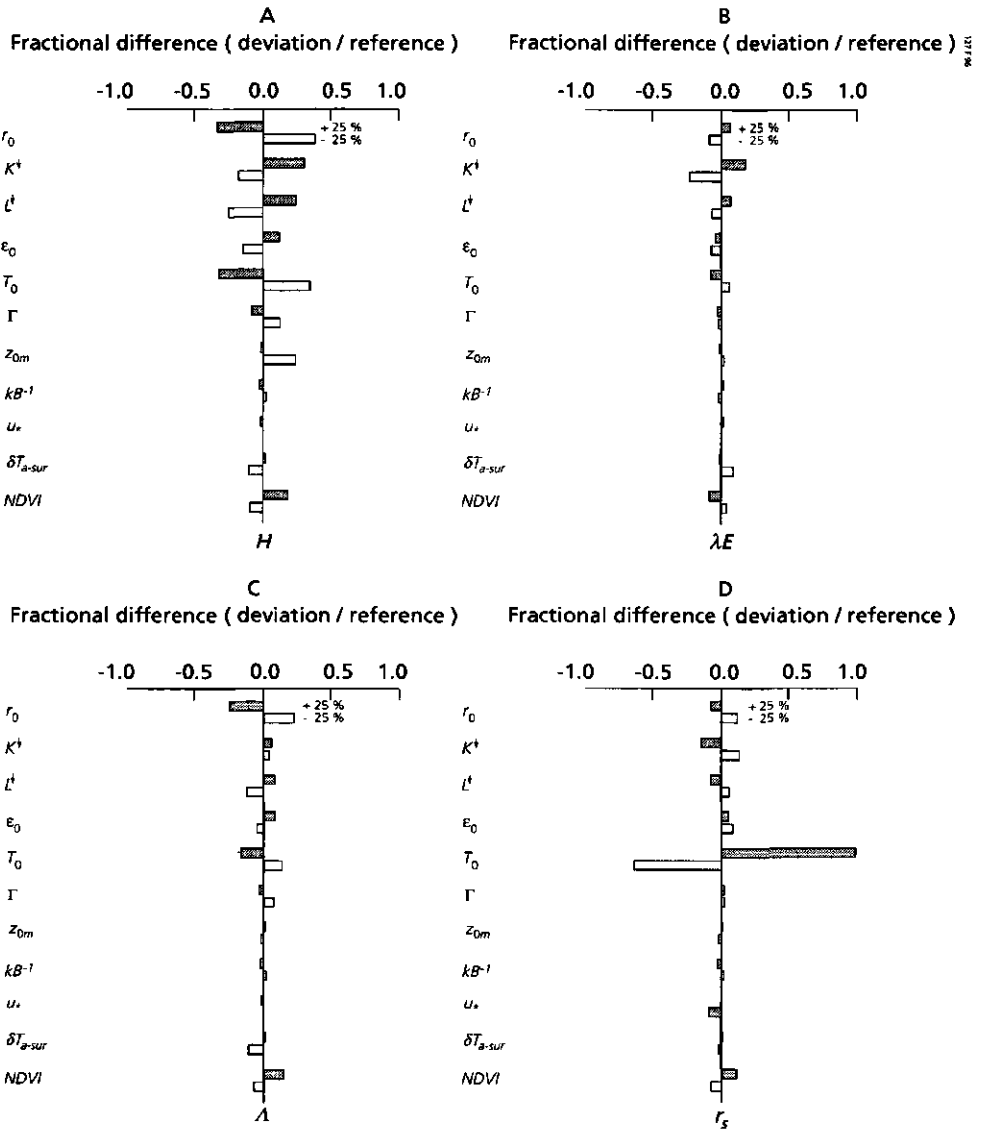


Fig. 9.6 Results of the sensitivity analysis of selected surface flux densities and moisture indicators for the aggregated Eastern Nile Delta and Eastern Desert ($g = 20$) with 25% positive (first bar) and negative (second bar) changes of SEBAL model parameters x_i . (Part A) Sensible heat flux density H , (Part B) latent heat flux density λE , (Part C) evaporative fraction Δ and (Part D) surface resistance, r_s .

Figure 9.4 shows that λE_{ice} is fairly insensitive for all x_i variables. This finding can be explained by the appearance of large Y_k^{ref} values for rice. Hence some absolute λE deviations yield small fractional differences. On the other hand, Y_k^{ref} for the desert unit

results into large fractional differences. The opposite is true for H , which implies that H can be less accurately calculated for wet land surfaces. Since Λ_{rice} ($j=3$) and Λ_{water} ($j=1$) do not differ much, the forced scaling of $\Lambda_{water}=1.0$ does lead automatically to very stable Λ_{rice} values, independent of the magnitude in x_j . The same comment applies to the desert surface. Apparently, changes in the relative magnitude of surface resistance, r_s , are larger than for Λ , because small changes in T_0 affect the saturated vapour pressure at the 'Big-Cavity' in a strongly non-linear manner. Furthermore, K^d was recognized to be a sensitive parameter for λE and r_s in rice crops.

Figure 9.5B shows that under desert conditions, H is rather insensitive to x_j . The values of the primary remote sensing parameters, r_0 , $NDVI$ and T_0 , turned out to be the most sensitive algorithm parameters in assessing H . As compared to r_s , Λ is in general less sensitive to variations of the model parameters under desert conditions.

The aggregated response of the 20 identified land clusters described by Z_k reveals a rather even partitioning between H and λE ($\tilde{\Lambda}=0.46$). Figure 9.6 illustrates that, \tilde{H} and \tilde{r}_s show higher relative sensitivities than $\tilde{\lambda E}$ and $\tilde{\Lambda}$. As was also observed for rice and desert, \tilde{r}_s is the most sensitive to \tilde{T}_0 . Since SEBAL uses δT_{a-sur} rather than $T_0 - T_a$, the sensitivity of \tilde{H} to \tilde{T}_0 is not high with encouraging prospects for the capability to assess H from thermal infrared images. Some impact of T_0 on H remains, because a surface with higher temperature emits more radiation, with consequently less energy available for H at a constant evaporative fraction. Although several sensitivity studies on the roughness length for momentum / heat ratio kB^{-1} have demonstrated that the success on H -mapping depends primarily on kB^{-1} , Figs. 9.4 to 9.6 indicate that the variable δT_{a-sur} and constant kB^{-1} approach in SEBAL eliminates the crucial role of kB^{-1} : The fractional difference for kB^{-1} was low in all cases.

9.4 Uncertainty analysis of surface flux densities and moisture indicators

For the uncertainty analysis, the random deviation of the SEBAL model parameters x_j is assumed to be normally distributed: The range of x_j -values is characterized by the mean value and the standard deviation is a pre-fixed percentage of the mean. Using large sets of the randomly distributed independent x_j -parameters, the output for Y_k can be computed by Monte Carlo simulation. Table 9.4 presents an example of the considered $x_7 \dots x_{10}$ mean values and standard deviation for rice ($j=3$). To estimate the variability of each x_j -parameter, all standard deviations were set at 5% of the reference parameter value. The possible deviations of the independent variables x_j should be estimated individually, but such in-depth field investigation was neither performed in the Qattara Depression, nor in EFEDA.

The Monte Carlo simulation can be used to get a better idea of the effects of simultaneous model parameter variability and how this variability propagates into deviations of flux densities and moisture indicators. The question posed is: *What is the probability of exceeding a certain deviation?* To calculate the pdf for $Y_{k,3}$, $Y_{k,20}$, and Z_k $m=3000$ repetitions * $n=10$ parameters * $g=20$ locations = $12 * 10^6$ random values are generated. The pdf of the $Z_{\lambda E}$ is shown in Figure 9.7. $\langle \lambda E \rangle$ was computed according to the procedure outlined in Eq. (9.4). The pdf has the shape of a normal distribution (mean 247 W m^{-2} , median 245 W m^{-2}), being to a relevant extent a consequence of assuming normal distributions on x_i .

Table 9.4 Variability in hydro-meteorological-parameters used in SEBAL for the rice unit in the Eastern Nile Delta ($j=3$)

Parameter string	Symbol	Unit	Mean	σ_d	Min. ($3\sigma_d$)	Max. ($3\sigma_d$)
s_1	r_0	-	0.113	0.006	0.095	0.131
s_2	L^1	W m^{-2}	310	16	291	329
s_3	ϵ_0	-	0.99	0.05	0.84	1.0
s_4	T_0	$^{\circ}\text{C}$	31.9	1.6	27.1	36.7
s_5	K^d	W m^{-2}	1019	51	866	1172
s_6	Γ	-	0.10	0.005	0.085	0.115
s_7	z_{0m}	m	0.13	0.007	0.109	0.151
s_8	kB^{-1}	-	2.3	0.12	1.9	2.7
s_9	u	m s^{-1}	0.89	0.04	0.77	1.01
s_{10}	δT_{a-surf}	$^{\circ}\text{C}$	0.02	0.001	0.017	0.023

The pdfs of the distribution of the differences $|Y_k - Y_k^{mean}|$ are presented in Figs. 9.8 to 9.10. Obviously, H is most reliably estimated at a mixture of land surfaces with a relative deviation of 34% at a 95% confidence level ($2\sigma_d$). Also the latent heat flux densities can be estimated best for heterogeneous land surfaces (33% deviation for rice, 350% deviation for desert and 22% deviation for all surfaces at a 95% probability level). Hence, there is a persistent tendency towards averaging out of deviations that occur at homogeneous surface units when considering heterogeneous land surfaces. The same conclusion can be drawn for Λ and r_s . On the basis of Figure 9.10, it may be concluded that the *most reliable parameter expressing the energy partitioning for heterogeneous surfaces according to the formulation of the SEBAL procedure is Λ .*

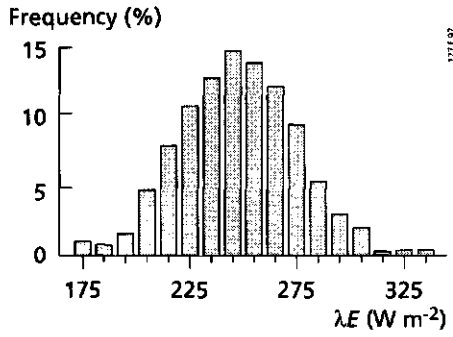


Fig. 9.7 Histogram of a Monte Carlo simulation of the area-average latent heat flux density, $\lambda\tilde{E}$, in the Eastern Nile Delta and Eastern Desert, July 27, 1987, based on 20 individual land surface clusters given a hypothetical equal weight

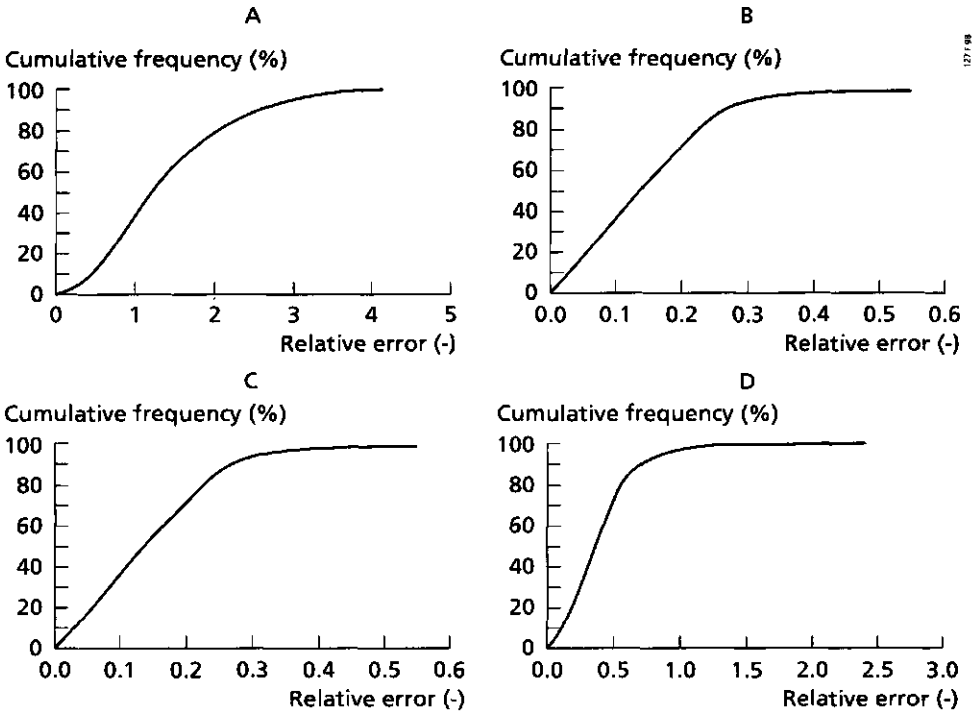


Fig. 9.8 Probability distribution function of the relative deviation from the mean model output obtained after a Monte Carlo simulation of surface energy balances in rice. (Part A) sensible heat flux density H , (Part B) latent heat flux density λE , (Part C) evaporative fraction Λ and (Part D) surface resistance, r_s

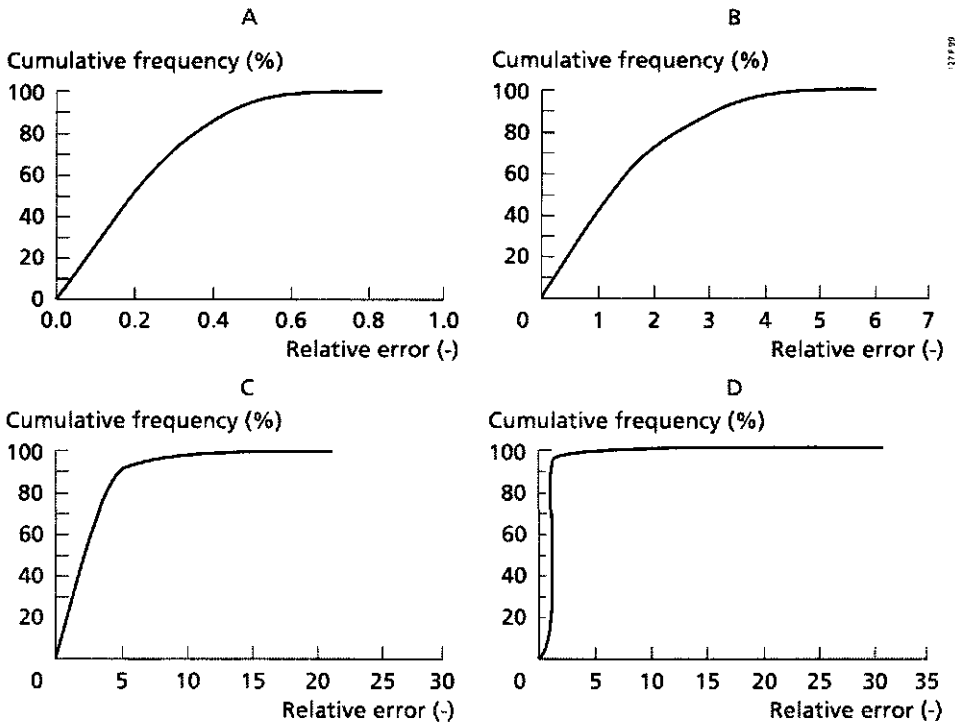


Fig. 9.9 Probability distribution function of the relative deviation from the mean model output obtained after a Monte Carlo simulation of surface energy balances in **desert**. (Part A) sensible heat flux density H , (Part B) latent heat flux density λE , (Part C) evaporative fraction Λ and (Part D) surface resistance, r_s .

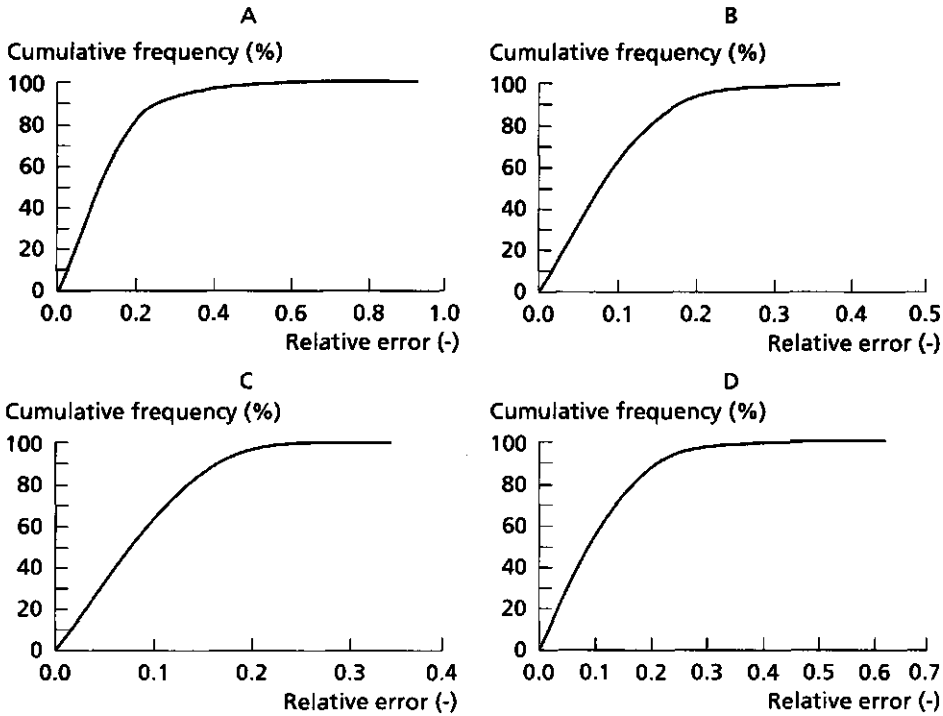


Fig. 9.10 Probability distribution function of the relative deviation from the mean model output obtained after a Monte Carlo simulation of surface energy balances in the Entire Eastern Nile Delta and Eastern Desert. (Part A) sensible heat flux density H , (Part B) latent heat flux density λE , (Part C) evaporative fraction Λ and (Part D) surface resistance, r_s .

9.5 Concluding remarks

The range over which λE was explored in the Eastern Nile Delta and Eastern Desert was rather large (desert, sebkha, irrigated agriculture) and therefore statements for wet, dry and mixed land surface types could be given. As compared to r_s , Λ is in general less sensitive to variations in SEBAL model parameters. The value for r_s seems to be especially sensitive to T_0 which determines e_{sat} in a highly non-linear way (see Eq. 2.29). The uncertainty analysis confirmed the results of the sensitivity analysis by recognizing a higher probability level of exceeding a certain error for Λ than for r_s . In general it can be concluded that λE can only be accurately estimated over wet surfaces and H over dry surfaces (if a correct pixel resolution in relation to the correlation length and semi-variance is chosen). Since λE over dry surfaces can not be obtained accurately using the residue surface energy budget approach, it is recommended that alternative

procedures based on the concept of calculating λE from r_s (Eq. 3.33) are investigated. Remarkable is that the sensitivity to T_0 and kB^1 in conventional remote sensing flux density algorithms has been entirely eliminated by means of the 'evaporative fraction-vertical air temperature difference' method.

The advantage of remote sensing data, especially high resolution data, is that a number of samples (i.e. pixels) can be used to obtain estimates at lower resolutions with smaller random errors. The estimation of surface flux densities and moisture indicators can be performed by averaging out the random error over a limited number of pixels (say 20), at the cost of a poorer resolution. This comment applies also to heterogeneous land surfaces: The uncertainty analysis revealed that the relative deviations in λE , Λ en r_s becomes less when moving from homogeneous to heterogeneous land surfaces. This was also noted in the validation studies of Egypt and Spain: The error averages out when several irrigation districts and patches are considered simultaneously. Section 8.1 has shown that, the root mean square error with field measurements at patch level yielded $\Delta(RMSE) \approx 0.10$ to 0.19 (relative error $\approx 30\%$) and at regional level comprising 10 to 13 patches was $\Delta\Lambda \approx 0.04$, which at $\bar{\Lambda} \approx 0.40$ is equal to a relative error of 10%.

10 Conclusions

Diurnal evolution of moisture indicators

- Heterogeneity of surface energy partitioning for short time spells can be expressed as the slope between semi-variance and lag distance of the evaporative fraction, i.e. latent heat flux density / net available energy fraction (Section 1.1);
- Evaporation of heterogeneous land surfaces can among others be described by means of a bulk surface resistance to account for soil moisture deficit. This bulk surface resistance can be analytically coupled to canopy and bare soil resistance which have a physical meaning (Section 3.3);
- Small pores retain water in the liquid phase down to very low pressure heads requiring a multi-phase flow theory to describe the bare soil evaporation process and to formulate the resistance to bare soil evaporation correctly (Section 2.2);
- The resistance to bare soil evaporation has a distinct diurnal fluctuation that is related to fast changing atmospheric moisture gradients and slow changing soil moisture gradients (Section 5.5);
- The evaporative fraction of homogeneous bare soils between 10⁰⁰ and 16⁰⁰ local time is fairly constant (CV=0.19, n = 96) (Section 5.4);
- The evaporative fraction of meso-scale heterogeneous land surfaces encompassing desert, sea and agricultural land is temporally stable during daytime (CV=0.20) (Section 8.3);
- The sensible heat/net radiation flux density ratio behaves temporally stable during daytime which can be explained by the narrow time shift between air heating and land surface heating by solar radiation (Section 5.4);
- The convex soil heat/net radiation, concave latent heat/net radiation and constant sensible heat/net radiation flux density ratios causes preserved evaporative fractions during daytime, also at extended bare soil surfaces (Section 5.4);
- Since net available energy is for manifold climate conditions a suitable proxy for potential evaporation, the evaporative fraction is a good indicator for relative evaporation (Section 5.6).

Land surface radiative properties measured by remote sensing

- Vertical land surface flux densities are characterized by a relationship between horizontal terrain properties and state conditions at one hand and vertical length scales for the integration of the eddy diffusivities at the other hand. This aspect needs consideration if the remotely sensed surface with a given horizontal sampling resolution, are applied to estimate local flux-profile relationships (Section 3.5);

- Under non-turbid conditions, hemispherical surface reflectance may be determined from the single observation planetary reflectance and the overall atmospheric transmittance in the shortwave range (Section 6.2);
- Remote sensing estimates of the surface energy balance terms in composite terrain can hardly be validated for a single high resolution pixel: The strength of the sources of the in-situ measured flux densities is variable and the total footprint encompasses usually several pixels (Section 8.1);
- Radiative properties of low resolution pixels reflecting composite terrain are not necessarily suitable for the estimation of local flux-profile relationships. The flux density of a small ensemble of low resolution pixels obtained by linear averaging reduces the uncertainty of the estimated surface flux densities substantially (Section 8.2).

Surface energy balance modelling aspects

- The convex soil heat/net radiation flux density ratio can be described by means of the diurnal trend of the surface temperature/surface hemispherical reflectance ratio;
- The relationship between surface temperature and hemispherical surface reflectance for regions with a wide contrast in hydrological conditions, provides the opportunity to allocate sub-areas (one or more pixels) with a zero evaporative fraction and sub-areas with an evaporative fraction of 1 (Sections 6.5 and 7.6);
- The vertical near-surface air temperature difference can be obtained from inversion of the sensible heat flux density for specific sub-areas where the evaporative fraction is 0 and 1 and air temperature measurements are not needed to achieve this (Section 7.6);
- Regional near-surface air temperature differences can be estimated in a distributed manner using surface temperature maps (being corrected for emissivity effects) from a linear relationship between surface temperature and near-surface vertical air temperature (Section 6.6);
- The *evaporative fraction-vertical air temperature difference* method ensures that the sensitivity of various model parameters and kB^{-1} especially to the surface energy balance is strongly reduced (Sections 7.6 and 9.2);
- The area-effective friction velocity can be estimated from those pixels where the slope between surface temperature and hemispherical surface reflectance is negative (Section 7.5);
- The necessity of ground data to execute the Surface Energy Balance Algorithm for Land (SEBAL) is reduced to a minimum: Ground data on atmospheric shortwave transmittance, surface temperature and surface roughness for momentum transfer remain however required (Section 7.8);
- The accuracy of a certain surface flux density and moisture indicator estimated by SEBAL is a function of (i) the degree of heterogeneity, (ii) the correlation length, (iii) the spatial resolution, (iv) the spatial scale and (v) the prevailing soil moisture conditions (Section 8.2);

- Parameter variability studies have indicated that uncertainty associated to the evaporative fraction is less than to the bulk surface resistance if both are estimated by SEBAL (Section 9.3);
- Despite the empirical character on certain computation steps and the ignorance of calibration with in-situ flux densities, the validation of SEBAL for EFEDA indicates a relative error in evaporative fraction of 20%, 10% and 1% at a scale of 1 km, 5 km and 100 km respectively. Hence, if a larger set of pixels is considered, the error averages out (Section 8.1). The same comment applies to uncertainty of the model predictions: the uncertainty of SEBAL output at a fixed probability level for homogeneous areas is larger than for heterogeneous areas (Section 9.4)

SEBAL can be used to:

- Study probability density functions and semi-variograms of several common hydro-meteorological parameters and the retrieval of their area-effective values;
- Initialize and validate large-area land surface parameterization schemes;
- Derive area-effective soil physical properties applying inversion techniques;
- Monitor long term land surface energy partitioning for detection of possible land degradation such as water logging, desertification and salinization;
- Improve the performance of irrigation water supply by comparing actual water use with actual water supply at different spatial scales;
- Support regional crop yield forecast models using distributed and crop wise averaged evaporation rates;
- Study air pollution processes being related to sensible heat flux densities;
- Design and allocate pilot areas in regional hydrological field studies.

References

(A list of publications from Universities and Research Institutes is presented separately)

Abbott, M.B., J.C. Bathurst, J.A. Cunge, P.E. O'Connell and J. Rasmussen, 1986. An introduction to SHE, structure of a physically based distributed modelling system, *J. of Hydr.* 87: 45-77

Ahern, F.J., D.G. Goodenough, S.C. Jain, V.R. Rao and G. Rochon 1977. Use of clear lakes as standard reflectors for atmospheric measurements, in *Proc. 11th Int. Symp. on Rem. Sens. of the Envir*: 731-755

Allen, R.G., M. Smith, A. Ferrier and L.S. Pereira, 1995. An update for the definition of reference evapotranspiration, *ICID Bulletin*, vol. 43, no. 2: 1-34

Andre, J.C., J.P. Goutorbe and A. Perrier, 1986. HAPEX-MOBILHY: A hydrological atmospheric experiment for the study of water budget and evaporation flux at the climatic scale, *Bull. Met. Soc.* 67: 138-144136

Andre, J.C. and C. Blondin, 1986. On the effective roughness length for use in numerical three-dimensional models, *Boundary-Layer Met.* 35: 231-245

Arino, O., G. Dedieu and Y. Deschamps, 1992. Determination of land surface spectral reflectances using METEOSAT and NOAA/AVHRR shortwave channel data. *Int. J. of Rem. Sens.*, vol 13, no. 12: 2263-2287

Asrar, G., R.B. Myneni and B.J. Choudhury, 1992. Spatial heterogeneity in vegetation canopies and remote sensing of absorbed photosynthetically active radiation: a modeling study, *Rem. Sens. Env.* 41: 85-103

Avissar, R., 1991. A statistical-dynamical approach to parameterize subgrid-scale land-surface heterogeneity in climate models, *Surveys in Geophysics* 12: 155-178

Avissar, R. and R.A. Pielke, 1989. A parameterization of heterogeneous land surfaces for atmospheric numerical models and its impact on regional meteorology, *Monthly Weather Review*, vol. 117: 2113-2136

Azzali, S., M. Menenti, I. Meuwissen and T.N.M. Visser, 1990. Mapping of crop coefficients in an Argentinian irrigation scheme using remote sensing techniques, in (ed.) M. Menenti, *Remote Sensing in evaluation and management of irrigation*, Instituto Nacional de Ciencia y Tecnica Hidricas (INCYTH), Mendoza, Argentina

Baldocchi, D.D., R. J. Luxmore and J.L. Hatfield, 1991. Discerning the forest from the trees: an essay on scaling canopy stomatal conductance, *Agr. and Forest Met.* 54: 197-226

Barton, I.J., 1979. A parameterization of the evaporation from non-saturated surfaces, *J. of Applied Met.*, vol. 18: 43-47

Bastiaanssen, W.G.M. 1991. Derivation of areal soil physical data from satellite measurements, XX General Assembly of the International Union of Geodesy and Geophysics, Viena, 11-24 August 1991, in Kienitz et al. (eds.) *Hydrological interactions between atmosphere, soil and vegetation*, IAHS Publication no. 204, IAHS press, Oxfordshire U.K. : 361-376

Bastiaanssen, W.G.M. and M. Menenti, 1990. Mapping groundwater losses in the Western Desert of Egypt with satellite measurements of surface reflectance and surface temperature, in J.C. Hooghart (ed.), *Water Management and Remote Sensing*, TNO-Proc. and Inform. no. 42, The Hague, The Netherlands: 61-90

Bastiaanssen, W.G.M. and K. Metselaar, 1990. Correlation between remotely sensed land surface parameters and soil resistances: the parameterization of soil hydraulic properties, Proc. Int. Symp. on remote sensing and water resources, ITC, 20-24 August 1990, Enschede, The Netherlands: 287-293

Bastiaanssen, W.G.M. and R.A. Roebeling, 1993. Analysis of land surface exchange processes in two agricultural regions in Spain using Thematic Mapper Simulator data, in (eds.) Bolle, Feddes and Kalma, Exchange processes at the land surface for a range of space and time scales, IAHS Publ. no. 212 IAHS press, Oxfordshire, U.K., : 407-416

Bastiaanssen, W.G.M., D.H. Hoekman and R.A. Roebeling, 1994a. A methodology for the assessment of surface resistance and soil water storage variability at mesoscale based on remote sensing measurements, A case study with HAPEX-EFEDA data, IAHS Special Publication no. 2, IAHS Press, Oxfordshire U.K.: pp. 66

Bastiaanssen, W.G.M., M. Menenti and P. Kabat, 1990. Simulation of capillary soil water flow under arid conditions: application to soil types in the Western Desert of Egypt, In Proc. Symp. on land drainage for salinity control in arid and semi-arid regions, ICID, Cairo, Febr. 25 to March 2, 1990, vol 2: 260-273

Bastiaanssen, W.G.M., M. Menenti, P.J. van Oevelen, D.H. Hoekman and R.A. Feddes, 1994b. Spatial variability and accuracy of remote sensing estimates of evaporation and soil moisture within EFEDA'91, Proc. Conference Trinity College Dublin, September 7 to 9, 1994: 175-192

Bastiaanssen, H. Pelgrum, T. van der Wal and R.A. Roebeling, 1995a. Aggregation of evaporative fraction by remote sensing from micro to macro scale, Proc. Remote Sensing for land degradation and desertification monitoring in the Mediterranean Basin, 13 to 15 June 1994, Valencia: pp. 20 (in press)

Bastiaanssen, W.G.M., C.W.J. Roest, H. Pelgrum and M.A. Abdel Khalek, 1992. Monitoring of the irrigation performance on the basis of actual evapotranspiration: Comparison of satellite data and simulation model results, in (Eds.) J. Feyen, E. Mwendera and M. Badji, advances in planning, design and management of irrigation systems as related to sustainable land use, Center for Irrigation Engineering and ECOWARM, Leuven: 473-483

Bastiaanssen, W.G.M., T. van der Wal and T.N.M. Visser, 1995b. Diagnosis of regional evaporation by remote sensing to support irrigation performance assessment, Irrigation and Drainage Systems, vol. 9, no. 4 (in press): pp 20

Bear, J., 1972. Dynamics of fluids in porous media, American Elsevier, New York: pp. 764

Becker, F. and Z.L. Li, 1990. Towards a local split window method over land surfaces, Int. J. of Remote Sensing, vol. 11, no. 3: 369-393

Beljaars, A.C.M. and A.A.M. Holtslag, 1991. Flux parameterization over land surfaces for atmospheric models, J. of Applied Meteorology, vol. 30, no. 3: 327-341

Blyth, E.M. and A.J. Dolman, 1995. The roughness length for heat of sparse vegetation, J. of Applied Met. 34: 583-585

Blyth, E.M., A.J. Dolman and N. Wood. 1993. Effective resistance to sensible and latent heat flux in heterogeneous terrain, Q.J.R. Met. Soc. 119: 423-442

Boels, D., Van Gils, J.B.H.M., Veerman, G.J. and K.E. Wit, 1978. Theory and system of automatic determination of soil moisture characteristics and unsaturated hydraulic conductivities, Soil Sci. 126: 191-199

- Bolle, H.J. et al., 1993. EFEDA: European field experiments in a desertification-threatened area, *Annales Geophysica* 11: 173-189
- Bougeault, B., 1991. Parameterization schemes of land-surface processes for mesoscale atmospheric models, in (Eds.) T.J. Schmugge and J.C. Andre, *Land surface evaporation*, Springer Verlag: 55-92
- Bougeault, B., P. Bret, P. Lacarrere and J. Noilhan, 1991. An example of spatial integration of a land-surface parameterization in a meso- β -scale model, in (Eds.) T.J. Schmugge and J.C. Andre, *Land surface evaporation*, Springer Verlag: 383-414
- Bowen, I.S., 1926. The ratio of heat losses by conduction and by evaporation from any water surface, *Phys. Rev.* 27: 779-798
- Bruin, H.A.R. de, and A.A.M. Holtslag, 1982a. A model for the Priestley-Taylor parameter α , *J. of Climate and Appl. Met.* 22: 572-578
- Bruin, H.A.R. de, and A.A.M. Holtslag, 1982b. A simple parameterization of the surface fluxes of sensible heat and latent heat during daytime compared with the Penman-Monteith concept, *J. of Applied Met.*, vol 21: 1610-1621
- Bruin, H.A.R. de, N.J. Bink and L.J.M. Kroon, 1991. Fluxes in the surface layer under advective conditions, In (eds.) Schmugge and Andre, *Land surface evaporation*, Springer Verlag: 157-169
- Brunet, Y., B. Itier, K.J. McAneney and J.P. Lagouarde, 1994. Downwind evolution of scalar fluxes and surface resistance under conditions of local advection. Part II: measurements over barley, *Agr. and Forest Met.* 71: 227-245
- Brunt, D., 1932. Notes on radiation in the atmosphere, *Q.J. R. Met. Soc.* 58: 389-420
- Brutsaert, W., 1982. *Evaporation into the atmosphere, theory, history and applications*, Reidel, Dordrecht. pp. 299
- Brutsaert, W. and M. Sugita, 1992. Application of self-preservation in the diurnal evolution of the surface energy budget to determine daily evaporation, *J. of Geophysical Res.*, vol 97, D17: 18,377-18,382
- Brutsaert, W., A.Y. Hsu and T.J. Schmugge, 1993. Parameterization of surface heat fluxes above forest with satellite thermal sensing and boundary layer soundings, *J. of Applied Met.*, vol. 32(5): 909-917
- Camillo, P.J., 1991. Using one- or two-layer models for evaporation estimation with remotely sensed data, In (eds.) Schmugge and Andre, *Land surface evaporation*, Springer Verlag : 183-197
- Camillo, P.J. and R.J. Gurney, 1986. A resistance parameter for bare soil evaporation models, *Soil science* 141: 95-105
- Carlson, T.N., E.M. Perry and T.J. Schmugge, 1990. Remote estimation of soil moisture availability and fractional vegetation cover for agricultural fields, *Agr. and Forest Met.* 52: 45-69
- Carman, P.C., 1956. *Flow of gases through porous media*, Butterworths, London: pp. 182
- Chamberlain, A.C., 1966. *Proc. Roy. Soc. London A*290: 236-265

Chanzy, A. and L. Bruckler, 1993. Significance of soil surface moisture with respect to daily bare soil evaporation, *Water Resources Research* 29 (4): 1113-1125

Chen, E., L.H. Allen, J.F. Bartholic and J.F. Gerber, 1983. Comparison of winter-nocturnal geostationary satellite infrared-surface temperature with shelter-height temperature in Florida, *Rem. Sens. of Env.* 13: 313-327

Choudhury, B.J., 1989. Estimating evaporation and carbon assimilation using infrared temperature data: Vistas in modeling, (ed.) G. Asrar. *Theory and applications of optical remote sensing*, John Wiley, New York: 628-690

Choudhury, B.J., 1991. Multispectral satellite data in the context of land surface heat balance, *Review of Geophysics*, 29,2: 217-236

Choudhury, B.J. and J.L. Monteith, 1988. A four-layer model for the heat budget of homogeneous land surfaces, *Q.J.R. Met. Soc.*, 114: 373-398

Choudhury, B.J., N.U. Ahmed, S.B. Idso, R.J. Reginato and C.S.T. Daughtry, 1994. Relations between evaporation coefficients and vegetation indices studied by model simulations, *Rem. Sens. of Env.* 50: 1-17

Choudhury, B.J., S.B. Idso and R.J. Reginato, 1987. Analysis of an empirical model for soil heat flux under a growing wheat crop for estimating evaporation by an infrared-temperature based energy balance equation, *Agr. and Forest Met.*, 39: 283-297

Choudhury, B.J., R.J. Reginato and S.B. Idso, 1986. An analysis of infrared temperature observations over wheat and calculation of latent heat flux, *Agr. and Forest Met.* 37: 75-88

Clap, R.B. and G.M. Homberger, 1978. Empirical equations for some soil hydraulic properties, *Water Resources Research* 14 (4): 601-604

Claussen, M., 1990. Area-averaging of surface fluxes in a neutrally stratified, horizontally inhomogeneous atmospheric boundary layer, *Atmospheric Environment*, vol 24A, no. 6: 1349-1360

Clifford, S.M. and D. Hillel, 1986. Knudsen diffusion: the effect of small pore size and low gas pressure on gaseous transport in soil, *Soil Science*, vol 141, no. 4: 289-297

Clothier, B.E., K.L. Clawson, P.J. Pinter, M.S. Moran, R.J. Reginato and R.D. Jackson, 1986. Estimation of soil heat flux from net radiation during the growth of alfalfa, *Agr. and Forest Met.* 37: 319-329

Crosson, W.L. and E.A. Smith, 1992. Estimation of surface heat and moisture fluxes over a prairie grassland, two-dimensional time filtering and site variability, *J. of Geophysical Res.*, vol. 97, no. D17: 18,583-18,598

Cure, W.W., R.B. Flagler and A.S. Heagle, 1989. Correlations between canopy reflectance and leaf temperature in irrigated and droughted soybeans, *Rem. Sens. of Env.* 29: 273-280

Curran, P.J., 1998. The semivariogram in remote sensing: an introduction, *Rem. Sens. of Env.* 24: 493-507

Cushman, J.H., 1986. On measurement, scale and scaling, *Water Resources Research*, vol. 22, no. 2: 129-134

Daughtry, C.S.T., W.P. Kustas, M.S. Moran, P.J. Pinter, R.D. Jackson, P.W. Brown, W.D. Nichols and L.W. Gay, 1990. Spectral estimates of net radiation and soil heat flux, *Rem. Sens. of Env.* 32: 111-124

Davis, P.A. and J.D. Tarpley, 1983. Estimation of shelter temperatures from operational satellite sounder data, *Climate and Applied Meteorology*, vol. 22: 369-376

Dedieu, G., P.Y. Deschamps and Y.H. Kerr, 1987. Satellite estimation of solar irradiance at the surface of the earth and of surface albedo using a physical model applied to METEOSAT data, *J. of Climate and Applied Meteorology*, vol 26: 79-87

Diak, G.R., 1990. Evaluation of heat flux, moisture flux and aerodynamic roughness at the land surface from knowledge of the PBL height and satellite-derived skin temperatures, *Agr. and Forest Met.* 52: 181-198

Dolman, A.J., 1992. A note on areally-averaged evaporation and the value of effective surface conductance, *J. of Hydr.* 138: 583-589

Dolman, A.J., 1993. A multiple-source land surface energy balance model for use in general circulation models, *Agr. and Forest Met.* 65: 21-45

Dolman, A.J. and E.M. Blyth, 1995. Patch scale aggregation of heterogeneous land surface cover for mesoscale meteorological models, *J. of Hydr.* (in press)

Doorénbos, J. and W.O. Pruitt, 1977. Guidelines for predicting crop water requirements, *FAO Irrigation and Drainage Paper 24*, FAO, Rome: pp. 144

Duffie, J.A. and W.A. Beckman, 1980. *Solar Engineering of Thermal Processes*, A Wiley-Interscience Publication, John Wiley & Sons, pp.

Dyer, A.J. and B.B. Hicks, 1970. Flux-gradient relationships in the constant flux layer, *Q. J.R. Met. Soc.* 96: 715-721

Edlefsen, N.E. and A.B.C. Anderson, 1943. The thermodynamics of soil moisture, *Hilgardia* 16: 31-299

Enthekabi, D. and P.S. Eagleson, 1989. Land surface hydrology parameterization for atmospheric general circulation models including subgrid scale variability, *J. of Clim.* 8: 816-831

Ergun, S., 1952. Fluid flow through packed columns, *Chem. Engng. Prog.* 48: 89-94

Ezzat, M.A., 1983. Impact of a future Qattara salt-water lake on the Nubian Sandstone aquifer system in the Western Desert of Egypt, *IAHS Publ no. 136*, IAHS press, Oxfordshire U.K.: 297-314

Famiglietti, J.S. and E.F. Wood, 1991. Evapotranspiration and runoff from large land areas: land surface hydrology for atmospheric general circulation models, *Surveys in Geophysics*, vol. 12: 179-204

Famiglietti, J.S. and E.F. Wood, 1994. Multiscale modelling of spatially variable water and energy balance processes, *Water Resources Research*, vol. 30, no. 11: 3061-3078

Feddes, R.A. and W.G.M. Bastiaanssen, 1992. Forecasting soil-water-plant-atmosphere interactions in arid regions, in (Eds.) H.J.W. Verplancke et al, *NATO Workshop for Water Saving Techniques for Plant Growth*, September 17-19, Gent, Belgium, NATO ASI-series: 57-78

Feddes, R.A., P. Kabat, P.J.T. van Bakel, J.J.B. Bronswijk and J. Halbertsma, 1988. Modelling soil water dynamics in the unsaturated zone - state of the art, *J. of Hydr.* 100: 69-111

Feddes, R.A., P.J. Kowalik and H. Zaradny, 1978. Simulation of field water use and crop yield, *PUDOC*, Wageningen, pp. 189

- Feddes, R.A., M. Menenti, P. Kabat and W.G.M. Bastiaanssen, 1993. Is large scale inverse modelling of unsaturated flow with areal average evaporation and surface soil moisture as estimated from remote sensing feasible?, *J. of Hydr.* 143: 125-152
- Fiedler, F. and H.A. Panofsky, 1972. The geostrophic drag coefficient and the effective roughness length, *Q.J.R.Met. Soc.* 98: 213-220
- Fraser, R.S. and Y.J. Kaufman, 1985. The relative importance of aerosol scattering and absorption in remote sensing, *IEEE Trans. Geosc. Rem. Sens.*, GE-23, 5: 625-633
- Fung, A.K., Zongqian Li and K.S. Chen, 1992. Backscatter from a randomly rough dielectric surface, *IEEE Trans Geosc. Rem. Sens.* vol. 30, no. 2: 356-369
- Gardner, W.R., 1958. Some steady-state solutions of the unsaturated moisture flow equation with application to evaporation from a water table, *Soil Sci.* : 228-232
- Garrat, J.R., 1978. Transfer characteristics for a heterogeneous surface of large aerodynamic roughness, *Q. J. Roy. Met. Soc.* 104: 491-502
- Gash, J.H.C. et al. 1995. The variability of evaporation during the HAPEX-Sahel intensive observation period, *J. of Hydr.* (submitted)
- Gay, L.W. and Ch. Bernhofer, 1991. Enhancement of evapotranspiration by advection in arid regions, in (Eds) Kienitz et al., *Hydrological interactions between atmosphere, soil and vegetation*, Proc Vienna conference, IAHS Publication no. 204 IAHS press, Oxfordshire, U.K.:147-156
- Gebhardt, A., 1986. Zur grobmaBstabigen differenzierung der bodenfeuchte mittels thermografie, *Arch. Acker Pflanzenbau*, Berlin 30, no. 11: 689-695
- Gelhar, L.W., 1993. *Stochastic Subsurface Hydrology*, Prentice-Hall Inc., a Simon&Schuster Company, New Jersey: pp.
- Genuchten, M.Th. van, 1980. A closed-form equation for predicting the hydraulic conductivity of unsaturated soils, *Soil Sci. Am. J.* 44: 892-898
- Goudriaan, J., 1989. Simulation of micrometeorology of crops, some methods and their problems and a few results, *Agr. and Forest Met.* 47: 239-258
- Goutorbe, et al., 1994. HAPEX SAHEL: A large scale study of land-atmosphere interactions in the semi-arid tropics, *Annales Geophysicae* 12: 53-64
- Goward, S.N., G.D. Cruickshanks and A.S. Hope, 1985. Observed relation between thermal emission and reflected spectral radiance of a complex vegetated landscape, *Rem. Sens. of Env.* 18: 137-146
- Graser, E.A. and C.H.M. Van Bavel, 1982. The effect of soil moisture upon soil albedo, *Agr. Met.* 27: 17-26
- McGuffie, K. and A. Henderson-Sellers, 1987. Climatology from space: data sets for climate monitoring and climate modelling, in R.A. Vaughan (ed.), *Remote sensing applications in meteorology and climatology*, D. Reidel Publishing Company: 375-389
- Griend, A.A. van de, and M. Owe, 1993. On the relationship between thermal emissivity and the Normalized Difference Vegetation Index for natural surfaces, *Int. J. of Rem. Sens.*, vol. 14, no. 6: 1119-1131

Griend, A.A. van de, and M. Owe, 1994. Bare soil surface resistance to evaporation by vapor diffusion under semiarid conditions, *Water Resources Research*, vol. 30, no. 2: 181-188

Hall, F.G., K.F. Huemmrich, S.J. Goetz, P.J. Sellers and J.E. Nickeson, 1992. Satellite remote sensing of surface energy balance: succes, failures and unresolved issues in FIFE, *J. of Geophysical Research*, vol. 97, no. D17: 19,061-19,089

Hanan, N.P., S.D. Prince, P.H.Y. Hiemaux, 1991. Spectral modelling of multicomponent landscapes in the Sahel, *Int. J. of Rem. Sens.* 12(6): 1243-1258

Hargreaves, G.H., 1993. Minimum climatic data for irrigation and drainage planning and design, ICID 15th Congress, The Hague, Question 44, R14: 157-167

Hatfield, J.L., 1988. Large scale evapotranspiration from remotely sensed surface temperature, Proc. on planning, now for irrigation & drainage IR Div/ASCE, Lincoln, NE, July 18-21: 502-509

Hofstee, C., J.D. Kalma, H.A. Cleugh and J.M. Hacker, 1993. Measurements and estimates of evaporation at a range of scales, in (eds.) Bolle et al., *Exchange processes at the land surface for a range of space and time scales*, IAHS Publication no. 212 IAHS press, Oxfordshire, U.K.: 381-388

Holtslag, A.A.M. 1984. Estimates of diabatic wind speed profiles from near-surface weather observations, *Boundary Layer Meteorology* 29: 225-250

Holtslag, A.A.M. and de Bruin, H.A.R., 1988. Applied modeling of the nighttime surface energy balance over land, *J. Applied Met.* 27: 684-704

Holtslag, A.A.M. and F.T.M. Nieuwstadt, 1986. Scaling the atmospheric boundary layer, *Bound Layer Met.* 36: 201-209

Holtslag, A.A.M. and Van Ulden, A.P., 1983. A simple-scheme for daytime estimates of the surface fluxes from routine weather data, *J. of Climate and applied Met.*, vol. 22, no. 4: 517-529

Horiguchi, I., H. Tani and T. Motoki, 1992. Accurate estimation of 1.5 m-height air temperature by GMS IR data, Proc. 24th Int. Symp. on Rem. Sens. of Envir., Rio de Janeiro, May 1991: 301-307

Huete, A.R. and C.J. Tucker, 1991. Investigation of soil influences in AVHRR red and near-infrared vegetation index imagery, *Int. J. of Rem. Sens.*, vol 12, no. 6: 1223-1242

Huete, A.R. and A.W. Warrick, 1990. Assessment of vegetation and soil water regimes in partial canopies with optical remotely sensed data, *Rem. Sens. of Env.* 32: 155-167

Hunt, E.R., S.W. Running and C.A. Federer, 1991. Extrapolating plant water flow resistances and capacitances to regional scales, *Agr. and Forest Met.* 54: 169-195

Itier, B., Y. Brunet, K.J. McAneney and J.P. Lagouarde, 1994. Downwind evolution of scalar fluxes and surface resistance under conditions of local advection. Part I: a reappraisal of boundary conditions, *Agr. and Forest Met.* 71: 211-225

Iqbal, M., 1983. *An introduction to solar radiation*, Academic Press, Toronto

Jackson, R.D., S.D. Idso, R.J. Reginato and P.J. Pinter, 1981. Canopy temperature as a crop water stress indicator, *Water Resources Research.* 17(4): 1133-1138

- Jackson, R.D., R.J. Reginato and S.B. Idso, 1977. Wheat canopy temperatures: A practical tool for evaluating water requirements, *Water Resources Research* 13: 651-656
- Jarvis, P.G., 1976. The interpretation of the variation in leaf water potential and stomatal conductance found in canopies in the field, *Phil. Trans. R. Soc. London Ser B* 273: 593-610
- Jochum, A.M., B.I. Michels and N. Entstrasser, 1993a. Regional and local variations of evaporation fluxes during EFEDA. *Conf. of Hydroclimatology*, 17-22 Jan 1993, Anaheim: pp. 4
- Jochum, A.M., M.G. Inclan and S.S. Saatchi, 1993b. Estimation of surface evapotranspiration from airborne SAR and in-situ data, 25th Int. Symp. Rem. Sensing and Global Env. Change, Graz, 4-8 April: pp. 9
- Jordan, W.R. and J.T. Ritchie, 1971. Influence of soil water stress on evaporation, root absorption and internal water status of cotton, *Plant Physiol.* 48: 783-788
- Justice, C.O., J.R.G. Townsend, B.N. Holben and C.J. Tucker, 1985. Analysis of the phenology of global vegetation using meteorological satellite data, *Int. J. of Rem. Sens.* 6-8: 1271-1318
- Kahle, A.B. and R.E. Alley, 1992. Separation of temperature and emittance in remotely sensed radiance measurements, *Rem. Sens. of Env.*, vol. 42: 107-112
- Kalma, J.D. and D.L.B. Jupp, 1990. Estimating evaporation from pasture using infrared thermometry: evaluation of a one-layer resistance model, *Agr. and Forest Met.* 51: 223-246
- Kane, O. J.P., 1991. Implications for remote sensing of natural switching from atmosphere-controlled to soil-controlled evaporation or infiltration, in (eds.) Schmugge and Andre, *Land surface evaporation*, Springer Verlag: 371-381
- Klaassen, W., 1992. Average fluxes from heterogeneous vegetated regions, *Boundary Layer Met.* 58: 329-354
- Klaassen, W. and W. van den Berg, 1985. Evapotranspiration derived from satellite observed surface temperatures, *J. of Climate and Applied Met.*, vol. 24: 412-424
- Knudsen, M., 1909. Die gesetze der molekularstromung und der inneren reibungsstromung der gase durch rohren, *Ann. Physik:* 28-75
- Koepke, P., K.T. Kriebel and B. Dietrich, 1985. The effect of surface reflection and of atmospheric parameters on the shortwave radiation budget, *Adv. Space Res.* 5: 351-354
- Kondo, J., N. Saigusa and T. Sato, 1990. A parameterization of evaporation from bare soil surfaces, *J. applied Meteorology* 29: 385-389
- Koster, R.D. and M.J. Suarez, 1992. Modeling the land surface boundary in climate models as a composite of independent vegetation stands, *J. of Geoph. Res.*, vol. 97, no. D3: 2697-2715
- Kroon, L.J.M. and H.A.R. de Bruin, 1993. Atmosphere-vegetation interaction in local advection conditions: effect of lower boundary conditions, *Agr. and Forest Met.* 64: 1-28
- Kumar, S. and W.G.M. Bastiaanssen, 1993. Simulation of the water balance in relation to crop water requirements in (semi-) arid zones, *Proc. International Committee on Irrigation and Drainage ICID*, Question 44, R28, The Hague, The Netherlands: 349-363

Kustas, W.P., 1990 Estimates of evapotranspiration with a one and two-layer model of heat transfer over partial canopy cover, *J. of Applied Met.*, vol 29: 704-715

Kustas, W.P. and C.S.T. Daughtry, 1990. Estimation of the soil heat flux/net radiation ratio from spectral data, *Agr. and Forest Met.* 49: 205-223

Kustas, W.P., B.J. Choudhury, M.S. Moran, R.J. Reginato, R.D. Jackson, L.W. Gay and H.L. Weaver, 1989. Determination of sensible heat flux over sparse canopy using thermal infrared data, *Agr. and Forest Met.* 44: 197-216

Kustas, W.P., M.S. Moran, K.S. Humes, D.I. Stannard, P.J. Pinter, L.E. Hips, E. Swiatek and D.C. Goodrich, 1994b. *Surface energy balance estimates at local and regional scales using optical remote sensing from an aircraft platform and atmospheric data collected over semiarid rangelands*, *Water Resources Research*, vol. 30, no. 5: 1241-1259

Kustas, W.P., M.S. Moran, R.D. Jackson, L.W. Gay, L.F.W. Duell, K.E. Kunkel and A.D. Matthias, 1990. Instantaneous and daily values of the surface energy balance over agricultural fields using remote sensing and a reference field in an arid environment, *Rem. Sens. of Env.* 32: 125-141

Kustas, W.P., R.T. Pinker, T.J. Schmugge and K.S. Humes, 1994a. Daytime net radiation estimated for a semiarid rangeland basin from remotely sensed data, *Agr. and Forest Met.* 71: 337-357

Lagouarde. J.P. and K.J. Mc. Aney, 1992. Daily sensible heat flux estimation from a single measurement of surface temperature and maximum air temperature, *Boundary-Layer Met.* 59: 341-362

Lhomme, J.P., B. Monteny and M. Amadou, 1994. Estimating sensible heat flux from radiometric temperature over sparse millet, *Agr. and Forest Met.* 68: 77-91

Mahfouf, J.F. and J. Noilhan, 1991. Comparative study of various formulations of evaporation from bare soil using in-situ data, *J. of Applied Met.*, vol. 30: 1354-1365

Makkink, G.F., 1957. Testing the Penman formula by means of lysimeters, *J. Int. of Water Eng.* 11: 277-288

Manabe, S., 1969. Climate of the ocean circulation, the atmospheric circulation and the hydrology of the earth's surface, *Mon. Wea. Rev.* 97: 739-774

Markham, B.L. and J.L. Barker, 1987. Thematic mapper bandpass solar exoatmospherical irradiances, *Int. J. of Rem. Sens.* 8(3): 517-523.

Marsily, G. de, 1986. *Quantitative hydrogeology*, Academic Press: pp. 440

Mason, P., 1988. The formation of areally averaged roughness lengths, *Q. J. R. Met. Soc.* 114: 399-420

Mason, E.A. and A.P. Malinauskas, 1983. *Gas transport in porous media: the dusty-gas model*, Elsevier, Amsterdam: pp 194

Menenti, M. and W.G.M. Bastiaanssen, 1993. Estimation of groundwater losses by evaporation with satellite observation in the deserts of Libya and Egypt, *Proc. Int. Symp. on Rem. Sens. in Arid & Semi-Arid Regions*, Lanzhou, China, 25 to 28 August, 1993: 42-49

- Menenti, M. and B.J. Choudhury, 1993. Parameterization of land surface evaporation by means of location dependent potential evaporation and surface temperature range, in (eds.) Bolle, Feddes and Kalma, Exchange processes at the land surface for a range of space and time scales, IAHS Publ. no. 212: 561-568
- Menenti, M. and J.C. Ritchie, 1994. Estimation of effective aerodynamic roughness of Walnut Gulch watershed with laser altimeter measurements, *Water Resources Research*, vol. 30, no. 5: 1329-1337
- Menenti, M., W.G.M. Bastiaanssen and D. van Eick, 1989a. Determination of hemispherical reflectance with Thematic Mapper data, *Rem. Sens. of Env. (special issue)* 28: 327-337
- Menenti, M., W.G.M. Bastiaanssen, D. van Eick and M.H. Abd El Karim, 1989b. Linear relationships between surface reflectance and temperature and their application to map actual evaporation of groundwater, *Advances in Space Research*, vol. 9(1): 165-176
- Miller, E.E. and R.D. Miller, 1956. Physical theory for capillary flow phenomena, *J. Appl. Phys.* 27: 324-332
- Mitsuta, Y., 1994. (ed.) Proc. Int. Symp. on HEIFE, Disaster Prevention Research Institute, Kyoto Univ.: pp. 722
- Monin, A.S. and A.M. Yaglom, 1971. *Statistical fluid mechanics: mechanics of turbulence*, 2 vol I, MIT Press, London
- Monteith, J.L., 1965. Evaporation and the environment, In: *The state and movement of water in living organisms*, XIXth Symposium, Soc. for xp. Biol, Swansea, Cambridge University Press: 205-234
- Monteith, J.L., 1981. Evaporation and surface temperature, *Q. J. R. Met. Soc.*, vol 107, no. 451: 1-27
- Monteith, J.L., 1994. Fifty years of potential evaporation, Proc. Conference Trinity College Dublin, September 7 to 9, 1994: 29-45
- Moran, M.S., T.H. Clarke, Y. Inoue and A. Vidal, 1994. Estimating crop water deficit using the relation between surface-air temperature and spectral vegetation index, *Rem Sens. of Env.* 49: 246-263
- Moran, M.S., 1994. Irrigation management in Arizona using satellites and airplanes, *Irrigation Science* 15: 35-44
- McNaughton, 1976. Evaporation and advection II. Evaporation downwind of a boundary separating regions having different surface resistances and available energies, *Q.J.R. Met. Soc.* 102: 193-202
- Nemani, P.R. and S.W. Running, 1989. Estimation of regional surface evaporation from NDVI and thermal-IR AVHRR data, *J. of Applied Met.* 28: 276-284
- Nichols, W.E. and R.H. Cuenca, 1993. Evaluation of the evaporative fraction for parameterization of the surface energy balance, *Water Resources Research*, vol. 29, no. 11: 3681-3690
- Nieuwenhuis, G.J.A., E.H. Smidt and H.A.M. Thunissen, 1985. Estimation of regional evapotranspiration of arable crops from thermal infrared images, *Int. J. of Remote Sensing* 6: 1319-1334
- Noilhan, J. and P. Lacarrere, 1995. GCM grid-scale evaporation from mesoscale modelling. *J. Climate* 8: 206-223

- Noilhan, J. and S. Planton, 1989. A simple parameterization of land surface processes for meteorological models, *Monthly Weather Review*, vol 117, no. 3: 536-549
- Noilhan, J., P. Lacarre, A.J. Dolman and E.M. Blyth, 1995. Defining area-average parameters in meteorological models for land surfaces with mesoscale heterogeneity (submitted to *J. of Hydr.*)
- Obukhov, A.M., 1946. Turbulence in an atmosphere with a non-uniform temperature, *Bound. Layer Met*, 2, 1971: 7-29
- Oevelen, P.J. van, W.P. Kustas and C.S.T. Daughtry, 1993. Estimation of the available energy for evapotranspiration with the use of remote sensing, a simple modelling approach, *EARSeL Advances in Remote Sensing*, vol. 2, no. 2-VI: 100-109
- Oh, Y., K. Sarabandi and F.T. Ulubay, 1992. An empirical model and inversion technique for radar scattering from bare soil surfaces, *IEEE Trans Geosc. Rem. Sens.*, vol. 30, no. 2: 370-381
- Ottle, C. DD. Vidal-Majar and R. Girard, 1989. Remote sensing applications to hydrological modeling, *J. of Hydr.* 105: 369-384
- Owe, M., 1992. Measurements of surface resistance, reflectance and thermal emissivity during EFEDA, *Proc. European Geophysical Society, Edinborough 1992, Supplement II to Vol 10: C280*
- Owe, M., A.A. van de Griend and D.C. Carter, 1993. Modelling of longterm surface moisture and monitoring vegetation response by satellite in semi-arid Botswana, *Geo-Journal* 29.4: 335-342
- Paulson, C.A., 1970. The mathematical representation of wind speed and temperature profiles in the unstable atmospheric surface layer, *J. Applied Met.* 9: 856-861
- Paw U, K.T. and W. Gao, 1988. Applications of solutions to non-linear energy budget equations, *Agr. and Forest Met.* 43: 121-145
- Pelgrum. H. and W.G.M. Bastiaanssen, 1995b. An intercomparison of techniques to determine the area-averaged latent heat flux from individual in-situ observations: A remote sensing approach with EFEDA data: (submitted to *Water Resources Research*)
- Penman, H.L., 1948. Natural evaporation from open water, bare soil and grass, *Proc. R. Soc. Land Ser. a*, 193:120-145
- Philip, J.R. and D.A. De Vries, 1957. Moisture movement in porous materials under temperature gradients, *Trans. Am. Geophys. Union* 38: 222-231 surface for a range of space and time scales: 331-342
- Pierce, L.L., J. Walker, T.J. Downing, T.R. Vicar, T.J. Hatton, S.W. Running and J.C. Coughlan, 1992. Ecological change in the Murray-Darling Basin-III: A simulation of regional hydrological changes, *J. of Applied Ecology* 30: 283-294
- Pinker, R.T., 1990. Satellites and our understanding of the surface energy balance, palaeography, palaeoclimatology, palaeocology (global and planetary change Section), 82: 321-342
- Pinty, B. and D. Ramond, 1987. A method for the estimate of broadband directional surface albedo from a geostationary satellite, *J. of Climate and Applied Met.* 26: 1709-1722

- Pinty, B., G. Szejwacj and J. Stum, 1985. Surface albedo over the Sahel from METEOSAT radiances, *J. of Climate and Applied Meteorology*, vol 24: 108-113
- Prevot, L., Y. Brunet, K.T. Paw U and B. Seguin, 1994. Canopy modelling for estimating sensible heat flux from thermal infrared measurements, in *Proc. Workshop on Thermal remote sensing of the energy and water balance*, La Londe les Maures, 20-23 Sept. France: 17-22
- Price, J.C., 1984. Land surface temperature measurements from the split window channels of the NOAA-7 advanced very high resolution radiometer, *J. Geophys. Res.* 89: 7231-7237
- Priestley, C.H.B. and R.J. Taylor, 1972. On the assessment of surface heat flux and evapotranspiration using large scale parameters, *Mon. Weather Rev* 100: 81-92
- Qualls, R.J., W. Brutsaert and W.P. Kustas, 1993. Near-surface air temperature as substitute for skin temperature in regional surface flux estimation, *J. of Hydrology* 143: 381-393
- Raschke, E., R. Stuhlmann, W. Palz and T.C. Steemers, 1991. *Solar radiation atlas of Africa*, Published for the Commission of the European Communities, Balkema: pp. 155
- Raupach, M.R., 1991. Vegetation-atmosphere interaction in homogeneous and heterogeneous terrain, *Vegetatio* 91: 105-210
- Raupach, M.R., 1994. Simplified expressions for vegetation roughness length and zero-plane displacement as functions of canopy height and area index, *Bound. Layer Met.* 71: 211-216
- Rosema, A. and J.L. Fiselier, 1990. METEOSAT-based evapotranspiration and thermal inertia mapping for monitoring transgression in the Lake Chad region and Niger Delta, *Int. J. Remote Sens.*, vol II, no. 5: 741-752
- Salisbury, J.W. and D.M. D'Aria, 1992. Emissivity of terrestrial materials in the 8-14 μm atmospheric window, *Rem. Sens. of Env.*, vol. 42: 83-106
- Schmugge, T.J., S. Hook and A. Kahle, 1995. TIMS observation of surface emissivity in HAPEX-Sahel, *Proc. IGARSS 1995 July*, Florence, Italy.
- Schmugge, T.J., T.J. Jackson, W.P. Kustas and J.R. Wang, 1992. Passive microwave remote sensing of soil moisture: results from HAPEX, FIFE and MONSOON90, *ISPRS J. of Photogrammetry and Remote Sensing* 47: 127-143
- Schuepp, P.H., M.Y. Lecler, J.I. Mackerson and R.I. Desjardins, 1990. Footprint prediction of scalar fluxes from analytical solutions to the diffusion equation, *Boundary Layer Meteorology* 50: 355-373
- Seginer, I., 1974. Aerodynamic roughness of vegetated surfaces, *Boundary Layer Met.* 5: 383-393
- Seguin, B. and B. Itier, 1983. Using midday surface temperature to estimate daily evaporation from satellite thermal IR data. *Int. J. of Rem. Sens.* 4: 371-383
- Seguin, B., E. Assad, J.P. Fréteaud, J.P. Imbernon, Y. Kerr and J.P. Lagouarde, 1989. Use of meteorological satellites for water balance monitoring in Sahelian regions, *Int. J. of Rem. Sens.* 10: 1101-1117
- Sellers, P.J., Y. Mintz, Y.C. Sud and A. Dalcher, 1986. A Simple Biosphere model (SiB) for use within general circulation models, *J. of the Atmospheric Sciences*, vol. 43, no. 6: 505-531

- Sellers, P.J., S.I. Rasool and H.J. Bolle, 1990. A review of satellite data algorithms for studies of the land surface, *Bulletin Am. Met. Soc.*: 1429-1447
- Shanin, 1985. Hydrology of the Nile basin, developments in water science 21, Elsevier: pp. 575
- Shuttleworth, W.J., 1988. Macrohydrology, the new challenge for process hydrology, *J. of Hydr.* 100: 31-56
- Shuttleworth, W.J. and J.S. Wallace, 1985. Evaporation from sparse crops an energy combination theory, *Q. J.R. Met. Soc.* 111: 839-855
- Shuttleworth, W.J., R.J. Gurney, A.Y. Hsu and J.P. Ormsby, 1989. FIFE: The variation in energy partitioning at surface flux sites, *Remote Sensing and Large-Scale Global Processes, Proc Baltimore Symp., IAHS Publ.* no. 186 IAHS press, Oxfordshire, U.K.: 67-74
- Sinclair, T.R., L.H. Allen and E.R. Lemon, 1975. An Analysis of errors in the calculation of energy flux densities above vegetation by a Bowen-ratio profile method, *Boundary Layer Met.* 8: 129-139
- Smith, R.C.G. and B.J. Choudhury, 1990a. On the correlation of indices of vegetation and surface temperature over South-eastern Australia, *Int. J. of Rem. Sens.* vol 11: 2113-2120
- Stewart, J.B., W.P. Kustas, K.S. Humes, W.D. Nichols, M.S. Moran and H.A.R. de Bruin, 1994. Sensible heat flux - radiometric surface temperature relationship for 8 semi-arid areas, in *Proc. Workshop on thermal remote sensing of the energy and water balance, La Londes les Maures, 20-23 Sept. France:* 27-30
- Stull, R.B., 1988. An introduction to boundary layer meteorology, *Atmospheric Sciences Library, Kluwer Academic Publishers:* pp. 666
- Sucksdorff, Y. and C. Otle, 1990. Application of satellite remote sensing to estimate areal evapotranspiration over a watershed. *J. of Hydr.* 121, 321-333.
- Sud, Y.C., P.J. Sellers, Y. Mintz, M.D. Chou, G.K. Walker and W.E. Smith, 1990. Influence of the biosphere on the global circulation and hydrologic cycle - a GCM simulation experiment, *Agr. and Forest Met.* 51.: 133-180
- Sugita, M. and W. Brutsaert, 1990. Regional surface fluxes from remotely sensed skin temperature and lower boundary layer measurements, *Water Resources Research*, vol. 26, no. 12: 2937-2944
- Thom, A.S., 1972. Momentum, mass and heat exchange of vegetation, *Q. J. Roy. Met. Soc.* 103: 345-357
- Thornwaite, C.W., 1944, Report of the Committee on Transpiration and Evaporation, *Transactions of the American Geophysical Union*, 25: 683-693
- Thorstenson, D.C. and D.W. Pollock, 1989. Gas transport in unsaturated zones: multicomponent systems and the adequacy of Fick's laws, *Water Resources Research*, vol. 25, no. 3: 477-507
- Thunnissen, H.A.M. and G.J.A. Nieuwenhuis, 1989. A simplified method to estimate regional 24-h evapotranspiration from thermal infrared data, *Rem. Sens. of Env.* 31: 211-225
- Townsend, A.A., 1965. The reponse of a turbulent boundary layer to abrupt changes in surface conditions, *J. Fluid. Mech.* 22: 799-822
- Tucker, C.J., 1986. (ed.) Monitoring the grasslands of semi-arid Africa using NOAA AVHRR data, *Int. J. of Rem. Sens. (special issue)*, 7-11: 1383-1622

- Verma, S.B., J. Kim and R.J. Clement, 1992. Momentum, water vapor and carbon dioxide exchange at a centrally located prairie site during FIFE, *J. of Geophysical Res.*, 6 vol. 97, no. D17: 18,629-18,640
- Vries, de D.A., 1958. Simultaneous transfer of heat and moisture in porous media, *Transactions American Geophysical Union*, vol. 39, no. 5: 909-916
- Vukovich, F.M., D.L. Toll and R.E. Murphy, 1987. Surface temperature and albedo relationships in Senegal derived from NOAA-7 satellite data, *Rem. Sens. of Env.* 22: 413-421
- Wallace, J.S., 1995. Calculating evaporation: resistance to factors, *Agr. and Forest Met.* 73: 353-366
- Wan, Z. and J. Dozier, 1989. Land surface temperature measurement from space: physical principles and inverse modeling, *IEEE Transactions on Geoscience and Remote Sensing*, vol. 27, no. 3: 266-278
- Wang, J and Y. Mitsuta, 1992. Evaporation from the desert: some preliminary results of HEIFE, *Boundary Layer Met.* 59: 413-418
- Wang, J., Y. Hu, K. Sahashi and Y. Mitsuta, 1994a. Outline of HEIFE field observations, in: Y. Mitsuta (ed.) *Proc. Int. Symp. on HEIFE, Disaster Prevention Research Institute, Kyoto Univ.*: 22-29
- Wang, J, M. Menenti, W.G.M. Bastiaanssen and Y. Mitsuta, 1995. Surface energy and water cycle in arid zone, study of land surface processes with the aid of satellite remote sensing, *Jap. Met. Soc.* (submitted)
- Wang, J., Y. Ma, L. Jia, K. Sahaski, E. Ohtaki, T. Maitani, O. Tsukamoto and Y. Mitsuta, 1994b. Downward sensible heat flux during daytime observed in the oasis station, in Y. Mitsuta (ed.) *Proc. Int. Symp on HEIFE, Disaster Prevention Research Institute, Kyoto Univ.* 449-457
- Webb, E.K., 1970. Profile relationships: the log-linear range and extension to strong stability, *Q. J. Roy. Met. Soc.* 96: 67-90
- Wieringa, J., 1986. Roughness-dependent geographical interpolation of surface wind speed averages, *Q. J. R. Met. Soc.* 112: 867-889
- Wieringa, J., 1992. Representative roughness parameters for homogeneous terrain, *Boundary Layer Met.* 63: 323-363
- Wood, E.F., K. Beven, M. Sivipalan and L. Band, 1988. Effects of spatial variability and scale with implication to hydrologic modelling, *J. of. Hydr.* 102: 29-47
- Wood, E.F., D.S. Lin, M. Mancini, D. Thongs, P.A. Troch, T.J. Jackson, J.S. Famiglietti and E.T. Engman, 1993. Intercomparison between passive and active microwave remote sensing, and hydrological modeling for soil moisture, *Adv. Space Research*, vol. 13, no. 5: 167-176
- Wooding, R.A., E.F. Brandley and J.K. Marshall, 1973. Drag due to regular arrays of roughness elements of varying geometry, *Boundary-Layer Met.* 5: 285-308
- Wukelic W.E., D.E. Gibbons, L.M. Martucci and H.P. Foote, 1989. Radiometric calibration of Landsat Thematic Mapper thermal band, *Rem. Sens. of Env.* (special issue) 28: 339-347

Publications from Universities and Research Institutes

Abdel Gawad, S.T., M.A. Abdel Khalek, D. Boels, D.E. El Quosy, C.W.J. Roest, P.E. Rijtema and M.F.R. Smit, 1991. Analysis of water management in the Eastern Nile Delta, DLO Winand Staring Centre, Drainage Research Institute Cairo, Reuse Report 30, Wageningen, The Netherlands: pp. 245

Anonymous, 1987. Description of the measurement network in the Nile Delta, DLO Winand Staring Centre/Drainage Research Institute Cairo, Reuse of Drainage Water Project Report 20, Wageningen, The Netherlands: pp. 146

Bastiaanssen, W.G.M., 1988a. New empirical aspects of the Bowen-ratio energy balance method, ICW note 1914, DLO Winand Staring Centre, Wageningen, The Netherlands: pp. 41

Bastiaanssen, W.G.M., 1988b. Diurnal variation of bare soil reflectance, ICW note 1954, DLO Winand Staring Centre, Wageningen, The Netherlands: pp. 28

Bastiaanssen, W.G.M., P. Kabat and M. Menenti, 1989. A new simulation model of bare soil evaporation in arid regions, EVADES, ICW note 1938, DLO Winand Staring Centre, Wageningen, The Netherlands: pp. 73

Blaney, H.F. and W.O. Criddle, 1950. Determining water requirements in irrigated areas from climatological and irrigation data, USDA (SCS) TP-96: pp. 48

Bolle, H.J. and B. Streckenbach, 1992. EFEDA first annual report, January 1992, Berlin

Bolle, H.J. and B. Streckenbach, 1993. EFEDA Final Report, August 1993, Berlin

Budyko, M.I., 1956. Evaporation under natural conditions, GIMIZ, Leningrad, English translation, Israel program of scientific translations, Jerusalem (1963)

Chanzy, A. 1991. Modelisation simplifiee de l'evaporation d'un sol nu utilisant l'humidite et la temperature de surface accesibles par teledetection, Ph.D. thesis, L'Institut National Agronomique Paris-Grignon: pp. 221

Dickinson, R.E., A. Henderson-Sellers, P.J. Kennedy and M.F. Wilson, 1986. Biosphere-Atmosphere Transfer Scheme (BATS) for the NCAR Community Climate Model, NCAR/TN-275+STR, National Center for Atmospheric Research, Boulder Colorado: pp. 69

Driedonks, A.G.M., 1981. Dynamics of the well mixed atmospheric boundary layer, Scientific Report 81-2, Royal Netherlands Meteorological Institute, KNMI, De Bilt, The Netherlands

Droogers, P., G.D. v.d. Abeele, J. Cobbaert, C.P. Kim, R. Rosslerova, M. Soet and J.N.M. Stricker, 1993. Basic data sets description and preliminary results of EFEDA-Spain, Agricultural University Wageningen, Department of Water Resources, Wageningen, The Netherlands, Report 37: pp...

Gallinaro, N. 1993. Heat fluxes at the land-atmosphere interface: measurements compared with models, DLO-Winand Staring Centre, Report 77, Wageningen, The Netherlands: pp. 77

Heinonen, R., 1985. Soil management and crop water supply, 4th edition, Department of Soil Sciences, Swedish Univ. of Agric. Sciences, Uppsala, Sweden: pp. 104

Hutjes, R., 1995. Transformation of near surface meteorology in a landscape with small scale forests and arable land, Ph. D. Thesis, University of Groningen (in prep.)

Kneizys, F.X., E.P. Shettle and L.W. Abreu, 1988. User's guide to LOWTRAN-7, Env. Res. Papers no. 10101, Report AFGL-TR-88-0177, Air Force Geophysics Laboratory, Hanscom Air Force Base, MA 01737: pp. 137

Menenti, M., 1984. Physical aspects and determination of evaporation in deserts applying remote sensing techniques, DLO Winand Staring Centre, ICW Report 10 (Ph.D. Thesis): pp. 202

Menenti, M., W.G.M. Bastiaanssen, K. Hefny and M.H. Abd El Karim, 1991. Mapping of groundwater losses by evaporation in the Western Desert of Egypt, DLO Winand Staring Centre, Report no. 43, Wageningen, The Netherlands: pp. 116

Michels, B.I., 1989. Chess or How to calculate atmospheric correction from global radiation data in desert areas, DLO Winand Staring Centre, Internal Note 19, Wageningen, The Netherlands: pp. 51

Miyake, M., 1965. Transformation of the Atmospheric Boundary Layer over Inhomogeneous Surfaces, Sc. Rep. Dep. Atmos. Sc. Univ. Washington

Moene, A., 1992. Intercomparison of energy fluxes measured during EFEDA, Wageningen Agricultural University, Dept. of Meteorology: pp. 33

Moran, M.S., 1990. A satellite-based approach for evaluation of the spatial distribution of evapotranspiration from agricultural lands. Ph.D. thesis, University of Arizona, Tucson, USA.

Neal, J.T., 1965. Geology, mineralogy and hydrology of US playas. Air force cambridge res. labs. Env. res. paper 96. Bedford, Mass.: pp. 176

Oevelen, van, P.J., 1991. Determination of the available energy for evapotranspiration with remote sensing, M.Sc. Thesis, Agricultural University of Wageningen, The Netherlands, 1991: pp. 68

Passerant de Silans, A., 1986. Transferts de masse et de chaleur dans un sol startifie soumis a une excitation atmospherique naturelle. Comparaison: Modeles-experience, Thesis, Institut National Polytechnique de Grenoble, France.

Pelgrum, H. 1992. Mapping areal surface energy balances during daytime using METEOSAT data, DLO Winand Staring Centre, Internal Note 195, Wageningen, The Netherlands, pp. 50

Pelgrum, H. and W.G.M. Bastiaanssen, 1995a. Determination of the regional surface energy budget of the EFEDA grid, DLO Winand Staring Centre, Internal Note 331, Wageningen, The Netherlands: pp. 50

Rijtema, P.E., 1965. An analysis of actual evapotranspiration, Ph.D. Thesis, Agricultural University of Wageningen: 107 pp.

Roerink, G.J., 1994. The impact of satellite sensor resolution on the regional evaporation statistics in large-scale irrigation schemes, a case study in the Mendoza Province, Argentina, DLO Winand Staring Centre, Internal Note 312, Wageningen, The Netherlands: pp. 58 & annexes

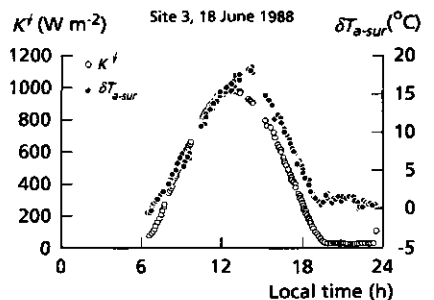
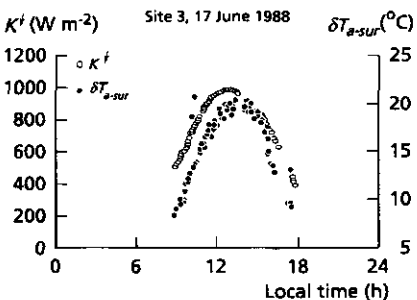
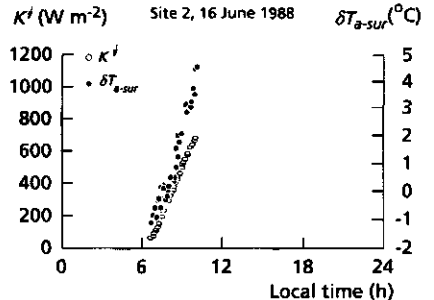
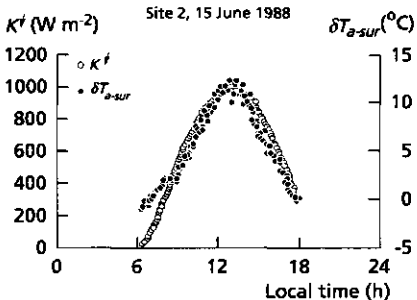
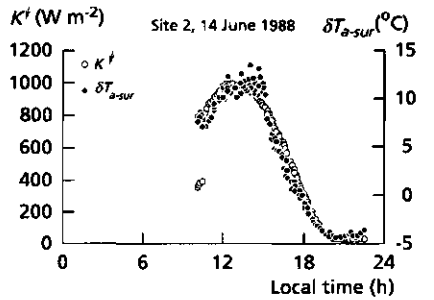
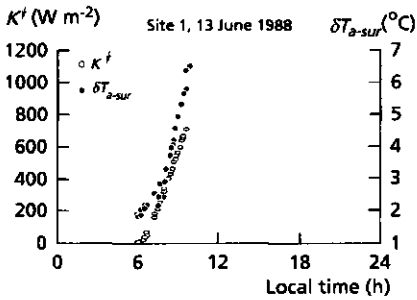
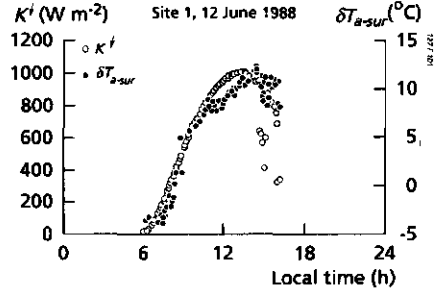
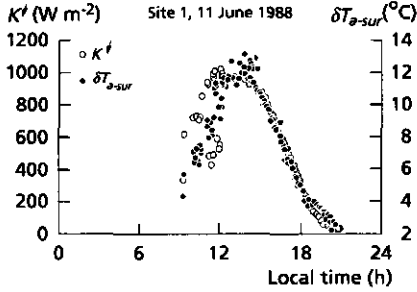
Roerink, G.J., 1995. SEBAL determinations of the areal patterns of sensible and latent heat fluxes over the HAPEX-Sahel grid, DLO Winand Staring Centre, Internal Note 364, Wageningen, The Netherlands.

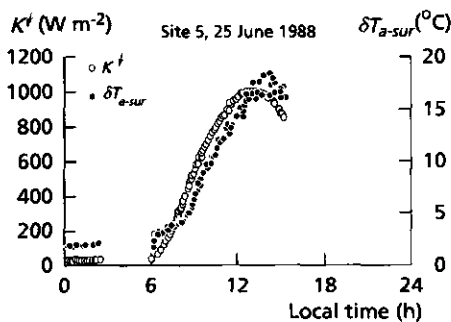
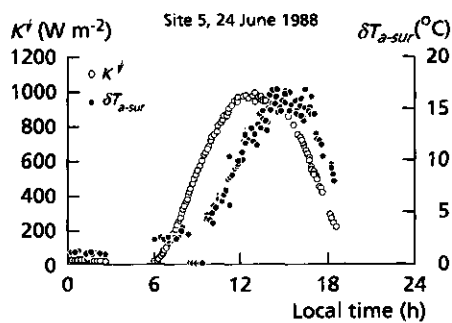
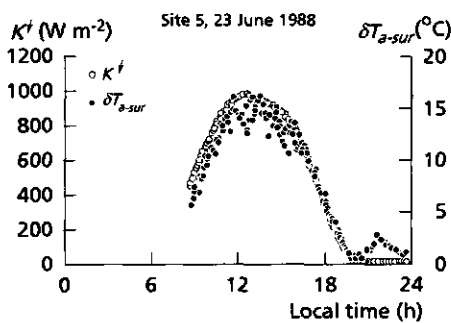
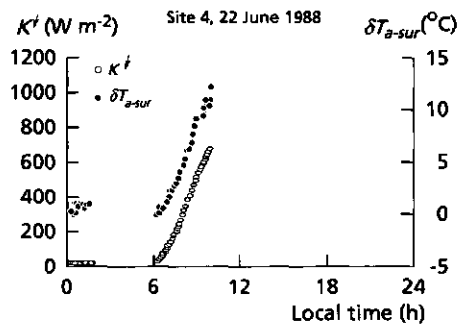
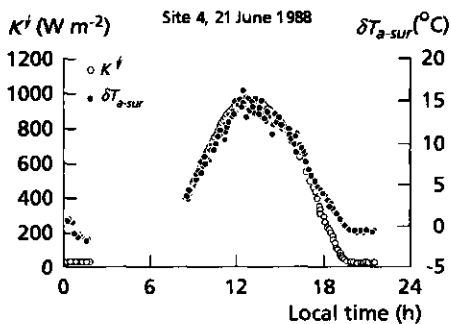
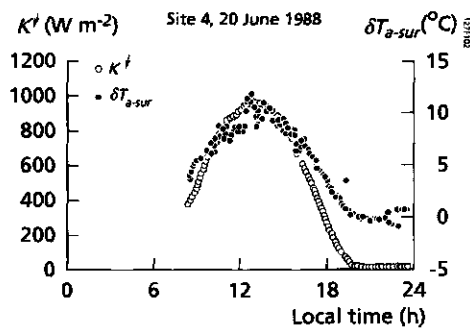
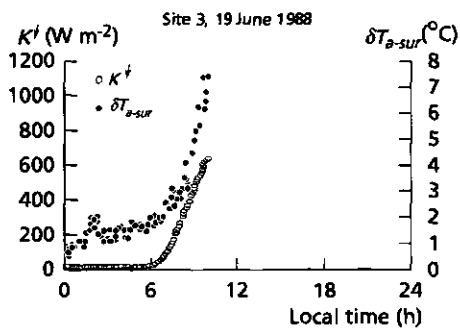
Shu Fen Sun, 1982. Moisture and heat transport in a soil layer forced by atmospheric conditions, MSc thesis, Dept. of Civil Engineering, Univ. of Connecticut: pp 72

Wai, van der, T., 1992. Survey of the land surface hydrology, an application study in the Eastern Nile Delta with Thematic Mapper data, Internal Note 258, DLO Winand Staring Centre, Wageningen, The Netherlands: pp. 40

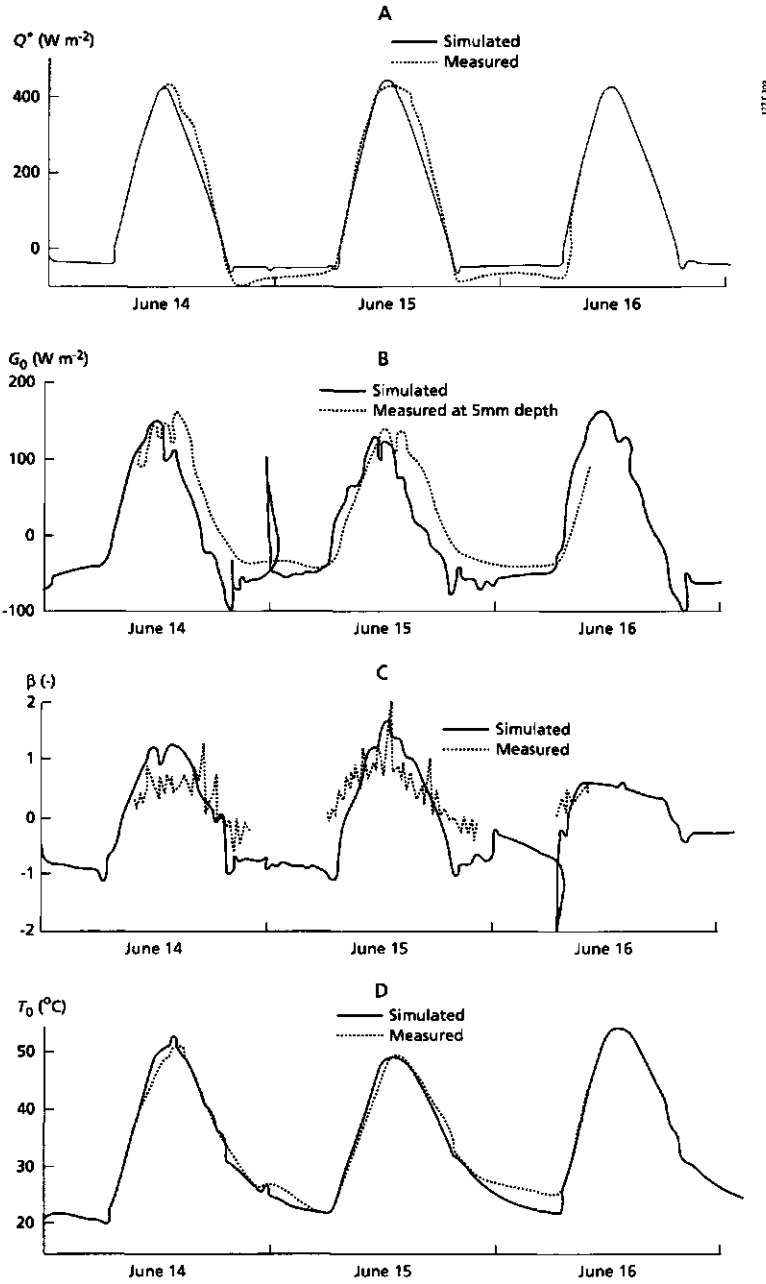
Wallace, J.S., J.H.C. Gash, D.D. McNeil and M.V.K. Sivakumar, 1986. Measurement and prediction of actual evaporation from sparse dryland crops, ODA Rep no. OD149/3 Inst. of Hydrology, U.K.: pp. 59

Annex 1 Solar radiation and near-surface vertical air temperature difference observations in the Qattara Depression





Annex 2 Calibration of EVADES simulations



Annex 3 EFEDA heat flux densities, June 29, 1991

Table A3.1: The error range of the energy fluxes are given between brackets ($W m^{-2}$).

Flux	Flux station	EFEDA partner	Land use	Ground based	SEBAL 25 pixels	SEBAL 91 pixels
Q'	1	Univ. Wageningen (Wat)	Fallow	411	496 (4)	484 (7)
Q'	2	Inst. of Hydrology	Vetch	452	523 (4)	524 (4)
Q'	3	Inst. of Hydrology	Vineyard	448	499 (7)	513 (17)
Q'	4	CNRM-4	Vetch	505	502 (5)	518 (19)
Q'	5	CNRM-2	Vineyard	498	490 (8)	484 (10)
Q'	6	Univ. Wageningen (Met)	Vineyard	488	487 (7)	490 (12)
Q'	7	Staring Centre	Vineyard	482	490 (7)	487 (10)
Q'	8	Univ. Copenhagen [^]	Vineyard	500	509 (7)	498 (12)
Q'	9	CNRM-6	Fallow	563	514 (3)	505 (12)
Q'	10	Univ. Karlsruhe	Maize	620	643 (3)	596 (39)
Q'	11	Univ. Karlsruhe	Fallow	401	508 (7)	523 (15)
H	1	Univ. Wageningen (Wat)	Fallow	263 (26)	332 (20)	311 (19)
H	2	Inst. of Hydrology	Vetch	196 (10)	326 (6)	332 (5)
H	3	Inst. of Hydrology	Vineyard	232 (12)	266 (9)	282 (13)
H	4	CNRM-4	Vetch	228 (23)	363 (10)	338 (15)
H	5	CNRM-2	Vineyard	198 (20)	310 (8)	312 (4)
H	6	Univ. Wageningen (Met)	Vineyard	239 (12)	306 (15)	306 (6)
H	7	Staring Centre	Vineyard	235 (35)	304 (15)	306 (6)
H	8	Univ. Copenhagen [^]	Vineyard	290 (15)	298 (6)	296 (6)
H	9	CNRM-6	Fallow	415 (42)	361 (7)	352 (2)
H	10	Univ. Karlsruhe	Maize	107 (5)	161 (11)	242 (3)
H	11	Univ. Karlsruhe	Fallow	292 (15)	401 (9)	390 (3)
λE	1	Univ. Wageningen (Wat)	Fallow	35 (8)	56 (15)	65 (16)
λE	2	Inst. of Hydrology	Vetch	53 (3)	9 (9)	84 (13)
λE	3	Inst. of Hydrology	Vineyard	13 (5)	131 (16)	123 (25)
λE	4	CNRM-4	Vetch	95 (23)	3 (13)	71 (49)
λE	5	CNRM-2	Vineyard	152 (36)	75 (12)	66 (13)
λE	6	Univ. Wageningen (Met)	Vineyard	8 (4)	76 (2)	79 (19)
λE	7	Staring Centre	Vineyard	83 (12)	8 (22)	77 (21)
λE	8	Univ. Copenhagen [^]	Vineyard	83 (4)	16 (1)	97 (12)
λE	9	CNRM-6	Fallow	67 (16)	57 (1)	59 (1)
λE	1	Univ. Karlsruhe	Maize	491 (25)	411 (12)	279 (114)
λE_o	11	Univ. Karlsruhe	Fallow	10 (1)	10 (27)	37 (27)

Table A3.1: General characteristics of the equipped sites.

Station number	EFEDA partner	Land use	Integration	Method-H time (min.)	Method-λE
1	Univ. Wageningen (Wat)	Fallow	30	sigma-T, Bowen-ratio	Bowen-ratio
2	Inst. of Hydrology	Vetch	60	eddy	eddy
3	Inst. of Hydrology	Vineyard	60	eddy	eddy
4	CNRM-4	Vetch	30	2 level profiles	residue
5	CNRM-2	Vineyard	30	2 level profiles	residue
6	Univ. Wageningen (Met)	Vineyard	10	eddy, sigma-T, profile	profile, residue
7	Staring Centre	Vineyard	5	Bowen-ratio interchange	idem
8	Univ. Copenhagen	Vineyard	10	eddy	eddy
9	CNRM-6	Fallow	30	2 level profiles	residue
10	Univ. Karlsruhe	Maize	10	eddy, 6 level profiles	eddy
11	Univ. Karlsruhe	Fallow	10	eddy, 6 level profiles	eddy
12	Univ. Reading	Vineyard	5	6 level profiles, sigma-T	residue
13	Univ. Reading	Vetch	5	5 level profiles, sigma-T	Bowen-ratio

Annex 4 EFEDA heat flux densities, June 12, 1991

Flux station	Super-site	EFEDA partner	Land use	x UTM	y UTM	Method H	Method λE	λ_{lower}
1	Barrax	Karlsruhe	Irrigated maize	575129.5	4324070.0	eddy	eddy	0.858
2	Barrax	Karlsruhe	Fallow	575039.5	4324460.0	eddy	eddy	0.186
5	Tomelloso	Reading	Vetch	504299.5	4333580.0	level	bowen	0.331
6	Tomelloso	Reading	Vineyard	509249.5	4333250.0	level	residue	0.385
8	Tomelloso	CNRM	Vineyard	506309.5	4332350.0	level	residue	0.484
10	Tomelloso	CNRM	Vetch	504689.5	4333580.0	level	residue	0.483
12	Tomelloso	SC-DLO	Vineyard	505859.5	4332320.0	bowen	bowen	0.242
13	Tomelloso	WAU Meteorology	Vineyard	506009.5	4332290.0	eddy	residue	0.215
14	Tomelloso	WAU Water Resources	Fallow	508919.5	4333460.0	bowen	bowen	0.322
16	Tomelloso	Copenhagen	Vineyard	506399.5	4330940.0	eddy	eddy	0.170
18	Rada de Haro	Berlin	Vineyard	533189.5	4380680.0	eddy	eddy	0.582
19	Rada de Haro	Berlin	Natural vegetation	533369.5	4380560.0	bowen	bowen	0.317
21	Rada de Haro	Copenhagen	Sunflower	534149.5	4378490.0	eddy	eddy	0.270

Annex 5 Radiative land surface properties of the main land use categories in the Eastern Nile Delta and Eastern Desert

Sub-grid	r_p (-)	r_o (-)	T_o^R (°C)	T_o (°C)	NDVI (-)
1	0.076	0.056	25.8	33.8	0.1
2	0.124	0.113	37.2	38.0	0.75
3	0.124	0.113	31.1	31.9	0.70
4	0.144	0.137	30.9	31.7	0.68
5	0.152	0.146	33.4	34.2	0.63
6	0.161	0.158	35.0	36.6	0.61
7	0.191	0.194	36.7	38.3	0.58
8	0.186	0.188	38.5	40.1	0.54
9	0.202	0.207	40.0	41.6	0.51
10	0.215	0.223	40.4	42.8	0.48
11	0.228	0.239	41.1	43.5	0.45
12	0.241	0.254	41.7	44.1	0.41
13	0.252	0.268	41.6	44.8	0.38
14	0.264	0.282	42.3	45.5	0.35
15	0.274	0.294	42.1	45.3	0.33
16	0.283	0.305	41.1	45.2	0.31
17	0.292	0.316	41.0	45.1	0.30
18	0.306	0.322	40.8	44.8	0.29
19	0.325	0.355	41.0	45.1	0.28
20	0.360	0.397	40.7	44.7	0.27

List of frequently used symbols

Some of the symbols used in a few consecutive equations falling outside the mean line of argument, are defined in the text only.

Symbol	Interpretation	Unit
A	total area	m^2
a	sub-area	m^2
a_s'	soil apparent thermal diffusivity	$m^2 s^{-1}$
b	bandwidth	μm
$C(h_m)$	differential soil water capacity	m^{-1}
c	entity	variable
c_s	soil specific heat	$J kg^{-1} K^{-1}$
c_p	air specific heat at constant pressure	$J kg^{-1} K^{-1}$
c_w	water specific heat	$J kg^{-1} K^{-1}$
D_a	air molecular diffusion	$m^2 s^{-1}$
D_v	soil iso-thermal molecular vapour diffusivity	$m^2 s^{-1}$
D_v^{eff}	effective soil vapour diffusivity	$m^2 s^{-1}$
D_v^f	Fick soil vapour diffusivity	$m^2 s^{-1}$
D_v^k	Knudsen soil vapour diffusivity	$m^2 s^{-1}$
D_θ	soil iso-thermal liquid diffusivity	$m^2 s^{-1}$
D_θ^{eff}	total soil liquid diffusivity	$m^2 s^{-1}$
$D_{\theta T}$	soil thermal liquid diffusivity	$m^2 s^{-1} K^{-1}$
D_r	drainage rate	$m s^{-1}$
d	zero-plane displacement	m
d_s	Earth-Sun distance	AU
E	actual evaporation rate	$kg m^{-2} s^{-1}$
E_o	open water evaporation rate	$kg m^{-2} s^{-1}$
E_i	evaporation rate of intercepted water	$kg m^{-2} s^{-1}$
E_s	actual surface soil evaporation rate	$kg m^{-2} s^{-1}$
E_p	potential evaporation rate	$kg m^{-2} s^{-1}$
E_{soil}	actual soil evaporation rate	$kg m^{-2} s^{-1}$
E_{sub}	substrate evaporation rate	$kg m^{-2} s^{-1}$
E_{sp}	potential soil evaporation rate	$kg m^{-2} s^{-1}$
E_c	actual canopy evaporation rate	$kg m^{-2} s^{-1}$
E_{cp}	potential canopy evaporation rate	$kg m^{-2} s^{-1}$
E_v	actual sub-surface soil evaporation rate	$kg m^{-2} s^{-1}$

E^{PM}	Penman-Monteith evaporation rate	$\text{kg m}^{-2} \text{s}^{-1}$
E^{PT}	Priestley & Taylor evaporation rate	$\text{kg m}^{-2} \text{s}^{-1}$
E_{24}	daily integrated evaporation rate (24 hours)	m d^1
e	water vapour pressure	mbar
e_{sat}	saturated vapour pressure	mbar
F_0	surface flux density	W m^{-2}
F_{ad}	adhesive force	N
G_{bot}	soil heat flux density at the lower side of a slab	W m^{-2}
G_0	surface soil heat flux density	W m^{-2}
g	acceleration due to gravity	m s^{-2}
H	sensible heat flux density	W m^{-2}
h	total pressure head	m
h_g	gravitational head	m
h_m	matric pressure head	m
h_{osm}	osmotic pressure head	m
h_p	pneumatic pressure head	m
h_v	vegetation height	m
I_r	irrigation water supply rate	m s^{-1}
J	Day number	-
J_s	near-surface soil heat storage	J m^{-2}
K	specific permeability	m^2
K_a	path radiation flux density	W m^{-2}
K^{\downarrow}	incoming shortwave radiation flux density	W m^{-2}
K^{\uparrow}	outgoing shortwave radiation flux density	W m^{-2}
K_{dt}^{\downarrow}	global diffuse radiation flux density	W m^{-2}
$K_{exc}^{\downarrow}(b)$	in band exo-atmospherical radiation flux density	W m^{-2}
K_{exo}^{\downarrow}	exo-atmospherical radiation flux density	W m^{-2}
K_{TOA}^{\downarrow}	radiation flux density perpendicular to the Top Of Atmosphere	W m^{-2}
$K_{TOA}^{\downarrow}(b)$	in-band radiation flux density perpendicular to the Top Of Atmosphere	W m^{-2}
$K_{TOA}^{\downarrow}(\lambda)$	bi-directional spectral radiance at the sensor	$\text{W m}^{-2} \text{sr}^{-1} \mu\text{m}^{-1}$
K^{\cdot}	net shortwave radiation flux density	W m^{-2}
K_h	eddy viscosity for heat transport	$\text{m}^2 \text{s}^{-1}$
K_m	eddy viscosity for momentum transport	$\text{m}^2 \text{s}^{-1}$
K_v	eddy viscosity for vapour transport	$\text{m}^2 \text{s}^{-1}$
k	Von Karman's constant	-
kB^{-1}	roughness for momentum/heat flux density ratio	-
$k(\theta)$ or $k(h_m)$	unsaturated hydraulic conductivity	m s^{-1}
k_{sat}	saturated hydraulic conductivity	m s^{-1}

L	Monin-Obukov length	m
L^{\downarrow}	incoming longwave radiation flux density	$W m^{-2}$
L^{\uparrow}	outgoing at-surface longwave radiation flux density	$W m^{-2}$
$L_{TOA}^{\uparrow}(\lambda)$	spectral outgoing longwave radiation at top of atmosphere	$W m^{-2} \mu m^{-1}$
$L_{atm}^{\uparrow}(\lambda)$	spectral atmospheric upward emitted radiation	$W m^{-2} \mu m^{-1}$
$L_{atm}^{\downarrow}(\lambda)$	spectral atmospheric downward emitted radiation	$W m^{-2} \mu m^{-1}$
$L_{land}^{\uparrow}(\lambda)$	spectral radiation leaving the land surface	$W m^{-2} \mu m^{-1}$
L^{\cdot}	net longwave radiation flux density	$W m^{-2}$
L_{λ}	spectral radiance at sensor aperture	$W m^{-2} \mu m^{-1}$
$L(\lambda)$	spectral radiance intensity	$W m^{-2} \mu m^{-1}$
$L(\lambda)^{bb}$	spectral black body radiance	$W m^{-2} \mu m^{-1}$
LAI	leaf area index	$m^2 m^{-2}$
l	parameter of van Genuchten model	-
lat	latitude	rad
$long$	longitude	rad
ℓ_m	mean molecular free path	m
M	molecular mass	$kg mol^{-1}$
$M(h_m)$	matric flux potential	$m^2 s^{-1}$
$NDVI$	normalized difference vegetation index	-
n	parameter of van Genuchten model	-
P	precipitation rate	$m s^{-1}$
p	total air pressure	mbar
Q	bottom flux density	$m s^{-1}$
Q^{\cdot}	net radiation flux density	$W m^{-2}$
q_{hx}	conductive soil heat flux density	$W m^{-2}$
q_{hc}	convective soil heat flux density	$W m^{-2}$
q_h^{tot}	total soil heat flux density	$W m^{-2}$
q_v^{tot}	total vapour flux density	$kg m^{-2} s^{-1}$
q_v^F	Fick's vapour flux density	$kg m^{-2} s^{-1}$
q_v^K	Knudsen's vapour flux density	$kg m^{-2} s^{-1}$
q_v^D	Darcy's vapour flux density	$kg m^{-2} s^{-1}$
q_v^{TUR}	turbulent soil air flux density	$kg m^{-2} s^{-1}$
q_{θ}	iso-thermal liquid flux density	$m s^{-1}$
$q_{\theta T}$	thermal liquid flux density	$m s^{-1}$
q_{θ}^{tot}	total liquid water density	$m s^{-1}$
q_a	air specific humidity	-
q^*	humidity scale	-
r_a	hemispherical reflectance of the atmosphere	-
r_d	atmospheric reflectance of diffuse radiation	-

r_m	effective pore radius	m
r_p	directional planetary reflectance	-
r_0	hemispherical surface reflectance at the land surface	-
r_{ah}	aerodynamic resistance to heat transport	$s\ m^{-1}$
r_{am}	aerodynamic resistance to momentum transport	$s\ m^{-1}$
r_{av}	aerodynamic resistance to vapour transport	$s\ m^{-1}$
R	runoff rate of surface water	$m\ s^{-1}$
R_u	universal gas constant	$J\ mol^{-1}\ K^{-1}$
r_c	canopy resistance	$s\ m^{-1}$
r_s	bulk surface resistance	$s\ m^{-1}$
r_{soil}	surface resistance to total bare soil evaporation	$s\ m^{-1}$
r_{sh}	soil resistance to heat transport	$s\ m^{-1}$
r_{sv}	soil resistance to water vapour transport	$s\ m^{-1}$
r_{sl}	soil resistance to water liquid transport	$s\ m^{-1}$
r_{st}	stomatal resistance to water vapour transport	$s\ m^{-1}$
S_e	degree of saturation	-
S_h	sink/source of heat	$W\ m^{-3}$
S_v	sink/source of water vapour	$kg\ m^{-3}\ s^{-1}$
S_0	sink/source of liquid water	s^{-1}
s_a	slope of the saturation vapour pressure curve in air	$mbar\ K^{-1}$
s_c	fractional soil coverage	-
T	temperature	K
T_a	air temperature	K
T_p	air potential temperature	K
T_s	soil temperature	K
T_{sat}	radiation temperature at sensor aperture	K
T_{z0h}	heat source temperature	K
T_{z0m}	aerodynamic surface temperature	K
T_0	surface temperature	K
T_0^R	surface radiation temperature	K
$T.$	temperature scale	K
t'	Greenwich Mean Time	h
t	local time	h
U	relative humidity	-
u	horizontal wind velocity	$m\ s^{-1}$
$u.$	friction velocity	$m\ s^{-1}$
v_a	laminar air flow velocity	$m\ s^{-1}$
v_a'	turbulent air flow velocity	$m\ s^{-1}$
v_m	molecular speed	$m\ s^{-1}$

W	soil water storage	m
x	distance	m
z	height	m
$ z $	depth	m
z_B	blending height	m
z_o	effective depth of zone of vaporization	m
z_{gwt}	depth to groundwater table	m
z_i	effective depth of zone with quasi constant liquid flow	m
z_{sur}	near-surface height	m
z_{om}	aerodynamical roughness length for momentum transport	m
z_{oh}	aerodynamical roughness length for heat transport	m
z_{ov}	aerodynamical roughness length for water vapour transport	m
α	parameter of the Priestley and Taylor model	-
α	parameter of van the Genuchten model	m^{-1}
β	Bowen ratio	-
Γ	G_o/Q' ratio	-
Γ'	proportionality factor in G_o/Q' ratio	-
Γ''	extinction factor in G_o/Q' ratio	-
γ	psychrometric constant	mbar K^{-1}
δ	solar declination	rad
δT_{a-sur}	near-surface vertical air temperature difference	K
ϵ_λ	spectral emissivity	-
ϵ'	apparent thermal infrared emissivity of atmosphere at ground level	-
ϵ_a'	effective thermal infrared emissivity of atmosphere at ground level	-
ϵ_o	surface emissivity	-
η_a	dynamic viscosity of air	$N\ s\ m^{-2}$
ξ	Monin - Obukhov's stability correction parameter	-
θ	volumetric soil water content	$m^3\ m^{-3}$
θ_r	residual soil water content	$m^3\ m^{-3}$
θ_{sat}	saturated soil water content	$m^3\ m^{-3}$
θ_o	surface soil water content	$m^3\ m^{-3}$
θ_{zi}	soil water content at depth z_i	$m^3\ m^{-3}$
λ	latent heat of vaporization	$J\ kg^{-1}$
λ	wavelength	μm
λE	latent heat flux density	$W\ m^{-2}$
λ_s^*	macroscopic soil thermal conductivity	$W\ m^{-1}\ K^{-1}$
λ_s'	apparent macroscopic soil thermal conductivity	$W\ m^{-1}\ K^{-1}$
Λ	evaporative fraction	-
ν_a	kinematic viscosity	$m^2\ s^{-1}$

$\rho_a c_p$	air heat capacity	$\text{J m}^{-3} \text{K}^{-1}$
$\rho_s c_s$	soil heat capacity	$\text{J m}^{-3} \text{K}^{-1}$
$\rho_w c_w$	water heat capacity	$\text{J m}^{-3} \text{K}^{-1}$
ρ_a	moist air density	kg m^{-3}
ρ_d	dry air density	kg m^{-3}
ρ_s	soil dry bulk density	kg m^{-3}
ρ_w	water density	kg m^{-3}
ρ_v	vapour density	kg m^{-3}
σ	Stefan Boltzmann constant	$\text{W m}^{-2} \text{K}^{-4}$
σ_{wa}	surface tension of water against air	N m^{-1}
τ	momentum flux density	N m^{-2}
τ_{sw}	atmospheric shortwave transmittance	-
τ_{sw}''	two-way atmospheric shortwave transmittance	-
τ_λ	spectral atmospheric transmittance	-
ϕ_m	Monin-Obukhov function for atmospheric momentum transport	-
ϕ_h	Monin-Obukhov function for atmospheric heat transport	-
ϕ_v	Monin-Obukhov function for atmospheric vapour transport	-
ϕ_{su}	sun zenith angle	rad
ψ_{su}	azimuth angle	rad
ψ_a	angle of contact	rad
ψ_h	stability correction for atmospheric heat transport	-
ψ_m	stability correction for atmospheric momentum transport	-
ψ_v	stability correction for atmospheric vapour transport	-
ω	weighing coefficient	-
ω_a	angular frequency	rad s^{-1}
Δe	water vapour pressure saturation deficit	mbar
\sim	proportional representation	
\approx	more or less equal to	
$\overset{\sim}{symbol}$	area-effective value	
$\langle symbol \rangle$	area-average value	
$symbol^{eff}$	process effective value	

LIST OF ACRONYMS

AV	Average
AVHRR	Advanced Very High Resolution Radiometer
BATS	Biosphere - Atmosphere Transfer Scheme
BCRS	Netherlands Remote Sensing Board
CNRM	Centre National de la Recherche Météorologique
CV	Coefficient of Variation
CWSI	Crop Water Stress Index
DLO	Dienst Landbouwkundig Onderzoek
DN	Digital Number
ECHIVAL	European international project on Climatic and Hydrological Interactions between Vegetation, Atmosphere and Land surfaces
ECMWF	European Centre for Medium range Weather Forecasts
EFEDA	Echival First field Experiment in Desertification threatened Area
ERA	Elementary Representative Area
EVADES	EVAporation in DESerts
FIFE	First ISLSCP Field Experiment
GEWEX	Global Energy and Water Cycle Experiment
GMT	Greenwich Mean Time
HAPEX	Hydrological and Atmospheric Pilot Experiments
IAHS	International Association for Hydrological Sciences
ICASVR	International Committee on Atmosphere-Soil-Vegetation Relations
ISLSCP	International Satellite Land Surface Climatology Project
LAI	Leaf Area Index
MOBILHY	Modélisation du Bilan Hydrique
NASA	National Aeronautics and Space Administration
ND	Normalized Difference
NDVI	Normalized Difference Vegetation Index
NIR	Near-InfraRed
NOAA	National Oceanic and Atmospheric Administration
PBL	Planetary Boundary Layer
REV	Representative Elementary Volume
SAR	Synthetic Aperture Radar
SC	Staring Centrum
SC-DLO	DLO Winand Staring Centre
SD	Standard Deviation
SEBAL	Surface Energy Balance Algorithm for Land
SEBI	Surface Energy Balance Index
SiB	Simple Biosphere model
SIWARE	Simulation of Water management in the Arab Republic of Egypt
SOP	Special Observation Period
SVAT	Soil Vegetation Atmosphere Transfer
SWATRE	Soil Water and Actual Transpiration Rate Extended
TIR	Thermal-InfraRed
TM	Thematic Mapper
TOA	Top Of Atmosphere
UTM	Universal Transfer Mercator
VIS	VISible
WDI	Water Deficit Index

Samenvatting

De toenemende belangstelling voor een duurzame leefomgeving heeft het aantal regionale milieu- en hydrologiestudies sterk vergroot. Meteorologische studies naar weer en klimaat worden zelfs uitgevoerd op sub-continentale en mondiale schaal. In al deze studies speelt de wisselwerking tussen land en atmosfeer een essentiële rol. Ofschoon het niet aan de fysische kennis ontbreekt om het verdampingsproces te beschrijven en om de intensiteit voor homogene gebieden te berekenen, is de kwantificering van de gemiddelde verdamping voor een heterogeen landoppervlak op regionale schaal inclusief het vaststellen van de ruimtelijke spreiding in verdamping, nog vrij onzeker. Dit kan worden toegeschreven aan de ruimtelijke spreiding van de bodemeigenschappen, de variatie in het landgebruik, een ongelijke bodembedekking en de verschillen in bodemvocht.

Landoppervlakte-eigenschappen kunnen met behulp van satellieten op grote schaal en met een vaste regelmaat worden gemeten. Deze remote-sensing-stralingsmetingen hebben betrekking op de fysische condities van het aardoppervlak en verdamping kan via vertaalfuncties (algoritmes) worden geschat. Reeds bestaande algoritmes zijn vaak ontwikkeld voor specifieke vormen van landgebruik. In (semi-) aride gebieden is de geometrie van de landschapselementen onregelmatig en is een classificatie van het landgebruik daardoor moeilijk uit te voeren. Voor een implementatie van remote-sensing algoritmes zijn aanvullende gegevens over de lokale hydro-meteorologische condities nodig. Dit is moeilijk te realiseren voor uitgestrekte heterogene gebieden waar weinig hydro-meteorologische meetgegevens verzameld worden.

Om aan de genoemde bezwaren tegemoet te komen, is in deze dissertatie het Surface Energy Balance Algorithm for Land (SEBAL) model ontwikkeld. Dit model heeft geen standaard synoptische meteorologische waarnemingen nodig. Wel is het noodzakelijk op enkele plaatsen metingen van oppervlakte-temperatuur, transmissiviteit van de atmosfeer en schatting van de terreinruwheden ter beschikking te hebben. SEBAL karakteriseert elk beeldelement met een waarde voor de oppervlakte-albedo, de vegetatie-index en de oppervlakte-temperatuur. Elk beeldelement van een satellietopname wordt vervolgens als een homogeen object beschouwd. De daarbij behorende micro-meteorologische wetmatigheden voor verticaal warmte- en vochttransport worden achtereenvolgens toegepast. Satellietmetingen met verschillen in afmetingen van de individuele beeldelementen kunnen worden gebruikt, zodat er een mogelijkheid ontstaat om voor verschillende ruimtelijke schalen en voor verschillende frequenties de verdamping te schatten.

Er is een nieuwe parameterizatie ontworpen voor de beschrijving van de dagelijkse gang in de bodemwarmtestroom. Deze remote-sensing parameterizatie karakteriseert de

fysische condities van de kale bodem met behulp van oppervlakte-temperatuur en oppervlakte-albedo. Voor de voelbare warmtestroom is gekozen voor een inverse berekening van de regionale spreiding in verticale luchttemperatuurverschillen omdat het karteren van de absolute waarden van oppervlakte-temperatuur en luchttemperatuur op afzonderlijke wijze een permanente bron van teleurstelling is. Het afleiden van de verticale verschillen in luchttemperatuur uit het desbetreffende studiegebied zonder meetgegevens kan worden gerealiseerd door de voelbare warmtestroom voor landeenheden met een oppervlakte-albedo kleiner dan 0-10% en een lage oppervlakte-temperatuur te verwaarlozen. Voor landeenheden met een oppervlakte albedo groter dan 0,30 en een hoge oppervlakte-temperatuur kan de latente warmtestroom worden verwaarloosd. Hiermee worden de extremen in voelbare warmtestroom *a priori* gekwantificeerd. De helling tussen de oppervlakte-albedo en oppervlakte-temperatuur is een maat voor de overdrachtsweerstand van de voelbare warmtestroom.

Het SEBAL concept is getest voor zowel verschillende landgebruikseenheden (woestijn, oase, geïrrigeerde landbouw, regenafhankelijke landbouw, natuurlijke vegetatie) als op verschillende schalen in Egypte en Spanje (1 t/m 1000 km). De modelresultaten zijn getoetst op een ruimteschaal tussen 1 km en 100 km. Bij een verdampingsfractie van 0,5 (latente warmtestroom/netto beschikbare energie) treedt voor een heterogeen gebied een fout van ongeveer 20% op bij een schaal van 1 km. Deze fout neemt af bij een toename van de gebiedsgrootte: Op een schaal van 100 km was in het geval van Spanje de fout ongeveer 5%. En dergelijke relatie tussen schaal en afwijking van de schattingen is ook voor Egypte geconstateerd. Het is aangetoond dat de fout in het algemeen verandert met de mate van heterogeniteit in de verdampingsprocessen, de correlatielengte van de verdamping, de afmetingen van een enkel beeldelement, de horizontale schaal waarop de verdamping dient te worden geschat en de vochtigheidscondities van het landoppervlak. De te verwachten fout verschilt dus met de keuze van resolutie in relatie tot de horizontale schaal waarvoor de schattingen dienen te worden gemaakt en deze aspecten verdienen aandacht bij de keuze van het beeldmateriaal.

De geschatte momentane warmtestromingen kunnen worden geïnterpreteerd naar vochtindicatoren. In deze dissertatie wordt aangetoond dat de verdampingsfractie tussen 10⁰⁰ en 16⁰⁰ uur lokale tijd voor zowel homogene als heterogene landoppervlaktes niet meer dan 20% varieert, waardoor tijdsintegraties van fluxdichtheden kunnen worden verwezenlijkt. Bovendien is aangetoond dat de verdampingsfractie (ten opzichte van een verdampingsweerstand) relatief ongevoelig is voor afwijkingen in de modelparameters. De fysische betekenis van een verdampingsweerstand van een heterogeen oppervlak is met behulp van een verklaring van de kale bodemweerstand voor verdamping en bodembedekking aangetoond. De ruimtelijke patronen kwamen volgens de theorie voor het meetgebied in Spanje goed overeen met de op een onafhankelijke manier gemeten bodemvocht patronen. Omdat de verdampingsweerstand slechts in geringe mate op veranderingen van de netto beschikbare energie reageert (in tegenstelling tot verdampingsfractie), is de weerstand geschikt om de hydrologische

toestand van een heterogeen landoppervlak voor een langere tijdsduur (week, maand, jaar) te beschrijven.

Met de ontwikkelde methode in deze dissertatie kunnen simulatiemodellen voor hydrologie, meteorologie, irrigatiewaterbeheer en landinventarisatie waar regionale verdamping een belangrijke rol speelt, worden verbeterd. Doordat het werkelijk watergebruik op regionale schaal kan worden uitgerekend, ontstaat een mogelijkheid in combinatie met informatie over wateraanvoer en neerslag, het waterbeheer van het landelijke gebied te verbeteren.

Curriculum Vitae

Wim (Wilhelmus Gerardus Maria) Bastiaanssen was born in Luttelgeest (North-East Polder) on November 7, 1960. He went to the College of Land and Water Management (HBCS, Velp) in 1982 and graduated in Hydrology and Irrigation Water Management in 1986. During his practical period in 1985, he investigated the efficiency of water conveyance and field application of irrigation water in an operational irrigation scheme in Thailand. In 1986, he became employed at the Department of Water Management in Arid Zones of the DLO Winand Staring Centre (SC-DLO) and investigated the hydrology of the Western Desert of Egypt. Based on this experience, he initiated a Doctoral Thesis in 1990 and elaborated the remote sensing methodology developed for Egypt with data from the EFEDA project being executed in Spain during 1991. His current assignment is to quantify water, salt, heat and energy balances across a range of scales. He further participated in numerous field programmes on regional evaporation (HAPEX-SAHEL Niger, HEIFE China). He designed and applied simulation models of the unsaturated zone moisture and heat dynamics.

As an irrigation and drainage consultant, he cooperates presently with institutes involved in water management in India and Argentina. The activities in India concern the design of practical guidelines to improve agricultural water management by means of modified irrigation and drainage techniques. He is a guest lecturer at the International Institute for Hydraulic and Environmental Engineering (IHE Delft, The Netherlands) and at the Aerospace Survey and Earth Sciences (ITC Enschede, The Netherlands). He lectured at the Global Energy and Water Cycle Experiment (GEWEX) NATO summerschool on Remote Sensing of Processes Governing Energy and Water Cycles in the Climate System, held at Plon (FRG), May 1995. The results of his work have been disseminated via various refereed papers. In July 1995, he received with two co-authors the annual International Association of Hydrological Sciences (IAHS) Tison-award for an outstanding publication in the field of evaporation resistances. Wim Bastiaanssen is married and has two children.